Green energy harvesting from CO_2 and NO_x by MXene materials: Detailed historical and future prospective

Hafiz Muhammad Adeel Sharif [a], Muhammad Rashad [b], Ijaz Hussain [c], Aumber Abbas [d], Obaid Fahad Aldosari [e], Changping Li [a,*]

[a] Research Center for Eco-Environmental Engineering, Dongguan University of Technology, Dongguan 523808, China
[b] Government College University Faisalabad, Pakistan
[c] Interdisciplinary Research Center for Refining & Advanced Chemicals, King Fahd University of Petroleum & Minerals, Dhahran 31261, Saudi Arabia
[d] Songshan Lake Materials Laboratory, University Innovation Park, Dongguan 523808, China
[e] Department of Chemistry, College of Science, Majmaah University, P.O. Box 66, Majmaah 11952, Saudi Arabia

ARTICLE INFO

ABSTRACT

Improving the carbon dioxide and nitrogen oxide reduction reactions (CO_2RR and NORR) can reduce anthropogenic greenhouse gas emissions while selectively producing chemicals needed for the fuel, plastic, and chemical industries. Efficient CO_2RR can be used to replace fossil fuels as well as repurpose captured CO_2, while new NORR pathways can be used to supplement or replace the energy-intensive Haber–Bosch process for NH_3 generation with no CO_2 emissions. Incorporating cocatalysts is an effective approach to enhance the performance of semiconductors in photocatalysis and electrocatalysis. Noble metals have traditionally been used as cocatalysts in photocatalysis; however, their high cost restricts their widespread application on a large scale. Therefore, this review article focuses on integrated, i.e., (photo)electrocatalytic and pure photocatalytic conversion of CO_2 and NO_x molecules into useful products, such as CO, methanol, formic acid (HCOOH), and ammonia (NH_3), using metal carbides/nitrides (MXenes) due to their advantageous features such as high surface area, tunable chemistry, and easily adjustable elemental compositions. Numerous novel materials, their preparations and performances have been discussed. Depending upon the nature of MXene-based materials, the synthesis techniques and photocatalytic mechanism of MXenes as co-catalyst are also summarized, including the strategies to enhance the catalytic activity of MXenes for target products. Notably, surface modification has emerged as a practical approach to improve the performance of MXenes further. Despite the remarkable developments, several challenges remain in using MXenes as catalysts for NO_xRR and CO_2RR. Addressing these challenges will pave the way for future advancements in this field. This review will shed light on these lingering challenges and provide insights into the future direction of MXenes development as catalysts for sustainable energy and environmental applications.

1. Introduction

1.1. Accumulation of CO_2 and NO_x in the environment and their impacts

The globe is currently dealing with severe environmental issues, and it is exponentially increasing day by day. It is imperative to cut down the existing pollution that is created by emissions and also have to devise techniques to minimize exhaust emissions [1]. The levels of carbon monoxide (CO), sulfur oxides (SO_x), carbon dioxide (CO_2), nitrogen oxides (NO_x), particulate matter (PM), and volatile organic compounds
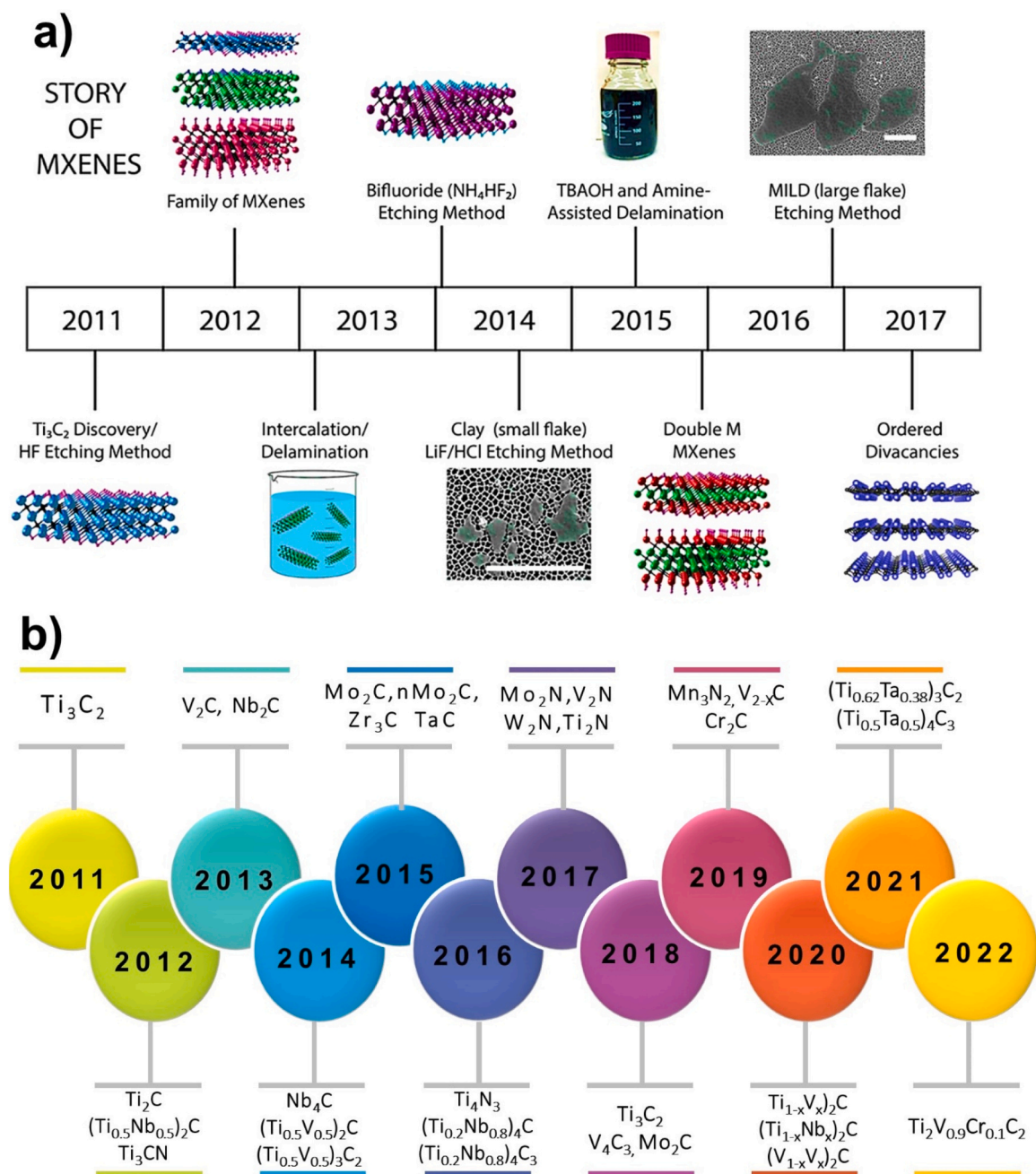
Fig. 1. a) Timeline of Mxene development from 2011 to 2020. Reprinted (adapted) with permission from Ref. [42]. B) History of synthesized Mxenes over time [43].

(VOCs) in polluted air are unacceptably high [2–4]. The direct emission of carbon dioxide into the environment is a risky proposition since carbon dioxide is primarily responsible (between 60– 63%) for the change in net irradiance among various layers of the atmosphere from 1979 to 2004 and continuing [5], and that's why, the natural greenhouse effect is getting stronger as the rising concentration of greenhouse gases in the atmosphere heats the climate of the world [6–9] which also increases the radiative force, leading to an increase in the temperature of the ocean's surface [10,11]. Researchers have been urged to develop innovative solutions in response to the challenging task of mitigating these challenges [12].

The natural ecosystem is thrown off balance if there is an increase in the concentration of acidic gases in the atmosphere, such as NO_x (NO_2, NO, and N_2O). These gases have low melting and boiling temperatures, rapidly dissolve in water, and are precursors to several harmful air

contaminants such as ozone (O_3) [13]. These contaminants enter the human body through the lungs, the skin, and the digestive tract. They cause damage to the lungs and contribute to a wide variety of respiratory disorders, including asthma, lung cancer, and chronic obstructive pulmonary disease (COPD) [14–17]. Their global emissions have increased over the previous century, primarily as a result of the actions of humans. N_2O concentrations are steadily increasing throughout the atmosphere, primarily as a result of microbial activity in nitrogen (N)-rich soils, which is directly tied to agriculture and fertilizing activities [18]. Within the troposphere, NO undergoes rapid oxidation to form nitrogen dioxide (NO_2). This compound subsequently reacts with volatile organic compounds (VOCs) and hydroxyl, forming organic nitrates and nitric acid, respectively [19].

Several decades ago, the United Nations introduced a sustainable development goal (SDG) pertaining to energy, specifically SDG11 and
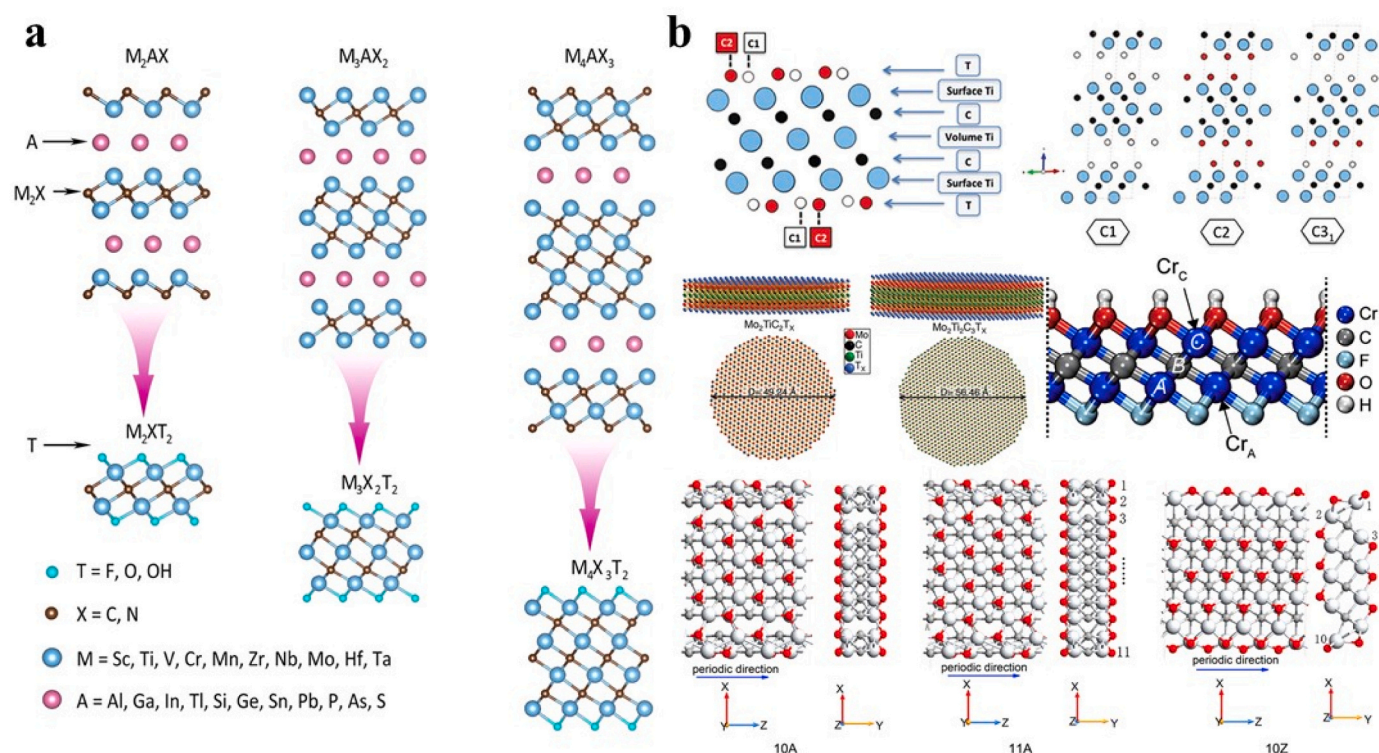
Fig. 2. a) Structure Schematic of M_2X, M_3X_2, and M_4X_3 (MAX PHASE). b) Different Structures for MXenes [44].

SDG13, which involves capturing and removing air pollutants. Theoretical estimations suggest that adherence to greenhouse gas (GHG) emission reduction plans could potentially prevent up to three million premature deaths by 2100. Furthermore, it has been recommended that aggressive measures to capture CO_2 and NO_x could prevent an estimated 0.3–0.7 million premature deaths annually. This number could potentially increase from 0.8 million to 1.8 million if the current trend of CO_2 capture is sustained [20]. The US Occupational Safety and Health Administration has established a permissible exposure limit (PEL) of 5000 parts per million (ppm) (or 0.5%) for carbon dioxide in the workplace with regard to ensuring worker safety. This limit is applicable for an 8-hour workday [21]. Despite the alarming climate change, it remains a reversible phenomenon. Additionally, implementing sustainable and clean energy practices can effectively mitigate the current environmental crisis and safeguard our planet [22].

Given the aforementioned situation, it is preferable to identify a resolution that mitigates the discharge of carbon and nitrogen-derived contaminants while concurrently generating sustainable energy. Photo/electrochemical methods have the potential to be a valuable approach for converting CO_2 and NO_x into high-energy and value-added compounds in a manner that is both cost-effective and environmentally sustainable. Implementing this measure would not only facilitate environmental remediation and prevent irreversible atmospheric damage but also yield valuable resources for the energy sector and serve as an agro-booster (in the case of NO_x exclusively), among other possible applications [23]. Numerous research endeavours have been undertaken to explore the potential of intelligent and versatile materials in mitigating the adverse impacts of NO_x and CO_2 emissions worldwide. In recent years, the physicochemical, mechanical, and electrochemical properties of Mxenes have garnered significant attention due to their association with surface terminations and elemental compositions.

In this comprehensive review article, we explore the potential of photo-electrocatalytic and photocatalytic methods as promising solutions to significant challenges in the field. Specifically, the attainable environmental application concludes adsorption, photo catalysis, a topping surface filtration system to eliminate various pollutants, and adsorption utilizing Mxenes as adsorbing systems to exclude natural and inorganic contaminants. The adsorption process not merely depends on the properties of the adsorbent but also environmental factors like pH, temperature, and the occurrence of organic derivatives. However, an inclusive exploration of the amputation of various environmental contaminants from Mxenes has yet to be undertaken. As a result, studying the adsorption and interaction of hazardous contaminants with Mxene-based materials is particularly important and intriguing. The major goal of this paper is to stipulate a better comprehension of the adsorption of various pollutants using various approaches. Hence, this review paper presents significant developments of Mxenes, from its exploration to the latest endeavours, emphasizing the different synthesis processes as well as the importance of data characterization. Moreover, this review summarizes the findings and characteristics of this category of compounds, as well as implementations to the deployment of Mxene-based nanomaterials for expelling harmful pollutants due to excellent contact area, greater specificity, reusability, and appealing mechanical characteristics. These attributes will surely assist in developing the suitable materials for specific purposes, as well as expedite the progression of Mxenes in the remediation of the environment from hazardous pollutants. Overall, this review article sheds light on significant trends and lessons learned in (photo)electrocatalytic and photocatalytic research, emphasizing the potential of Mxene catalysts to advance next-generation technologies with reduced energy consumption and greenhouse gas emissions.

1.2. A brief history of Mxene (new wonder materials)

Since the initial discovery of graphene, a two-dimensional (2D) material, in 2004, there has been a significant amount of research conducted on 2D materials due to their exceptional photo electronic and electrochemical properties [24,25]. Two-dimensional (2D) materials typically exhibit a notable specific surface area, rendering them suitable as a substrate for catalyst growth and impeding catalyst aggregation. This novel category of materials has demonstrated significant utility across diverse academic domains due to their exceptional electrical,
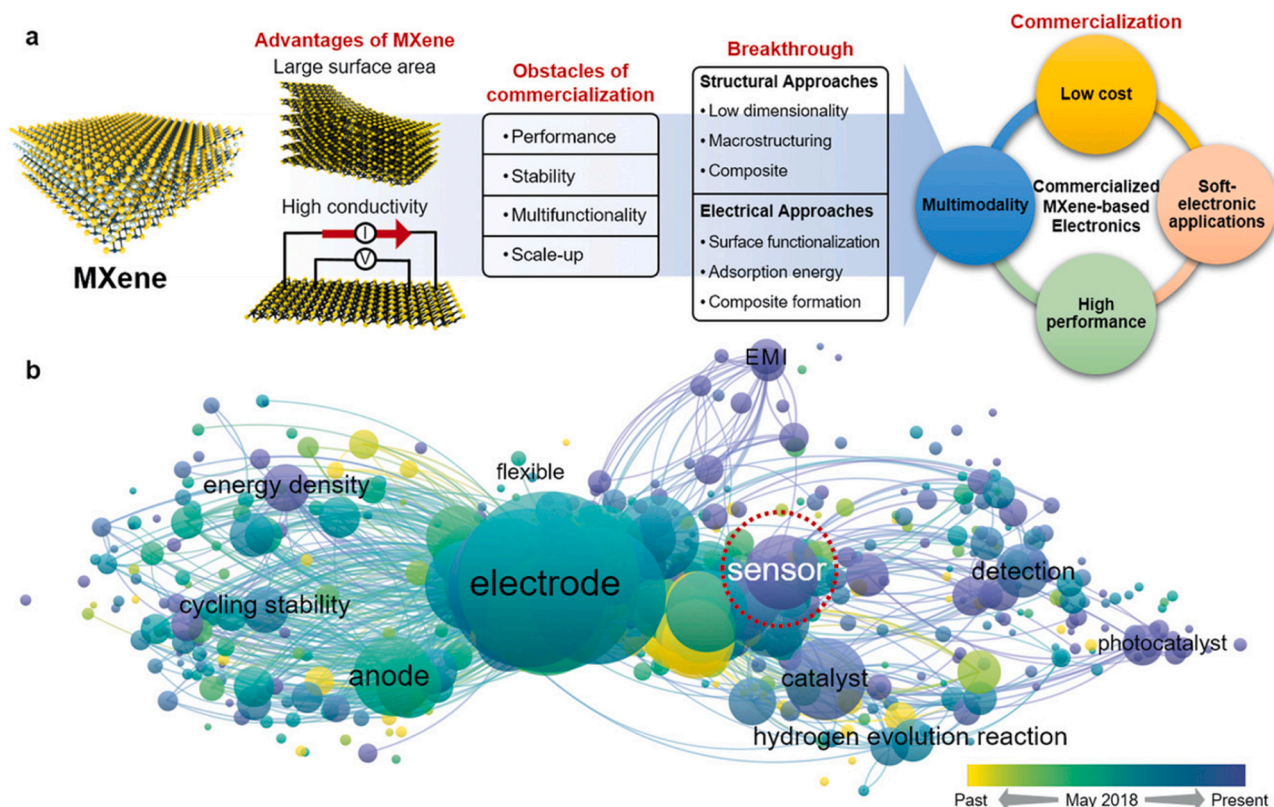
Fig. 3. a) A flowchart of the electronics based on MXene's development process is shown. b) The visual representation of current MXenes research trends and associated keywords. The relevance of keywords, frequency of their appearance, and the average publication date are represented by the lines connecting two keywords, size of circle of each keyword, and color of circle, respectively [26].

mechanical, and biological attributes, such as their elevated electrical conductivity, dispersibility in water, extensive specific surface area, antimicrobial efficacy, effective electromagnetic interference (EMI) shielding, and heightened energy capacity [26]. The Mxene material, which falls under the 2D category of transition metal carbides and/or nitrides, has garnered significant interest. Its discovery dates back to 2011 when it was identified in the Ti_3AlC_2 MAX state [27,28]. These materials are esteemed as the epitome of next-generation luxury in the realm of two-dimensional (2D) substances, as they boast unparalleled physicochemical properties that make them ideal for a plethora of wealthy applications, including but not limited to photocatalysis, electrocatalysis, supercapacitor, lithium-ion battery, and biomedicine [29–32]. A diverse array of over 50 Mxene species were synthesized through the utilization of various M and X atoms in varying quantities, thereby yielding a broad spectrum of functional capacities [33–35]. Fig. 1a depicts the publication trend of Mxene and Mxene composite in scholarly literature. The research community has shown a significant interest in Mxene in recent years, as evidenced by the rapidly increasing number of studies on this topic. Fig. 1b depicts a brief chronology of Mxenes, while Fig. 2 visually represents the diverse MAX phases and Mxenes structures. The transformation of the MAX phase into an Mxene structure is evident through etching the A atom. Mxenes have demonstrated significant utility across diverse domains, including their ability to enhance the distinctive characteristics of polymeric composites. Thus, it is imperative to consider their fundamental function in proficient polymeric nanocomposites. Moreover, Mxene is regarded as a competitive candidate for other 2D materials and has been widely explored for various photocatalytic applications, including water splitting [36,37], CO_2 reduction [29,38], pollutant degradation [39,40], and N_2 fixation [41].

In contrast to other 2D materials like graphene, researchers at Drexel University created a 2D material in 2010. However, little attention was given to this material at the time. The material known as "Mxene" was coined by Michel W. Barsoum and Yury Gogotsi, researchers at Drexel University's A.J. Drexel Nanomaterials Institute. This nomenclature was derived from etching and exfoliating atomically thin layers of aluminum from layered carbides, also known as "MAX phases," as depicted in Fig. 2a-b. Recent scientific and theoretical study has shown that MXenes have a lot of potential because of their chemical nature, strong electrochemistry, and high hydrophilicity [45,46]. The current state of MXene-based materials for CO_2 reduction reaction (CO_2RR) and environmental remediation is characterized by an absence of literature. This can be attributed to the fact that the development of MXene is still in its nascent stage and undergoing continuous refinement. MXene's production method, characteristics, and potential applications in energy conversion and storage were the primary topics of the published papers. The present review is deemed imperative for the scientific community concerned with MXenes-based substances, as there exists no all-encompassing summary of the literature pertaining to the role of these materials and their parameters in augmenting their photocatalytic and electrocatalytic CO_2RR and NO_xRR performance. Using MAX as a starting material, the Ti_3AlC_2 phase was placed in an HF solution to create the first member of MXene, Ti_3C_2. Using selective etching techniques, numerous kinds of MXenes are fabricated. MAX-layered networks are best created using uninterrupted out-diffusion since A layers are typically less stable than MAX layers. The process of generating MXene through the exfoliation of the MAX phase has not been observed to be impacted by the presence of molten metals or salts.

In the end, MAX phases were introduced into HF, which caused MAX multi-layers to emerge while simultaneously rejecting A layers. The presence of surface functional groups, such as -O, -F, and -OH, on MXene nanosheets has been observed to facilitate the production of semiconducting functionalized MXene. It should be noted that $M_{n+1}X_nT_x$ represents the pure MXene, while $M_{n+1}X_n$, also known as [Ti_3C_2], and

denotes the metallic material [47]. Three unique kinds of MXene-based materials have been identified based on their atomic lattice (M) and chemical modification: ordered mono-M, ordered double-M, and solid-solution-M. In order to selectively etch their MAX/non-MAX precursors, the majority of MXenes are created from the bottom up utilizing chemical transformations. It's easier, cheaper, and yields more than other ways. MXene is regarded as a groundbreaking two-dimensional material across multiple academic disciplines [26]. So, a lot of work has been done to see if MXenes can be used in different types of sensors, such as chemical, biological, mechanical, and visual sensors. Machine learning models were trained to predict key parameters related to OSCs, such as energy level (HOMO and LUMO), UV/visible absorption maxima in solution and film states, and power conversion efficiency (PCE). About 5000 new SMAs were designed and screened based on the predicted properties [48,49]. A lot of active surface sites are provided by MXene's 2D structure, which is favourable to functionalization employing various terminal groups. These locations have the potential to act as a sensory platform that is highly receptive to a variety of stimuli from the outside world. In addition, the desirable attribute of achieving low noise in sensory responses can be attributed to the high electrical conductivity of MXenes. Hence, the aforementioned attributes serve as evidence of MXenes' potential as a viable substitute sensor material that can attain heightened sensitivity, remarkably reduced limit of detection (LOD), and minimal detectable quantity of analytes in diverse sensor implementations. Last but not least, MXenes are further favourable in processing since their water dispersibility makes it easier to fabricate and modify them in an environmentally responsible manner (Fig. 3a). A number of recent studies on MXene-based sensors were conducted to construct various structural and electrical methods to take use of MXene's exceptional features and improve sensor performance. For instance, MXene macrostructuring can boost sensor sensitivity and minimize LOD [50]. Fig. 3b depicts the interrelatedness of keywords in 2375 research papers centred on MXenes, which have been published subsequent to their discovery in 2011.

In contrast to its counterparts in the realm of two-dimensional materials, MXene has swiftly gained recognition as a potential "wonder-material" since its inception in 2011 [51,52]. The remarkable properties exhibited by MXene have resulted in its widespread utilisation and considerable attention across diverse domains. MXene-based materials have been successfully applied as catalysts [53,54], in ion sieving [55], in FET (field-effect transistors) [56]. MXene exhibits several limitations that researchers are actively attempting to mitigate GHG's. This article provides an overview of the recent developments in MXene-based materials that exhibit various functionalities of energy storage. Additionally, it discusses the potential applications of MXene materials and their interfaces in the context of utilizing single C/N (CO_2 and NO_x).

1.3. Overview of CO_2 reduction techniques

Secondary pollutants are produced as a result of the combustion of fossil fuels, which releases energy and CO_2 while interacting at high temperatures. With its lengthy atmospheric retention period, CO_2 contributes to over 81% of greenhouse gas emissions [57]. For the capture and storage of carbon dioxide as well as its use in other processes like the creation of sustainable energy, several strategies have been proposed. CO_2 separation methods include absorption and adsorption. The utilization of amine scrubbing for the absorption of CO_2 from flue gases is a conventional approach within the realm of carbon separation technologies. Due to a few technological issues, this technology cannot be used effectively. On the other hand, there are several reasons why adsorption is better than absorption. The absorption technique is a commonly employed post-combustion method utilized to separate carbon dioxide from power generation facilities and chemical manufacturing operations. The aforementioned procedure is executed through diverse techniques, including chemical and physical absorption. The utilization of chemical absorption technology for carbon dioxide (CO_2) capture has

gained widespread adoption due to its compatibility with existing power plants and relatively lower operational expenses than alternative absorption technologies [58]. In physical absorption, the entire process occurs without any chemical reaction between the liquid absorbent and CO_2. The desorption process, on the other hand, is accomplished by adjusting the pressure or temperature depending on the specific absorption liquid used [59]. While amine-based absorption technology is widely employed, it does have certain limitations, particularly in terms of energy consumption during the regeneration process [60]. Additionally, the breakdown of the amine molecule significantly influences the kinetic rate and CO_2 absorption capacity [61]. The considerable susceptibility of these entities leads to the depletion of a substantial quantity of chemicals and water, thereby exposing the ecosystem to potential harm [62].

Adsorption, which follows after the disadvantages of absorption techniques, is the other way. Adsorption is considered a favourable method due to its diverse operational phenomena, effectiveness in dilute gas mixtures, greater capacity for CO_2 capture, faster processing, and absence of water. Additionally, it is noteworthy that adsorption is influenced by operating conditions such as temperature and pressure [63]. Adsorption, an alternative method to address the drawbacks of absorption techniques, is considered favourable for several reasons. It offers flexibility in terms of operating conditions such as temperature and pressure, does not require the presence of water, demonstrates effectiveness in capturing CO_2 from dilute gas mixtures, has a higher capacity for CO_2 capture, and generally allows for a faster process [64]. Zeolites, activated carbon, silica material, and MOFs (metalorganic frameworks) are a few examples of typical adsorbents used for the adsorption of CO_2 [65].

Due to its (Mxene) environmental friendliness, less need for energy, lower capital expenditure, better use of available space, and greater applicability in remote places, membrane technology has been widely employed for CO_2 separation [66]. For separating CO_2 from flue gas throughout the past few decades, membranes have drawn significant interest. The crucial factors in membrane development are permeability and selectivity, as the effectiveness of CO_2 separation is highly contingent upon these variables [66]. With these parameters in mind, various membrane types have been developed, including ceramics, polymers, inorganic membranes, mixed matrix membranes (MMMs), carbon molecular sieve membranes (CMSMs), and microporous organic polymers (MOPs) [67]. Although CO_2 capture methods based on adsorption, absorption, and membrane separation have shown promise and are somewhat efficient, they are also expensive to operate and maintain due to their high energy requirements. Even though TSA is now utilized extensively for the regeneration of CO_2-loaded adsorbents, ESA has a number of advantages over TSA, including a lower heat need and a faster rate of heating. As a result, it is essential to take note of ESA. Notwithstanding, there remains a need for the creation of appropriate adsorbents that possess a high capacity for CO_2 adsorption. [68]. The conversion of carbon dioxide into valuable C-based commodities and the transformation of industrial ammonia production are two significant scientific endeavours that hold promise in addressing pressing global concerns related to energy and greenhouse gas emissions.

1.4. Overview of NO_x reduction techniques

EPA Report 450/1–78-001 contains a compendium of NO_x control strategies devised for the United States Environmental Protection Agency (EPA) [69]. Pretreatment, a preventative method to reduce NO_x creation, is the initial strategy for reducing NO_x emissions. Pretreatment decreases NO_x emissions from entering input materials (fuel, oxidizer, and/or material being heated) [70]. Using additives, switching the oxidizer, switching the fuel, and switching the product are a few possibilities. These won't be further studied because they are typically not workable possibilities at most refineries. The reduction of NO_x formation can be achieved by eliminating any nitrogen that could potentially be
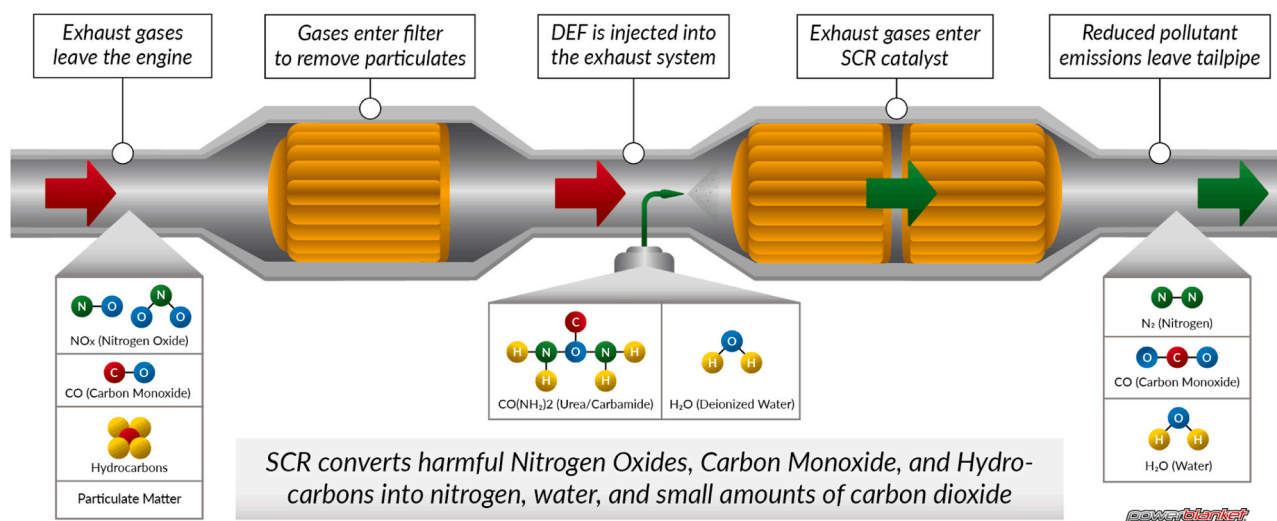
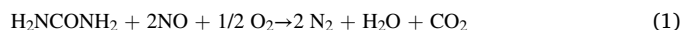**Fig. 4.** Air pollution (NO_x) reduction with SCR technology [74].

present in the feed materials. California and Texas are known for implementing some of the most stringent regulations within the United States, and it is anticipated that other regions will emulate their approach. According to federal NO_x reduction regulations, many states have created State Implementation Plans (SIP). Combustion modification, the second method for lowering NO_x, aims to stop NO_x from developing by altering the combustion process. The combustion process has been altered for reduced NO_x using a variety of techniques. A common technique uses low NO_x burners, specially engineered burners that produce less NO_x than earlier burner technologies.

Flue gas recirculation, fuel and/or air staging, pulse combustion, and advanced mixing are a few methods that low NO_x burners may use to reduce NO_x. Techniques for air preheat reduction, staging, gas recirculation, reburning, and other common combustion modification methods [70]. NO made up the majority of the NO_x during combustion operations, with minor levels of nitrogen dioxide (NO_2) and nitrous oxide (N_2O). The oxidation of NO to NO_2 in the atmosphere leads to the formation of acid rain and smog through its reaction with other atmospheric pollutants, including moisture and volatile organic carbons [71]. Chronic bronchitis, dyspnea, and pulmonary edema are some of the adverse effects of these substances on people. The pre-combustion process can be regulated by decreasing the nitrogen concentration in the fuel through fuel refinement. Combustion modification is a technique employed to regulate NOx emissions by manipulating the operational parameters to attain the least feasible concentration [72]. The combustion modification technique was employed by Makansi et al. to attain a reduction efficiency of up to 50%. However, it is noteworthy that contemporary emission standards necessitate the complete clean-up of flue gas [73]. The operation and maintenance of many of these approaches in industrial furnace conditions are not simple and require a certain level of sophistication. A catalyst is needed for catalytic reduction procedures, for instance, and over time, contaminated flue gases may clog or poison the catalyst. The methods used for post treatment frequently need a significant investment of resources. In the event of a malfunction of the treatment equipment, it is typically necessary to suspend production. Furthermore, it is typically observed that post-treatment procedures do not confer any advantageous effects on the production process. As an illustration, it does not augment production or enhance energy efficiency and is solely an additional expense.

SCR is a proven NO_x abatement method with moderate temperature ranges (200–500 °C), the system requires more capital investment and operational costs. A removal efficiency of more than 75% of NO_x can be attained with this approach. The selective catalytic reduction (SCR) technology facilitates the conversion of nitrogen oxides (NO_x) that are

present in the flue gas stream into nitrogen (N_2) and water (H_2O) through a catalytic process. The use of SCR procedures can lead to a number of issues and difficulties. Introducing a catalyst into the system results in a pressure drop, causing a rise in the power demands of the gas-handling equipment. When burning liquid fuels, such as leftover oil, the catalyst may become clogged or contaminated in unclean exhaust streams. To achieve effective mixing, the ammonia must be properly injected into the flue gases at the correct temperature window and position, and it must be injected in the right quantity to provide the desired level of NO_x reduction without letting any unreacted ammonia pass through. A consistent window of operation is necessary for SCR systems to operate at their best efficiency, hence they are not very tolerant of continually changing conditions. Dealing with the used catalyst is another issue. The cost of regeneration may be more than purchasing a new catalyst, yet it is often the most financially viable option. The expenditure associated with the disposal of the utilized catalyst may be substantial due to its frequent categorization as a hazardous waste, particularly when the catalyst comprises vanadium, which is frequently observed. According to a study conducted by the Environmental Protection Agency (EPA), the selective catalytic reduction (SCR) method was determined to be the costliest approach for reducing nitrogen oxide (NO_x) emissions [70]. A typical schematic SCR with significant NO_x reduction steps is represented in Fig. 4.

Secondly, Selective Non-Catalytic Reduction (SNCR), also known as Thermal DeNO$_x$, reduces NO_x without a catalyst at high temperatures (900–1000 °C). Ammonia and urea are frequently employed as reducing agents in this particular procedure. Complex chemistry and free radical reactions make SCR chemical reactions similar. The reduction of NO_x using urea as a reducing agent can be represented by the following overall reaction (Eq. 1):

$$H_2NCONH_2 + 2NO + 1/2\ O_2 \rightarrow 2\ N_2 + H_2O + CO_2 \qquad (1)$$

The operating cost of SNCR is comparatively lower than that of SCR due to the additional benefit of not utilizing costly catalysts. The SNCR has some drawbacks. The first is that post-treatment methods, such as low NO_x burners, are typically more expensive. Whilst the implementation of Selective Non-Catalytic Reduction (SNCR) technology may result in a reduction of nitrogen oxide (NO_x) emissions, it is important to note that there is a possibility of an increase in other unfavourable emissions such as carbon monoxide (CO), nitrous oxide (N_2O), and ammonia (NH_3). This is due to the potential occurrence of unreacted injected chemicals slipping through the exhaust, commonly referred to as "ammonia slip". The utilization of ammonia (NH_3) in SNCR raises safety apprehensions about its transportation and storage. One of the
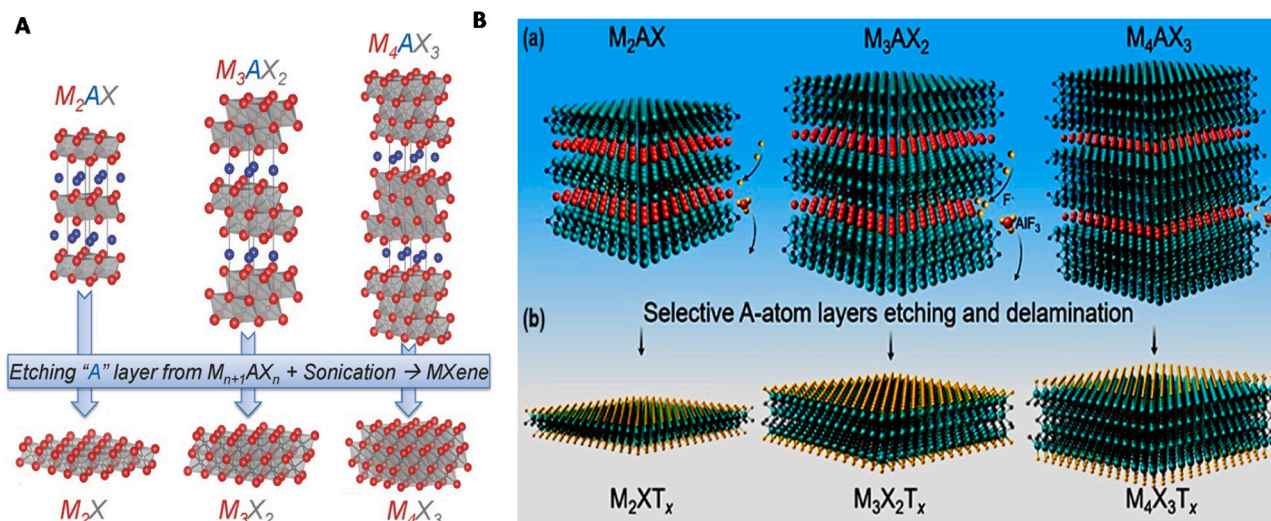
Fig. 5. (A) The MXenes that correspond to MAX phases in terms of structure [86]. (B) The synthesis of precursors for MXenes. (a) The present study discusses three distinct categories of Mono-M MAX phases, namely M_2AX, M_3AX_2, and M_4AX_3, along with the process of selective etching of the A-group layers (red atoms). (b) The production of surface terminations, denoted by the yellow atoms, is a necessary step in the synthesis of MXenes through selective etching [87].

primary obstacles associated with this technology pertains to identifying the appropriate stage for introducing the chemicals. The chemicals must be introduced, when the flue gases are within a relatively restricted temperature range to ensure optimal efficiency. Additionally, it is crucial to administer the appropriate quantity of chemicals, as an excessive amount may result in some chemicals slipping through unreacted, while an insufficient amount may not yield adequate NOx reductions [75,76]. Furthermore, achieving sufficient mixing of the chemicals with the flue gas products is essential, necessitating both good mixing and residence time to enable the reactions to reach completion [70].

However, this review elaborates on the synthesis of MXene, its tailoring by the addition of various metals, functional groups as well as the factors that govern the characteristics of MXene. Finally, it explained inclusively the MXene applications for transforming greenhouse gases (GHG's; CO_2 and NO_x) into green energy. This will not only lead towards cutting down pollution but also enlighten the harvesting of green energy, which is a practically sustainable approach to treat the real exhaust emission towards a green environment.

1.4.1. Challenges in existing techniques for CO_2/NO_x mitigation

The engineering perspective has been utilized to provide an overview of potential options for mitigating CO_2 emissions. Several mitigation strategies have been put forth, and they can be categorized into three groups: **1.** decrease of energy intensity; **2.** reduction of carbon intensity; and **3.** carbon sequestration. This paper provides a comprehensive review of several mitigation options, with a particular emphasis on carbon sequestration strategies.

Energy savings result from a decrease in energy intensity. Turning to sources of energy with fewer GHG's contents could reduce the intensity of carbon emissions. According to the IPCC's 2001 report, the global potential for reducing emissions due to energy intensity is between 1900 and 2600 metric tons of carbon dioxide equivalent in 2010 and between 3600 and 5050 metric tons of carbon dioxide equal per year in 2020. Implementing these solutions has economic benefits and no adverse effects. The augmentation of CO_2 natural sinking rates and the direct release of anthropogenic CO_2 are the two categories into which the carbon sequestration options can be categorized. In the first category, there are several applicable sequestration options, such as enhancing rock weathering, ocean fertilization sequestration, and terrestrial vegetation sequestration. The direct discharge alternatives entail capturing and separating CO_2 emissions from significant point sources,

such as thermal power plants. The separated CO_2 is subsequently conveyed and injected into underground or oceanic repositories. Despite the relatively higher cost per unit of CO_2 reduction associated with sequestration options in comparison to alternative methods, it is imperative to prioritize the advancement of technical capabilities in this domain for the following justifications: **1.** There exists a substantial capacity for carbon sequestration. **2.** Carbon sequestration facilitates the uninterrupted utilization of fossil fuels, which is inevitable until the transition to renewable energy sources is achieved. Depending on the location, duration, and volume of sequestration, each approach offers pros and cons regarding capacity, cost, time of sequestration, stability of sequestered CO_2, and extra environmental implications. Thus, reliable evaluations of the mitigation efficiency are essential for each sequestration option upon implementation [77]. Efficient photocatalysts or electrocatalysts that possess long-term stability play a crucial role in the selective conversion of CO_2 into energy-rich molecules and NO_3^- into NH_3. These catalysts can potentially address the global energy demand and mitigate environmental issues, offering a promising solution for future energy sources. Transition metal (TM)-based catalysts, known for their variable oxidation states, are essential in improving catalytic activity within this context [78]. For this issue, MXene is a potential choice, exhibiting distinctive characteristics such as a substantial surface area, adjustable charge distribution, notable inter-layer spacing, and abundant reactive surface sites accompanied by surface functional groups. These attributes render it a favoured catalyst for CO_2 and NO_x reduction reactions (CO_2RR and NO_xRR) in photo-catalytic and electro-catalytic applications [79]. Transition metals (TM) can effectively initiate electron transfer due to their occupation of d–orbitals with comparable energy levels to the highest occupied molecular orbital (HOMO) and the lowest unoccupied molecular orbital (LUMO) of CO_2 and NO_x. As a result, research and structure of engineered-based multifunctional materials are the constant attention of the scientific community. Recent studies have demonstrated that MXenes can be efficient catalysts for the photocatalytic and electrocatalytic reduction of CO_2 and NO_x due to their extraordinary electronic, mechanical, and optical properties as well as their alternating carbon and hydrogen coordination with reaction intermediates, which disrupts the scaling relationships on TM active sites [78].
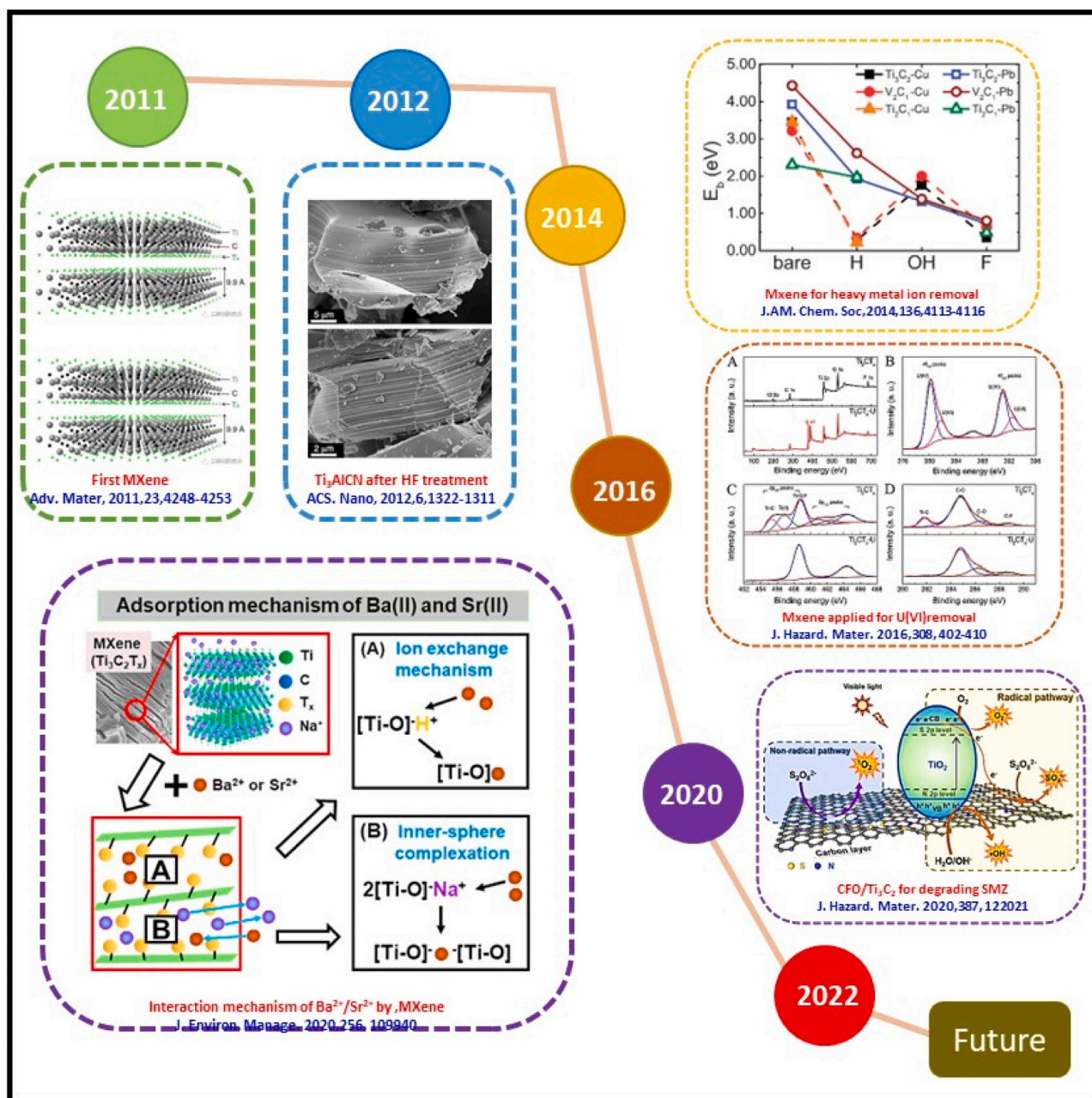
Fig. 6. Advancements of MXene synthesis from its birth (2011) to now.

2. Advancements in MXene synthesis

2.1. MAX phase and earlier MXene/discovery

In general, the synthesis of MXene involves the selective etching of specific atomic layers (such as Al, Si, and Ge) from the parent MAX phase, utilizing either HF or a combination of strong acid (HCl) and fluoride salt (NaF, LiF, and NH_4F) [34]. The materials comprising GHB encompass a diverse range of essential constituents, including carbides and nitrides. These constituents can be synthesized in their purest form, with the M, A, and X components denoting an initial transition metal such as Ti, Nb, V, Ta, and so on [80]. The structural formula of MXene is represented as $M_{n+1}X_nT_x$, wherein M denotes the early transition metal (such as Ti, V, Zr, and Nb), X signifies the C and/or N elements, and T represents the surface functional groups (e.g., –O, –OH, and –F) [81, 82]. To put it another way, the MAX phase structure can be thought of as two-dimensional (2D) layers of early transition metal carbides and/or
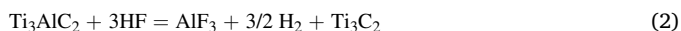
nitrides that are "glued" with an A element (Fig. 5 A) [83,84]. M_2AX, M_3AX_2, and M_4AX_3 are three different kinds of MAX phase structures displayed in Fig. 5Ba. At temperatures above 1300 °C in a controlled atmosphere, MAX phases are often created by reactively sintering their elemental powder in stoichiometric ratios, such as 3 M:1 A:2 C for M_3AC_2. Mechanical exfoliation is difficult because the M-A bonds are the main bonds. These bonds exhibit relatively lower strength than the M-X bonds, thereby facilitating targeted chemical etching of the A constituent while preserving the integrity of the M-X bonds [85]. Transition metals are uncovered in $M_{n+1}X_n$ after selective removal of the A-group layers. Upon exposure, M-elements undergo termination with surface functional groups (T_x), resulting in the formation of the chemical formula ($M_{n+1}X_nT_x$) (Figure 5B(b)). Due to MXenes' top-down synthesis approach, the $M_{n+1}X_n$ composition is derived by the composition of their MAX phase precursors, as shown in Fig. 4B(a–b).

Seventy MAX phases have so far been developed, with Ti-based MXene like $Ti_3C_2T_x$ and Ti_2CTdisplaying a variety of environmental

applications. Many applications have been found for carbides, nitrides, carbamates, and MXene based on the element titanium. On the other hand, it has been established that the production of carbamates and nitrides is exceedingly challenging, thereby restricting their application in the field of environmental remediation [88]. To date, over seventy types of MXene have been identified since its discovery. However, only a limited number of these (20 varieties) have been applied significantly, with Ti_2C and Ti_3C_2 being particularly noteworthy. The existence of other MXene variants, such as V_4C_3Tx and Nb_2CTx, has only been revealed through theoretical calculations [89]. In addition to other properties, MXene possesses an exceptional specific surface area, superior chemical performance, and sensible thermal conductivity.

Environmental factors, including pH, temperature, and the presence of natural molecules in addition to the characteristics of the sorbent, are what control the sorption technique. pH affects the surface charge of MXene, altering its electrostatic interactions with target molecules. It can also influence ion exchange processes and chemical reactions on the MXene surface. Temperature impacts sorption kinetics and thermodynamics. Higher temperatures can accelerate sorption but may also increase desorption rates. Temperature can impact the thermodynamics of sorption, influencing factors such as sorption capacity and selectivity. Some sorption processes are endothermic, favouring them at higher temperatures, while others are exothermic. Moreover, natural molecules in the environment can compete with the target species for sorption sites on the sorbent. This competitive sorption can reduce the sorption capacity for the target species. To control sorption techniques with their practical applications, it is crucial to consider and optimize these environmental factors [89].

Moreover, the surface of 2D MXene sheets has been modified with metal oxide, sulfides, and alloys, as reported in academic literature sources [90–93], and has also been explained in the later sections. This modification has led to improved conductivity and structural stability, resulting in enhanced cycle and rate performances. For example, Liu et al. [94] used the Van der Waals interaction to build TiO_2 nanorods on MXene nanosheets, and the material performed well in LIB. TiO_2-based materials have been found to exhibit excellent performance as anodes for lithium-ion batteries. These materials are produced through the direct oxidation of Ti-based MXenes, such as Ti_3C_2Tx or Ti_2CTx, using H_2O_2 or through high-temperature treatment [85]. The preparation of Ti_3C_2Tx was conducted by extracting Al layers from the Ti_3AlC_2 phase, as reported in a groundbreaking experiment [75]. The present study illustrates the chemical reactions that occur between solutions of HF and Ti_3AlC_2.

$$Ti_3AlC_2 + 3HF = AlF_3 + 3/2 H_2 + Ti_3C_2 \tag{2}$$

$$Ti_3C_2 + 2 H_2O = Ti_3C_2(OH)_2 + H_2 \tag{3}$$

$$Ti_3C_2 + 2HF = Ti_3C_2F_2 + H_2 \tag{4}$$

Reactions (3) and (4) result in the formation of -OH and -F terminals, respectively. After being separated by centrifugation, the solids were then rinsed with water. Multilayered structures are present in MXenes prior to delamination. To create single- or few-layer MXenes, the material was subsequently processed using sonication and DMSO intercalation [86]. Hexagonally close-packed (HCP) is the most common crystal structure for MXenes. In 2012, Enyashin et al. [87] investigated and researched the atomic networks and consistency of $Ti_2C(OH)_2$ and $Ti_3C_2(OH)_2$. The initial etching agent utilized was hydrofluoric acid (HF), [95,96], but the fact that this material is extremely dangerous, however, makes it noteworthy that it poses a severe threat to the environment. Thus, multiple etchants were needed. A more optimal amalgamation of hydrochloric acid (HCl) and lithium fluoride (LiF) was presented in the year 2014 [97]. The problem still exists, nevertheless, because HF gases are produced on-site [98]. HF wasn't used because people came up with other ways to solve the problem. To address the high demand for etchants that are less damaging than HF combination,
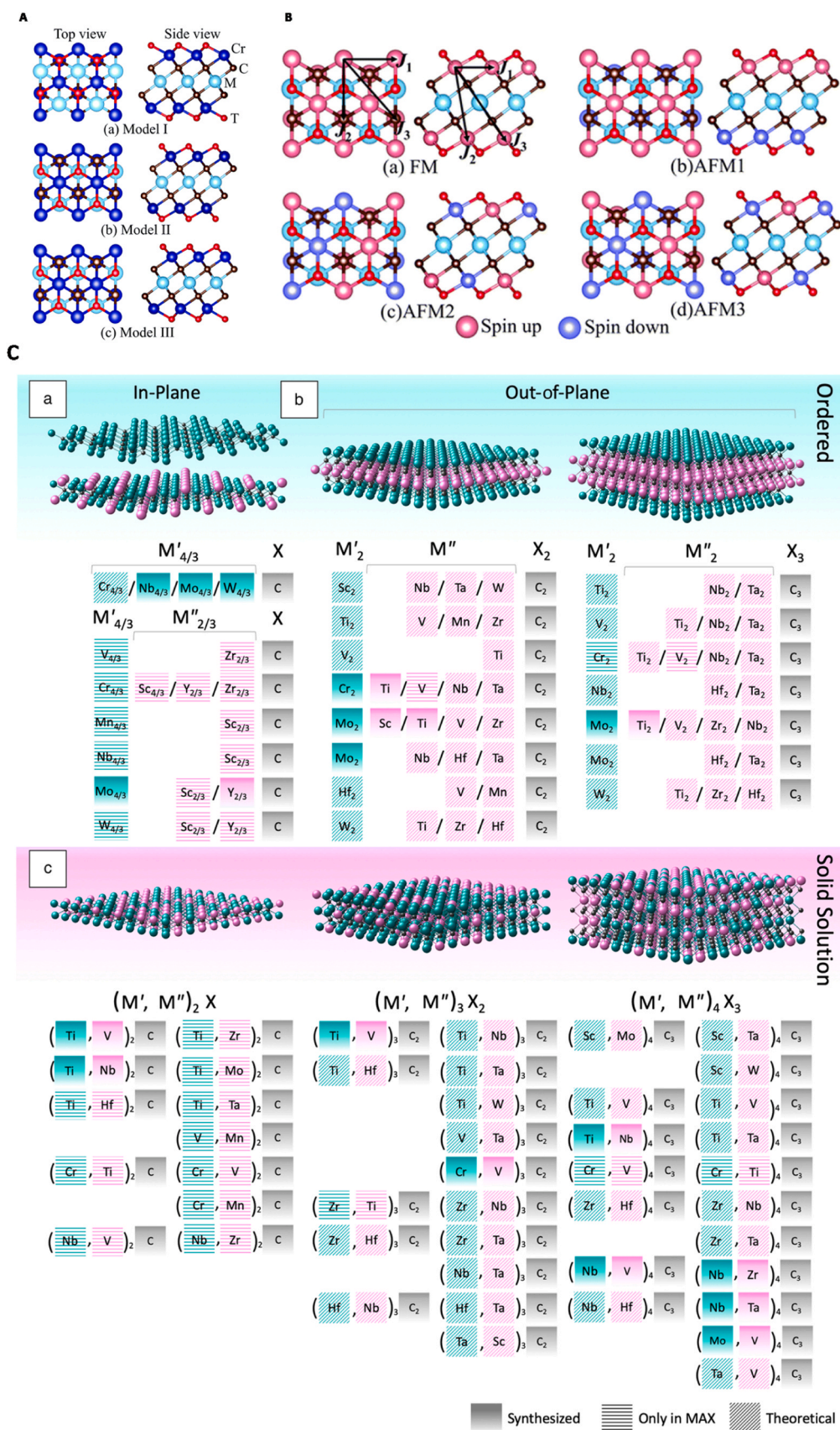
as emphasized in, a variety of researchers have developed and unveiled unique etching processes that use ammonium ion fluoride or HCl with LiF rather than HF resolution, as displayed in 6.

Recent years have seen an increase in interest in MXene preparation techniques, with numerous techniques falling into two main categories: top-down methods (such as etching from MAX or non-MAX precursors) and bottom-up approaches (such as chemical vapor deposition (CVD) [89]. Several research findings have extensively covered the overall background of MXene manufacturing, and they claim that preparation of MXene has progressed through a sequence of development beginning in 2011 when MXene was revealed for the very first moment by researchers at the University of Drexel [85]. The described engraving process used a solution of 50% concentrated hydrofluoric acid (HF), which is still among the most frequently utilized and efficacious etchants now [99]. Post their release, supplementary ranges of stacked MXenes with various rudiments of MAX intermediates were created using the moist substance engraving method. By inserting massive organic chemicals, like CH_4N_2O(urea), C_2H_6OS (dimethyl sulfoxide), C_3H_9N (isopropyl amine), and $C_{16}H_{37}NO$ (tetrabutylammonium hydroxide) in between strata, intercalation, which is a component of the delamination phase, was used to synthesize single-layered MXenes. In general, MXenes can be easily synthesized by using different methods (Fig. 5), such as the etching method and delamination method. The etching method is further divided into (a) hydrofluoric acid (HF) etching and (b) in situ hydrofluoric acid, while the delamination method is divided into (a) intercalation and (b) sonication [100].

The MXenes were initially obtained by selectively removing the A layers from an MAX phase material. The nomenclature of the MAX phase is based on the typical chemical formula given above, where M and X denote identical elements as observed in the MXenes, while A typically represents an element from group IIIA or IVA, such as Al or Si [42,86]. The metal is packed closely with the X atoms filling the octahedral interstitial spaces in the hexagonal P63/mmc layered structure of the MAX phase [92]. The covalent, metallic, and ionic natures of M-X bonds are mixed with those of M-A bonds, which are metallic in constitution. By leveraging the disparities in bonding strengths among the MAX phases, it becomes feasible to achieve targeted etching of the A layer [100]. A hexagonal-close packed structure is what the resultant MXene looks like overall. However, depending on the MXene stoichiometry, the metal atom's ordering alters.

2.2. Single and double metal-based MXene and their properties

The simultaneous improvement of structural stability and the elimination of contaminants may be accomplished by modifying MXenes with other materials [101]. According to our knowledge, numerous studies have centred on the usage of nanomaterials with a carbon basis [102,103], nZVI [104,105], LDHs [106,107], MOFs [108,109]. The utilization of titanium dioxide (TiO_2), graphitic carbon nitride (g-C_3N_4), and oxide materials has been proposed as a viable means of modifying MXenes to improve the elimination of environmental pollutants. This is achieved through the enhancement of stable sites and surface area [110–112]. The physicochemical properties of MXenes have garnered significant interest due to their versatility and exceptional characteristics. Notably, these materials exhibit promising potential for durable supports for single-atom catalysts [113]. The synthesis of a mono-layer of single-phase MXene presents a significant challenge to researchers. As a result, MXenes have been categorized into two types: double transition metal (DTM) MXene, where the symbol D denotes two distinct transition metals represented by M' and M'' [87,114]. Two types of MXenes were investigated in the study: (i) multi-TM MXene, which contains multiple transition metals, such as Ti, V, and Nb, and is denoted as $Ti_{2-3}V_{1-2}Nb_1$-2 C, with x representing the surface termination, and (ii) mono-TM MXene, which only contains a single type of transition metal, such as Ti, V, or Nb, and is denoted as Ti_2CTx, V_2CTx, Ti_3C_2Tx. The sole distinction between DTM MXene and mono-transition metal MXene is

Fig. 7. (A)Top and side views of different termination configuration models for DTM MCr$_2$CT$_x$. (B) Top and side views of possible magnetic order configurations for DTM MCr$_2$CT$_x$: (a) FM, (b) AFM1, (c) AFM2, (d) AFM3. The spin exchange paths are marked in (a) [114]. (C) Experimentally synthesized and theoretical double transition-metal (DTM) M$_2$X, M$_3$X$_2$, and M$_4$X$_3$ MXenes. The green and purple elements correspond to M′ and M″ transition metals, respectively. (a) In-plane order (M′4/3 M″2/3X shown below) and in-plane divacancy order (M′4/3X shown above). (b) Out-of-plane order (M′2 M″X2 and M′2 M″2 ×3). (c) Solid-solution MXenes are disordered, with M′ and M″ transition metals occupying random sites [87].

the occupancy of metal sites, wherein two transition metals are present in DTM MXene instead of one in mono-TM MXene [115]. Double transition metal MXenes with inherent magnetic characteristics were created by Zhang et al. [114]. Based on the chemical formula of M$_2$C (M = Sc, Y, Ti, Zr, Hf, V, Nb, Ta, Mo, W), they created and thoroughly examined 50 double transition metal (DTM) MXenes MCr$_2$CTx (T = H, O, F, OH, or bare). They further emphasized that the DTM MXenes have attained ferromagnetic half-metallicity, semiconduction, and half-metallicity. The terminations on MXene could be in one of three atomic forms, as shown in Fig. 7 A. Model I and Model II are indicated by up and down terminations that are positioned towards the C atoms; Model II is indicated by up and down terminations that are set above the middle M atoms; and Model III is indicated by up terminations that are positioned above the C atoms and down terminations that are placed on the middle M atoms. As shown in Fig. 7B, we took into consideration these three DTM MCr$_2$CT$_x$ models with nonmagnetic (NM), ferromagnetic (FM), and three antiferromagnetic (AFM) orders since magnetic states may have an impact on the stability of the structures. DTM MXenes are further divided into ordered [116,117] and unordered [118] categories. Fig. 7 C (a-c), and solid-solution MXenes [119,120] showed MXenes (such as Mo$_4$/3Y$_2$/3CT$_x$), with two distinct transition metals occupy the M layers in particular sites, which are described as being in-plane order [121] or a non-plane arrangement (like Mo$_2$TiC$_2$T$_x$), (Mo$_2$Ti$_2$C$_3$T$_x$) [118].

In view of current scientific advancements in MAX phase precursors, there are more potential DTM MXenes options available. Although they
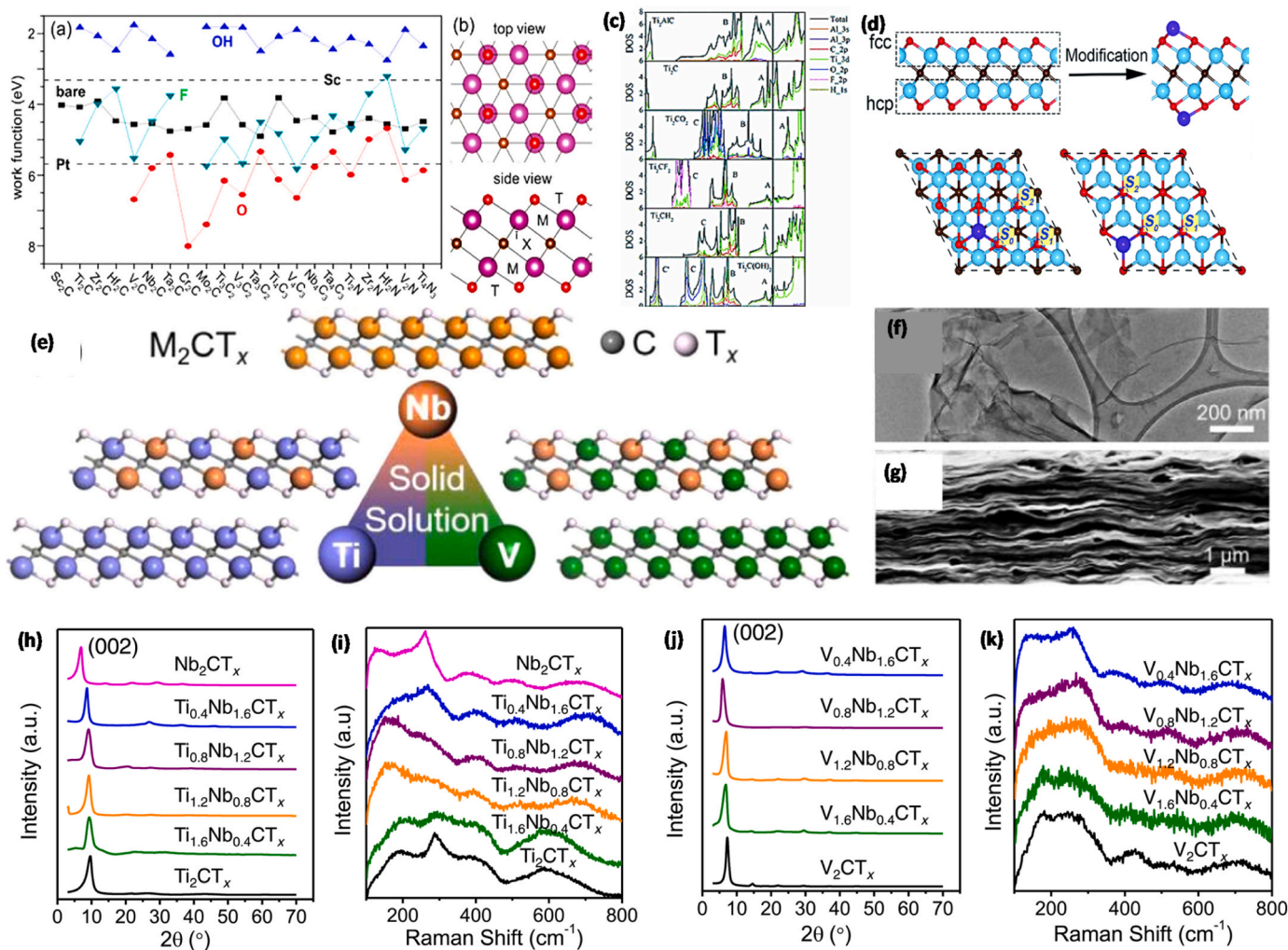

Fig. 8. (a): Work functions of MXenes with various terminations. Bare surface: black square; O termination: red circle; OH: blue up-triangle; F: cyan down-triangle. For comparison, the work functions of Sc and Pt metal are indicated by dashed lines. (b): Atomic structure of a representative M$_2$XT$_2$. M: purple; X: gray; T: red [127] (c)Total and partial DOS of Ti$_2$AlC, Ti$_2$C, Ti$_2$CO$_2$ and Ti$_2$C(OH)$_2$, illustrating changes in the density of states upon removal of Al from the parent MAX phase to produce MXene, and further changes upon termination of the MXene surface by different T [128]. (d) Representation of O-terminated MXenes, modified surface of MXene via TM. Adopted with permission [129]. Copyrights, 2018, Royal Society of Chemistry. (e) Schematic diagram of niobium-containing solid-solution MXenes (Ti$_{2-y}$Nb$_y$CT$_x$ and V$_{2-y}$Nb$_y$CT$_x$) with different discrete compositions. (f)Transmission electron microscopy (TEM) image of a Ti$_{1.6}$Nb$_{0.4}$CT$_x$ flake. (g) Scanning electron microscopy (SEM) image of the Ti$_{1.6}$Nb$_{0.4}$CT$_x$ film cross-section. X-ray diffraction (XRD) patterns (h) and Raman spectra (i) of Ti$_{2-y}$Nb$_y$CT$_x$, XRD patterns (j), and Raman spectra (k) of V$_{2-y}$Nb$_y$CT$_x$ with different Nb contents.
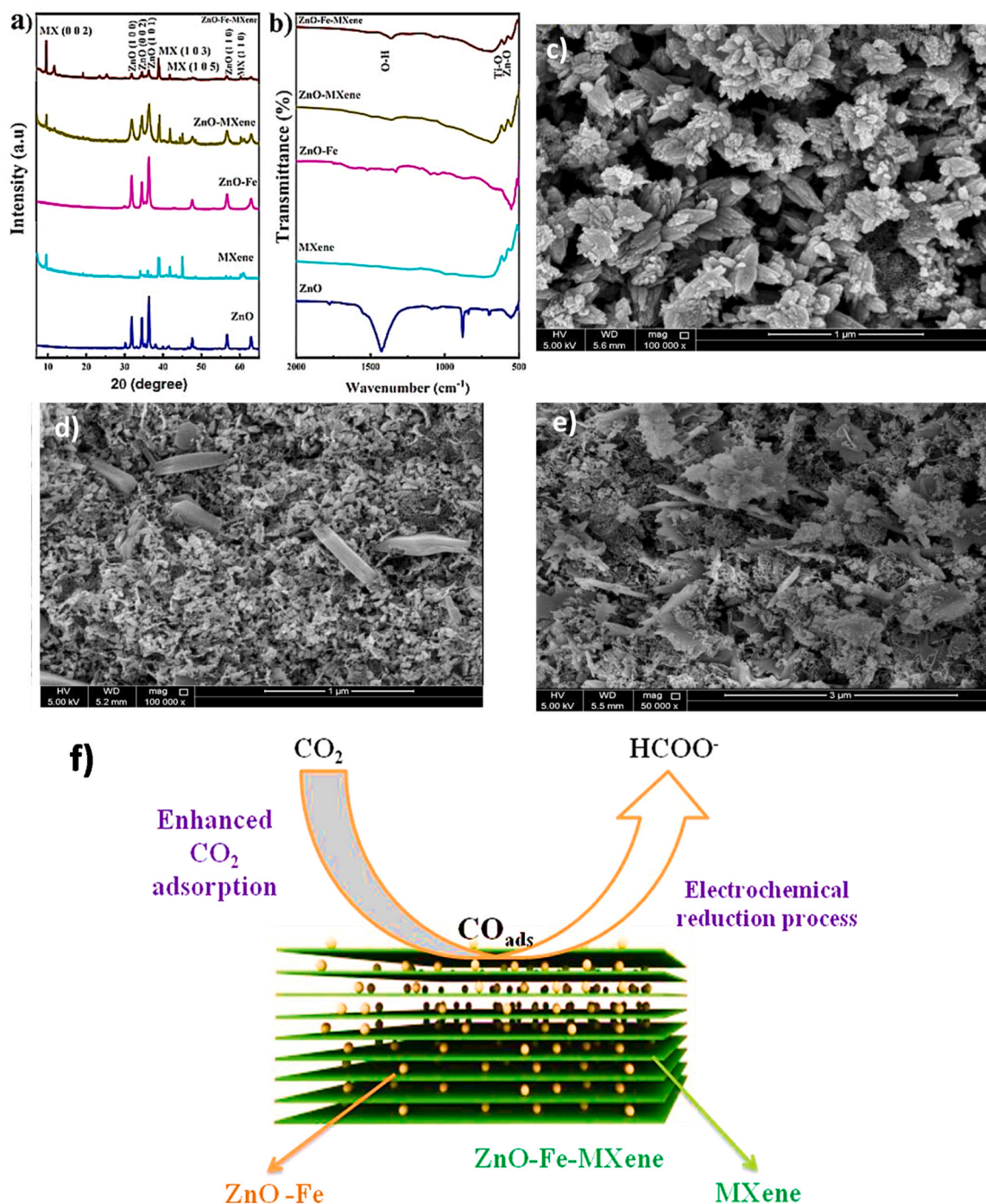
Fig. 11. a) XRD pattern; (**b**) FTIR spectra of the ZnO, MXene, ZnO-Fe, ZnO-MXene, and ZnO-Fe-MXene nanocomposites. SEM images of the (**c**) ZnO-Fe, (**d**) ZnO-MXene, and (**e**) ZnO-Fe-MXene nanocomposites, f) Reaction mechanism of the eCR on ZnO-Fe-MXene hybrids [136].

have been synthesised, ordered and solid-solution DTM MAX phases have not yet been etched to their corresponding DTM MXenes. However, some mono-M nitride and carbonitride MXenes have been experimentally realised. Additionally, current research has only focused on DTM MXenes made from carbide MAX phases; no nitride or carbonitride DTM MXenes have been investigated. Because they have different characteristics than their carbide counterparts in energy-storage applications, nitride and carbonitride MXenes [122,123] Potential DTM nitride/-carbonitride MXene characteristics are anticipated to be influenced by nitrogen or carbon/nitrogen as X in MXene. Rare-earth elements, including Ce, Pr, Nd, Sm, Gd, Tb, Dy, Ho, Er, Tm, and Lu are now part of the family of in-plane ordered DTM MAX phases [124]. It opens the door

for f-block element MXenes if controlled etching circumstances can be used to create rare-earth MXenes. This might result in previously undetected new behavior in MXenes. Last but not least, multi-principal element MXenes, which can expand MXenes towards high-entropy 2D materials, have not yet been investigated computationally or physically. These MXenes contain three or more transition metals. More complicated MXene compositions may provide new methods for managing characteristics.

Due to their advantageous geometric and electrical structures compared to their bulk equivalents, single-atom catalysts have attractive electrocatalytic activity for various chemical processes. By using quaternary MAX phases ($Ti_3(Al_{1-x}Cu_x)C_2$) to etch hybrid A layers (Al and

Cu) selectively, Zhao et al. [125] demonstrate an effective method for producing single atom copper immobilized MXene for electrocatalytic CO_2 reduction to methanol. Cu atoms are effectively retained after selective etching of Al in the hybrid A layers, and they are also bound onto the resulting MXene with a dominating surface functional group (Cl_x) on the outermost Ti layers (referred to as $Ti_3C_2Cl_x$) via Cu-O bonds from quaternary MAX phases ($Ti_3(Al_{1-x}Cu_x)C_2$). The essence of this approach is selectively removing one element by employing the easy sublimation properties of their A-containing product ($AlCl_3$) and leaving the other unreacted A element (Cu) onto MXene with the dominant surface functional group (Cl_x) on the outmost Ti layers (denoted as $Ti_3C_2Cl_x$). Consequently, the as-prepared single-atom Cu catalyst exhibits a high Faradaic efficiency (FE) value of 59.1% to produce CH_3OH and good electrocatalytic stability. According to the synchrotron-based X-ray absorption near-edge structure (XANES) and extended X-ray absorption fine structure (EXAFS) analysis, the single atoms of Cu are coordinated by three O atoms with unsaturated electronic structure ($Cu^{\delta+}$, $0 < \delta < 2$). Moreover, the DFT calculations reveal that the single atoms of Cu prefer the easier downhill type for the conversion of OCHO* to absorbed HCOOH* intermediate and deliver a low energy barrier for the rate-determining step (conversion of HCOOH* to absorbed CHO* intermediate), benefiting electrocatalytic CO_2 reduction to CH_3OH.

2.3. Electrochemical properties of MXene

MXenes cover various electronic properties ranging from metallicity and semi-conductivity to topological insulation due to their high compositional diversity, different surface functionalization possibilities, and flexible thickness controllability [126,127]. Among them, all the bare MXenes and most surface-functionalized MXenes are metallic. Interestingly, the calculated work functions (WFs) of metallic MXenes can vary in an extensive range, from 1.8 eV to 8 eV, as shown in Fig. 8a-b. It is seen that the WFs of MXenes are sensitive to their surface chemistry: for a given MXene, compared with the bare surface, the OH (O) decoration always decreases (increases) its WF, whereas the F decoration displays either trend relying on the specific material. It is worth mentioning that all the OH-terminated MXenes show ultralow WFs (<2.8 eV), lower than that of Sc which is nearly the lowest among those of elemental metals. On the other hand, the WFs of some O-terminated MXenes are even larger than that of Pt, which has the highest WF of all elemental metals. The WFs of F-terminated MXenes always fall between those of OH- and O-terminated counterparts. The change of WF after surface functionalization comes from the shift in surface dipole moment induced by functionalization [127].

MXene has numerous properties that play important roles in the performance of electrochemical devices and photo-electrocatalysts. The different applications are underlain by the electronic, transport, and band-gap properties. Moreover, the layer structure and thermal and mechanical properties could also make a significant difference. For example, as the lithium-ion battery (LIB) anode materials, MXene has excellent electronic conductivity, a low operating voltage range of − 0.2-0.6 V versus Li/Li$^+$, and low diffusion barriers (due to the terminated groups) that are favourable for high-rate performance and exceptional mechanical properties that are invariant to Li adsorption [130]. The electronic properties of MXenes are of special interest as they can, in principle, be tuned by changing the MXene elemental composition and/or their surface terminations. The MXenes' band structure and electron density of states (DOSs) have been extensively studied by DFT. Bare MXene monolayers are predicted to be metallic, with a high electron density near the Fermi level [85,131,132]. Interestingly, the electron DOS near the Fermi level ($N(E_f)$) for bare individual MXene layers is higher than in their parent MAX phases. To understand these changes, one needs to examine the partial electron density of states (Fig. 8c) [131, 128,133]. In the MAX phases, $N(E_f)$ is dominated by M $3d$ orbitals. Referring to Ti_2AlC (Fig. 11i), it is clear that the valence states below E_f group into two sub-bands: sub-band A, which is near E_f and is made up of

hybridized Ti 3d-Al 3p orbitals, and sub-band B, which is between –10 and –3 eV below E_f and is due to hybridized Ti 3d-C 2p and Ti 3d-Al 3 s orbitals. In other words, sub-bands A and B give rise to the Ti-Al and Ti-C bonds, respectively. Removal of the A layers results in a redistribution of the Ti 3d states, or "dangling bonds", from the missing Ti–Al bonds into delocalized Ti–Ti metallic-like bonding states that appear around E_f in Ti₂C (Figure 8ii). Thus, in MXenes, $N(E_f)$ is 2.5–4.5 times higher than in the corresponding MAX phases for $Ti_{n+1}C_n$ and $Ti_{n+1}N_n$, according to Shein et al. [131], or 1.9–3.2 times higher for $Ti_{n+1}C_n$ and 2.8–4.8 times higher for $Ti_{n+1}N_n$ according to Xie et al. [128], where the range of studied n was broader. The high $N(E_f)$ values in $Ti_{n+1}X_n$, contributed by the Ti 3d states, can lead to a magnetic instability if the Stoner criterion $I·N(E_f) > 1$ (where I is Stoner exchange parameter, equal to 0.9 eV for $3d$ elements) [134] is satisfied, resulting in magnetic MXenes [131,128, 135]. Magnetic MXenes can be both ferromagnetic (such as Cr_2C, Cr_2N, or Ta_3C_2) or antiferromagnetic (such as Ti_3C_2 or Ti_3N_2) [135]. The acquired total magnetic moments per unit cell are 2–3 μ_B for $Ti_{n+1}C_n$ or fluctuate around 1.2 μ_B for $Ti_{n+1}N_n$ as n increases from 1 to 9.

Although magnetism is an important property, for the most part, it is only predicted for MXene with bare surfaces. When surface terminations (T, even when T = H) are present, the magnetism disappears due to the formation of p–d bonds between the M atoms and T groups, leading to a partial depopulation of the near Fermi states, which reduces $N(E_f)$ (Ti_2CO_2, Ti_2CF_2, Ti_2CH_2, and $Ti_2C(OH)_2$ in Figure 8iii, d-e, respectively). Prominent exceptions are Cr_2C and Cr_2N, which are predicted to retain significant magnetic moments in their terminated state (T = O, OH, or F) up to nearly room temperature. Unfortunately, to date, there have been no reports of experimentally produced Cr_2XT_x MXenes to test this important prediction. To understand these changes, it is necessary again to examine the partial electron density of states (Fig. 8c). In addition to sub-bands A and B, mentioned above, in surface terminated MXenes a new sub-band C, corresponding to Ti–T bonds, is formed below sub-band B, causing a shift of the gap between sub-bands A and B to lower energies and a depletion in the $N(E_f)$. In another study [137] high Seebeck coefficients were predicted for MXenes by DFT. The Seebeck coefficients ≈ 1000 $\mu V\ K^{-1}$ predicted for semiconducting Ti_2CO_2 and $Sc_2C(OH)_2$ at ≈ 100 K are comparable to the reported giant Seebeck coefficients of $SrTiO_3$ (850 $\mu V\ K^{-1}$ at ≈90 K). This prediction opens a totally new area of potential applications for these surface-terminated MXenes. Bare MXene species, such as $Ti_{n+1}Xn$, are known to be metallic in behavior [138]. However, the metallic properties weaken as n values increase due to the formation of additional Ti-X bonds [139]. In terms of X atoms, titanium nitrides exhibit more metallic properties than titanium carbides do, simply because the N atom possesses one more electron than the C atom. By contrast, terminated MXene sheets are narrow-band-gap semiconductors or metals, depending on the species and orientations of surface groups [132,140]. To the best of our knowledge, the six terminated MXenes of Ti_2CO_2, Zr_2CO_2, Hf_2CO_2, Sc_2CO_2, Sc_2CF_2, and $Sc_2C(OH)_2$ have band gaps. However, the band gaps of the first five listed terminated MXene sheets are indirect, while $Sc_2C(OH)_2$ has a small direct band gap [137]. For this reason, it is essential to tune the electronic structure to achieve a direct band gap, especially in the fields of optoelectronics and optics. Lee et al. investigated the effects of applied strain on the band gap of Sc_2CO_2 [141], as stress can change interatomic distances and the relative positions of atoms within a material. As the tensile strain increases, the band gap gradually decreases. At a critical tensile strain, the indirect band gap transfers to a direct one. In addition, they found that Sc_2CO_2 could also experience an indirect-to-direct band gap transition under an external electric field due to the distinction of the responses of each point in the lowest conduction band to the electric field [142]. Here, we must emphasize the significance of choosing the correct exchange-correlation functionals in DFT computations of band gaps, as different results will be generated based on the chosen functional [135]. Hybrid functionals, such as HSE06, are known to give more accurate results in predicting band gaps and thus are strongly recommended [128], despite their much higher required computational
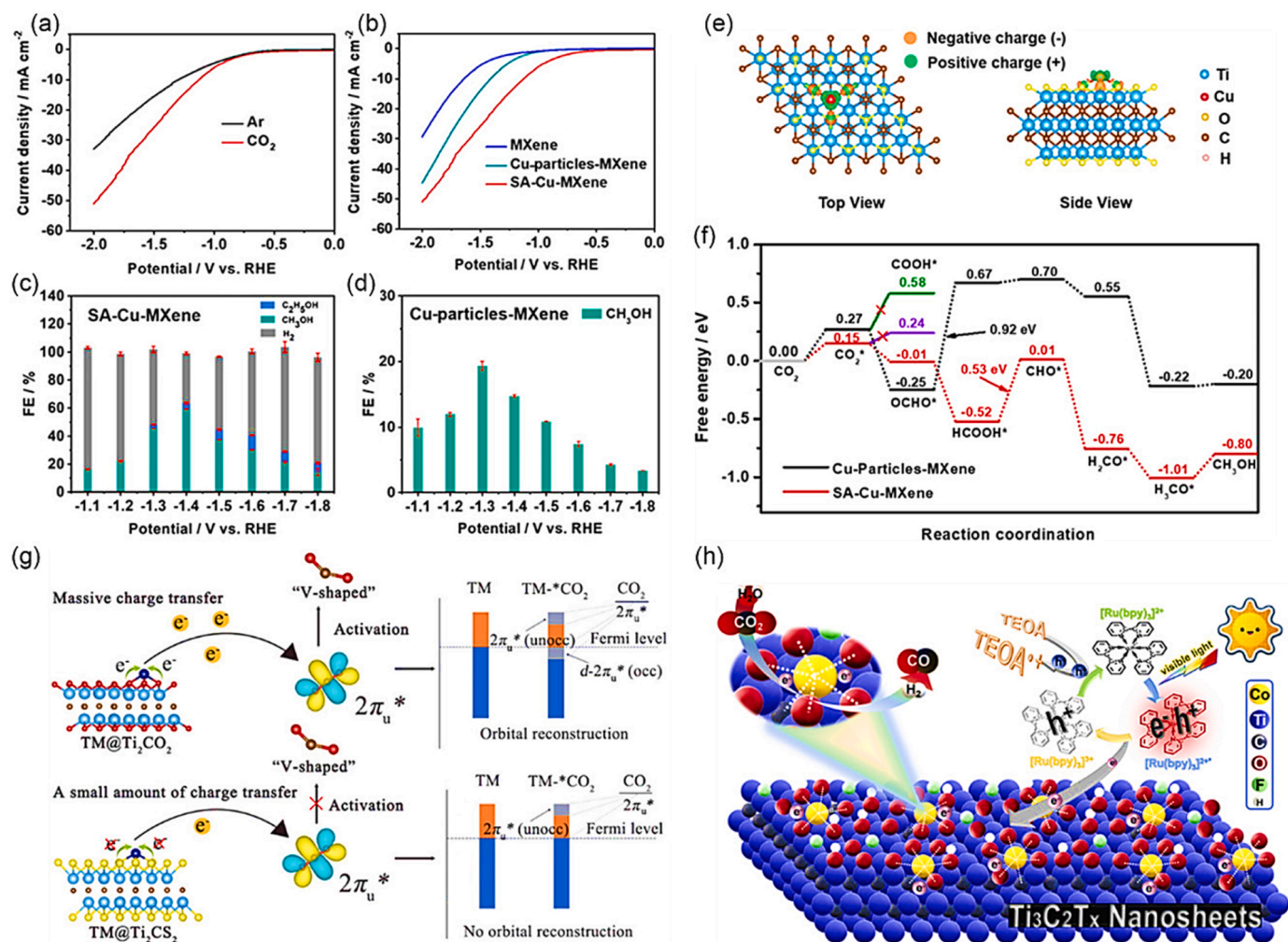
Fig. 9. . a,b) Linear sweep voltammetry (LSV) curves of SA–Cu–MXene in 0.1M KHCO₃. Faraday efficiencies (FEs) of c) SA–Cu–MXene and d) Cu–particles–MXene. e) Charge density difference of SA–Cu–MXene. f) Free energy diagram of CO_2 to CH_3OH on Cu–O₃ structure [125]. g) Schematic diagram of CO_2 activation mechanism on TM/Ti₂CT $_x$ [147]. h) Mechanism of photocatalytic CO_2 reduction [148].

capacity. MXenes display many encouraging properties due to the presence of TMs possessing vacant d-orbitals. Therefore, an abrupt change in properties may be anticipated via substituting M-atoms with various species in ordered layers-atoms of MXene. For instance, Li et al. reported that TM ad-atoms can alter the electronic features of an anion on a surface via chemical interaction and electronic re-distribution on the MXene surface (Fig. 8d). The report also provides a theoretical scheme for the electrocatalytic hydrogen evolution reaction and the mechanism. It led to the discovery of a novel protocol to improve the catalysis of MXene-based composites [129].

Currently, more than 30 stoichiometric MXene compositions and about 20 solid solutions have been experimentally synthesized. However, most studies focus on Ti₃C₂Tₓ or a few other single-M MXenes, and little is known about the electrochemical properties of solid-solution MXenes. Herein, two sets of niobium-based solid-solution MXenes (Ti₂₋ᵧNbᵧTₓ and V₂₋ᵧNbᵧTₓ; $0 \leq y \leq 2$) were synthesized, and the dependence of their electrochemical properties on the ratio of M elements in the structure was investigated. Fig. 8e shows that their capacitive behavior and cycling stability can be tuned by modification of the M-site chemistry. As the niobium content increases, the redox peak prominence decreases while the cycling stability is enhanced. Moreover, niobium content is correlated with capacitance retention of Ti₂₋ᵧNbᵧCTₓ: from less than 1% (y = 0, i.e., Ti₂CTₓ) to 78% (y = 1.6, i. e., Ti₀.₄Nb₁.₆CTₓ) after 20,000 cycles at 200 mV/s. Considering there are more than 100 predicted stoichiometric MXene compositions and a

limitless number of solid solutions [143–145], this illustrates the viability of adjusting MXene electrochemical properties by tuning the M-site chemistry. The Nb and Ti/V atoms in the MAX phases and MXenes are randomly distributed in M-layers. X-ray diffraction (XRD) patterns of Ti₂₋ᵧNbᵧCTₓ and V₂₋ᵧNbᵧCTₓ are shown in Fig. 8f-k. The disappearance of higher order peaks with only (00 l) peaks remaining confirms that the Al layers were removed entirely, delamination was successful, and no impurity phases remained in the films. Since the number of MXene solid solutions is virtually limitless, the approach to controlling and optimizing the electrochemical properties of MXenes by combining transition metals in different proportions is certainly promising.

The electrochemical system directly influenced CO_2 fate and specially its reduction dependent on applied voltage, and range of applied voltage decide the number of generated products, nature and selectivity. An important example given here; 1.4 V of voltage was applied via SA-Cu-MXene for CO_2 reduction into methanol in 0.1 M KHCO₃ that was saturated with CO_2. This process had substantially better efficiency than Cu nanoparticles, with a maximum FE of 59.1%. (Fig. 9a-d). Theoretical calculations showed that the transformation from HCOOH* to CHO* was a rate-determining step for the SA–Cu–MXene (Fig. 9e-f). Additionally, 1.04 wt% of Cu was added to Ti₃C₂Tₓ by using a simple standing method, and this material converted CO_2 to formic acid with an efficiency of 58.1%, which is four times that of Ti₃C₂Tₓ [146]. Theoretical calculations demonstrated that various
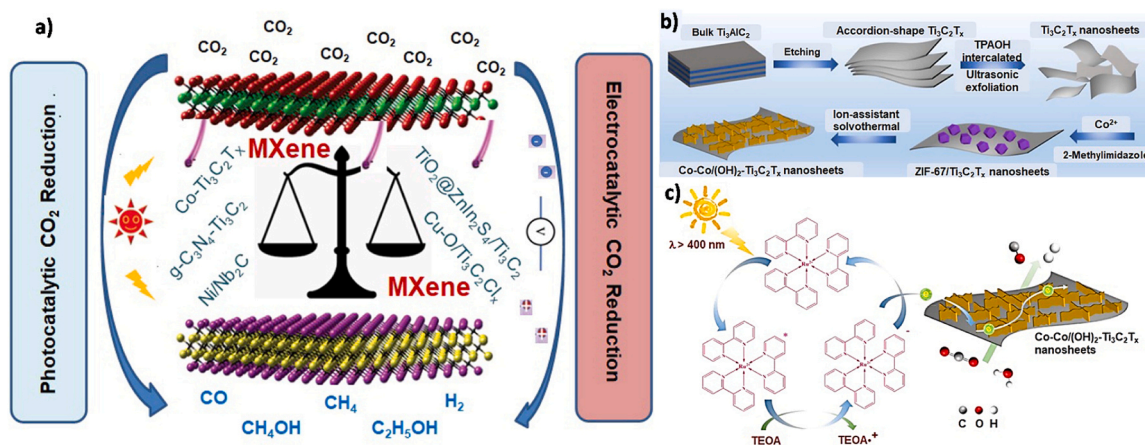
Fig. 10. a) Diagrammatic representation of the photocatalytic and electrocatalytic reduction of carbon dioxide (CO_2) utilizing diverse nanomaterials based on MXene. b) Schematic illustration of the synthetic process of Co-Co/(OH)$_2$-Ti$_3$C$_2$T$_X$ nanosheets, and (c) Proposed photocatalytic mechanism of Co-Co/(OH)$_2$-Ti$_3$C$_2$T$_X$ composite with [Ru(bpy)$_3$]Cl$_2$ for the visible-light-driven photocatalytic CO_2 reduction reaction; TEOA = triethanolamine [171].

transition metals, including Ti$_2$CO$_2$, as well as Cu species had a favorable impact on the augmentation of CO_2RR activity [147]. With TM bonds, oxygen-functional groups added extra electrons into CO_2's 2 *u orbital, splitting it into the 2 *u (unocc) and d-2 *u (occ) orbitals (Fig. 9 g). This orbital reconstruction caused the linear CO_2 structure to change to a V-shaped structure, which is advantageous for the initial hydrogenation phase. High CO_2RR selectivity was also demonstrated by the fact that the maximum Gibbs-free energy (G max) on Cr-anchored Ti$_2$CO$_2$ during CO_2RR was lower than that during HER. Additionally, the CO_2RR was used to synthesis Co-Ti$_3$C$_2$T$_x$ via a coordination process made possible by electrostatic contact (Fig. 9 h) [148].

3. Current applications of MXene for electro-photo CO_2 reduction

3.1. Importance of CO_2 reduction and functionalities of MXene

The combustion of fossil fuels has resulted in an overabundance of carbon dioxide (CO_2) emissions, which has caused significant and potentially irreversible consequences on the climate and environment. These consequences include global warming, elevated sea levels, acidification of the oceans, and the melting of glaciers. Given the projected rise in atmospheric CO_2 concentration from 404×10^{-6} in 2017 to 600×10^{-6} by 2100, there is a pressing imperative to mitigate the carbon footprint resulting from anthropogenic activities [149,150]. The primary issue associated with the traditional combustion of fuels pertains to the elevated over-potential requirement for the transformation of CO_2. The electrochemical reduction of carbon dioxide (CO_2) in fuels presents a carbon-neutral process that offers significant benefits in terms of sustainability and the potential mitigation of climate change [136]. Considerable endeavours have been directed towards developing various technologies such as CO_2 capture and storage, CO_2 emission suppression at the source, and direct conversion of CO_2 into value-added fuels and chemicals to address the escalating concentration of CO_2. The conversion of CO_2 gas into high-value fuels and chemicals, commonly referred to as the CO_2 reduction reaction (CO_2RR), is a promising strategy for mitigating the issue of excessive CO_2 emissions. This approach has the potential to yield a range of valuable C1 (CO, HCOOH, CH$_3$OH, and CH$_4$) and C^{2+} (CH$_3$COOH, C$_2$H$_4$, C$_2$H$_5$OH, and C$_3$H$_7$OH) products, making it an attractive option among emerging technologies [151] [152]. In addition, it is worth noting that the energy densities of products resulting from CO_2 electrochemical reduction reactions, such as methanol (15.6 MJ/L) and ethanol (24 MJ/L), surpass those of the most advanced battery technologies. This renders them highly suitable models to store intermittent renewable energy [136]. Photocatalytic

reduction of CO_2 has been extensively studied in this context using various semiconductors, including TiO$_2$, CdS, g-C$_3$N$_4$, BiOBr, and Fe$_3$O$_4$ [153–156]. TiO$_2$ is the primary contender and a standard for comparison due to its efficacy, eco-friendliness, and ability to maintain its photochemical stability [157,158]. However, the practical implementation of TiO$_2$ for photocatalytic CO_2 reduction remains a formidable task, primarily attributable to its limited light harvesting efficiency and prompt electron-hole recombination [159,160]. Numerous strategies, such as surface modification, co-catalyst loading, impurity doping, and heterojunction construction, have been suggested to improve the photocatalytic efficiency of TiO$_2$ [161,162]. MXene/MXene-based nanocatalysts have garnered significant interest for various energy and environmental applications owing to their distinctive characteristics, such as hydrophilic properties, non-toxicity, redox reactions, substantial surface areas, remarkable mechanical strength, exceptional melting points, environmentally-friendly flexibility, outstanding electrical conductivity, and high biocompatibility [163]. As 2D materials, MXenes have the advantages of a large surface area and stable and abundant active sites at the edges. They could thus be considered ideal adsorbents. Progress has been made in applying MXenes to adsorption through both theoretical and experimental research. The adsorption ability of various gases including NH$_3$, H$_2$, CH$_4$, CO, CO$_2$, N$_2$, NO$_2$, and O$_2$ on monolayer Ti$_2$CO$_2$ by first-principles simulations was reported [164]. The modification of the raw MXene is sometimes necessary to improve the capacities of adsorption. For instance, Liu's group prepared a new urchin-like rutile TiO$_2$-C/TiC 2D material with a high amount of (110) facets by in situ solvothermal alcoholysis of MXene in FeCl$_3$ solution [165]. The Fe (III) ions in MXene played an important role in transforming the intermediate product of anatase TiO$_2$-C (1-ATC) into rutile TiO$_2$-C (u-RTC), and the u-RTC displayed a higher Cr(VI) adsorption capacity than that of raw MXene. The improved adsorption capacity is possibly due to the inhibition of H$_2$O adsorption by bridging oxo-groups according to the first-principle calculation.

Notably, out of the countless MXenes that exist, Ti$_3$C$_2$T$_x$ and its derivatives have been the subject of more comprehensive research in the realm of energy storage and delivery, as well as certain environmental applications [164]. Nevertheless, the photoelectrocatalytic abilities of other kinds of MXenes, such as Cr$_2$TiC$_2$, Mo$_2$ScC$_2$, Mo$_2$Ti$_2$C$_3$, (Nb0.8Zr$_{0.2}$)$_4$C$_3$, Ti$_3$CN, (Nb$_{0.8}$Ti$_{0.2}$)$_4$C$_3$, Ti$_2$C, Nb$_2$C, TiNbC, (Ti$_{0.5}$Nb$_{0.5}$)$_2$C, and V$_2$C,$_{25}$ Zr$_3$C$_2$ still need to be evaluated for CO_2 reduction along with other properties such as semiconductor, electron mobility and charge separation. In contemporary research, novel photocatalysts or electrocatalysts for CO_2 reduction have been developed utilizing MXene-based nanocomposites such as Co/Ti$_3$C$_2$T$_X$, Ti$_3$C$_2$/-graphitic carbon nitride (g-C$_3$N$_4$), TiO$_2$ @ZnIn$_2$S$_4$/Ti$_3$C$_2$,
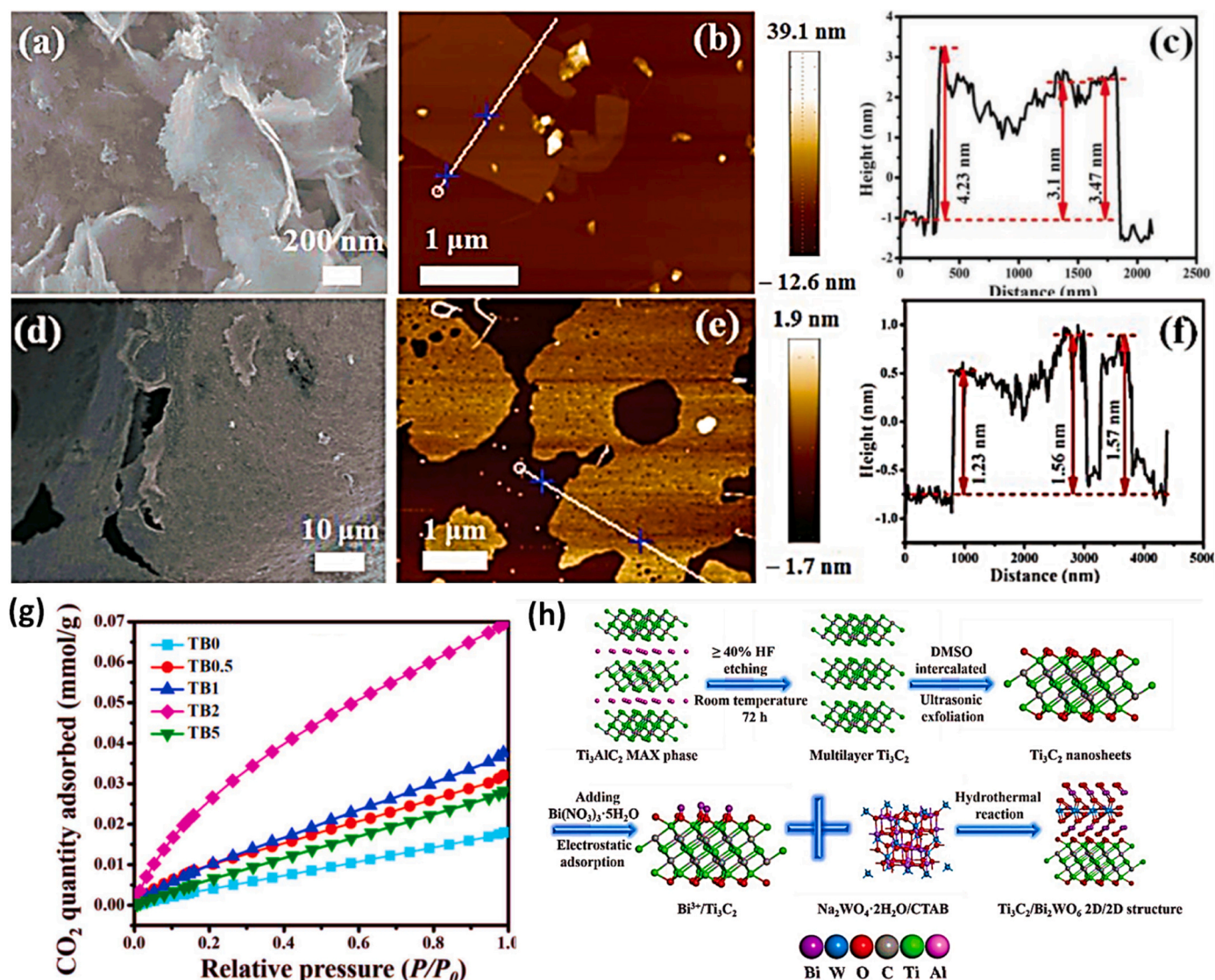
Fig. 12. a–c) Typical FESEM, AFM images and height cutaway view of Bi_2WO_6, d–f) Ti_3C_2 nanosheets g) CO_2 adsorption curves of as-prepared samples. h) Schematic illustration of the synthetic process of 2D/2D heterojunction of ultrathin Ti_3C_2/Bi_2WO_6 nanosheets [179].

Cu/O/$Ti_3C_2Cl_x$, and Ni/Nb_2C [148,165–170]. The present study differs significantly from prior research, as previous investigations have been restricted to examining Ti_3C_2 MXene and have focused on either photocatalytic or electrocatalytic CO_2 reduction. The primary objective of our review is to comprehensively examine the latest discoveries and advancements in the utilization of MXene-based nanomaterials for efficient conversion of CO_2 into valuable fuels such as CO, CH_4, H_2, CH_4OH, and C_2H_5OH. Our approach will be systematic in nature. Furthermore, we have provided a concise outline of potential research areas for MXene-based photoelectrocatalysts in the context of CO_2 reduction. The schematic depicted in Fig. 10a provides a general overview of the photocatalytic and electrocatalytic reduction of CO_2 utilizing diverse MXene-based nanomaterials.

In this regard, Chen et al. [171] fabricated Co-Co/$(OH)_2$-$Ti_3C_2T_X$ nanocomposite with a unique three-dimensional hierarchical structure using an in-situ metal-organic framework (ZIF-67) derived method. Fig. 10b illustrates the schematic representation of the Co-Co/$(OH)_2^-$$Ti_3C_2T_X$ synthesis process. The Co-Co/$(OH)_2Ti_3C_2T_X$ composites exhibited notable functional and physical benefits due to active Co species and conductive $Ti_3C_2T_X$. These features led to a substantial increase in the conversion of CO_2 to CO (1.25×10^4 μmol h^{-1} g^{-1}) with a remarkable quantum efficiency (0.92%) and exceptional stability.

Fig. 10c illustrates an appealing explanation for the CO_2 photoreduction capabilities of Co-Co/$(OH)_2Ti_3C_2T_X$. Upon exposure to light with a wavelength of 400 nm, [Ru(bpy)$_3$]Cl$_2$ undergoes a reduction process, resulting in the formation of a reduced state ([Ru(bpy)$_3$]Cl$_2^-$). This reduced state is effectively suppressed by triethanolamine, which acts as an electron donor. As a result, ([Ru(bpy)$_3$]Cl$_2^-$) facilitates electron transfer to Co-Co/$(OH)_2Ti_3C_2T_X$, enabling efficient transmission of electrons to the catalytically active regions of Co through the intricate interface. The production of CO is ultimately attributed to the activation of CO_2 that has been adsorbed on the catalytically active regions. The Co-Co/$(OH)_2Ti_3C_2T_X$ material exhibits appropriate flat band potentials, which facilitate the acquisition of excited electrons from [Ru(bpy)$_3$]Cl$_2$. This process leads to the reduction of CO_2 to CO [172]. The Co-Co/$(OH)_2Ti_3C_2T_X$.composite serves a dual function in photocatalytic CO_2 reduction. Firstly, it creates active sites that facilitate the reduction of CO_2. Secondly, it enhances the transfer of electrons from [Ru(bpy)$_3$] Cl$_2^-$ to the active surface sites of Co-Co/$(OH)_2Ti_3C_2T_X$, thereby promoting CO_2 reduction [171].

Similarly, Khan et al. [173] studied the synthesis of a novel 2D/3D architecture, namely TTC-CoAlLa-LDH, which is fabricated by integrating O-vacancy-rich trimetallic $Co_2Al_{0.95}La_{0.05}$ LDH (CoAlLa-LDH) with TiO_2/Ti_3C_2 (TTC) multilayers. The primary objective of this

research is to enhance the photocatalytic CO_2 reduction process. The study observed that the photocatalytic reduction of CO_2 with H_2O resulted in the formation of CO and CH_4. The generation rates of these gases were measured to be 46.3 and 31.0 μmol h^{-1} g^{-1}, respectively, in the presence of TTC-CoAlLa-LDH. These rates were significantly higher than those observed in the cases of pristine Ti_3C_2, CoAlLa-LDH, and CoAl-LDH. Specifically, the generation rates of CO and CH_4 in these cases were measured to be 13.3 and 5.34 μmol h^{-1} g^{-1}, 21.8 and 25.5 μmol h^{-1} g^{-1}, and 6.12 and 9.13 μmol h^{-1} g^{-1}, respectively. Moreover, Low et al. [174] investigated the photocatalytic CO_2 reduction activity of a TiO_2/MXene Ti_3C_2 composite, which yielded promising results. The TiO_2/Ti_3C_2 composite that was optimized demonstrated a significantly greater photocatalytic CO_2 reduction performance for CH_4-production (0.22 μmol h^{-1}) compared to commercial TiO_2 (P25), with a 3.7-fold increase. The exceptional photocatalytic efficacy can be attributed to the distinct morphology and characteristics of the composite's constituent elements. The surface area is a crucial factor in facilitating the exceptional effectiveness of CO_2 reduction. Kannan et al. [136] synthesized ZnO-Fe-MXene-based nanocomposites to enhance the efficiency of CO_2 reduction. The X-ray diffraction (XRD) analysis presented in Fig. 11a confirmed the hexagonal arrangement of ZnO, MXene, and ZnO-Fe-MXene nanocomposites. The (XRD) analysis of the hybrids indicates that the peaks exhibit expansion and reduced intensities. This phenomenon can be attributed to etched MXene in conjunction with Fe-doped ZnO nanoparticles. The hybrid composites exhibit prominent peaks of ZnO and MXene across all materials, indicating the successful synthesis of the composites [175]. The results obtained from Fourier Transform Infrared Spectroscopy (FTIR) indicated the presence of distinctive vibrational frequencies associated with ZnO and MXene, as illustrated in Fig. 11b. This (FTIR) analysis confirmed the vibrational modes of saturated hydrogen bonds (−OH), hydrocarbons (−CH), and carbonyls (−CO) through their respective bending and stretching motions. A robust and extensive peak within the 1362–3443 cm^{-1} range may be attributed to the bending and stretching oscillations of O-H functional groups. The scanning electron microscopy (SEM) micrographs revealed the presence of nanoparticles exhibiting a flower-like morphology, as illustrated in Fig. 11c-e.

The electrocatalytic reduction efficiency of a nanocomposite consisting of ZnO, Fe, and MXene was evaluated using cyclic voltammetry and electrochemical impedance spectroscopy techniques. The electrode composed of ZnO-Fe-MXene was observed to exhibit a significant current density of 18.75 mA cm^{-2} when subjected to a CO_2 environment. These outcomes suggest that the composite might modify both the geometric and electronic structures of the catalytically active sites. The modification of the ZnO-Fe-MXene catalyst electronic structure is directly communicated to transitional binding (CO−%), which can manipulate the pathway reaction (Fig. 11f) for formate creation [136]. Overall, a significant decline in the impedance of the ZnO-Fe-MXene layer was observed, which suggests a rapid transfer of charges between the Zn and MXene layers. Furthermore, this electrochemical investigation sheds light on novel characteristics of ZnO-Fe-MXene for effective CO_2 reduction.

As Mxenes are used as a photocatalyst and electrocatalyst for the reduction of CO_2 [163,176] [177,178], Cao et al. [179] fabricated a heterogeneous junction of $Ti_3C_2T_x$/Bi_2WO_6 in a two-dimensional/two-dimensional configuration. The resulting composite exhibited remarkable performance in the reduction of CO_2 through photocatalysis. The investigation of the microstructure and morphology of the samples was conducted through the utilization of field-emission scanning electron microscopy (FESEM) (as depicted in Fig. 12a-c), transmission electron microscopy (TEM), and atomic force microscope (AFM) (Fig. 12d-f). The study reveals that the heterostructured hybrids of Ti_3C_2/Bi_2WO_6, comprising multiple atomic layers, exhibit a significantly improved efficiency in the process of photocatalytic CO_2 reduction. The total yield of CH_4 and CH_3OH obtained from these hybrids is 4.6 times higher than that obtained from pristine
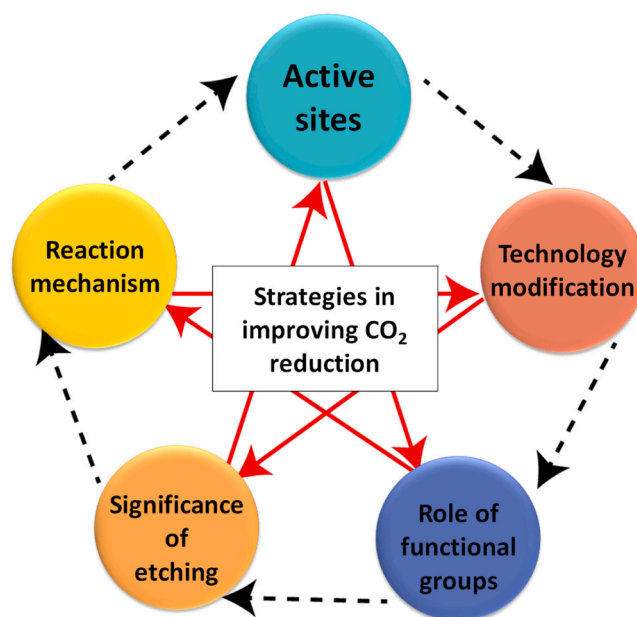

Fig. 13. Modifications for the high efficiency of CO_2 reduction.

Bi_2WO_6 ultrathin nanosheets. The CO_2 adsorption curves for the samples that were prepared have been illustrated in Fig. 12 g. The TB2 curve exhibits superior CO_2 adsorption capacity compared to the remaining curves. Specifically, the TB2 curve shows a notably swifter ascent than the remaining curves within the low-pressure spectrum, a phenomenon that can be ascribed to the presence of micropores. As the relative pressure increases, the visible distinctions among the samples become more pronounced, attributable to variations in their specific surface area and pore volume. At a pressure ratio of P/P0 = 1.0, the carbon dioxide adsorption capacities of TB0, TB0.5, TB1, TB2, and TB5 are 0.018, 0.032, 0.038, 0.069, and 0.028 millimoles per gram, respectively. The efficient transfer of electrons from the photocatalyst (Bi_2WO_6) to the cocatalyst (Ti_3C_2) is attributed to the large interface contact area and short charge transport distance of the Ti_3C_2/Bi_2WO_6 2D/2D heterojunction. In addition, the enhanced specific surface area and pore structure of the 2D/2D heterostructured ultrathin nanosheets result in a significantly improved capacity for CO_2 adsorption, thereby promoting the efficiency of photocatalytic reactions. Fig. 12 h portrays the depiction of this process.

The utilization of MXenes as catalysts for CO_2 reduction holds promise for the development of sustainable and efficient techniques for the conversion of CO_2 into valuable products. It is noteworthy that MXenes exhibit promise in the realm of CO_2 reduction. However, additional investigation and refinement are requisite to enhance their efficacy, augment their specificity, and expand their manufacturing capacity to enable their practical implementation, as shown in Fig. 13.

3.2. Engineering in MXene for increasing active sites

Prior research has demonstrated that the catalytic efficacy of MXenes is significantly influenced by their termination groups, surface defects, and electronic configurations. This has spurred extensive research initiatives aimed at customizing the structural characteristics of MXenes to attain improved catalytic performance [180]. The augmentation of interaction sites may play a crucial role in CO_2 capture. This is because multiple sites tend to exhibit a higher affinity for CO_2, while simultaneously requiring less energy for desorption. This phenomenon has been observed in MXene and MXene-derived materials [181]. In addition, enhancing the proportion, dimensions, and pore arrangement of MXene might enhance the electrocatalytic capacity for CO_2RR and the CO_2
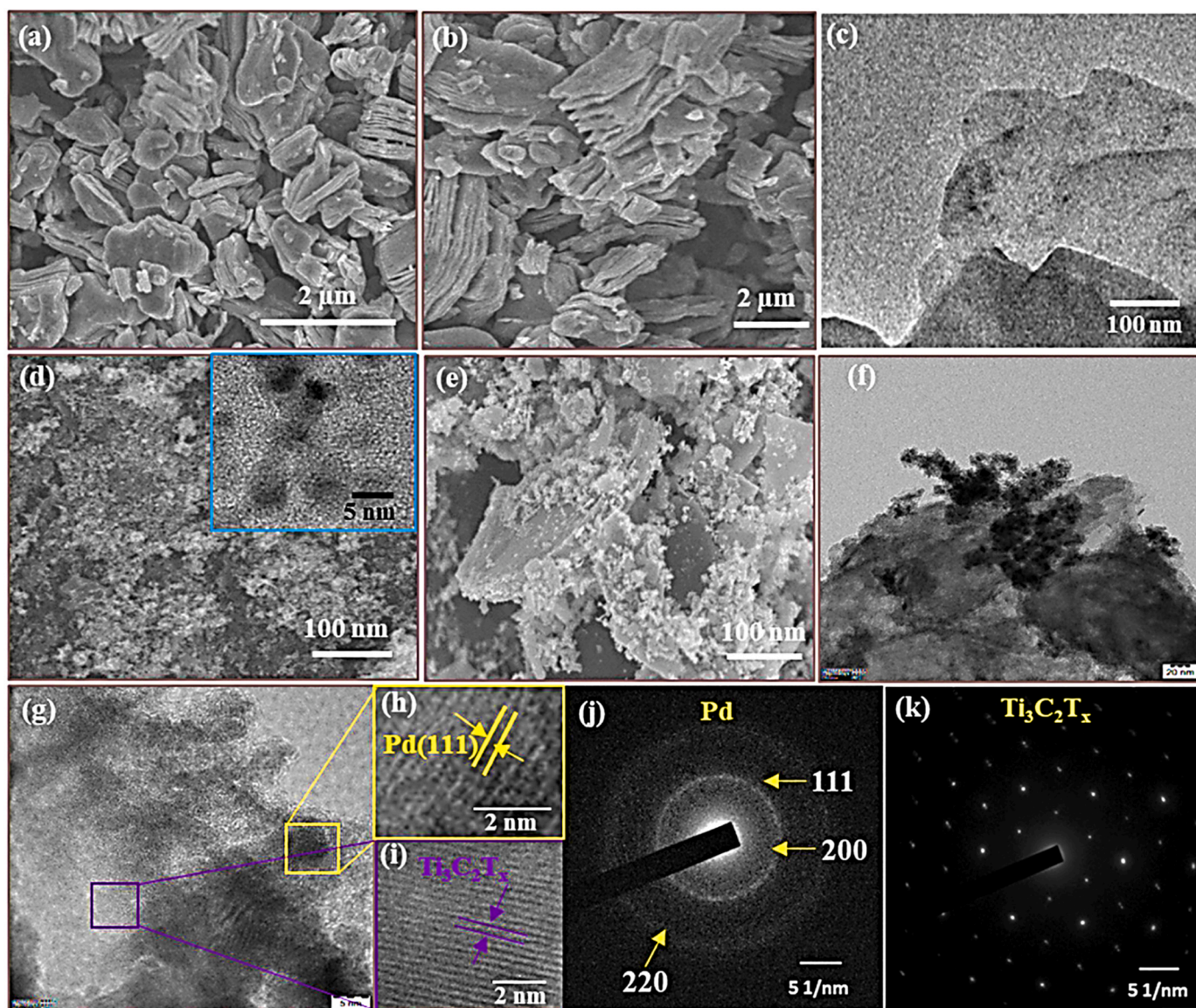
Fig. 14. (**a,b**) SEM with different micrographic pictures of pristine MXene powder; (c) TEM image of exfoliated MXene; (d) SEM image of Pd NPs with inset of TEM of Pd NPs; (e) SEM micrographic image of Pd-MXene nanocomposites; and (f,g) TEM with different magnification images of Pd-MXene nanocomposites. (h) an HR-TEM image of individual Pd in the nanocomposites, (i) an HR-TEM image of MXene ($Ti_3C_2Ti_x$) in the nanocomposites, (j) an SAED pattern of Pd, and (k) an SAED pattern of MXene ($Ti_3C_2Ti_x$) in the nanocomposites [185].

sequestration potential of solid MXene-derived adsorbents. As exemplified by the findings of Zhon et al. [182], a greater specific area of MXene was observed to enhance CO_2 capture, thereby corroborating the notion of potential interference from other variables in the CO_2 capture process. The findings revealed that $Ti_3C_2T_x$ exhibited a noteworthy adsorption capacity of 5.79 mmol g^{-1}, which is comparable to the commonly employed CO_2 absorbent, owing to its specific surface area of 21 m^2/g. In contrast to the process of producing composite materials, interfacial engineering is a subtle modification that necessitates robust interplay between two phases at a reduced dimensional scale. Using two distinct stages for interfacial engineering presents an effective approach for constructing catalysts with heightened activity. Reactive metal-support interaction (RMSI) is a chemical phenomenon that involves the interaction between a metal and a support, leading to the formation of bimetallic structures that are not readily achievable through alternative synthetic techniques. Wu et al. have demonstrated that the (RMSI) can effectively modulate the catalytic active sites through the interaction between noble metal nanoparticles and MXenes

[183]. The RMSI effect observed in both Pt and MXenes is a widespread phenomenon in the $Pt/Ti_3C_2T_x$ system. The utilization of bimetallic interfaces may prove advantageous in developing catalysts with enhanced activity and selectivity [184]. Govindan et al. [185] investigated the Pd-decorated 2D MXene (2D-$Ti_3C_2Ti_x$) as a high-performance electrocatalyst for converting carbon dioxide into fuels to mitigate the effects of climate change. SEM, TEM, and SAED analysis were utilized to investigate the morphological and structural properties of MXene powder, exfoliated MXene nanosheets, as-prepared Pd NPs, and Pd-MXene nanocomposites. Fig. 14a-b shows micrographs taken with a scanning electron microscope (SEM) of multilayered MXene, showing that the nanosheets of MXene are stacked together with 10 to 15 other nanosheets. Sonication was employed with DMSO and an aqueous solution to exfoliate multilayered MXene nanosheets into a small number of single-layered MXene sheets. The TEM of these sheets are depicted in Fig. 14c. The scanning electron micrograph of Pd NPs shown in Fig. 14d reveals that the particles have a consistent size and do not agglomerate in any way. It shows a scanning electron micrograph of Pd NPs, which
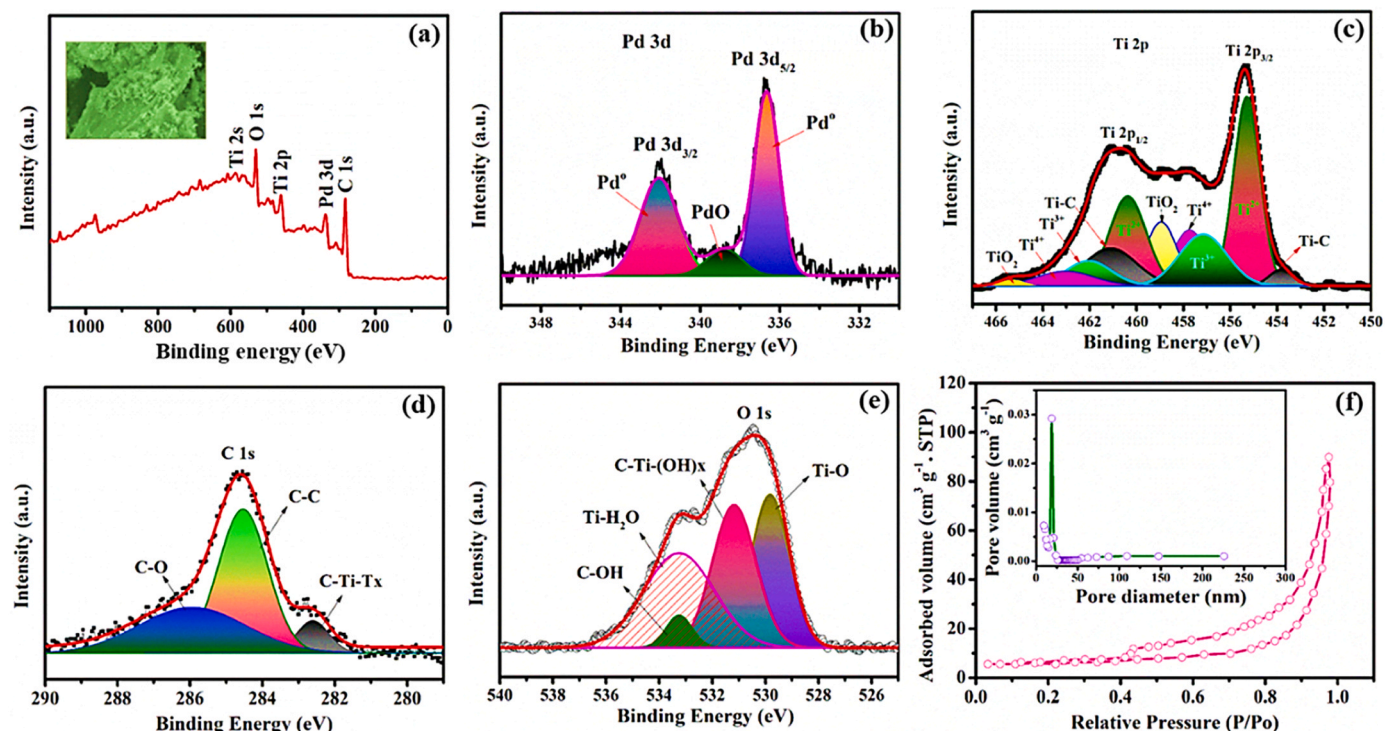
Fig. 15. (**a**) The XPS survey spectra of Pd-MXene nanocomposite, (**b–e**) high-resolution deconvoluted spectrums of Pd 3d, Ti 2p, C1s, and O1s, and, (**f**) Nitrogen adsorption and desorption isotherms with BJH pore size distribution of Pd-MXene nanocomposites [185].

reveals that the particles have a uniform size and do not agglomerate in any way. This information may be found by clicking here. Fig. 14e is a scanning electron micrograph demonstrating how successfully the Pd NPs were integrated into the exfoliated MXene nanosheets. In addition, TEM micrographs of varying magnification indicated that spherical-like Pd NPs with a diameter of 5 to 6.5 nm were adorned on the surfaces of MXene nanosheets; these NPs were covered in a metallic layer. as shown in Fig. 14f-g. Furthermore, Fig. 14 h shows in the crystal plane (111) of the fcc Pd NPs, the enlarged HR-TEM picture of the Pd NP and its lattice interplanar distance is estimated to be 0.22 nm. [186].

As shown in Fig. 14i, The hexagonal MXene nanosheets that were seen using HR-TEM have lattice fringes with d-spacing of 0.27 nanometers. In addition to this, the SAED pattern shown in Fig. 14j, The XRD findings are more reliable when interpreted because the Pd catalytic sites display the lattice planes (111), (200), and (220). Additionally, the MXene nanosheets in hybrid nanocomposites have a hexagonal configuration, as shown by the SAED pattern in Fig. 14k. This is another attractive property of these materials. XPS was utilized to investigate the surface property as well as the chemical state of Pd-MXene nanocatalysts. As shown in Fig. 15a, The XPS examine spectrum unequivocally demonstrates the presence of carbon, palladium, oxygen, titanium dioxide, and titanium disulfide in Pd-MXene nanocatalysts, suggesting that the Pd-MXene was synthesized by subjecting it to irradiation from a microwave. In Fig. 15b, $Pd3d_{5/2}$ and $Pd3d_{3/2}$ are double peaks corresponding to metallic Pdo, as indicated by the deconvoluted Pd 3d XPS spectra of the Pd-MXene nanocatalysts. These peaks are positioned at 336.69 and 342.13 eV, respectively. $NaBH_4$ can completely reduce Pd^{2+} ions into metallic PdO when subjected to the impact of microwave radiation, as shown by the appearance of a minor peak at 338.5 eV that corresponds to Pd-O. This is evidenced by the rise in the energy spectrum [186]. Fig. 15c shows MXene's deconvoluted Ti 2p XPS spectra were seen when it was embedded in hybrid nanocatalysts. The Ti 2p core level exhibits two doublets of $Ti 2p_{3/2}$ and $Ti 2p_{1/2}$ at 455.0 and 461.7 eV, correspondingly. The two aforementioned doublets show a separation of 5.7 electron volts between them. The Ti 2p X-ray

photoelectron spectroscopy spectrum of MXene in the hybrid nanocatalysts was deconvoluted. The observed peak at 453.8 eV indicates the presence of Ti-C in the MXene material [187]. The spectrum of C1, which has been deconvoluted, reveals the existence of three primary peaks located at 283.3, 284.5, and 286.5 eV. These peaks correspond to C-Ti-Tx, C-C, and C-O bonds, respectively, as depicted in Fig. 15d. Furthermore, the O 1 s spectrum depicted in Fig. 15e displays four components at 530.9, 531.3, and 533.2 eV that correspond to Ti-O, C-Ti-(OH)x, Ti-H2O, and C-OH, respectively. This observation suggests that DMSO predominantly facilitates the introduction of OH ions onto the surfaces of MXene nanosheets [188]. Moreover, the presence of hydroxyls (OH) and oxygen-functional groups augment the hydrophilic nature of Pd-MXene, thereby facilitating increased ionic conductivity during electrocatalytic processes. Furthermore, an analysis of N2 adsorption-desorption isotherms was conducted to investigate the textural characteristics of Pd-MXene nanocomposites (as depicted in Fig. 15f). The Pd-MXene exhibited a specific surface area (SSA) of 97.5 m^2g^{-1}, surpassing the reported values of MXene-based nanocatalysts [188–190]. The term "inset" refers to a small illustration or map included within a larger document or image. The Pd-MXene nanocatalysts' Barrett-Joyner-Halenda (BJH) pore size and pore volume distribution are depicted in Fig. 15f. The Pd-MXene nanocatalysts demonstrated superior characteristics compared to various MXene-based nanocomposites, with pore sizes and total pore volumes ranging from 8–20 nm and 0.289 cm^3g^{-1}, respectively [190,191]. Higher SSA and pore channels could improve the electrocatalytic activities of Pd-MXene nanocatalysts. This enhancement could improve electro-redox behavior and CO_2 adsorption, ultimately reducing CO_2 into fuels.

3.3. Modified technologies for CO2 reduction

To CO_2 in a better way with high reaction rates, various techniques have been used, including chemical reduction, photochemical reduction, electrochemical reduction, and biological transformations. [192].

Since it efficiently modifies reaction rates and products by altering their potential, current, and electrolyte, the CO_2 electroreduction reaction (CO_2RR) is more promising than the others. The two distinct groups of heterogeneous and homogeneous reactions are used to categories all CO_2RR routes. [192]. Major reaction locations in the heterogeneous process are at the solid-liquid and solid-gas interfaces. The CO_2 bonds with the electrodes (or catalysts) first, and then the electrons move between the two components. Energy conversion is one of the most important CO_2RR applications because it directly relates to humankind's core objectives. To overcome the aforementioned challenges and enable effective energy conversion, improving electrocatalysts is a crucial electroreduction issue [193]. CO_2 is usually transformed into various carbonous compounds, including carbon monoxide (CO), methane, and other hydrocarbons, as one of the methods for converting carbon dioxide into energy. The entire reaction occurs in the electrolytic cell cathode, while the oxygen evolution reaction is the primary reaction of the anode [194]. Multiple CO_2RR techniques have been motivated to convert CO_2 into useful C-based materials, including as C-based fuels and plastics, as a result of the growing worries about anthropogenic fossil fuel consumption, greenhouse gas emissions, and related climate change [195]. The CO_2RR could lead to the highly desirable outcome of "zero-carbon emission" in conjunction with altering processes to reduce CO_2 emissions. It takes the right catalysts to activate the CO_2 molecule and change it into a variety of chemical compounds for catalytic CO_2 conversion to become a reality. The arduous task of CO_2 activation is attributed to the low solubility and chemical inertness of CO_2, which can result in the prevalence of HER over CO_2RR. A necessary condition for effective dissociation/weakening of the CQO bond and subsequent electron transduction to produce energy-rich molecules with high specificity is the satisfactory adsorption (either physisorption or chemisorption) of CO_2 on the surface of a catalyst [196,197]. The utilisation of conventional homogeneous and heterogeneous catalysts, including metal-organic complexes, Cu, Ag, and Au, in CO_2 reduction reaction (CO_2RR) is associated with several drawbacks, such as inadequate chemical stability, exorbitant expenses, or lack of photo-activity [198]. The scientific community focused on CO_2 reduction reactions is increasingly interested in 2D MXenes that exhibit adjustable surfaces. Of the myriad MXenes available, $Ti_3C_2T_x$ and $Ti_3C_2T_x$-based nanomaterials have been the subject of extensive research in the fields of energy storage and delivery, as well as certain environmental applications [164]; nevertheless, the photoelectrocatalytic abilities of other kinds of MXenes, such as Cr_2TiC_2, Mo_2ScC_2, $Mo_2Ti_2C_3$, $(Nb0.8Zr_{0.2})_4C_3$, Ti_3CN, $(Nb_{0.8}Ti_{0.2})_4C_3$, Ti_2C, Nb_2C, $TiNbC$, $(Ti_{0.5}Nb_{0.5})_2C$, and $V_2C,25$ Zr_3C_2 still need to be evaluated for CO_2 reduction along with other properties such as semiconductor, electron mobility and charge separation. Li et al. were able to attain a notable increase in efficiency for CO_2 photoreduction through the utilisation of a proficient cocatalyst (Ti_3C_2-OH/ZnO) prepared via a straightforward electrostatic self-assembly technique. This was accomplished by substituting the -F group of F-doped ZnO with surface-alkalinized 2 D Ti_3C_2 with a terminal -OH functional group [199]. The rates of CO and CH_4 production on Ti_3C_2-OH/ZnO (7.5 wt%) were significantly greater (30.3 and 20.3 $\mu molg^{-1}h^{-1}$, respectively) compared to those observed on unmodified ZnO (4.66 and 0.58 $\mu molg^{-1}h^{-1}$, respectively). The process of photocatalytic CO_2 reduction is subject to the influence of various parameters, including but not limited to the effective surface areas, light absorption abilities, electronic band structures, and charge migration rates of photocatalysts, as well as the CO_2 adsorption/activation abilities of photocatalysts [200]. The impact of surface area on CO_2 reduction was observed in Ti_3C_2-OH/ZnO (39.1 m^2g^{-1}), albeit to a lesser extent than in ZnO and Ti_3C_2/ZnO (47.2 and 34.8 m^2g^{-1}, respectively). The study demonstrates that introducing Ti_3C_2-OH significantly improves the transfer of photoinduced charge carriers in ZnO, as evidenced by the results of photoluminescence, transient photocurrent, and electrochemical impedance spectroscopy analyses. In general, when subjected to light irradiation, electrons are stimulated from the valence band to the

conduction band of ZnO, resulting in the presence of holes in the valence band. The exceptional electrical conductivity of Ti_3C_2 has enabled Ti_3C_2-OH to function as an electron trap, effectively capturing the photoinduced electrons in ZnO. The electron transfers from the conduction band of ZnO to Ti_3C_2-OH occurred rapidly, facilitated by the narrow interface between the two materials and the lower Fermi level of Ti_3C_2-OH. This process significantly improved the separation and transfer of electrons and holes [127]. The 2-dimensional surface of Ti_3C_2-OH facilitates the creation of electron-rich surroundings in this instance. As a result of the remarkable adsorption and activation properties of CO_2 molecules on Ti_3C_2-OH, the photoinduced electrons promptly reduced the adsorbed CO_2 molecules into reactive intermediates, namely HCO^{3-} and CO_3^{2-}. The aforementioned intermediates were subsequently transformed into carbon monoxide and methane [201]. Hence, the noteworthy electrical conductivity and CO_2 adsorption/activation capability establish Ti_3C_2-OH as a significant cocatalyst for significantly enhancing photocatalytic CO_2 reduction [199].

The present study reports the construction of a 3D nanocomposite, resembling hydrangea, comprising $InVO_4$ and $Ti_3C_2T_x$. The nanocomposite was synthesised in situ, and it was observed that $InVO_4$/Ti_3C_2Tx exhibited a remarkable ability to trap photons and possessed a multitude of reactive sites. Furthermore, incorporating $Ti_3C_2T_x$ enhanced the CO_2 capture capacity of $InVO_4$ [202]. The enhancement of the concentration of $Ti_3C_2T_x$ resulted in an improvement of the specific surface areas and 3D hierarchical structures of $InVO_4$/$Ti_3C_2T_x$ nanocomposites. The $InVO_4$/$Ti_3C_2T_x$ nanocomposites are likely to possess a significant number of surface-active sites readily accessible for photocatalytic reactions [203]. The principal reduction products in a reactor that involves a gas-solid system are CO and CH_4. Under the influence of lighting, there was a modest linear increase in the amount of CO produced while both $InVO_4$ and $InVO_4$/$Ti_3C_2T_x$ were present. In the case of pure $InVO_4$, the primary product was CO at a rate of 4.49 mol $h^{-1}g^{-1}$, while the amount of CH_4 produced was minimal at 0.09 mol h^{-1} g^{-1}. When compared to the yield of CO achieved over $InVO_4$, the CO selectivity achieved over $InVO_4$/$Ti_3C_2T_x$ was 92%, resulting in a greater total yield of CO. At a wavelength of 385 nm, the quantum efficiency of $InVO_4$/$Ti_3C_2T_x$ was measured to be 0.041% [203]. Dimensional complemented simple electrostatic self-assembly was used to produce 2D/2D nanocomposites of $InVO_4$ and $Ti_3C_2T_x$, and the resulting nanocomposites had superior CO_2 adsorption capabilities compared to those of pure $BiVO_4$ nanoparticles [204]. In addition, the successfully coordinated two-dimensional, and this two-dimensional mixed shape expedited the transit and separation of photogenerated charges. The $BiVO_4$/$Ti_3C_2T_x$ nanocomposites demonstrated a significantly higher photocatalytic generation of CH_3OH, with a rate of 20.1 μmol $h^{-1}g^{-1}$, compared to the pure $BiVO_4$ nanoparticle, which exhibited a rate four times lower. Moreover, Tahir et al. [205], fabricated composite material consisting of 2D porous g-C_3N_4 (PCN) coupled with exfoliated 3D Ti_3C_2TA MXene (TiC) nanosheets and TiO_2 nanoparticles (NPs) through an in-situ growth process facilitated by HF treatment. It was possible to successfully synthesise the various exfoliated TiC structures to alter the HF etching time to one of three different values:(24 h, 48 h and 96 h). After being subjected to UV–visible irradiation, g-C_3N_4 was responsible for the production of e^- and h^+, which were then used in the oxidation of H_2O/H_2/CH_3OH. The effective separation of charge carriers was observed due to the smaller conduction band of TiO_2, which facilitated the transportation of e^- to this band. Conversely, the smaller Fermi level of Ti_3C_2 resulted in the migration of e^- towards Ti_3C_2 [206]. The generated h^+ was used for H_2O and H_2 oxidation [174]. At pH 7, the pairings CO_2/CO and CO_2/CH_4 show potential selectivity of these products throughout the CO_2 reduction cycle. Because the conduction band of g-C_3N_4 is more negatively charged than the reduction potential of CO_2/CO, it is theoretically possible to produce CO by employing two e^- and two h^+ during the reduction of CO_2. This is because the reduction potential of CO_2/CO is greater than the conduction band of g-C_3N_4 [207]. The Fermi values of pure Ti_3C_2 and g-C_3N_4, measured in relation
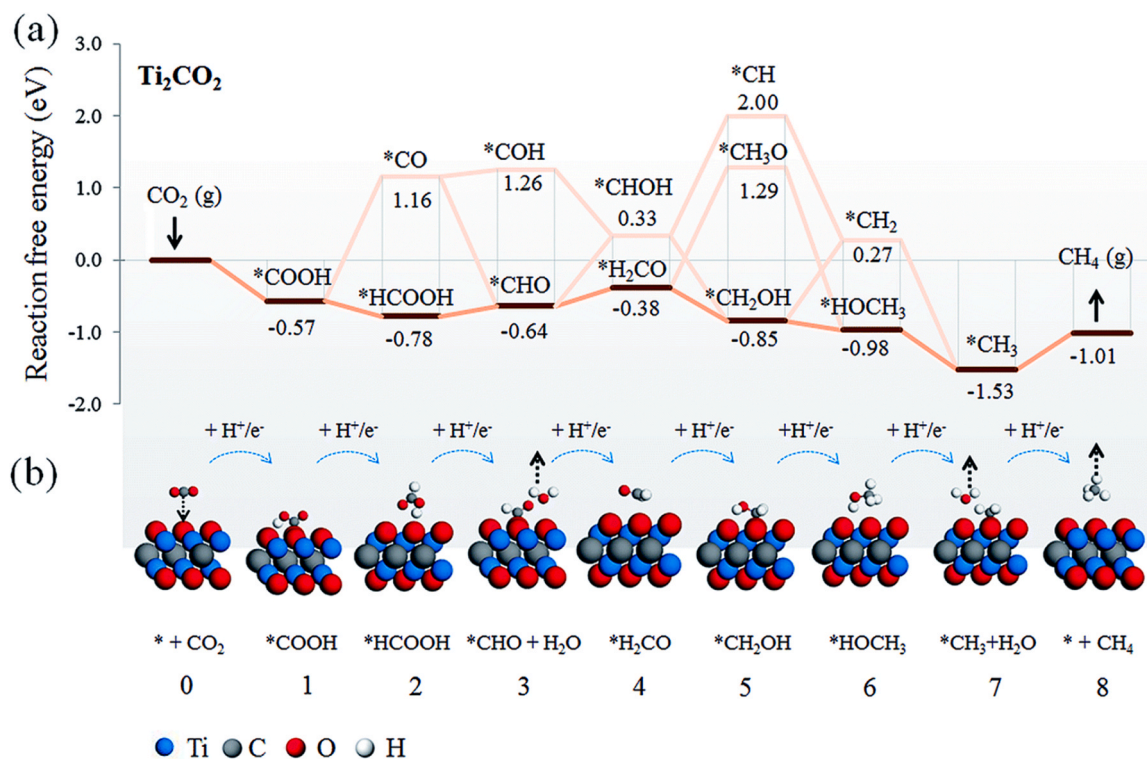
Fig. 16. (a) Free energy diagram and (b) ball-and-stick model representing the various possible pathways for the reduction of CO_2 to CH_4 on O-terminated Ti_2CO_2 MXene. The pathway through *C was excluded because it cannot be stably adsorbed and resulted in removal of O termination group in the final configuration [216].

to a standard H electrode at a pH of 7, were determined to be 0.45 and 0.91 V, respectively [165]. Because Ti_3C_2 has a lower Fermi level and higher electrical conductivity, the photogenerated electrons were swiftly transferred from the conduction band of g-C_3N_4 to Ti_3C_2 for CO_2 reduction. This was possible because the Fermi level is lower in Ti_3C_2 [208–210]. In spite of this, the Ti_3C_2TA/g-C_3N_4/TiO_2 heterojunction is superior to the Ti_3C_2/g-C_3N_4 nanocomposite when it comes to separating photogenerated charges. In addition, the synergistic effect of TiO_2/Ti_3C_2TA operating over g-C_3N_4 makes it possible to transmit and separate charge carriers effectively. Overall, Ti_3C_2TA functions as an e⁻-trap, while the TiO_2 nanoparticles function as a conduit to transport e⁻ from g-C_3N_4 to Ti_3C_2; however, the TiO_2 nanoparticles have a lower efficiency. In addition, the synthesis of e⁻ rises with a boost in the amount of light (from 20 to 100 mW/cm²), which enables the formation of more CO and CH_4 under the same conditions. Therefore, these nanocatalysts display a greater separation of charge carriers, and the presence of an e⁻-rich atmosphere over the Ti_3C_2TA surface facilitates the continuous reduction of CO_2 to CO/CH_4 when the material is illuminated [205].

The potential applications of MXene-based nanomaterials in photocatalytic CO_2 reduction are analogous to the functions of MXene-based electrocatalysts in electrochemical CO_2 reduction, as evidenced by recent evaluations [125,211–213]. The efficacy and specificity of carbon dioxide reduction on MXenes are intricately linked to the hydrogenation mechanism and the active sites terminated on the surface. Xiao et al. conducted a theoretical study on the hydrogenation of CO_2 on MXene surfaces of M_3C_2 (where M represents Sc, V, Mn, Zr, Nb, Hf, Hf, Mo, and W) [214]. The stimulation of taken in CO_2 and its subsequent combination with surface hydrogen to form bicarbonate species has been shown to result in increased selectivity for the CO_2 reduction reaction (CO_2RR) over the hydrogen evolution reaction (HER). The study examines the various routes of transforming carbon dioxide into methane and concludes that the bicarbonate (HCO_2) species is the most energetically favourable reaction pathway. Additionally, the intermediate product of the CO_2RR process is primarily HCHO. The computational

findings have indicated the existence of two distinct pathways for CO_2 reduction reaction (CO_2RR) on M_3C_2 MXenes, which can be differentiated based on the initial protonation step. The final outcome of both pathways is the production of methane. The generation of bicarbonate intermediate entities *HCO_2 through the process of CO_2 conversion and subsequent protonation as described (*HCO_2 →*H_2CO_2 →*H_2COOH→*H_2CO →*H_3CO → *O (+ *CH_4) →*OH → *H_2O). For the majority of the MXenes that have been studied, the energetically favourable pathway is the one, meanwhile, the mechanism behind this remains unclear. *COOH →*HCOOH → *CHO → *HCHO→*H_2COH →*H_3COH → *CH_3 → *CH_4.

The catalysts Ta_3C_2 and W_3C_2 are comparatively more favorable. The M-O-C or M-C-O binding has been proposed as the determining factor for the binding features of HCO_2 or COOH. The previously mentioned results highlight a crucial characteristic of MXenes, namely that the surface of unmodified MXenes is capable of dissociating molecules with high stability, such as CO_2, which typically represent the rate-limiting steps of the reactions under investigation. Theoretical investigations have been conducted on the impact of oxygen and hydroxide MXene-termination groups on CO_2RR. Because of the hydrogen-bond interaction between *HCOOH and the surface groups, particularly –O, a peculiar CO_2RR behavior has been seen on Ti_2CT_x and Mo_2CT_x MXenes. This behavior is characterized by the fact that the *HCOOH pathway dominates the surface CO_2RR rather than the *CO pathway, which is typical for most transition metal catalysts. The carbon atoms on its surface determine the surface characteristics of MXene. Typically, the *COOH moiety exhibits binding affinity towards the –OT_x moiety on MXene surfaces via the C atom, while the *HCOOH moiety binds via the H atom. The preferences of HCOOH intermediate lead to non-linear scaling with COOH in relation to their binding energies due to the distinct coordination of these two intermediates on the surfaces of MXene [215]. The energy barrier reduction for CO_2 reduction to CH_4 over $Cr_3C_2T_x$ and $Mo_3C_2T_x$ was observed with the surface functionalization of -O and -OH, compared to the MXenes that were not functionalized [184]. Handoko et al. [216] have published a study on the

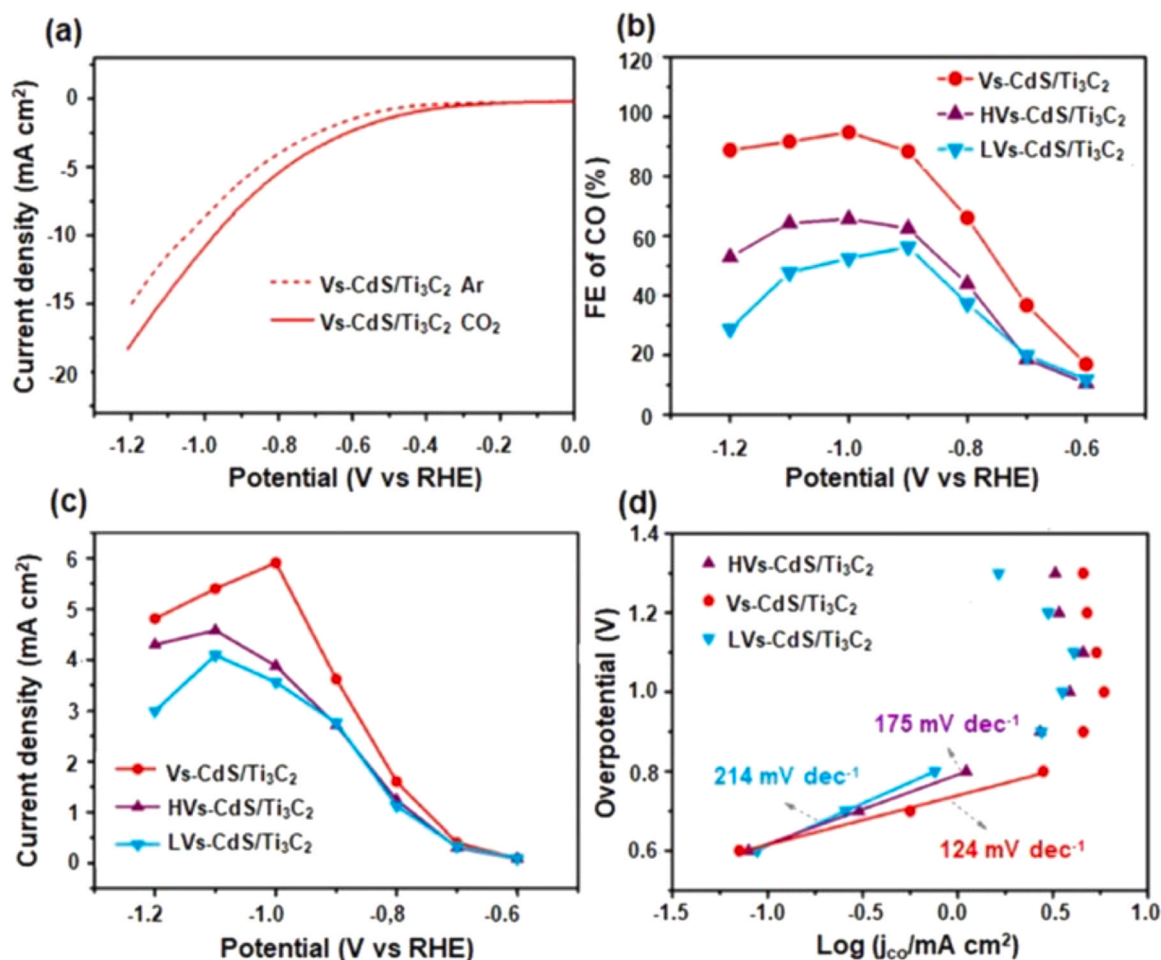**Fig. 17.** (a) Linear sweep voltammogram curves of V_S-CdS/Ti_3C_2 in CO_2 (solid line) and Ar (dash line) saturated 0.1 M KHCO$_3$ aqueous solution. (b) faradic efficiency (FE) for CO, (c) current density, and (d) Tafel plots of LV_S-CdS/Ti_3C_2, V_S-CdS/Ti_3C_2, and HV_S-CdS/Ti_3C_2 (j_{co} = CO partial current density) [163].
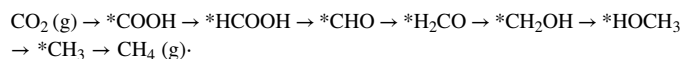
reduction of CO_2 using O-terminated MXene catalysts. The catalysts prefer for binding CO, resulting in the selective production of CH_4 at low overpotentials. The researchers concluded that W_2CO_2 and Ti_2CO_2 exhibit significant potential as MXenes for CO_2 reduction reaction, with respective theoretical overpotentials of 0.52 and 0.69 V [216]. The electrochemical reduction of carbon dioxide to methane can be expressed through the subsequent chemical Eq. 5:

$$CO_2 + 8\ H^+ + 8e^- \rightarrow CH_4 + 2\ H_2O \qquad (5)$$

The process entails eight successive steps of proton and electron transfer. Shown in Fig. 16a. The free energy diagram for the reduction of CO_2 on Ti_2CO_2 MXene has been computed, and the pathway with the highest degree of favorability is highlighted in a dark brown hue. On this surface, the first reaction step of CO_2 (g) adsorption and protonation was found to be exergonic at zero potential. Upon CO_2 adsorption, the terminal oxygen of CO_2 undergoes attachment with incoming H, resulting in the formation of an intermediate *COOH. This intermediate is bonded to Ti_2CO_2 through the C atom. (Fig. 16b). They point out that 15 out of the 19 M_2XO_2 MXene families investigated here require energy input for the synthesis of *COOH, indicating that the spontaneous initial step demonstrated on Ti_2CO_2 is an anomaly rather than the rule. There were two options for the second hydrogenation stage.

The first mechanism is well known to those who work with transition metal catalysts; it involves the binding of incoming hydrogen to the OH group on the COOH molecule, which results in the production of CO and the release of water [217]. The elevated reaction energy, denoted by ΔG = 1.73 eV, suggests that the pathway in question is unfavorable on the

Ti_2CO_2 surface and possesses a lower probability of occurrence. The formation of *HCOOH via the addition of forthcoming hydrogen to the C atom of *COOH was observed to be considerably more favorable as a second potential pathway. Upon following the HCOOH pathway, it is observed that the Ti_2CO_2 substrate exhibits the minimum energy path for the production of CH_4, which can be described as follows:

CO_2 (g) → *COOH → *HCOOH → *CHO → *H$_2$CO → *CH$_2$OH → *HOCH$_3$ → *CH$_3$ → CH$_4$ (g).

It is noteworthy that the coordination of intermediates on the O-terminated MXene surface alternates between –C and –H binding. The functional groups *COOH, *CHO, *CH$_2$OH, and *CH$_3$ exhibit binding to the MXene surface via the carbon atom, whereas *HCOOH, *H$_2$CO, and *HOCH$_3$ demonstrate binding to the MXene surface via the hydrogen atom (Fig. 16b) [218].

Moreover, Chen et al. [219] employed first principles approaches based on thermodynamics and kinetics to investigate the reduction of CO_2 over a range of (–OH)-terminated M_2C and M_2N MXenes, where M represents Hf, Nb, Sc, Ta, Ti, V, Y, and Zr. The simulations led to the discovery of a potentially limiting phase known as * (H)COOH *CO for the majority of the OH-terminated MXenes. In this phase, the adsorbed *CO is stabilized by accepting H atoms from the OH termination group. $Sc_2C(OH)_2$ and $Y_2C(OH)_2$ have been identified as the most favorable catalysts for the breakdown of CO_2 to CH_4, owing to their easy access to the peak of the volcano curve. These catalysts exhibit the least negative limiting potential of − 0.53 V and − 0.61 V, respectively, under aqueous reaction conditions.
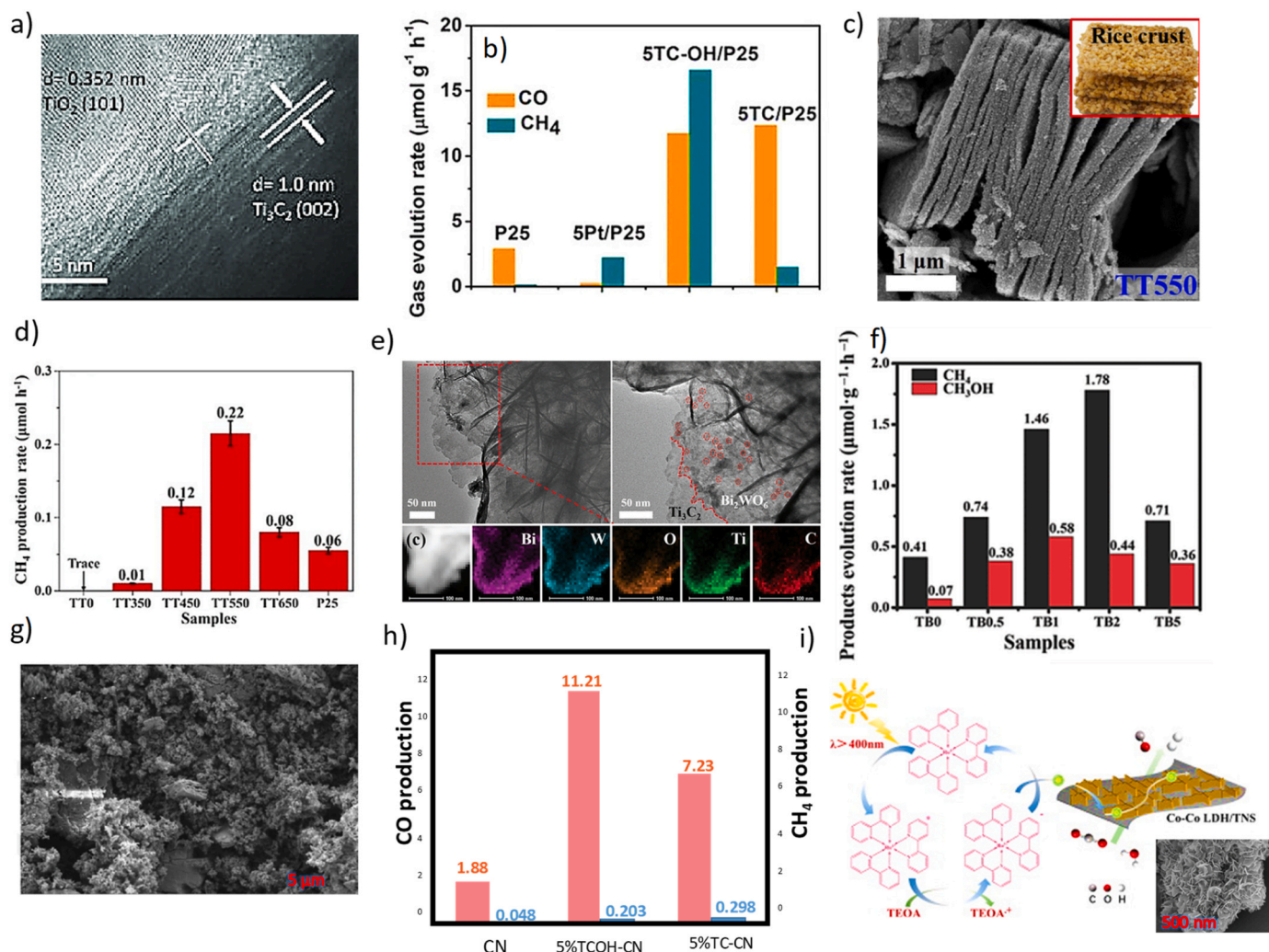
Fig. 18. (a) HRTEM image of the interface structure of Ti_3C_2–OH and TiO_2 P25 NPs. (b) Evolution rates of CO and CH_4 over P25, 5% Pt/P25 (5Pt/P25), 5% Ti_3C_2/P25 (5TC/P25), 5% Ti_3C_2–OH/P25 (5TC-OH/P25) under irradiation by a 300 W Xe lamp [222]. (c) Field emission scanning electron microscope (FESEM) image of rice-crust like TiO_2/Ti_3C_2 composite. (d) Comparison of the photocatalytic CO_2 reduction of the TiO_2/Ti_3C_2 composite samples without calcination and with calcination (TT350, TT450, TT550 and TT650 were defined as the TiO_2/Ti_3C_2 prepared under different calcination temperatures) and P25 for CH_4 production [223]. (e) TEM image of 2% Ti_3C_2 in Ti_3C_2/Bi_2WO_6 and the element mappings of Bi, W, O, Ti, C of the selected area. The red circles indicate the Bi particles derived from Bi_2WO_6 nanosheets under the high-power electron beam. (f) Photocatalytic activity of TB0 to TB5, where TBX = Ti_3C_2/Bi_2WO_6 and X = thewt% of Ti_3C_2 [179]. (g) SEM image of 5% Ti_3C_2/g-C_3N_4 sample. (h) 5 h accumulated production of CO and CH_4 on g-C_3N_4 (CN), 5% Ti_3C_2-CN (5% TC-CN), and 5% Ti_3C_2–OH–CN (5% TCOH-CN) [224]. (i) Co–Co layered double hydroxide/ Ti_3C_2Tx nanosheets (LDH/TNS) for CO_2 reduction with triethanolamine (TEOA) as a sacrificial agent. Inset is the SEM image of the catalyst morphology [225].

Subsequently, two distinct MXenes, namely Mo_2C and Ti_3C_2, were utilized as electrocatalysts for the purpose of CO_2 reduction with faradaic efficiencies of 90% (250 mV overpotential) and 65% (650 mV overpotential), respectively, in the conversion of CO_2 to CO in an ionic solution containing acetonitrile [185]. The study found that the faradaic efficiencies of both catalysts in generating CO during CO_2 reduction were dependent on the cathodic overpotential. The faradaic efficiency of Mo_2C exhibited a decline of roughly 80% and 50% at the respective potentials of 600 mV and 750 mV. A corresponding increase in the production of H_2 at the provided voltages accompanied the decrease in the faradaic efficiency of Mo2C for CO production. The overpotential necessary for the early formation of CO during CO_2 reduction over Ti_3C_2 was around 650 mV. This significantly increased compared to the overpotential required for synthesizing CO over Mo_2C, which was only 200 mV. At the potentials that were applied for 30 min, there was a minor consistency in the rate at which CO_2 was reduced to CO over $Ti_3C_2H_2$ evolution over Mo_2C that is lower than those required for Ti_3C_2 [163]. The aforementioned findings suggest that the active sites on the

surface of MXene may be identical in driving both the catalytic reduction of CO_2 to CO and the evolution of H_2 in an aqueous setting. In addition, CdS/Ti_3C_2 nanocomposites were successfully synthesized through a simple solvothermal method in conjunction with H_2/Ar treatment, incorporating varying quantities of cadmium acetate. These nanocomposites were employed as electrocatalysts for CO_2 reduction. The surface of Ti_3C_2 was coated with CdS nanoparticles featuring multiple openings, which provided active sites for the reduction of CO_2. The assessment of CO_2 reductions throughout the aqueous solutions of electrocatalysts was conducted in both Ar (0.1 M $KHCO_3$) and CO_2-saturated electrolytes. The voltammograms depicting linear sweep of Ti_3C_2 in both Ar- and CO_2 saturated electrolytes exhibited high similarity, indicating that the electrochemical reduction in aqueous solution is inert. The CdS/Ti_3C_2 material demonstrated notably elevated currents in the CO_2-saturated electrolyte as compared to the Ar-saturated electrolyte, as depicted in Fig. 17a. In contrast to the electrochemical CO_2 reduction activity of Ti_3C_2 predicted by density functional theory, the H_2 generation rate over Ti_3C_2 was roughly two orders of magnitude greater

than the CO production rate [197]. The observed trend can be attributed to the use of an aqueous electrolyte because many MXenes, including Ti_3C_2, Mo_2C, and Ti_2C, have been shown to achieve adequate electrochemical CO_2 reduction rates in non-aqueous electrolytes [211,215]. The faradaic efficiency of CdS/Ti_3C_2 for CO generation significantly enhanced up to roughly 95% in the potential range of -0.6 to -1.0 V vs the reversible H_2 electrode (Fig. 17b). The presence of a significant quantity of titanium on the surface of the LVS-CdS/Ti_3C_2 material that included 150 mg of cadmium acetate was shown to be the cause of the material's comparatively low faradaic effectiveness. LVS-CdS/Ti_3C_2 has a predictable, competitive reaction that lowers CO generation faradaic efficiency. VS-CdS/Ti_3C_2 without cadmium acetate had the highest CO partial current density at all potentials, indicating the highest electrochemical CO_2 reduction activity (Fig. 17c). The lowest Tafel slope was 124 mV dec^{-1}, slightly similar to the expected Tafel slope (118 mV dec^{-1}), indicating that the rate-limiting step was the generation of $CO_2\bullet^-$ via the transfer of 1 e$^-$ (Fig. 17d). The Tafel slope value of VS-CdS/Ti_3C_2 was observed to be considerably lower than that of LVS-CdS/Ti_3C_2 (214 mV dec^{-1}) and LVS-CdS/Ti_3C_2 containing 450 mg cadmium acetate (175 mV dec^{-1}), which suggests that VS-CdS/Ti_3C_2 exhibits superior kinetics for CO generation.

The coupling of MXenes to other photoactive materials is a significant approach for CO_2 photoreduction, given that the majority of MXenes demonstrate metallic behavior. For CO_2 photoreduction, Ye and his colleagues linked TiO_2 nanoparticles (P25) to Ti_3C_2–OH MXenes (Fig. 18a) [220]. The MXene/TiO_2 heterostructures exhibit enhanced electrical conductivity and charge carrier separation capabilities, in addition to ample sites for CO_2 adsorption and activation. The heterostructures demonstrate superior performance in CO_2 reduction reactions, generating higher yields of CO (11.74 mmol g^{-1} h^{-1}) and CH_4 (16.61 mmol g^{-1} h^{-1}) compared to bare P25 (Fig. 18b) and for P25 loaded with 5 wt% Pt (5Pt/P25). The process of annealing a precursor of Ti_3C_2 MXene has been employed to generate hybrids of TiO_2/Ti_3C_2, which exhibit a distinct structure resembling that of a "rice-crust" (Fig. 18c) [221]. The exceptional photocatalytic performance observed in the reduction of CO_2 to CH_4, with a rate of 0.22 mmol h^{-1}, was facilitated by efficient interfacial charge transfer. This rate was found to be 3.7 times greater than that of a P25 TiO_2 control (Fig. 18d). Moreover, ultrathin nanosheets of Ti_3C_2/Bi_2WO_6 were synthesized by Cao et al. using hydrothermal techniques (Fig. 18e) [179]. Photoexcited electron transport from Bi_2WO_6 nanosheets to metallic, O-terminated Ti_3C_2 and the consequent reduction of adsorbed CO_2 were triggered by the interface energies of this heterostructure. As demonstrated in Fig. 18f, the optimum Ti_3C_2 loading of 2% in Ti_3C_2/Bi_2WO_6 (TB2) yielded 1.78 and 0.44 mmol h^{-1} g^{-1} CH_4 and CH_3OH, respectively, surpassing pristine Bi_2WO_6.

Tang et al. observed photocatalytic CO_2RR dependence on MXene fraction for heterostructures between graphitic carbon nitride (g-C_3N_4) and Ti_3C_2–OH (Fig. 18g) and the composite demonstrated optimal performance, resulting in CO and CH_4 yields that were approximately six and four times higher than those achieved with pure g-C_3N_4, respectively (Fig. 18h) [224]. Furthermore, Liu and colleagues synthesized a composite material consisting of CeO_2@Ti_3C_2. This composite material achieved a Schottky junction through the electric field built between CeO_2 and MXene [226]. This photocatalyst demonstrated the highest CO yield of 40.2 mmol m^{-2}h^{-1} under visible illumination, which is approximately 1.5 times greater than that of pure CeO_2. A recent study has demonstrated the utilization of nanocomposites that pair Co–Co layered double hydroxides with $Ti_3C_2T_x$ for CO_2RR photocatalysis (Fig. 18i). The enhanced conductivity and surface activity of MXene facilitate rapid electron transfer and provide sufficient catalytic sites for efficient separation and utilization of electrons. The CO_2RR quantum efficiency displayed was commendable, measuring at 0.92%, specifically at 420 nm. Additionally, the stability of the process was tested and proven reliable, withstanding 5 cycles of 5 h each to produce CO. The CO generation yield exhibited significantly superior performance

compared to the pristine Co–Co photocatalyst, achieving an impressive 12,500 mmol g^{-1} h^{-1} under visible-light irradiation (4400 nm) [171].

3.4. Role of functional groups (F, -OH, -O) in reduction of CO_2

Functional groups are essential in facilitating the reduction of carbon dioxide (CO_2) through their ability to participate in diverse chemical reactions. These functional groups, namely hydroxyl (-OH), carboxyl (-COOH), amino (-NH_2), carbonyl (C=O), and amide (-$CONH_2$), exhibit distinct properties that enable them to engage with CO_2 and facilitate its transformation into various compounds. In the etching procedure, the removal of "A" atoms resulted in the retention of functional groups (-O, -OH, or -F) on the surface of MXene, thereby passivating the outer-layer metal atoms. MXene phases exhibit various configurations that possess diverse unique properties, depending on the specific functional groups present. Numerous theoretical investigations have demonstrated that unmodified MXene materials exhibit metallic behavior, while a significant portion of MXene compounds are rendered non-metallic through the passage by -OH, -F, and -O functional groups. Remarkably, a subset of M_2C (where M represents Ti, Zr, Hf, Sc) MXenes exhibit a transition from a metallic state to a semiconducting state through the process of surface functionalization, specifically involving the introduction of -O, -OH, or -F moieties. As a result of this modification, these MXenes acquire band gaps ranging from 0.24 to 1.8 electron volts [137]. The obvious band gaps of surface-functionalized MXenes indicate their pronounced capacity for visible-light absorption and their potential for utilization in photocatalytic applications. Xiong et al. [227] conducted a rigorous computational analysis employing first-principle computation techniques. Their study aimed to elucidate the impact of various surface-group types on the intricate interplay of structural, electronic, and optical properties exhibited by Sc_2CT_2 (T = -O, -OH, -F) MXenes. Amongst the various geometries encompassing the Sc_2CT_2 MXenes, it is noteworthy that the geometry denoted as I, wherein the functional groups are positioned above the Sc atoms on the opposing side, stands as the structure with the most minimal energy. Consequently, the Sc_2CF_2-I, Sc_2CO_2-I, and $Sc_2C(OH)_2$-I compounds, which exhibit a notable energetic preference, have been chosen for subsequent assessment of their photocatalytic capabilities. It has been determined that Sc_2CO_2-I exhibits metallic properties, whereas Sc_2CF_2-I and $Sc_2C(OH)_2$ display characteristics of semiconductors, including visible-light absorptions and encouraging carrier mobilities. In contrast to the $Sc_2C(OH)_2$-I, the Sc_2CF_2-I exhibits a more favourable band gap of 1.91 eV and possesses enhanced redox potential for photo-induced carriers. Consequently, it is anticipated that the Sc_2CF_2-I would demonstrate superior photocatalytic performance. Furthermore, it is worth noting that the Sc_2CF_2-I MXene exhibits a remarkable reduction potential of -1.038 V (vs. SHE). This characteristic renders it highly suitable for applications involving photocatalytic reduction of carbon dioxide or hydrogen generation through photocatalysis. Theoretical computations elucidate the extent to which diverse metallic constituents in MXene govern the stability of M-T_x, thereby delineating the number of tunable T_x populations [228,229]. In this regard, it has been computed and observed that MXenes terminated with -O exhibit a reduced lattice factor and thinner inter-layer thickness compared to their -F and -OH terminated counterparts. This leads to enhanced mechanical strengths in the -O terminated MXenes. The heightened semiconducting characteristics of MXenes can be ascribed to the existence of T_x terminations and the unique hybridization of electron orbitals, resulting in variations in the bandgap. Consequently, this alteration in electronic properties is observed, as both -F and -OH terminations can only accept a single electron, exhibiting analogous electronic behavior [145]. Furthermore, it is worth noting that the $Ti_3C_2T_x$ material, which is terminated with -OH groups, exhibits a greater propensity for the adsorption of carbon dioxide when compared to its counterpart completed with F- groups. Also, the occupation of surface termination sites in MXene involves the introduction of functional groups such as -OH, -F, and -O, with the exception of MXene synthesized
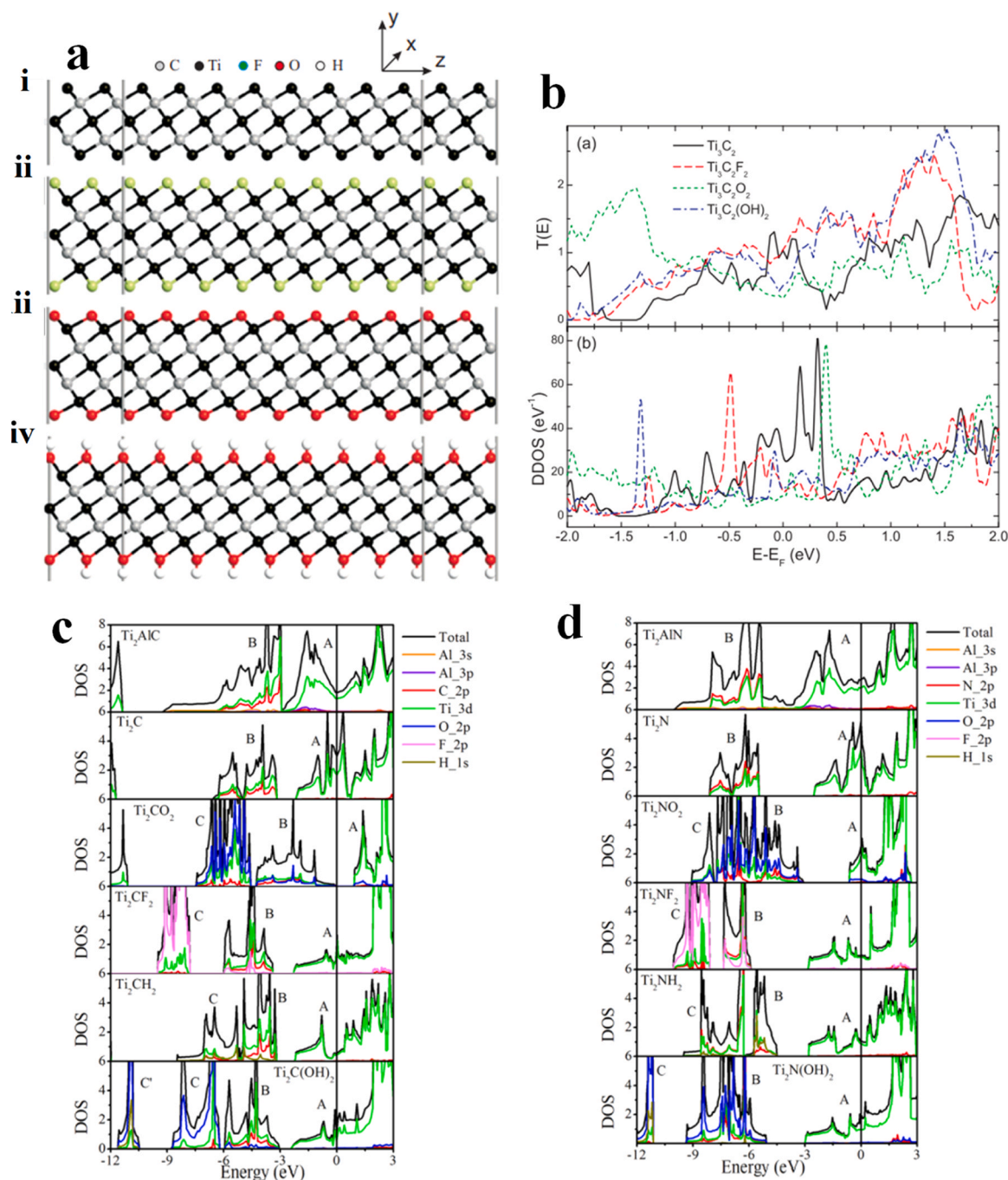
Fig. 19. (a)(i) Surface-terminated Ti_3C_2 MXene, having various functional groups, (ii-iv) representation of -F, -O, -OH terminated Ti_3C_2 MXene, $Ti_3C_2F_2$, $Ti_3C_2O_2$, and $Ti_3C_2(OH)_2$, respectively. (b) (v) Zero-bias transmission spectra, and (vi) DOS of Ti_3C_2, $Ti_3C_2F_2$, $Ti_3C_2O_2$ and $Ti_3C_2(OH)_2$ [231]. (c) and (d) Partial density of states of Ti_2CT_2 and Ti_2NT_2, and related MXenes and MAX phase computed using the HSE06 functional [128].

via the chemical vapor deposition (CVD) technique, wherein unadorned Mo_2C species are cultivated on molten Cu/Mo substrates derived from CH_4 precursor [230].

Berdiyorov et al. [231] used theoretical calculations and non-equilibrium Green's functional formalism to determine how surface functionalization affects Ti_3C_2's electrical characteristics. Using optimal architectures, they created two probe device geometries with left, right, and middle (scattering) sections. We placed metallic electrodes at the left and right corners of the sample with in-plane periodic boundary conditions perpendicular to the metal contacts. An electron gas with a set chemical potential is assumed to be at the metallic contact. The transmission is calculated along the z-direction, and the system is

periodic in the x- and y-directions (Fig. 19a(i-iv)). It has been noted that surface termination substantially impacts these materials' electronic characteristics. For example, the process of fluorination enhances electron transmission across a wide range of energy levels, whereas the oxidized sample hinders the transport of low-energy electrons. This hindrance may be attributed to the localization of electronic states and oscillations in the electrostatic potential, primarily influenced by surface chemistry (Fig. 19b(v-vi)). It has been observed that the surface termination of the material has a notable influence on its transport properties. As an illustration, fluorination leads to increased transmission across a wide range of electron energies, while the sample undergoing oxidation exhibits the lowest electron transport. The observed differences in the

transmission spectra can be assigned to the localization of electronic states and the oscillations in the electrostatic potential profile. Surface chemistry highly influences these characteristics. These investigations provide an opportunity for future studies on MXene to explore the potential of modifying its mechanical, structural, and electronic properties through chemical modification of functional groups on the surface of MXene.

Similarly, Xie et al. [128] conducted a study on the electronic properties of surface-terminated $Ti_{n+1}C_n$ and $Ti_{n+1}N_n$ MXenes, specifically focusing on the terminations of O, OH, H, and F. Fig. 19c displays the partial density of states (DOS) for Ti_2AlC and the corresponding MXenes, considering their surface terminations. The DOS in the vicinity of the Fermi energy (Ef) for the MAX phase is primarily influenced by the titanium (Ti) 3d orbitals, (as depicted in Fig. 19c). When the aluminum (Al) layers are removed from the MAX phase, the Ti 3d orbitals undergo redistribution or delocalization, forming metallic bonds between titanium atoms (Ti-Ti). The presence of surface terminations results in the depletion of electronic states in close proximity to the Fermi energy (Ef). The metallic Ti_2C exhibits a narrow band gap upon the introduction of O_2 surface termination groups. The band gap is determined to be 0.24 eV using the PBE functional and 0.88 eV using the HSE06 hybrid functional. The metallic nature of all other materials remains unchanged. However, a noticeable reduction in the DOS near the Fermi energy (Ef) is observed. A comparable outcome is computed for Ti_2AlN and its corresponding MXenes, as depicted in Fig. 19d. Additionally, it was observed that the outcomes obtained from the PBE and HSE06 methods exhibit a high degree of similarity. In the absence of functional groups, MXenes exhibit magnetically ordered ground states. All materials under investigation exhibit metallic properties, except Ti_2CO_2, for which a semiconductor behavior is anticipated. The density of states at the Fermi level of MXenes with a thickness of $n \geqslant 5$ exhibits a significantly greater magnitude than thinner MXenes. This disparity suggests that various characteristics, including electronic conductivity and surface chemistry, must manifest distinctively between the two categories. Typically, carbides and nitrides exhibit distinct behaviors when interacting with identical functional groups.

In contrast to the unblemished $Ti_3C_2T_x$ MXene surface, the researchers have observed a decline in the density of states (DOS) near the Fermi level (Ef) for the MXene with a high concentration of defects. This outcome was anticipated to result in a reduction in conductivity. Nonetheless, varied Ti vacancy levels on OH-terminated Ti_3C_2 MXene exhibited almost identical DOS; consequently, strong conductivity close to pristine surfaces was projected. The theoretical results presented in this study are corroborated by the recent experimental findings conducted by Hart et al. [232]. The researchers investigated the impact of surface termination and intercalants on the electronic characteristics of Ti_3CNT_x, $Ti_3C_2T_x$, (TBA^+), Ti_3CNT_x and $Mo_2TiC_2T_x$ (delaminated using tetrabutylammonium hydroxide, TBAOH). The process of vacuum annealing resulted in the partial elimination of surface terminations, specifically those involving F, OH, and O. It was observed that O terminations exhibited greater stability compared to F terminations. The enhancement of electronic conductivity was observed in all the probed MXenes upon the elimination of surface terminations.

In relation to the specific carbon dioxide reduction reaction (CO_2RR) and nitrogen reduction reaction (NRR) discussed in this review, it is worth mentioning that the unmodified surface of MXenes exhibits inherent reactivity and possesses low energy barriers for the dissociation of CO_2 and NO_2, which are typically the determining factors for the reaction rate. The intriguing surface-determining activity and selectivity exhibited by MXenes have been thoroughly investigated and will be elaborated upon in the subsequent sections [233]. Additionally, the generation of terminal -OH functional groups provides numerous sites for both the adsorption and the activation of CO_2 molecules. The investigation of the photocatalytic reduction of carbon dioxide through different reforming methods, such as the photocatalytic dry reforming of methane (CH_4) and bi-reforming of methane, demonstrated that the

bi-reforming of methane exhibited higher rates of carbon monoxide (CO) and hydrogen (H_2) production. This can be attributed to the effective reaction of the reactants occurring at electron-rich defect sites. In general, the utilization of MXenes with diverse functional groups has expedited the investigation pertaining to the augmentation of charge carrier separation, the enhancement of CO_2 adsorption capabilities, the adjustment of work function, and the provision of active sites for the process of photocatalytic or electrocatalytic CO_2 reduction [163].

3.5. Significance of etching

As previously mentioned in this section, it has been established that the primary method of synthesizing MXene involves the selective etching of aluminum from the MAX phase. The manufacturing of MXene can be classified into two distinct categories based on the methodology employed: (i) Top-Down synthesis method, specifically selective etching, and (ii) Bottom-Up synthesis method, specifically chemical vapor deposition (CVD). Additionally, the Top Down synthesis method can be further classified into two distinct types: (a) the conversion from the 3D MAX phase to the 2D MXene phase, and (b) the transformation from non-MAX materials to the 2D MXene phase [34,86,234].

In addition, the process of mechanical exfoliation is employed to facilitate the exfoliation of graphite into two-dimensional graphene. However, this method cannot be applied in MXene synthesis due to a robust metallic bond between the M and A elements within the MAX phase. However, due to the greater susceptibility of M-A bonds compared to M-X bonds, the A element, primarily Al, can be selectively removed through etching processes to produce MXene. The etchants that are frequently employed include aqueous hydrofluoric acid (HF), HF-containing etchants (HF/HCl), HF forming (LiF/HCl), molten salt etchant (KF, LiF, NaF), alkaline etchant, and/or hydrothermal treatment (e.g., NaOH followed by H_2SO_4 treatment) [34,235]. Given that etching is primarily carried out using acids, it is common practice to terminate MXene with functional groups such as OH, F, O, and so on. The exceptional conductivity and hydrophilicity of MXene can be attributed to the appearance of functional groups. The synthesis of MXene materials, such as $Zr_3C_2T_x$ and $Hf_3C_2T_x$, involves the utilization of non-MAX phase precursors like $Zr_3Al_3C_5$ and $Hf_3Al_4C_6$, respectively [96,236]. When comparing the Top-down method to the Bottom-up method, it is evident that the latter is more advantageous for synthesizing 2D materials with a substantial surface area, thereby ensuring high quality. For this evidence, Xu et al. [237] fabricated two-dimensional ultrathin MoC_2 crystals using the chemical vapor deposition (CVD) technique. In this experiment, a Cu/Mo bilayer substrate was subjected to thermal treatment at temperatures exceeding 1085 °C within a tube furnace. Following this, a minute quantity of CH_4 was introduced into the system to facilitate the initial formation of α-Mo_2C crystals. The synthesis of WC or TaC crystals can be achieved by substituting Mo foil with W or Ta foils, employing a similar methodology [34].

In a broad sense, it can be stated that $Ti_3C_2T_x$ MXene inherently possesses the characteristics of a two-dimensional nanomaterial. The primary method employed for synthesizing 2D $Ti_3C_2T_x$ MXene involved direct HF etching, although an alternative approach utilizing acid-containing fluoride ions can also yield the desired result. The utilization of the direct HF etching technique will result in the production of $Ti_3C_2T_x$ MXene comprising multiple layers of sheets. In order to achieve a more thorough separation of the individual layers, it is necessary to utilize intercalating agents, such as dimethyl sulfoxide (DMSO), to facilitate the exfoliation and delamination process. However, the application of fluoride ions containing acid, referred to as the in-situ HF technique, can cause the layer to separate into a single layer of $Ti_3C_2T_x$ MXene during the etching process. The utilization of diluted hydrochloric acid (HCl) can facilitate the etching of the aluminum (Al) atom, whereas the inclusion of lithium (Li^+) ions aids in the process of delamination. The synthesis of zero-dimensional quantum dot (QD) $Ti_3C_2T_x$ MXene can be achieved through either a bottom-up or top-down
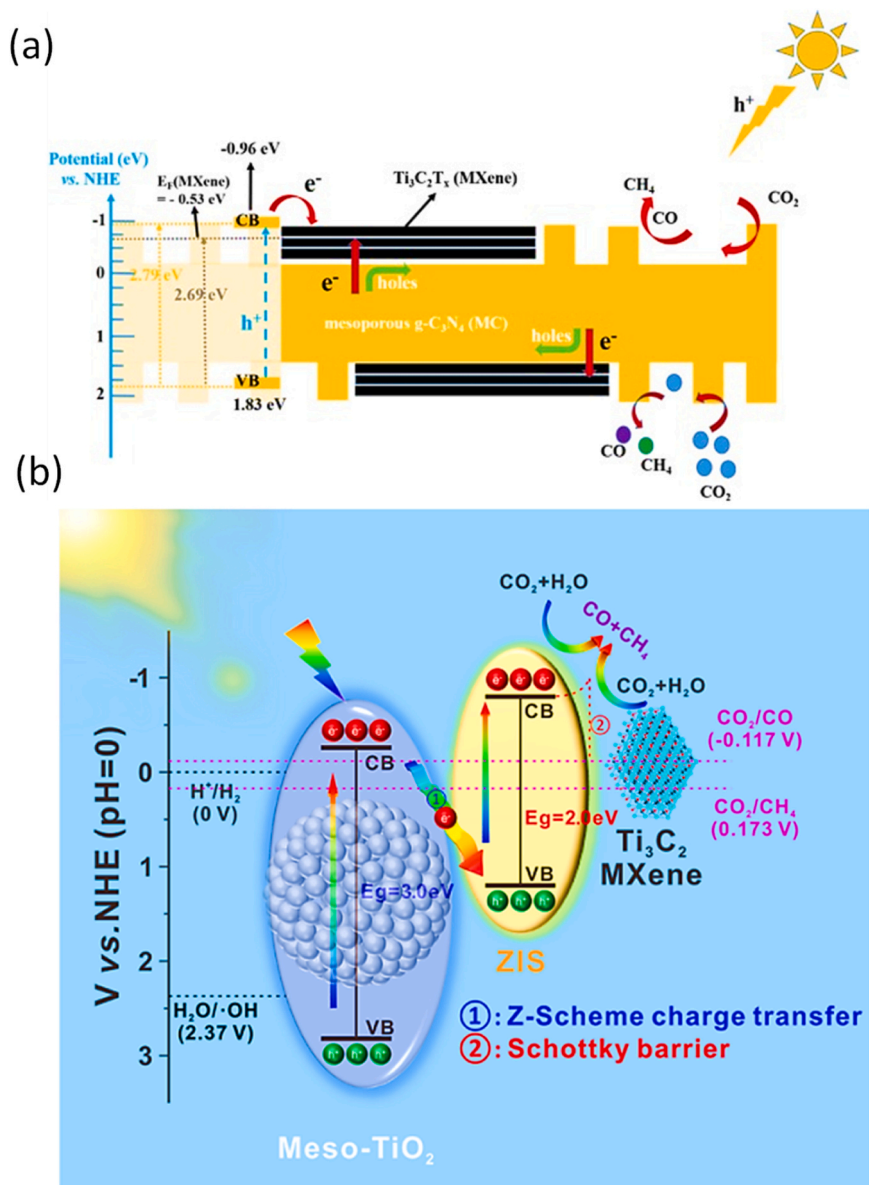
Fig. 20. (a) Photocatalytic process of Mesoporous g-C$_3$N$_4$/Ti$_3$C$_2$T$_x$ (MCT) for CO$_2$ reduction [241], (b) Illustration of the proposed reaction mechanism for photocatalytic CO$_2$ reduction with H$_2$O over the ternary composite of t-zis-m under UV–vis light irradiation.

methodology. The utilization of the bottom-up approach facilitated enhanced control over the shape and size of the synthesized materials at the atomic level.

In contrast, the top-down approach necessitated the disintegration of the whole material into nanostructures through methods like etching and ball milling. The three-dimensional morphological architecture of Ti$_3$C$_2$T$_x$ MXene can be achieved by fabricating composite materials. The self-assembly technique can create a three-dimensional composite by self-assembling additional semiconductors onto Ti$_3$C$_2$T$_x$ MXene. Additionally, the observation of the growth of alternative semiconductor materials using the in-situ decoration technique via hydrothermal treatment of Ti$_3$C$_2$T$_x$ MXene resulted in the formation of three-dimensional morphological Ti$_3$C$_2$T$_x$ MXene nanoflowers [238]. Moreover, the electrocatalyst was synthesized using Nb$_4$AlC$_3$, a Max phase compound, by subjecting it to etching with hydrofluoric acid (HF) [239]. The presence of surface termination groups such as fluorine (F), oxygen (O), and hydroxyl (OH) in the Nb$_4$AlC$_3$–180 catalyst, which was magnetically stirred for a duration of 180 h, has been determined through the analysis of X-ray photoelectron spectroscopy (XPS) and

Fourier-transform infrared spectroscopy (FTIR) data. The enlargement of the reaction area in Nb$_4$AlCl$_3$–180 due to the presence of surface functional groups leads to an increased number of active sites for the hydrogen evolution reaction (HER), thereby resulting in superior electrochemical performance.

The aforementioned studies have demonstrated that the etching process plays a significant role in influencing the activity of Mxenes. This process is crucial as it enhances the electrical behavior of Mxenes and increases the number of their active sites. The etching process involves the disruption of the chemical bond between the M and A element within the MAX phase, resulting in the subsequent removal of the A element. The M–X bond exhibits a hybrid character of covalent, metal, and ionic bonding, whereas the M–A bond is primarily characterized by metallic bonding [240]. When subjected to elevated temperatures, the breaking of both the M–A bond and M–X bond occurs, resulting in the formation of a three-dimensional structure resembling that of a rock [86]. Furthermore, during the etching process using chlorine, a highly corrosive substance, both the M and A elements are removed, resulting in the formation of carbide derivatives. Hence, it is imperative to

Table 1

Electro and photocatalytic reduction of CO_2 with the help of MXenes.

Sr no	Catalyst	Synthesis method	Process condition	Yield	Key findings	Ref.
1	TiO_2/Ti_3C_2	Calcination method	T = 350 °C, 450 °C, 550 °C and 650 °C Light source = UV-LED (3 W, 365 nm) Electrolyte = 0.5 M Na_2SO_4	$CH_4 = 0.22$ μ mol h^{-1}	In situ growth advancements have facilitated close contact and the development of a distinct rice crust-like structure, resulting in a significantly larger specific surface area.	[174]
2	2D/2D Ti_3C_2/Bi_2WO_6	Hydrothermal treatment method	pH = 7 Light source = Xe lamp	$CH_4 = 1.78$ μ mol g^{-1} h^{-1} $CH_3OH = 0.44$ μmol g^{-1} h^{-1}	Ti MXene's distinctive 2D/2D structure, effective electron attraction, and favorable surface properties are key factors enabling efficient electron transfer and successful CO_2 reduction.	[179]
3	Ti_3C_2 QDs/Cu_2O nanowires/Cu (NWs) heterostructure	Progressive electrostatic self-assembly strategy	Light source = 300 W Xe lamp T = 80 °C - 150 °C Ramping rate = 10 °C/min	$CH_3OH = 153.38$ ppm cm^{-2}	The production of CH_3OH over Ti_3C_2 QDs/Cu_2O NWs/Cu is 8.25 times higher than that over Cu_2O NWs/Cu, and 2.15 times higher than that over Ti_3C_2 sheets/Cu_2O NWs/Cu because it serve as a cocatalyst and offers active sites for the CO_2 reduction reaction.	[38]
4	$Ti_3C_2T_x$ and V_2CT_x	Exfoliation of MAX phases	Pressure = 0–4 MPa T = 298 K	44.2 mmol g^{-1}	The specific surface area (SSA) of as-prepared $Ti_3C_2T_x$ and V_2CT_x was 21 m^2 g^{-1} and 9 m^2 g^{-1}. which was increased to 66 m^2 g^{-1} and 19 m^2 g^{-1} after intercalation with dimethylsulfoxide.	[223]
5	Ti_3C_2 MXene (Cocatalyst) with titania P25	Hydrofluoric acid (HF) etching method Mechanical mixing method	Light source = 300 W Xe lamp.	$CO = 11.74$ μmol g^{-1} h^{-1} $CH_4 = 16.61$ μmol g^{-1} h^{-1}	Surface alkalinization of Ti_3C_2 dramatically enhances the activity and, especially, the selectivity for CH_4 evolution. Moreover, the surface −OH groups serve as active sites for CO_2 molecules.	[220]
6	$CsPbBr_3$/MXene-20	Etching Sonication In situ growth	Light source = 300 W Xe lamp with a cut off filter > 420 nm	$CO = 26.32$ μmol·g^{-1}·h^{-1} $CH_4 = 7.25$ μmol·g^{-1}·h^{-1}	Efficient fluorescence quenching of the $CsPbBr_3$ NCs, together with photoluminescence lifetime and photoconductivity measurements, confirmed efficient charge transfer between MXene and $CsPbBr_3$ NCs.	[245]
7	2D/2D Ti_3C_2/g-C_3N_4 heterojunction	One-pot strategy	Light source = visible light irradiation (λ ≥ 420 nm) pH = 6.7	$CO = 5.19$ μmol h^{-1} g^{-1} $CH_4 = 0.044$ μmol h^{-1} g^{-1}	Ti_3C_2 stimulates the transfer of photo-generated electron-hole pairs, retarding the recombination. 2D/2D Ti_3C_2/g-C_3N_4 heterojunction boosts the photoreactivity of g-C_3N_4 for CO_2 reduction.	[246]
8	3D hierarchical Co-Co layered double hydroxide/$Ti_3C_2T_X$	In-situ MOF-derived strategy	Light source = 5 W LED lamp	$CO = 1.25 \times 10^4$ μmol h^{-1} g^{-1} Quantum efficiency (0.92%)	MXene provide fundamental guidance to improve photocatalytic performance by rational engineering of complex hierarchical architecture materials.	[171]
9	ZnO-Fe-MXene	Hydrothermal method	0.5 M NaOH solution Sweep rate of 50–200 mVs^{-1}	-	The charge transfer resistance on ZnO-Fe-MXene is decreased when the electrode is utilized for the eCR reaction. This suggests that the surface of the electrode is not only reducing the CO_2 but also stops it from departing during structural reorganization	[136]
10	2D/2D/0D $TiO2/C3N4/Ti3C2$ MXene composite	Hydrothermal induced solvent-confined monomicelle self-assembly HF etching	-	$CO = 4.39$ μmol g^{-1} h^{-1} $CH_4 = 1.20$ μmol g^{-1} h^{-1}	The S-scheme heterojunction between TiO_2 and C_3N_4 made photogenerated carriers with strong redox abilities. This synergistic cooperation of the S-scheme heterojunction and TCQD highly enhanced the photocatalytic CO_2 reduction.	[247]
11	2D/2D $Bi_2O_2SiO_3/Ti_3C_2$ heterojunction	Hydrothermal method.	Solid-gas reactor Light source = solar irradiation	CO selectivity = 90% CH_3OH selectivity = 65.7% $CO = 17.8$ μmol g^{-1} h^{-1} $CH_3OH = 2.07$ μmol g^{-1} h^{-1}	The optimized sample BOSO/TC-2 are found to own remarkably enhanced activities with 3.8 times yield as compared to that of pristine $Bi_2O_2SiO_3$ because of the unique 2D/2D heterojunction, large interface contact area, and short charge transport distance.	[243]
12	$Cs_2AgBiBr_6$ / MXene	Mutual electrostatic attraction	-	50.6 μmol g^{-1} h^{-1}	The efficient charge separation and electron extraction, the $Cs_2AgBiBr_6$/MXene heterostructures achieve a high photoelectron consumption for photocatalytic CO_2 reduction, which surpasses most previously reported lead-free perovskite-based catalysts.	[248]
13	12 FLTC/BCN (few-layer Ti_3C_2 MXene (FLTC))	Thermal pyrolysis Etching Ultra sonification	pH = 7 Time = 5 h	CO selectivity = 69.7% CH_4 selectivity = 12.9% H_2 selectivity = 17.5%	12FLTC/BCN showed excellent stability during the cycling experiment and it produce 3.2- and 8.9-times higher CO and CH_4 yields, respectively, than bare g-C_3N_4 under visible light.	[249]
14	CeO_2/Ti_3C_2-MXene	Hydrothermal method	Light source = Xe lamp Drying temperature = 80 °C	CeO_2/MX-3% = 29.7 μmol m^{-2} h^{-1} CeO_2/MX-5% = 40.2 μmol m^{-2} h^{-1}	Upon exposure to solar light, this MXene hybrid exhibited enhanced performance in photocatalytic tetracycline degradation and CO_2 reduction, with activities 6.3 and 1.5 times	[250]

Table 1 (*continued*)

Sr no	Catalyst	Synthesis method	Process condition	Yield	Key findings	Ref.
				CeO_2/MX-7% = 27.3 μmol m^{-2} h^{-1}	greater than those of pristine CeO_2, respectively.	
15	Ti_2CT_x	HF, KF-HCL etching	Electrolyte = 0.1 M $KHCO_3$	Formic acid (Faradaic efficiency of 56%) H_2 is main product, alongside trace of CO, CH_4, and other hydrocarbons.	The critical role of the T_x group: a smaller overpotential is found to occur at lower amounts of –F termination.	[215]
16	Mo_2CT_x	HF etching	48% HF	Formic acid (partial current density of -2.5 mA cm^{-2}) H_2 is main product, alongside trace of CO, CH_4, and other hydrocarbons.	The nature of surface terminating group appears to control the CO_2RR activity.	[215]

carefully select the appropriate etching methods for the purpose of etching, and to employ a method that can effectively and selectively remove the A element.

3.6. Reaction mechanism of MXene in CO₂RR and improvements

The study conducted by Li et al. [241] involved the analysis of a heterojunction between mesoporous g-C₃N₄ and MXene (Ti₃C₂Tₓ) as a means of facilitating efficient photocatalytic reduction of CO₂. Mesoporous structures exhibit a significant number of absorption sites that can accommodate a large quantity of CO₂ molecules. According to the findings depicted in Fig. 20a, it can be observed that upon illumination, the mesoporous (MCT) material experiences a phenomenon where electrons transition from the valence band to the conduction band, resulting in an excited state. Subsequently, these excited electrons traverse through the MCT structure, moving from its interior to its exterior. Upon reaching the crystal plane, the electrons exhibit the capability to transition onto the surface of Ti₃C₂Tₓ (MXene), whereas the holes lack this ability. After the migration of electrons towards the surface, the MXene material undergoes a transformation into a highly effective capacitor. This process leads to a reduction in the electron concentration in the vicinity of Ti₃C₂Tₓ (MXene), thereby facilitating the rapid
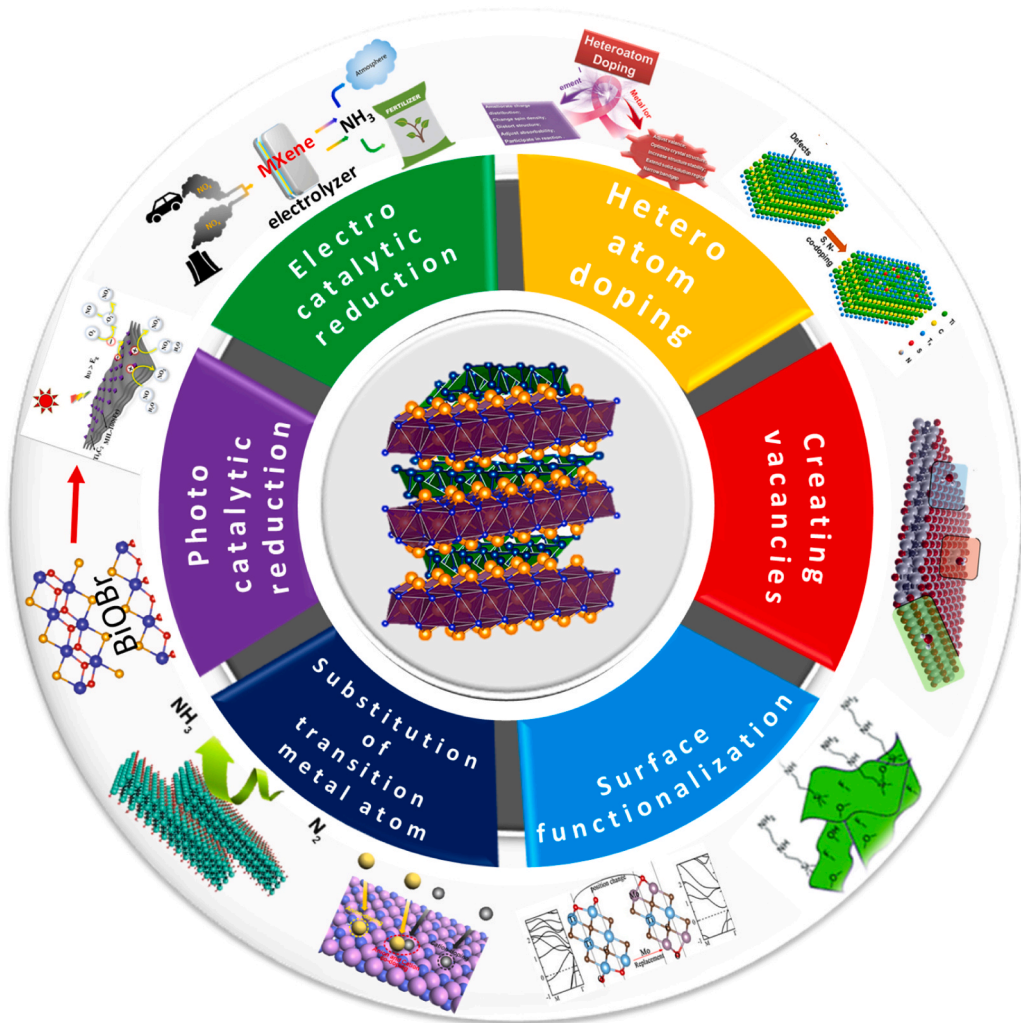

Fig. 21. NO$_x$ reduction over MXene and strategies for the increase of efficiency.

movement of free electrons within the crystal structure [206,242]. In addition, mesoporous architectures facilitate the localization of CO_2 molecules on the surface, whereas MXene serves as a proficient capacitor to facilitate the rapid transmission of electrons, thereby mitigating the recombination of electrons and holes. The aforementioned processes collectively contribute to the substantial enhancement of photocatalytic carbon dioxide reduction. Furthermore, Wang et al. [243] have successfully synthesized a novel type of photocatalysts, namely Bi_2O_2. SiO_3/Ti_3C_2 2D/2D heterojunction photocatalysts. As a result of the distinctive 2D/2D heterostructure characterized by atomic layers of varying thickness, the process of photogenerated electron transfer is facilitated. Specifically, these electrons are able to efficiently move from the surface of $Bi_2O_2SiO_3$ to the interface of the heterojunction, ultimately reaching the surface of the Ti_3C_2 atomic layer. The efficiency of photocatalytic CO_2RR can be significantly enhanced by utilizing optimized two-dimensional/two-dimensional heterojunctions. The development of nonprecious catalysts for the reduction of CO_2 that exhibit high efficiency, selectivity, and low overpotential is a crucial aspect in the advancement of renewable energy. Wang et al. [244] have successfully synthesized a Z-Scheme Core-Shell meso-TiO_2 @$ZnIn_2S_4/Ti_3C_2$ MXene composite that exhibits improved selectivity for visible light-driven CO_2-to-CH_4 conversion. The efficacy of the synthesis is contingent upon a biphasic approach encompassing hydrothermal and electrostatic self-assembly methodologies. The ternary heterojunction demonstrates favorable characteristics in the context of photocatalytic

carbon dioxide reduction. In general, a preliminary mechanism for the photocatalytic reduction of CO_2 in the T-ZIS-M ternary photocatalyst is suggested. According to the data presented in Fig. 20b, it can be observed that the conduction bands of ZIS and meso-TiO_2 exhibit negative values in comparison to the CO_2 reduction potential. Specifically, the CO_2/CO reduction potential is theoretically determined to be -0.117 V vs NHE, while the CO_2/CH_4 reduction potential is theoretically determined to be 0.173 V vs NHE at a pH of 0 [222]. In this context, the utilization of a Z-scheme reaction pathway may be potentially viable. Under ultraviolet-visible light, both TiO_2 and ZIS exhibit the emergence of excited electron-hole pairs. The electrons with lower energy levels originating from the conduction band of titanium dioxide (TiO_2) have the ability to undergo a transfer process to the valence band of ZIS. Due to the advantageous electrical conductivity exhibited by MXene, the photogenerated electrons are able to efficiently migrate towards MXene, which possesses a large number of active sites. This characteristic ensures the successful construction of the photocatalytic system. Table 1 presents a comprehensive overview of diverse composites and materials derived from MXene for the purpose of electrochemical and photocatalytic reduction of carbon dioxide (CO_2) into multiple products, including hydrogen (H_2), carbon monoxide (CO), and methane (CH_4).
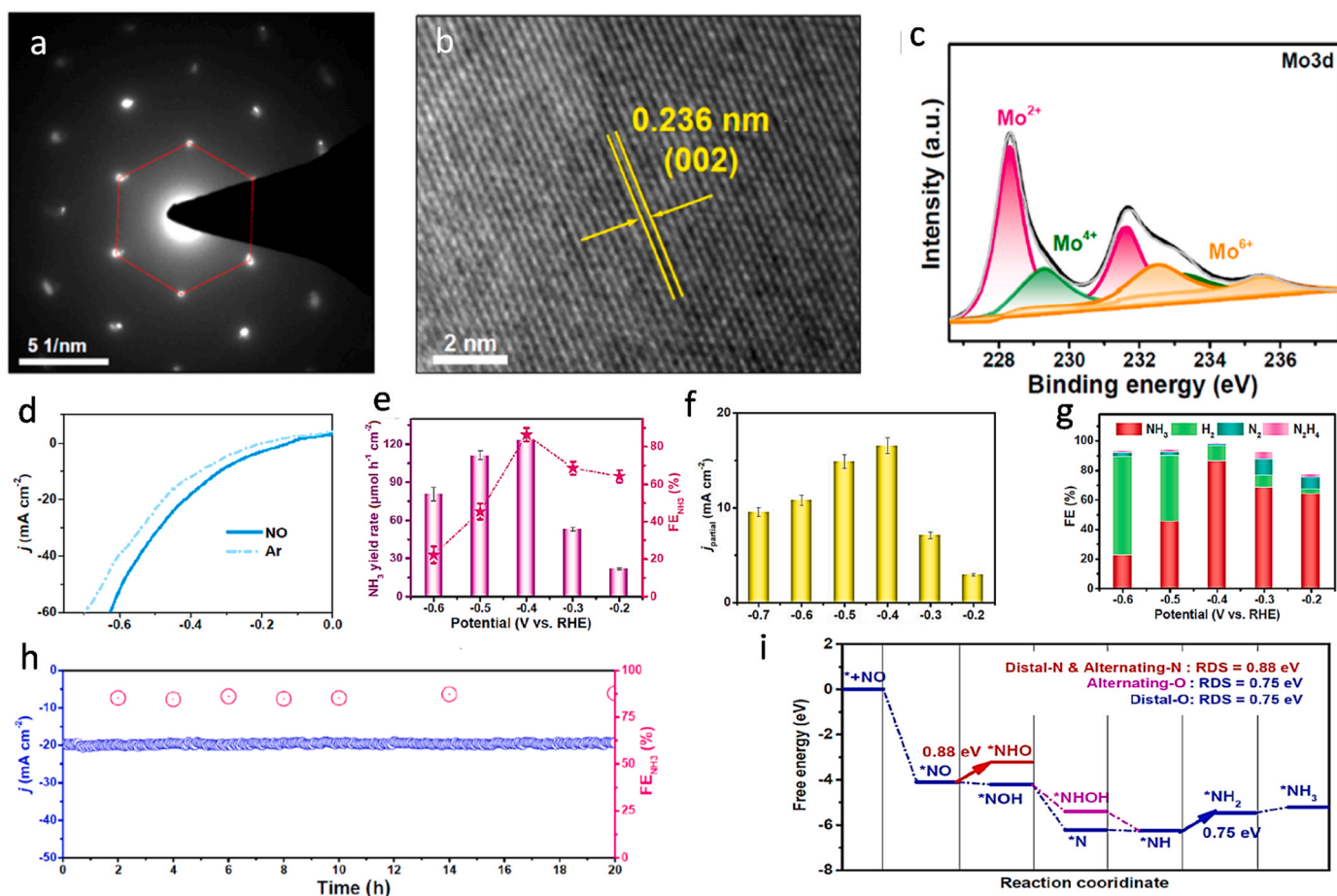

Fig. 22. showcases the characterization and performance evaluation of Mo_2C nanosheets. Here is a breakdown of the different panels in the figure:(a) Selected area electron diffraction (SAED) pattern.(b) High-resolution TEM (HRTEM) image.(c) X-ray photoelectron spectroscopy (XPS) spectra Mo 3d.(d) Linear sweep voltammetry (LSV) curves of Mo_2C under different conditions.(e) NORR performance of Mo_2C at various potentials.(f) NH_3 partial current densities of Mo_2C at various potentials.(g) Faradaic efficiencies (FEs).(h) Long-term stability measurements over Mo_2C.(i) Free energy diagram illustrating the NORR reaction pathway on Mo_2C. These characterizations and performance evaluations provide valuable insights into the structural properties, electrochemical behavior, catalytic activity, selectivity, and stability of Mo_2C nanosheets [262].
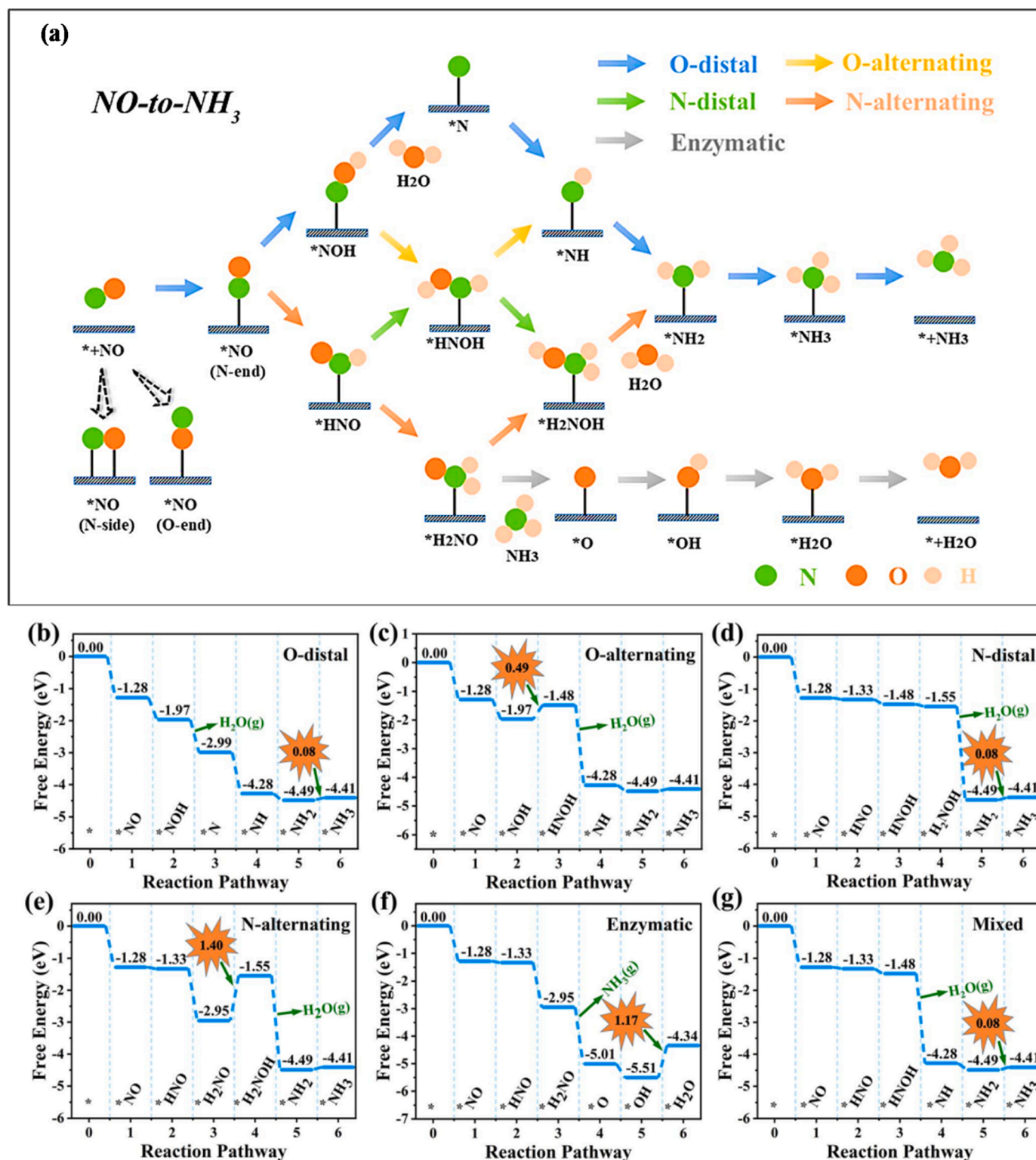
Fig. 23. Schematic illustration of possible mechanisms of NORR catalysis of NH_3. (b–g) The present study investigates the free energy diagram of electrochemical NORR in Ti_2CS_2 MXenes using different reaction methods [266].

4. Recent advancements in MXenes for electro- and photocatalytic NO_x reduction

The increased use of fossil fuels to meet daily energy needs has increased atmospheric pollution [251,252]. Our health and ecosystems suffer constantly, acutely, from NO_x emissions. The use of MXenes is a promising approach in the electrophotocatalytic reduction of NOx

pollutants, which is an important research field in sustainable aspects affecting air pollution processes to facilitate the expression. The strong surface reactivity, hydrophilicity, adsorption capacity, and large surface area of MXenes, which have the potential to act as potential multifunctional materials, have attracted interest for a variety of applications, including catalysts, ion batteries, gas storage media, and sensors [170, 253]. Traditional methods for removing NO_x emissions often struggle to

achieve energy efficiency and cost-effectiveness. However, the emerging electrophotocatalytic reduction offers promising new techniques using the principles of electrochemistry as well as photochemistry and implementing several strategies for the enhancement of NO_x reduction, as depicted in Fig. 21. This paper focuses on the potential of MXenes in electrophotocatalytic reduction to reduce NO_x pollution. By analyzing the underlying mechanisms and their relevance, this study sheds light on how MXene types can contribute to the fight against air pollution. The study also highlights the effectiveness of MXenes and the promise of effective and efficient reduction of NO_x by providing insights into alternative methods for combating air pollution.

4.1. Electrochemical reduction of NO_x to NH_3

Electrocatalytic reduction of the NO (NORR) process, which has attracted increasing attention, offers a potential solution to NH_3 synthesis and NO removal challenges, but the inherent linear scaling relationship severely limits the catalytic efficiency of this process lies between the adsorption energies of NORR [254]. The publication emphasizes the important role of ammonia in the development of socio-economic development. Ammonia is an essential ingredient in various industries and applications, including agriculture, construction, and energy production. What matters is its versatility as a nutrient, chemical, and energy carrier [255]. However, the current industrial process for ammonia production, known as the Haber-Bosch process, is associated with significant greenhouse gas emissions and high energy consumption [256]. Electrochemical nitrogen fixation has emerged as a

viable and environmentally friendly alternative method for synthesizing ammonia (NH_3) under mild operating conditions, [257–259]. However, the electrochemical nitrogen fixation method faces challenges such as low Faraday efficiency (FE_{NH_3}) and ammonia yield rates, primarily caused by the limited solubility of nitrogen gas (N_2) in aqueous electrolytes, the strong inertness of the nitrogen-nitrogen (N≡N) bond, and the highly competitive hydrogen evolution reaction (HER) [260]. On the other hand, environmental problems caused by excessive combustion of fossil fuels, resulting in nitrogen oxides (NO_x) emissions, have become an important global issue with implications on human health in question, in this case, electrocatalytic conversion of nitric oxide (NO) to ammonia (NH_3), which produces NO. Known as to-NH_3 replacement (NORR), NO offers a promising solution for pollution reduction. This process is highly efficient for electrochemical ammonia synthesis due to the high solubility of NO compared to nitrogen gas (N_2) and the low energy associated with bonding [261]. The NORR method, despite its appeal, faces challenges in terms of efficiency, mainly due to the slowness of five-electron transport and competing lateral reactions (hydrogen evolution reaction; HER). It happened to be so. The AHDO (ammonia-selective hydroxylamine degradation) pathway appears to be the most important pathway for NORR to produce ammonia (NH_3), as described below [262]:

$$NO \text{ (g)} + (H^+ + e^-) \rightarrow NOH^* \tag{6}$$

$$NOH^* + (H^+ + e^-) \rightarrow N^* + H_2O \tag{7}$$

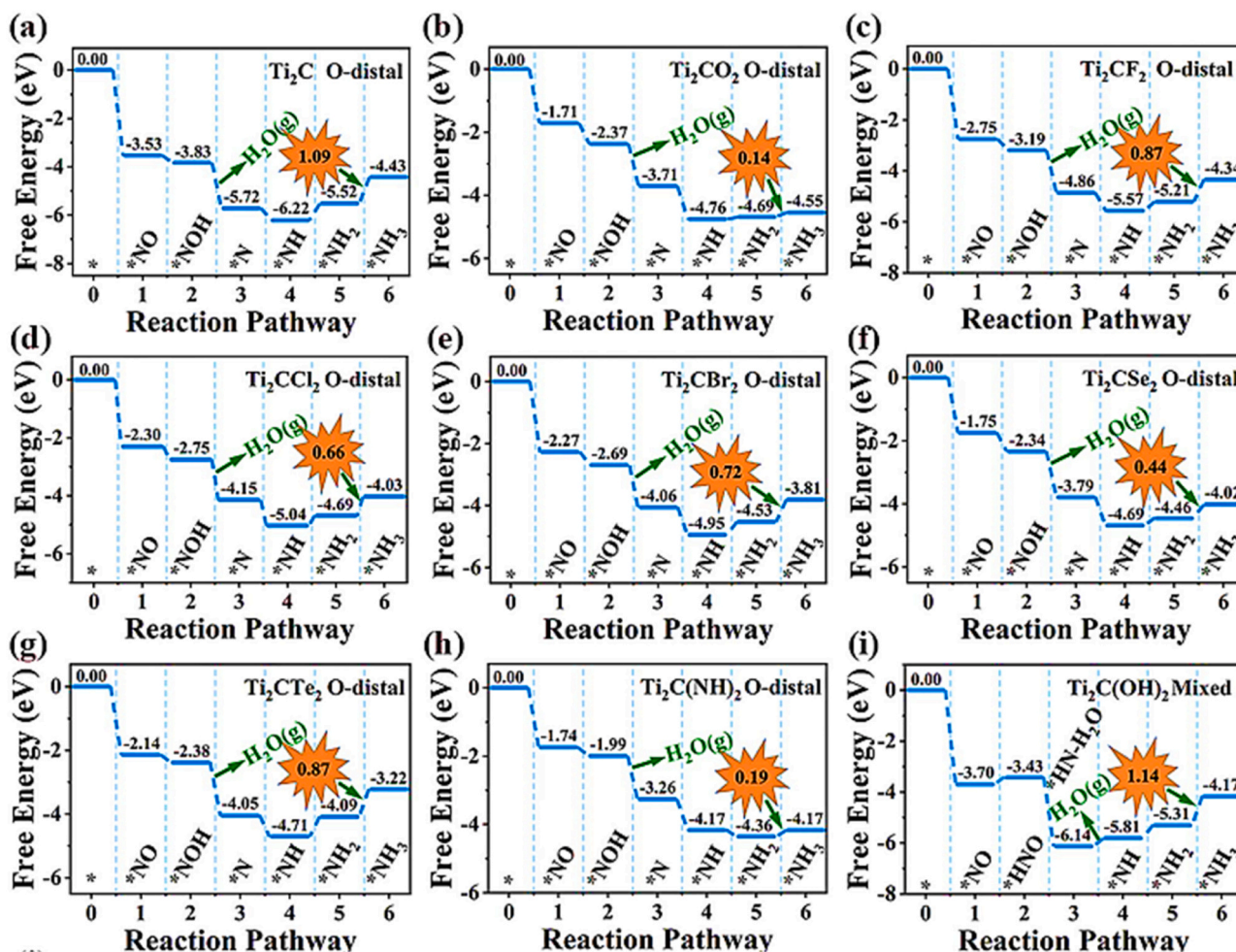$$N^* + (H^+ + e^-) \rightarrow NH^* \tag{8}$$

Fig. 24. Figures showing the free energy change for the NORR catalyzed on (a) bare Ti_2C, (b) Ti_2CO_2, (c) Ti_2CF_2, (d) Ti_2CCl_2, (e) Ti_2CCl_2, (f) Ti_2CSe_2, (g) Ti_2CTe_2, (h) Ti_2C $(NH)_2$, and (i) $Ti_2C(OH)$ via the most advantageous pathway [266].
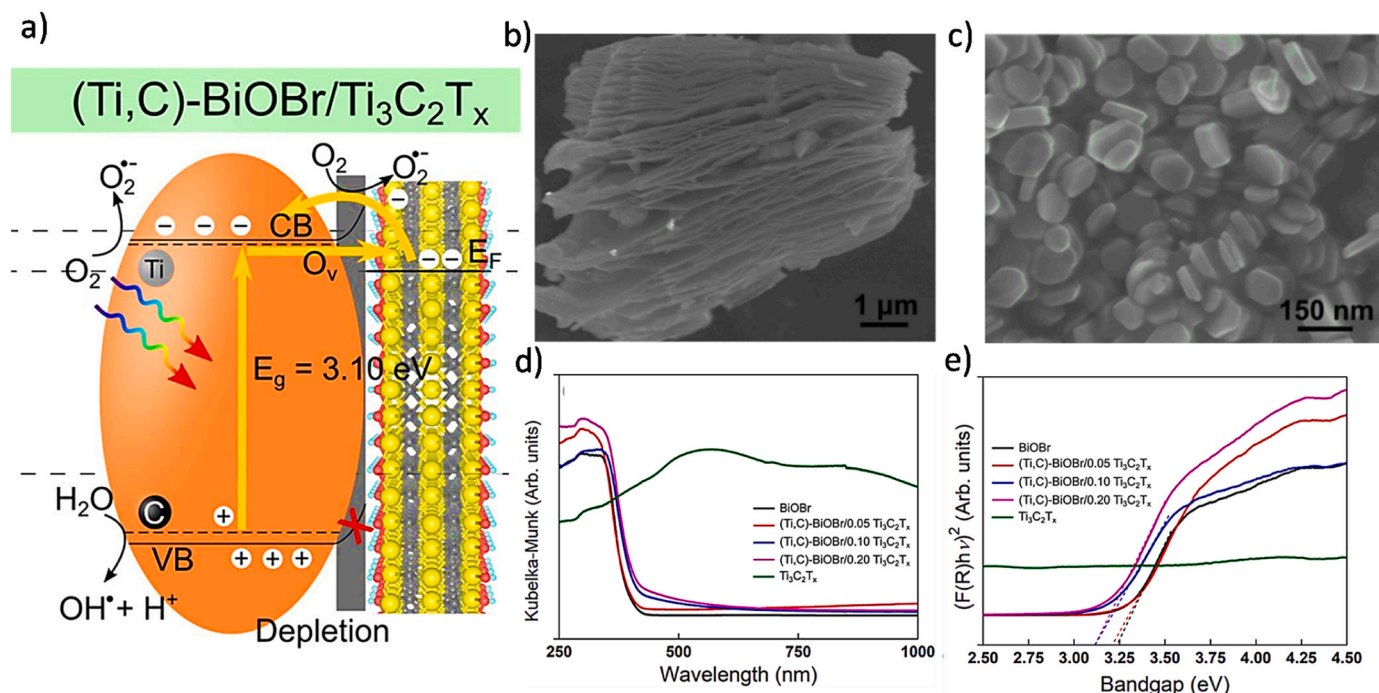
Fig. 25. a) Photocatalytic NO$_x$ degradation mechanism of (Ti,C)-BiOBr/ Ti$_3$C$_2$T$_x$. SEM images of (b) Ti$_3$C$_2$T$_x$ MXene (c) BiOBr, (d) Kubelka-Munk absorption spectra and, (e) corresponding Tauc's plot of BiOBr, Ti$_3$C$_2$T$_x$ MXene, and (Ti,C)-BiO,Br/ Ti$_3$C$_2$T$_x$ nanocomposites [270].

$$NH^* + (H^+ + e^-) \rightarrow NH_2^* \qquad (9)$$

$$NH_2^* + (H^+ + e^-) \rightarrow NH_3 (g) \qquad (10)$$

In a study conducted by Chen et al. [263], In a report, it was found that molybdenum carbide (Mo$_2$C) demonstrates remarkable activity and selectivity as a catalyst for NORR. To prepare the Mo$_2$C catalyst, researchers utilized a liquid-phase exfoliation technique to create MoO$_3$ nanosheets. These nanosheets were then subjected to thermal annealing in an environment conducive to carbonization, forming Mo$_2$C nanosheet [264]. The SAED structure (Fig. 22a) reveals the Mo$_2$C crystal structure as square. HRTEM image (Fig. 22b) shows a lattice spacing of 0.236 nm, corresponding to the Mo$_2$C (002) phase. By analyzing the XPS Mo 3d spectra (Fig. 22c) of Mo$_2$C, different oxidation states can be identified: Mo^{2+} (228.3/231.6 eV), Mo^{4+} (229.2/233.2 eV), Mo^{6+} (232.6/235.5 eV) and Mo^{2+} With existence of Mo species in Mo$_2$C, whereas Mo^{4+}/ Mo^{6+} species are due to surface oxidation, which is consistent with previous reports on the Mo$_2$C Electrochemical NORR activity of Mo$_2$C followed the methodology of previous studies a followed by the use of gas-tight H-. Cell lines are analyzed to test the NORR activity of Mo$_2$C, and the researchers performed LSV analysis, as shown in Fig. 22d. The results showed that Mo$_2$C exhibited a significantly higher NH$_3$ yield of 122.7 μmol h^{-1} cm^{-2} with 86.3% FENH$_3$ at − 0.4 V (partial current density of 16.6 mA cm^{-2}, Fig. 22 f). These values were approximately higher than most other reported NORR catalysts, as shown in Fig. 22e. Furthermore, Mo$_2$C exhibited high selectivity for NO-to-NH$_3$ conversion, as low FEs indicate (Fig. 22 g). The durability of Mo$_2$C was also good, as evidenced by the relatively low damage in FENH$_3$ and the current density during continuous 20 h electrolysis (Fig. 22 h).

Further analysis (Fig. 22i) revealed that the distal-N and altering-N pathways were not energetically feasible due to the high initial energy barrier for *NHO formation (0.88 eV). Moreover, the hydrogenation of *NOH to form *N was found to be more favorable than its conversion to *NHOH. This suggests that Mo$_2$C predominantly follows the distal O pathway (*NO → *NOH → *N → *NH → *NH$_2$ → *NH$_3$) to facilitate the NORR process. The rate-determining step (RDS) in the distal-N pathway

was identified as *NH → *NH$_2$, with an energy barrier of 0.75 eV. This barrier was found to be lower than that of most previously reported catalysts, indicating favorable reaction energetics of Mo$_2$C for the NORR [265]. Overall, these findings demonstrate that the surface-terminated Mo atoms in Mo$_2$C play a crucial role in activating NO, enhancing protonation energetics, and suppressing proton adsorption. This contributes to the high activity, selectivity, and stability of Mo$_2$C as a catalyst for the NORR.

In another study, Zhao et al. [266] proposed a design principle to enhance the catalytic activity of MXenes for the nitrogen oxide reduction reaction (NORR). Their goal was to break the linear scaling relations of key intermediates in the NORR, which would improve the thermodynamics of the reaction. The catalytic activity of MXenes was evaluated using the limiting potential (UL), where UL represents the maximum Gibbs free energy change along the entire reaction pathway. Fig. 23a identifies possible reactive pathways for NORR, including O-terminal, O-substituted, N-terminal, N-substituted, enzymatic pathways, and mixed pathways. These pathways depend on nitrogen oxide (NO) and hydration series in the adsorption process. To determine the most energetic method and its corresponding UL, the researchers optimized all possible NORR-mediated adsorption processes using Ti$_2$CS$_2$ MXene as a model (Fig. 23b-g).

In the first hydrogenation step, *NO can react with O or N atoms, resulting in *NOH or *NHO, respectively. Subsequently, forming *HNOH from *NOH in the second hydrogenation step requires an increased free energy of 0.49 eV. In contrast, the phase coupled with *NOH + H$^+$ + e$^-$ = *N + H$_2$O(g) is exothermic, with an energy decrease of 1.02 eV. Consequently, the O-remote approach is preferable to the O-alternative approach. Moving on to the third and fourth hydrogenation steps, successive *N and H$^+$/e$^-$ pairs react to form *NH and *NH$_2$, with spontaneous energy decreases of − 1.29 and − 0.21 eV, respectively including, respectively. Finally, the final step of hydrogenation from *NH$_2$ to *NH$_3$ are exothermic, with a small negligible energy barrier of 0.08 eV. This is a potential identification step (PDS) for the entire NORR system.

Furthermore, functional Ti$_2$CT$_2$ MXenes, with the exception of Ti$_2$C (OH)$_2$ MXenes, exhibit a preferred NORR mode known as O-distal,
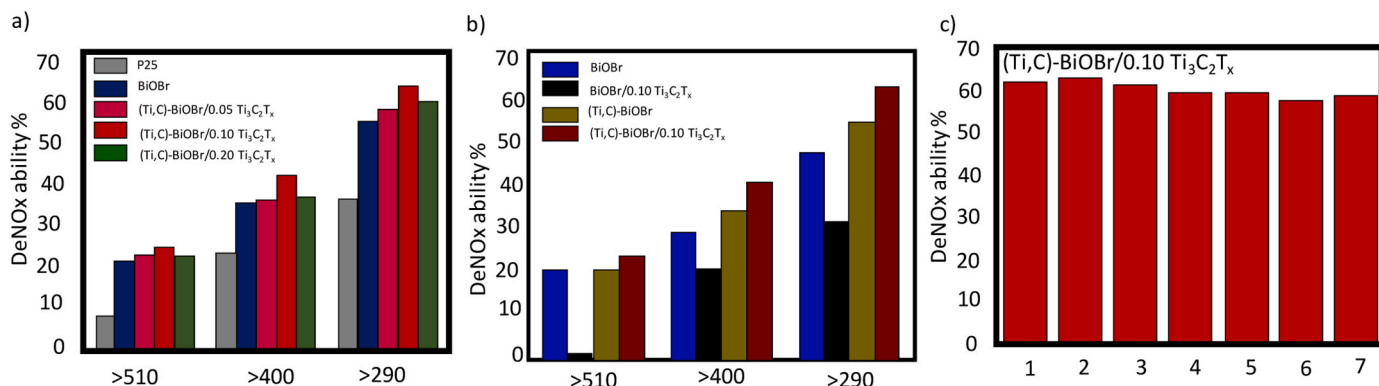
Fig. 26. (a-b) The photocatalytic NO$_x$ conversion efficiency of samples prepared with P25, pristine BiOBr, and nanocomposites under different wavelengths of illumination was evaluated, c) shows the conversion stability of (Ti,C)-BiOBr/0.10 Ti$_3$C$_2$Tx nanocomposite especially at > 290 nm photoirradiation breed [270].

characterized by the sequence *NO → *NOH → *N → *NH → *NH$_2$ → * in the. NH$_3$ Interestingly, Ti$_2$C(OH)$_2$ MXenes show the distinct reaction path *NO → *NHO → *NH–H$_2$O → *NH → *NH$_2$ → *NH$_3$, which has been identified as the preferred mode with a limiting potential of − 1.14 V. Fig. 24a-i summarizes the effect of surface activity on the NORR catalytic activity of Ti$_2$CT$_2$ MXenes. The limiting potentials of most active Ti$_2$CT$_2$ MXenes range from − 0.87 to − 0.08 V, except for Ti$_2$C(OH)$_2$ MXenes (−1.14 V). For comparison, bare Ti$_2$C MXenes exhibit a limiting potential of − 1.09 V for NORR. This suggests that modification of the surface activity of the MXenes is an effective strategy for NORR to enhance their catalytic activity, especially for NH$_3$ synthesis. Different surface functionalities of MXene significantly influence NORR performance, highlighting the importance of a customized process for effective catalytic activity.

4.2. Photocatalytic reduction of NO$_x$

In addition to their application as electrocatalysts, MXenes are widely used as photocatalysts for the photocatalytic reduction of NO$_x$. Many photocatalytic materials have been developed since Fujishima and Honda discovered the water-splitting ability of TiO$_2$ under photoirradiation [267]. More attention is paid to established ion-hybridized semiconductor materials, one containing two or more ions in the crystal. One such class of materials is the series of bismuth oxyhalides (BiOX, where X represents Cl, Br, or I), which have been extensively studied as photocatalysts because of their nontoxicity, wide photoabsorption range and due to their high stability [268,269]. Hermawan et al., [270] proposed a bismuth oxybromide (BiOBr) photocatalyst incorporated efficiently with 2D Ti$_3$C$_2$T$_x$ MXene by solvothermal treatment of (Ti, C)-BiOBr/ Ti$_3$C$_2$Tx MXene used for NOx. The photocatalytic removal of the gas was monitored in a laboratory-built flow generator. The photocatalytic mechanism is shown in Fig. 25a. The microstructure analysis using SEM and TEM is shown in Fig. 25b. The SEM image (Fig. 25c) clearly indicates the platelet-like morphology of uniformly sized BiOBr. The addition of Ti$_3$C$_2$T$_x$ MXene to BiOBr slightly increased the visible fluorescence, and as the concentration of Ti$_3$C$_2$T$_x$ MXene increased, the visible fluorescence also increased. Fig. 2d shows the absorbance of pristine BiOBr, Ti$_3$C$_2$T$_x$ MXene, and (Ti, C)-BiOBr/0.10 Ti$_3$C$_2$T$_x$ nanocomposites. Band gaps were calculated.

The efficiency of the prepared samples to break down NO$_x$ by photocatalysis was evaluated. Fig. 26a shows the results of the photocatalytic deNO$_x$ activities from BiOBr, (Ti,C)-BiOBr/0.10 Ti$_3$C$_2$Tx nanocomposites and the P25 photocatalyst used as a benchmark. Different filters (> 510 nm, > 400 nm, and > 290 nm) were used to test the photocatalytic ability of the samples in the visible UV regions. Surprisingly, (Ti,C)-BiOBr/0.10 Ti$_3$C$_2$T$_x$ nanocomposites achieved more than 40% conversion, with pristine BiOBr and P25 titania photocatalysts above both. In addition, more than 60% of the NO$_x$ emissions were

converted in the ultraviolet region (>290 nm). These data indicate that the nanocomposites of Ti,C-doped BiOBr and Ti$_3$C$_2$Tx MXene are efficient photocatalysts. To confirm this hypothesis, the photocatalytic activity of physically hybrid BiOBr/ Ti$_3$C$_2$T$_x$ nanocomposite and (Ti,C)-doped BiOBr was tested (Fig. 26b). Although (Ti,C)-BiOBr showed a slight improvement compared with BiOBr, its activity (Ti,C)- was lower than that of the BiOBr/0.10 Ti$_3$C$_2$T$_x$ nanocomposite. Thus, it is important to incorporate Ti$_3$C$_2$Tx MXene into BiOBr nanostructures by solvothermal method, as the combination of the two materials alone or relying on the co-doping method alone is not sufficient to enhance the photocatalytic performance of the catalytic materials after, in Fig. 26c presents the results of cyclic photocatalytic studies of (Ti,C)-BiOBr-HT/ 0.10 Ti$_3$C$_2$T$_x$ nanocomposites. It is clear that even after several reaction cycles, NOx conversion capacity decreases only marginally. This finding indicates that nanocomposites have the potential to act as highly stable and stable photocatalysts for long-term applications.

The findings suggest that the deNO$_x$ activity was not significantly influenced by the specific surface areas. According to these findings, it is optimal for the photogenerated electrons to avoid reacting with O$_2$, ads due to the relatively positive CB potential compared to the O$_2$/O$_2$ adspotential. It would prevent the degradation of NO$_x$. However, it should be noted that the valence band potential of BiOBr is situated at a lower level than that of H$_2$O/HO·potential. Consequently, the photocatalytic efficacy of BiOBr is solely attributed to the oxidation process of H$_2$O, resulting in the formation of HO• radicals. These radicals subsequently degrade NO$_x$, leading to the production of HNO$_2$. Hierarchical macroporous or mesoporous designs are better able to absorb visible light irradiation due to the realisation of multiple reflections and scattering effects since the surface morphology and structure of the photocatalyst have a significant impact on the photocatalytic activity. The reduction of recombination rates and subsequent increase in photocatalytic activity can be attributed to two factors: the shortening of the diffusion length of photogenerated electron/hole pairs and the creation of interfacial fields. Furthermore, sufficiently high-energy photogenerated species is imperative for facilitating the migration of photocatalysts to the surface, where redox reactions can occur with adsorbed reactants. This is contingent upon the reduction and oxidation potentials being more positive and negative, respectively than the conduction band and valence band levels [271].

In a similar study, Wang et al. [272] developed a novel heterojunction catalyst by incorporating Ti$_3$C$_2$ MXene quantum dots (QDs) into SiC. The resulting Ti$_3$C$_2$ MXene QDs/SiC composite exhibited a remarkable 74.6% efficiency in removing NO pollutants under visible light irradiation, which was 3.1 and 3.7 times higher than the bare Ti$_3$C$_2$ MXene QDs and SiC, respectively. Ti$_3$C$_2$ MXene QDs in SiC facilitated efficient electron and hole transfer. The enhanced visible light absorption, increased production of superoxide radicals, and strong oxidation capability contributed to the superior photocatalytic performance of the
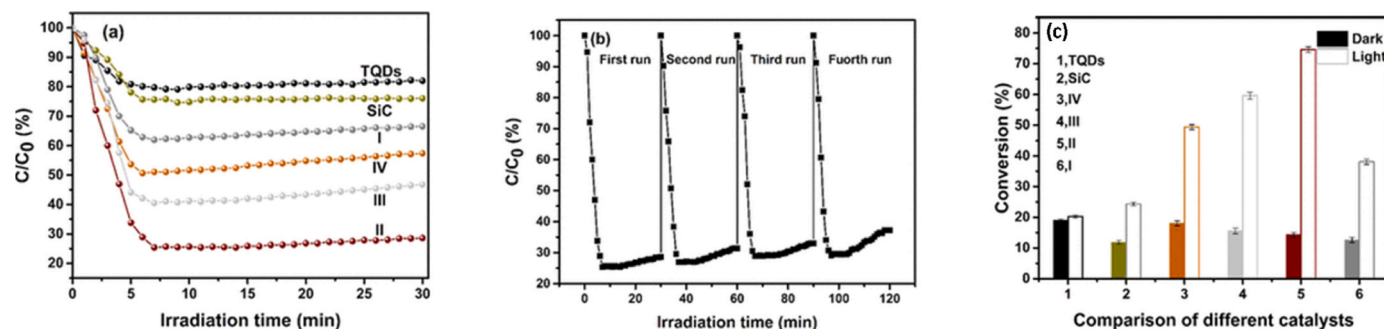
Fig. 27. (a) Visible photocatalytic removal of NO of all samples and (b) cycling test of II. (c) Removal efficiency of NO for different catalysts in the dark or under irradiation [273].

Table 2
Different interfaces of MXenes for the electro and photocatalytic reduction of NO_x.

Sr no.	Catalyst	Synthesis method	Process condition	Key findings	Ref.
1	g-C_3N_4/ TiO_2/Ti_3C_2	two-step synthetic route	300 W xenon lamp, gas flow rate = 3 L min^{-1}	Under visible light, NO removal efficiency of the composite photocatalyst can reach up to 66.3%, which is significantly better than the g-C_3N_4 or TiO_2-Ti_3C_2.	[274]
2	Ti_3C_2 MXene QDs/SiC	self-assembly process	300 W Xenon lamp ($\lambda > 420$ nm), light intensity was 72.16 mW/cm^2	The Ti_3C_2 MXene QDs/SiC composite showed 74.6% efficiency in NO pollutant removal under visible light irradiation	[272]
3	Ti_3C_2/g-C_3N_4	one-step in-situ thermopolymerizaiton method	KL 2500 LCD lamp (SCHOTT), gas flow rate = 100 mL/min	The NO oxidation removal ratio of the optimized catalyst (TC-CN 4) could reach a maximum of 57%, which was 1.6 times higher than pristine g-C_3N_4	[275]
4	(Ti,C)-BiOBr/ $Ti_3C_2T_x$	solvothermal method	450 W mercury lamp, gas flow rate = 200 mL/min	Ti,C-doped BiOBr and $Ti_3C_2T_x$ MXene are exceptional candidates as efficient photocatalysts with 60% NO_x gas conversion	[270]
5	Ti_2CS_2	MAX phase synthesis	Limiting voltage = −0.08 V	Ti_2CS_2 MXene possess superior selectivity towards NH_3 by inhibiting the competing production of H_2	[266]
6	Ti_3C_2 @TiO_2/g-C_3N_4	In-situ hydrothermal process	300 W Xenon lamp with a 400 nm cut off filter	The 20 TCTO-CN composites exhibited an NO removal rate of 28.9%	[276]
7	Nb_2O_5/Nb_2C MXene	hydrothermal reaction followed by heat treatment	300 W xenon lamp with a 400 nm cut off filter, the gas flow rate = 1.2 L min^{-1}	Nb_2O_5/Nb_2C possesses high NO removal rate of around 80% at relative humidity of 25%, 50% and 75%	[277]
8	Ti_2CO_2	MAX phase synthesis	Limiting voltage = −0.14 V	Modifying surface functionalization of MXenes can efficiently modulate the surface electric properties of MXenes to break the linear scaling relations between the adsorption energies of *NH_2 and *NH_3	[266]

Ti_3C_2 MXene QDs/SiC composite for NO_x removal. Fig. 27a demonstrates the significant removal efficiency of all the samples, reaching maximum values within the first 6 min. Subsequently, the removal rate decreased as the reaction intermediates and products accumulated and occupied the active sites [273]. Eventually, a removal equilibrium was reached. It can be concluded that Ti_3C_2 QDs/SiC exhibited more effective photocatalytic activity compared to SiC (24.3%) and Ti_3C_2 QDs (20.3%). Among the samples, TQDs/SiC-20 demonstrated the highest activity (74.6%), surpassing SiC and Ti_3C_2 QDs by factors of 3.1 and 3.7, respectively. Furthermore, the photostability of TQDs/SiC-20 was evaluated over 120 min with four evacuations after every 30 min of irradiation, as shown in Fig. 27b. After four cycles, TQDs/SiC-20 exhibited a slight decrease in NO removal ratio, indicating its relative stability.

In Fig. 27c, NO removal was studied under dark conditions and visible light. It was observed that under visible light, all samples exhibited higher NO reduction compared to dark conditions. The NO removal efficiency of Ti_3C_2 QDs in the dark is higher than that of SiC. This can be attributed to the large surface area (SBET) and total pore volume (Vtotal) of Ti_3C_2 QDs, which allows them to adsorb more NO molecules. Table 2 shows different interfaces of MXenes for the electro and photocatalytic reduction of NO_x.

4.3. Strategies to improve the activity of MXene for effective NO_x removal and its conversion

The utilization of MXene-based catalysts for effectively removing and converting nitrogen oxides (NO_x) has become increasingly important in recent times. However, achieving enhanced activity for efficient NO_x removal and conversion requires implementing various strategies. These strategies involve modifying the composition of MXenes through doping and alloying, enhancing their adsorption and reactivity through surface functionalization, creating additional active sites through defect engineering, and harnessing synergistic effects through coupling with other catalytic materials. By employing these strategies, MXenes can be customized and optimized to exhibit improved activity in removing and converting NO_x, ultimately contributing to cleaner air and reduced environmental pollution.

4.3.1. Surface functionalization and hetero-atoms doping

A powerful approach to improve the efficiency of NO conversion in photocatalysts is surface modification [278–280]. The presence of a wide variety of surface functional groups, such as oxygen (-O), fluorine (-F), hydroxyl (-OH) and chloride (-Cl) on the surface provides high efficiency and versatility [281]. Recently, surface modification of covalently and non-covalently conjugated local MA-M MXenes has led to the synthesis of functional M_x. Noncovalent surface modification is induced by a combination of van der Waals forces, hydrogen bonding and

Table 3
Modified MXenes and background processes.

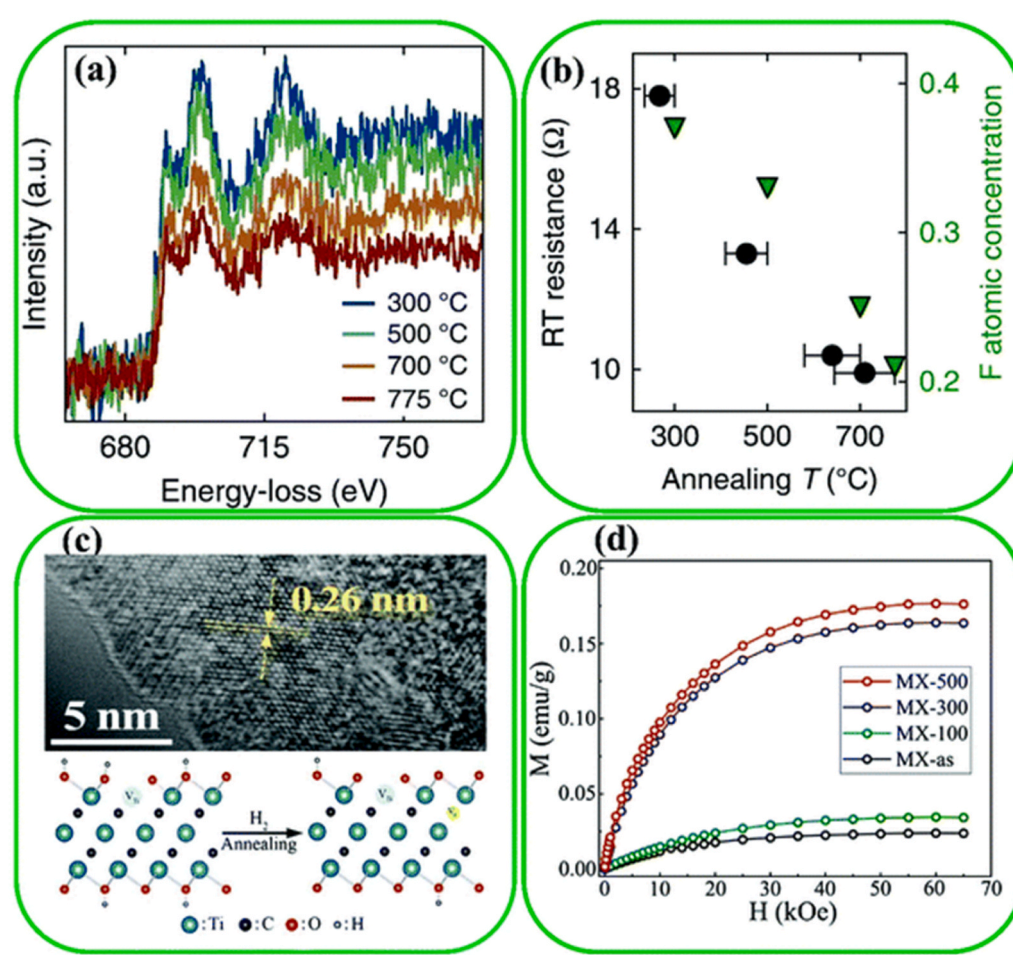| Surface functionalized 2D MXenes	Catalyst	Synthesis method	Solvent or atmosphere reaction	Temperature (°C)	Ref.
Functionalized MXenes by small molecules	$NaAlH_4$-modified Ti_3C_2	Ball milling	Ar	—	[290]
	FePc-modified Ti_3C_2	Self-assembly	Dimethylformamide (DMF)	—	[291]
	$C_{12}E_6$-modified Ti_3C_2	Sonication	Water	40	[292]
	Et-modified Nb_2C	Hydrothermal approach	Ethanol	100	[293]
Functionalized MXenes by macromolecules	Sodium alginate modified Ti_3C_2	Vacuum-assisted filtration	Deionized water	Room temperature	[294]
	PPy modified Ti_3C_2	In situ polymerization	Deionized water	Room temperature	[295]
	PS modified Ti_3C_2	Electrostatic assembly	Deionized water	50	[296]
	PVA modified Ti_3C_2	Vacuum-assisted filtration	Deionized water	Room temperature	[297]
	PDDA modified Ti_3C_2	Vacuum-assisted filtration	Deionized water	Room temperature	[297]
Functionalized MXenes by single heteroatoms	V-Doped Ti_3C_2	Hydrothermal approach	Water	120	[298]
	S-Doped Ti_3C_2	Solution blending	Deionized water	155	[299]
	S-Doped Ti_3C_2	Heat and milling treatment	Ar	1650	[300]
	N-Doped V_4C_3	Heat treatment	Ammonia	350–550	[301]
	N-Doped Nb_2C	Hydrothermal approach	Deionized water	150	[302]
	P-Doped V_2C	Heat treatment	Ar	300–500	[303]

Fig. 28. Effect of surface terminations on MXene conductivity; (a) Loss of -F during annealing measured by Ti_3C_2 in situ electron energy loss spectroscopy, and (b) -F concentration (green square) and comparison of -F concentration (green square) with Ti_3C_2 room temperature resistance after annealing (circled black) [232]. (c) Schematic of high-resolution transmission electron microscopy representing structural changes after annealing in H_2, and (d) comparison of magnetic properties as a function of applied field H recorded at 2 K [289].

electrostatic attraction [282]. The -OH and -O rich groups on the surface of MXenes can be used as active sites for covalent binding by controlled surface termination Surfactant initiators, small molecules and polymers [261,283]. Due to MXene's hydrophilicity [284,285] MXene performance can easily be enhanced with the right functional groups. The chemical mechanism of the MXene surface has been extensively studied. Table 3 shows the modified MXene types and the surface treatment

methods used to prepare them. In addition, the surface function influences the structural and dynamic stability of the MXene materials [286]. Surface modification of MXenes under the control of the T group enables the optimization of physical properties of MXenes, such as the number and properties of electrochemically active sites and electronic structures [287]. In his recent DFT calculations, he also points out the possibility of tuning the structural and electronic properties of MXene
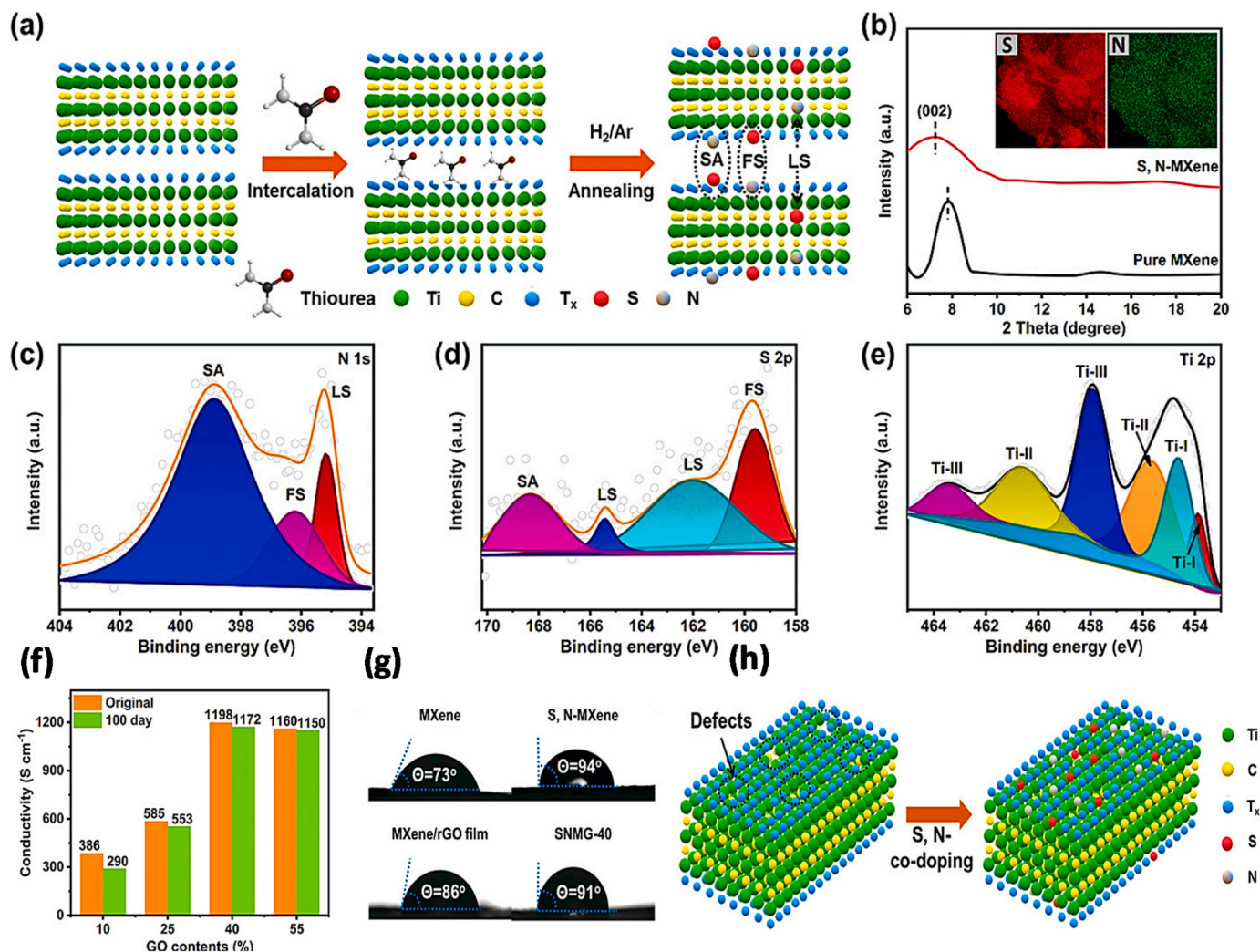
Fig. 29. a) A schematic diagram depicting the synthesis process of S, N-codoped MXene. The X-ray diffraction (XRD) patterns of the (002) peaks of both pure MXene and S, N-MXene were analyzed. Additionally, the EDS mapping images of S and N elements were included as insets. The present study showcases high-resolution X-ray photoelectron spectroscopy (XPS) spectra pertaining to the N 1 s, S 2p, and Ti 2p of S, N-MXene. The conductivities of the SNMG-40 film were measured both in its original state and after a period of 100 days. The contact angles of the pristine MXene film, S, N-MXene film, MXene/rGO film, and SNMG-40 film were determined. The present diagram provides a schematic representation of the structures of both pristine MXene flake and S, N-MXene flak [307].

through surface functionalization [85,128,288]. Density Functional Theory (DFT) was used to investigate the effect of surface finish on the electron density [232]. The density of states (DOS) at the Fermi level in MXene is known to influence surface termination. Treatment with Ti_3C_2 reduced the -F terminus from 300 °C to 775 °C. This was confirmed by in situ electron energy loss spectroscopy (Fig. 28a). The significant improvement in electronic conductivity is attributed to the reduction of -F terminations during annealing at 700–775 °C (Fig. 28b). Furthermore, Tang et al. studied the saturation magnetization of his Ti_3C_2 due to the formation of Ti-C vacancies upon H_2 annealing [289]. These showed similar amounts of –O after annealing at 100–500 °C in H_2, but the C-Ti-OH functional groups changed to O-Ti-O and C-Ti-O during the annealing process Ti-C Vacancies, Ti vacancies are formed (Fig. 28c). Theoretically, the completed Ti_3C_2MXene was nonmagnetic, while the older Ti_3C_2 was ferromagnetic. The influence of Ti-C vacancies on the enhanced saturation magnetization was confirmed by DFT calculations and magnetization development (Fig. 28d).

In a study, Kumar et al. established that the MXene material (Nb_2CT_x) exhibits favourable characteristics for potential gas sensor applications, specifically in its large surface area and abundant surface functional groups [304]. Nevertheless, the primary constraint of MXenes is atmospheric instability. The present study employed (3-aminopropyl)

triethoxysilane (APTES), a widely used silane coupling agent, to modify the surface of MXene at varying concentrations (0.1, 0.2, 0.3 mL). The process involves the formation of a uniform and substantial protective layer on the Nb_2CT_x MXene structures through covalent bonding via silylation techniques, effectively reducing the oxidation of the MXene. This method also enables the incorporation of supplementary reactive groups (-NH_2) concurrently. The synthesized materials were subjected to characterization techniques such as X-ray diffraction (XRD), field emission scanning electron microscopy (FESEM), high-resolution transmission electron microscopy (HR-TEM), X-ray photoelectron spectroscopy (XPS), Fourier-transform infrared spectroscopy (FT-IR), ultraviolet-visible spectroscopy (UV-Vis), and zeta potential analysis to assess their functionalization and stability. The electron-donating property of the hydrophilic -NH_2 group facilitates the detection of acidic gases, such as nitrogen dioxide (NO_2). The APTES-functionalized Nb_2CT_x MXene exhibited a superior sensing response of 31.52% towards NO_2 gas at a concentration of 25 ppm compared to the unmodified Nb_2CT_x MXene, which displayed a sensing response of 12.5%. Moreover, the former demonstrated stability for exceeding 45 days at ambient temperature (~25 °C). The results indicate that the APTES-functionalized Nb_2CTx MXene exhibits superior sensitivity, with values of 1.2314 ppm^{-1} compared to 0.492 ppm^{-1} for Nb_2CT_x and
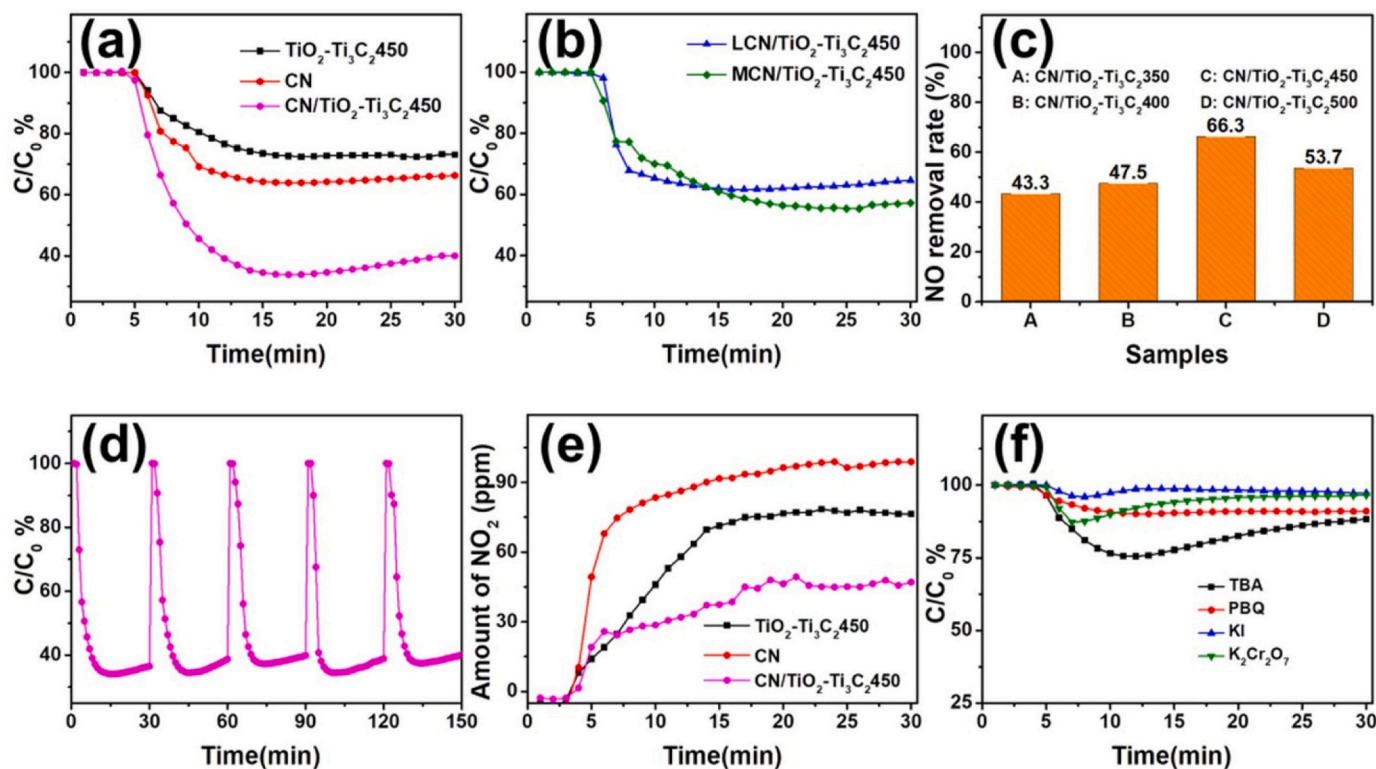
Fig. 30. The photocatalytic performances of the photocatalysts for NO degradation are shown in (a), (b), and (c). Five cyclic tests of CN/TiO$_2$-Ti$_3$C$_2$ (continuous reactor), NO$_2$ generated during photocatalysis, and capture studies on CN/TiO$_2$-Ti$_3$C$_2$ [274].

Nb$_2$CT$_x$-0.2 APTES, respectively. The Nb$_2$CT$_x$-0.2 APTES sensors can detect NO$_2$ gas at the detection limit (LOD) of 3 ppb and quantification limit (LOQ) of 12 ppb. The Nb$_2$CTx sensor in its original state exhibits a LOD of 15 ppb and LOQ of 52 ppb. This indicates that the Nb$_2$CTx sensor, which has been functionalized with APTES, is capable of detecting extremely low levels of the gas with a high degree of sensitivity. The utilization of Polydopamine (PDA) as an appropriate agent for surface modification of MXene is attributed to the presence of numerous amino and catechol groups in its backbone. These groups can establish non-covalent and covalent interactions with organic and inorganic surfaces [305]. The technique of surface-initiated polymerization represents an additional approach for surface functionalization of MXenes. Silane reagents possessing diverse functional groups, including but not limited to phenyl, chloro, vinyl, epoxy, methacrylate, amine, and diamine, can facilitate the formation of robust linkages between inorganic and organic moieties [306]. In general, the surface modification or functionalization of MXene materials is a critical factor in enhancing their stability, tuning their properties, improving their dispersion and compatibility, and facilitating functional integration. This, in turn, broadens their potential applications in diverse fields.

Liao et al. [307] used a heteroatom doping technique to improve the surface functionality of MXene. Highly reduced graphene oxide (rGO) was then added as a conductive linker to form a deformable S, N-MXene/rGO (698.5 F cm) with remarkable mechanical strength (about 45 MPa) and energy storage (698.5 F cm). Fig. 29a shows the doping mechanism, XRD pattern of MXene, EDS mapping images of S and N elements, and high-resolution XPS spectra. Importantly, the SNMG-40 film exhibits exceptional long-term cycling, with a capacitance retention of about 98% after 30,000 cycles. This stability is maintained at ambient conditions or when exposed to H$_2$SO$_4$ electrolyte for over 100 days. Furthermore, the asymmetric supercapacitor (aMGSC) based on SNMG-40 film exhibits a very high energy density of 22.3 Whkg^{-1}, which exceeds previously reported MXene-based materials Furthermore, the aMGSC exhibits mechanical in which good stability has been

exhibited under deformation conditions. As a result, this design increases the competitiveness of MXene products for real-world applications such as sensitive electronics and electronic surge protection. The high-resolution decompositions of N 1 s, S 2p, and Ti 2p in Fig. 29c-e reveal the presence of three types of nitrogen bonds and quaternary sulfur bonds, originating from different doping sites in S, N, respectively -MXene occurs. The reason is different valence states. To investigate the stability of the prepared SNMG films, the changes in conductance were measured in their fresh state and after 100 days of storage under ambient conditions (Fig. 29f). In order to evaluate the viscosity, the water interactions with the different films (pristine MXene film, S, N-MXene film, MXene/rGO film, and SNMG-40 film) (Fig. 29g) were measured from 73° (old MXene film) to 94° (S), N-MXene film) to an increased contact angle suggests that sulfur nitrogen doping via thermal annealing can remove or replace the hydrophilic OH groups on the MXene surface, resulting in a decrease in the hydrophilicity of the S, N-MXene film. Fig. 29h shows the structures of pristine MXene flakes and S, N-MXene flakes to shed light on the effect of sulfur and nitrogen doping on MXene stability.

Hu et al. [274] developed photocatalysts based on ternary g-C$_3$N$_4$/TiO$_2$/Ti$_3$C$_2$ MXene S-scheme heterojunctions to remove NO$_x$ under visible light. They observed that a larger BET-specific surface area is advantageous for light absorption and the oxidation of NO, which helps prevent the deactivation of the photocatalyst due to poisoning. The analysis of pore size distribution showed the presence of mesopores ranging from 2–4 nm and 10–40 nm in CN/TiO$_2$-Ti$_3$C$_{2450}$. These mesopores enhanced the adsorption of NO and facilitated the efficient transport of reactants and products during photocatalytic reactions [308]. The NO degradation curves of the prepared photocatalysts were presented in Fig. 30a, with CN/TiO$_2$-Ti$_3$C$_2$ demonstrating the highest degradation efficiency of 66.3%. This value was significantly higher than that of TiO$_2$-Ti$_3$C$_2$ (~28.0%) and CN (~34.0%). Lower or higher concentrations of CN in LCN/ TiO$_2$-Ti$_3$C$_2$ and MCN/ TiO$_2$-Ti$_3$C$_{2450}$ resulted in lower NO removal ratios compared to CN/ TiO$_2$-Ti$_3$C$_2$
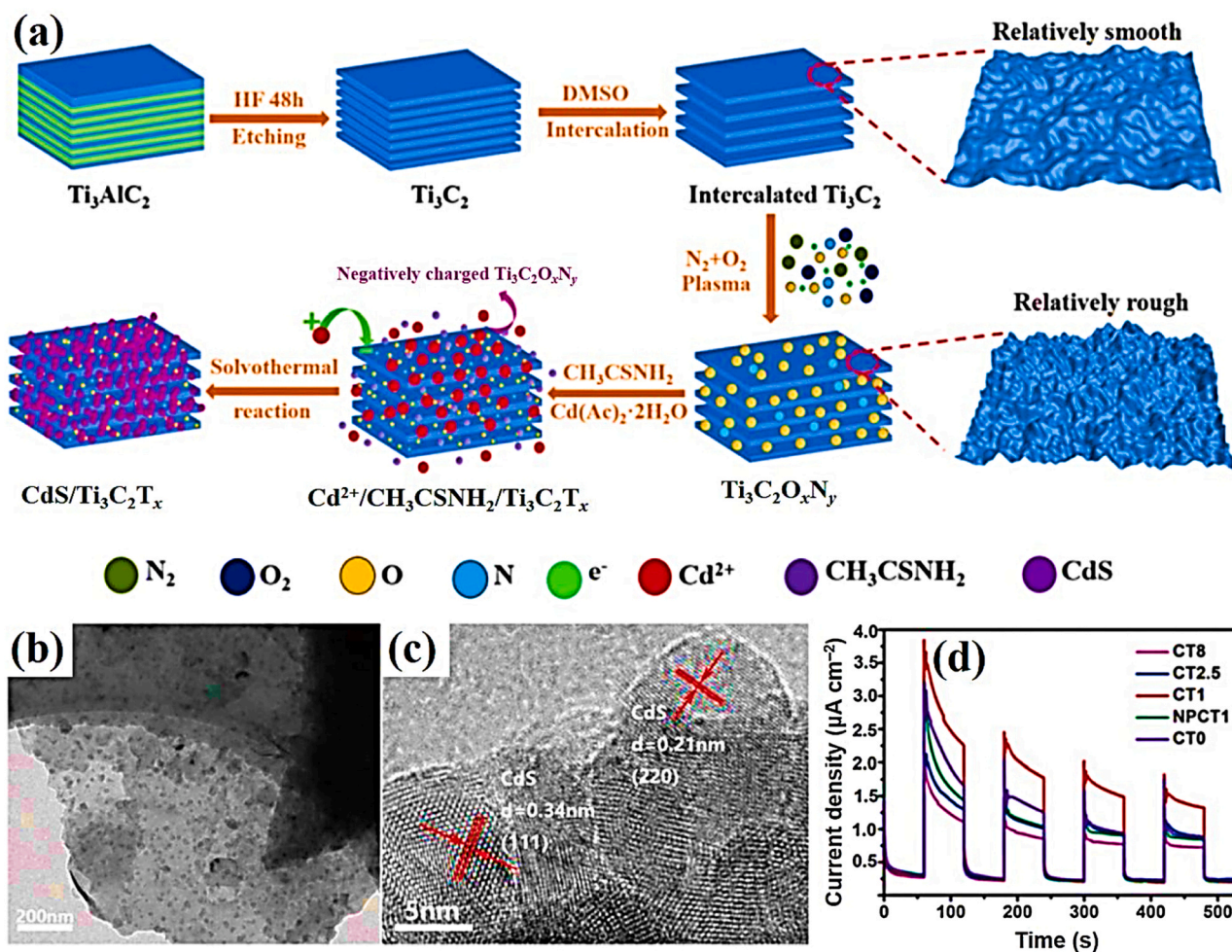
Fig. 31. (a) Diagrammatic representation of the CdS/Ti$_3$C$_2$ preparation process. TEM (b) and HRTEM (c) pictures of CdS/Ti$_3$C$_2$. (d) Photocurrent density curves for CdS loaded with 0 wt% (CT$_0$), 1 wt% (CT1), 2.5 wt% (CT2.5), and 8 wt% (CT8) of plasma-treated Ti$_3$C$_2$ and CdS loaded with normal Ti$_3$C$_2$ (NPCT1) [317].

(Fig. 30b). This suggests the need for careful control of the ratio between CN and TiO$_2$-Ti$_3$C$_2$ to achieve excellent photocatalytic activity. The calcination temperature of TiO$_2$-Ti$_3$C$_2$ during the initial preparation step also influenced the NO removal efficiency (Fig. 30c). Additionally, CN/ TiO$_2$-Ti$_3$C$_2$ exhibited excellent NO removal efficiency even after five consecutive catalytic experiments, indicating the maintenance of its catalytic activity (Fig. 30d). The amount of intermediate NO$_2$ generated during the photocatalytic reaction on CN/ TiO$_2$-Ti$_3$C$_2$ was significantly lower than that on CN and TiO$_2$-Ti$_3$C$_2$ (Fig. 30e), suggesting that the active species produced effectively converted NO into NO$_3$ [309]. To gain further insights, scavengers such as tert-butanol (TBA), p-benzoquinone (PBQ), potassium iodide (KI), and potassium dichromate (K$_2$Cr$_2$O$_7$) were used to capture hydroxy radicals, superoxide radicals, holes, and electrons, respectively [310]. Fig. 30f demonstrated that each capture agent inhibited the photocatalytic conversion of NO to varying degrees. The most significant inhibitory effect was observed with KI (capturing h$^+$), followed by PBQ (capturing·O$_2^-$) and K$_2$Cr$_2$O$_7$ (capturing e$^-$). TBA (capturing·OH) had the least inhibitory effect among the four scavengers. These findings emphasize the potential of TiO$_2$-Ti$_3$C$_2$ as a promising material for producing high-performance ternary heterojunction photocatalysts through precise control of the oxidation conditions. Furthermore, the two-dimensional MXene material shows excellent promise for photocatalytic air purification.

The introduction of elemental doping has been observed to considerably modify the lattice structure of layered MXenes, creating defects, lattice distortion, and changes in interlayer distance. This modification generates many electrochemically active sites that exhibit potential for

utilization in various fields, such as energy storage, catalysts, optoelectronic devices, sensors, environmental remediation, and biomedicine. As such, incorporating elemental doping in layered MXenes presents promising opportunities for practical applications. Furthermore, drawing from the aforementioned various techniques of compound doping, the implementation of multidirectional coordination enhances the physical and chemical characteristics of individual MXenes. It is noteworthy that the computational simulation predicted a significant impact of heteroatom doping on the physicochemical properties of MXenes, which facilitated the expeditious advancement of element-doped MXenes [311]. The present investigation on the elemental doping of MXenes is a topic of significant interest. However, the corresponding mechanism of doping remains ambiguous.

4.3.2. Create vacancies to increase the active sites of MXenes for NO$_x$ reduction

To enhance the photocatalytic capabilities of semiconductor materials, numerous methods have been devised. The regulation of morphology represents a viable approach to augmenting the particular surface area and enhancing the quantity of active sites [312,313]. Due to its remarkable mechanical properties and large surface area, MXene has emerged as a powerful excipient to achieve uniform growth and microdispersion of various photocatalysts such as, Ti$_3$C$_2$. An interesting feature of MXene materials is that they can partially oxidize in situ, forming metal oxide/MXene heterojunctions [314]. The close integration of metal oxides and MXene on these heterojunctions Translocation of photogenerated carriers greatly enhances separation, resulting in
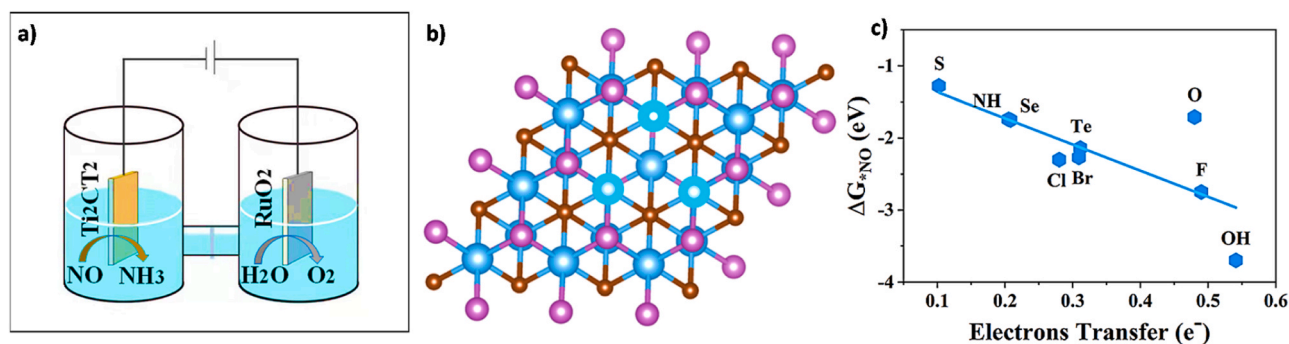
Fig. 32. a) A schematic illustration of an electrochemical cell with an anode like RuO_2 and a cathode like Ti_2CT_2 MXene for the NORR and OER, respectively. b) An illustration of the NORR's active centers, which are shown as cyan balls on an MXene. (c) The relationship between the number of electrons transferred from three "active" Ti atoms to NO molecules and the calculated DG*NO on functionalized Ti_2CT_2MXenes [254].

improved photocatalytic performance. A common MXene species, Nb_2C, can be in situ oxidized to form Nb_2O_5/Nb_2C heterojunctions [166,315]. Moreover, MXene not only serves as a robust support material but can also act as a precursor for the in-situ growth of related metal oxide photocatalysts. This in situ growth approach simplifies the synthesis process and improves efficiency. For example, in the work by Low et al. [174], TiO_2 was directly grown on Ti_3C_2 using Ti_3C_2 as a precursor, enabling intimate contact between the two materials. This close contact promotes the separation and migration of photogenerated charge carriers, leading to enhanced photocatalytic activity [174]. Another advantage of MXene-based photocatalysts is their fluffy structure, significantly increasing their specific surface area. The size of the photocatalyst is crucial for photocatalytic activity, but high surface energy often causes photocatalysts to aggregate into larger sizes, reducing their contact area with reactants. MXene-based materials, prepared via wet chemical etching methods, possess a large number of surface functional groups, making them an excellent platform for controlling the size of the photocatalyst. The negatively charged surface of MXene can adsorb metal cations and facilitate the uniform growth of photocatalysts [316]. This results in MXene-based photocatalysts with high specific surface area, providing more surfactant sites to enhance photocatalytic activity.

For instance, Li et al. [316] used low-temperature wet chemistry to create $Ti_3C_2T_x$/CdS composites with uniformly dispersed CdS nanoparticles on $Ti_3C_2T_x$. The diameter of the CdS nanoparticles supported by $Ti_3C_2T_x$ was less than 50 nm, according to the microstructural analysis, whereas the average size of the naked CdS nanoparticles generated without $Ti_3C_2T_x$ was 60 nm. More surface-active sites are made available for the photocatalytic reaction by the smaller photocatalyst supported by MXene, which improves the efficiency of the reaction. In light of this, Ti_3C_2 was plasma-treated to enhance its surface functional groups before being used as a cocatalyst to boost the photocatalytic activity of CdS by Xiang et al. [317]. As shown in Fig. 31a, the surface roughness of the resulting ultra-thin Ti_3C_2 was improved by subjecting it to an O_2-N_2 plasma treatment, which allowed for the formation of massive oxygen surface functional groups on the Ti_3C_2. The homogenous distribution of the CdS NPs on the Ti_3C_2 and the close contact between the two materials can be seen in the TEM images of the manufactured samples (Fig. 31b-c). The electrochemical photocurrent characterization was then used to determine how effectively the produced samples separated photogenerated charge carriers as depicted in Fig. 31d. According to this research, the improved surface functional groups on MXene could be useful for producing intimate active sites on the MXene and the photocatalyst as well as large surface-active sites for the photocatalytic reaction.

Recent studies have highlighted the importance of high surface area and porous structures in enhancing the active sites for various reactions. Kamysbayev et al. [318] have successfully synthesized MXenes with different terminations such as NH, S, Cl, Se, Br, and Te. Building on these achievements, Zhao et al. [254] conducted density functional theory

(DFT) calculations to assess the potential of Ti_2CT_2 MXenes (where T = S, O, F, Cl, Br, Se, Te, NH, and OH) for direct electrochemical reduction of NO to NH_3. However, the catalytic activities of Ti_2CT_2 MXenes in the NO reduction reaction (NORR) were found to be limited due to the lack of exposed metal active sites required to initiate the reaction. These exposed "active" Ti atoms are expected to act as active sites for the absorption and reduction of NO in the electrochemical cell. Hence, the exposed "active" Ti atoms are expected to act as active centres for NO adsorption and reduction within the electrochemical cell as displayed in Fig. 32a. Adsorption configurations of NO molecules on functionalized Ti_2CT_2 MXenes found out that three Ti atoms formed a hole web page, which acted as an active web site liable for NO adsorption and reduction as displayed in Fig. 32b. Bader charge evaluation was employed to quantitatively examine the number of electrons transferred from functionalized Ti_2CT_2 MXenes upon NO adsorption. The researchers hooked up a courting between the Gibbs loose electricity (DG*NO) and the number of electrons transferred, as proven in Fig. 32c, indicating a linear correlation. This study not only contributes to the development of novel catalysts for NO elimination and NH_3 synthesis but also emphasizes the crucial role of surface functionalization in enhancing the catalytic performance of MXenes in NORR. As a consequence, the generation of vacancies within a material leads to an increase in the number of active sites that are available for NO_x reduction reactions, thereby enhancing the catalytic performance. The introduction of vacancies in a catalyst's structure can improve its ability to adsorb NO_x, create catalytic sites, and influence the reaction kinetics. This can result in a more efficient reduction of NO_x and a reduction in harmful emissions.

4.3.3. Substituting transition metal-atoms and its influence on the NO_x reduction

The incorporation of transition metal atoms into different materials, including catalysts, presents an opportunity to enhance their catalytic properties. In the case of reducing nitrogen oxides (NO_x), such substitution can greatly improve the catalytic activity of the material, leading to more efficient NO_x reduction. Factors such as the choice of transition metal atom, the method of substitution, the concentration of the metal atom, and the structural properties of the material all contribute to influencing its catalytic activity for NO_x reduction. The specific transition metal atom introduced into MXene materials directly impacts their catalytic performance in NO_x reduction. Copper (Cu) and iron (Fe) have been identified as particularly effective catalysts for NO_x reduction. When Cu or Fe is substituted into MXene materials, it enhances their ability to reduce NO_x, especially at lower temperatures.

Onyia and colleagues conducted density functional theory (DFT) studies on transition metal-doped Ti_3N_2 MXene monolayers [319]. Their research revealed that transition metal dopant atoms, as well as transition metal vacancies, can be feasibly formed in these materials. Similarly, Zhou et al. employed first-principles calculations based on DFT to
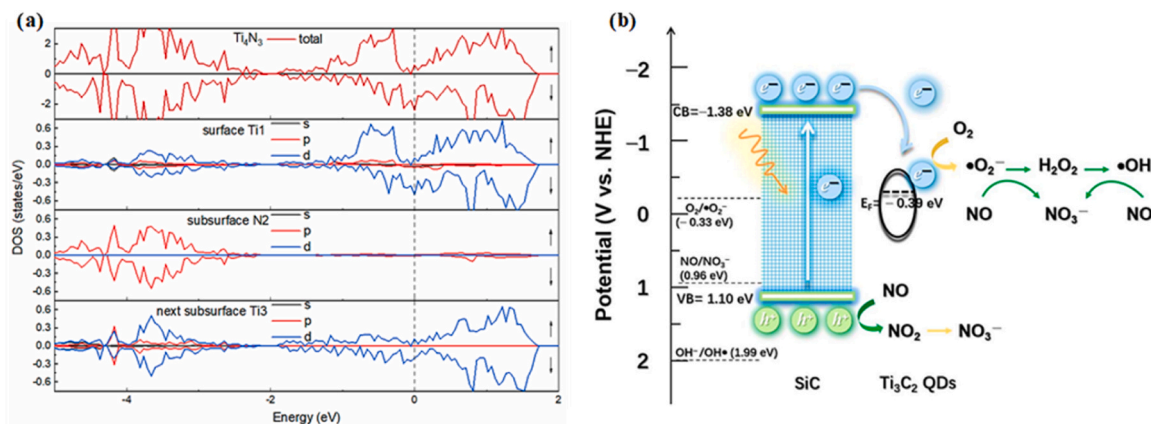
Fig. 33. a) Ti$_4$N$_3$ nanosheet with total density of states (TDOS) and partial density of states (PDOS). The spin-up and spin-down orbitals are denoted by and, respectively. The vertical dashed line represents the Fermi level, which is zero. TDOS is transferred to a simple cell. [320]. b) The photocatalytic mechanism of NO degradation by TQDs/SiC heterojunctions under visible light irradiation [272].

explore the impact of atomic vacancy defects, Frenkel-type defects, and transition metal doping (Z = Sc, V, and Zr) on the magnetic and electric properties of Ti$_4$N$_3$ MXene nanosheets [320]. In Fig. 33 of their study, the total density of states (TDOS) and partial density of states (PDOS) were depicted. Notably, near the Fermi surface, a large valley was observed in the spin-up channel, with the Fermi level positioned at the bottom of this valley. Conversely, the spin-down band exhibited a relatively large peak crossing the Fermi level. Consequently, the Ti$_4$N$_3$

nanosheet displayed significant spin polarization, exceeding 80%, as indicated by its spin-polarizability. Although, incorporation of transition metals in MXene sheets increases the performance by reducing band gaps between valance and conduction levels, which ultimately boots the NO/NO$_x$ removal efficiency. But Wang et al., observed the NO-removal capacity upto multi-folds by doping SiC (group IV elements) in Ti$_3$C$_2$-layers coupled with light energy as shown in the following mechanism, Fig. 33b [272].
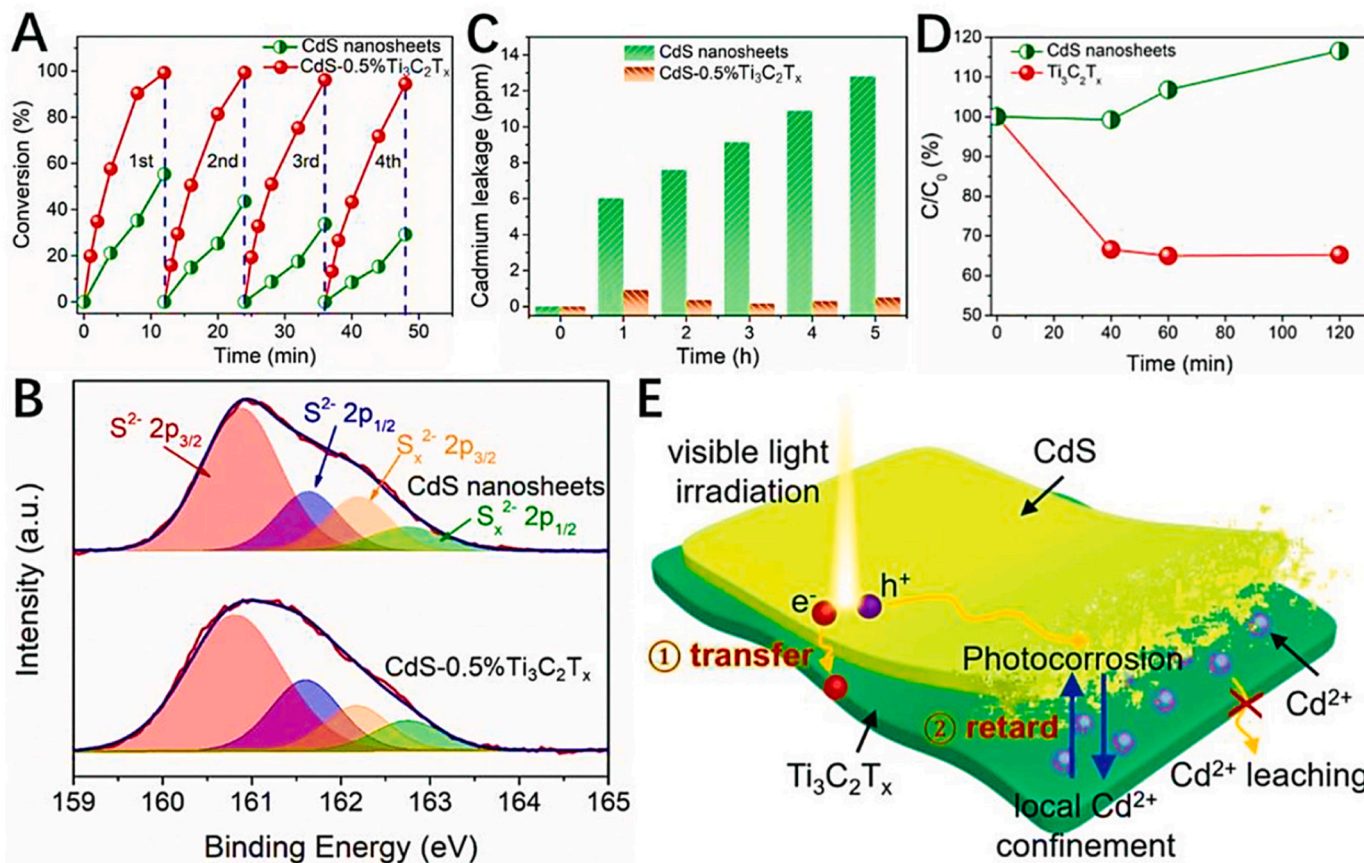

Fig. 34. (A)The study examines the photostability of pure CdS nanosheets and CdS-0.5%Ti$_3$C$_2$T$_x$ in the photoreduction of 4-nitroaniline under visible light irradiation ($\lambda \geq 420$ nm). Additionally, high-resolution XPS spectra of S 2p for the used pure CdS nanosheets and CdS-0.5%Ti$_3$C$_2$T$_x$ after photocatalytic reduction of 4-nitroaniline are analyzed. The study also investigates the Cd^{2+} leakage profiles under visible light irradiation over CdS nanosheets and CdS-0.5% Ti$_3$C$_2$T$_x$ as well as the adsorption of Cd^{2+} over CdS nanosheets and Ti$_3$C$_2$T$_x$ in the dark. Finally, the study provides a schematic illustration of Ti$_3$C$_2$T$_x$ enhanced photostability of CdS [331].

The introduction of Frenkel-type defects in the system led to a decrease in the total magnetic moment. This decrease was attributed to the enhanced indirect magnetic exchange between surface Ti atoms, bridged by the external N atom. The Frenkel-type defect system exhibited a relatively high spin polarization of approximately 70%. Additionally, the effects of doping with transition metals (Z = Sc, V, Zr) on the Ti_4N_3 MXene nanosheet were systematically investigated. The results demonstrated that all the doped systems maintained structural stability and exhibited significant magnetism, resulting from the directed magnetic exchange between surface Z and Ti atoms. The relaxation of surface atoms also played a crucial role in determining the material's magnetism and electronic properties. Notably, the Ti_4N_3-Sc doped system demonstrated a particularly high spin polarization ratio. Therefore, the Ti_4N_3 MXene nanosheet doped with Sc could be a promising candidate for applications in spintronics. These studies on atomic defects and transition metal doping in MXene nanosheets, specifically Ti_4N_3, contribute to a better understanding of the electronic and magnetic characteristics of real 2D materials and aid in the development of new Ti-based MXene materials in the 2D domain [320].

In summary, the substitution of transition metal atoms in MXenes has shown promise in enhancing the catalytic activity for NO_x reduction, resulting in a more efficient reduction of NO_x emissions. However, there is still a need for additional research to comprehensively understand the underlying mechanisms responsible for the catalytic activity of MXenes in NO_x reduction. This understanding is crucial for further optimizing the performance of MXenes and enabling their practical application in addressing NO_x emissions.

5. Stability and long-term utilization of MXene

The stability and properties of MXenes can be modified through various approaches. Surface chemistry plays a crucial role in improving their stability, and the interaction of free electrons with transition metals (TMs) allows for changes in the surface chemistry of MXenes [44, 321–324]. Surface terminations and the composition of MXenes (different M and X elements) can also be adjusted to fine-tune their mechanical, oxidative, and thermal stabilities [325]. Strong M-X bonds and appropriate surface terminations are necessary for achieving mechanical stability, and surface functionalization has been shown to increase the mechanical elasticity of MXenes significantly [326]. The stability of MXenes is influenced by the number of layers, with thicker MXenes generally exhibiting lower stability than thinner ones [327]. The thickness of the MXene layers affects their mechanical characteristics, with the thinnest MXenes showing the highest elastic moduli values [328]. The outermost layer atoms primarily govern the surface properties of MXenes, while the number of layers has minimal impact on surface properties [329]. The catalytic activity of MXenes can vary depending on the number of layers, as different numbers of layers result in variations in the accessibility and tunability of active sites.

To enhance the stability of MXenes, several strategies have been proposed. These include optimizing the synthesis of MAX phases (precursors to MXenes), modifying the preparation of MXenes to increase their lateral size and achieve ordered assembling, controlling storage conditions (such as frozen storage under inert gas atmosphere), and applying shielding or encapsulation techniques using suitable additives and polymers [330].

The majority of MXenes are chemically unstable, which can lead to a number of issues such oxidation, restacking, instability in colloidal solution, swelling, and thin film deterioration. This reduces their catalytic, storage, and electron shielding capacities, severely restricting further study and industrial-scale application. Therefore, it has been a pressing problem to develop creative ways to enhance stability. Additionally, for practical applications, the long-term chemical stability of photocatalysts is quite important. According to reports [226,331], MXenes can improve the stability of CdS and Ag_3PO_4 by reducing their photo-corrosion reactions. For instance, as shown in Fig. 34 A [331], the addition of a small amount of Ti_3C_2Tx (e.g., 0.5 wt%) to CdS nanosheets improves the stability of the composite as compared to pure CdS nanosheets toward 4-nitroaniline reduction under visible light irradiation (420 nm). The signals of S2 and polysulfides existing as Sx2 (x = 2–8) are seen in the X-ray photoelectron spectroscopy (XPS) results of both regenerated pure CdS and CdS-0.5% Ti_3C_2Tx composite (Fig. 34B) [332]. This implies that the S2 in CdS is oxidized into polysulfides in the system. It is interesting to note that the Sx2 ratio for recycled CdS nanosheets is estimated to be 26.0%, however, this value drops to 17.1% for CdS-0.5%$Ti_3C_2T_x$, demonstrating the anti-photo corrosion of CdS by the addition of Ti_3C_2Tx. The Cd^{2+} leakage under visible light irradiation for these two samples has been examined to understand the underlying process that allows Ti_3C_2Tx to delay the photo corrosion of CdS. Fig. 34 C shows that whereas the leaching of Cd^{2+} is minimal within 5 h for the CdS-0.5% $Ti_3C_2T_x$ composite, it increases noticeably with prolonged light irradiation time for pure CdS nanosheets. Additionally, Ti_3C_2Tx can successfully adsorb Cd^{2+} in the dark, in contrast to CdS nanosheets, as shown by the initial stage's nearly unchanged Cd^{2+} concentration (Fig. 34D). The slow disintegration of pure CdS nanosheets in water is demonstrated by the rise in Cd^{2+} concentration in the CdS nanosheets aqueous suspension over time. Due to the high binding energy of Cd^{2+} on Ti_3C_2Tx, these results demonstrate a substantial adsorption affinity between the two materials [333]. Le Châtelier's principle [334] states that this causes the photocorrosion-released Cd^{2+} to become locally contained around the CdS rather than leaking into the solution, which slows down the hole-induced photocorrosion of CdS. This is demonstrated in Fig. 34E. Due to the adsorption-enabled Cd^{2+} confinement effect of $Ti_3C_2T_x$, these results and the recycling test results demonstrate that the introduction of $Ti_3C_2T_x$ can prevent the photo corrosion of CdS [335].

Considering the potential impact of MXene oxidation on the photo-activity of MXenes-based composites, it is necessary to carefully select appropriate synthesis approaches for MXenes-based composites and control photocatalytic reaction conditions. Parameters such as temperature, atmosphere, solvent, light irradiation wavelength, and possible additives should be carefully considered to ensure reliable and accurate investigation of the photoactivity of MXenes-based composites. In conclusion, by modifying the surface chemistry, altering the surface terminations, adjusting the MXene composition, and improving the synthesis and storage conditions, the stability of MXenes can be improved. The long-term stability and oxidative resistance of MXenes have been improved with fluoride-free etching techniques, opening up new possibilities for their practical uses. By addressing these aspects and conducting comprehensive research on MXenes' stability, the field of MXenes-based materials can advance, opening up new possibilities for their utilization in various applications, including photocatalysis.

5.1. Factors affect the stability of MXene

MXene materials can be modified and optimized based on specific requirements, leading to variations in their electrochemical, photothermal, microwave absorption, hydrophilic, and hydrophobic properties. Exploring MXene's properties, such as friction, adhesion, conductivity, and photothermal conversion, is essential for expanding its application fields. The stability of MXene materials is influenced by several factors, including the choice of preparation method, applied conditions (temperature and pH), type of etching agents and the nature of the materials involved effectively impact the stability of MXenes. The composition of MXenes, surface terminations, and their interactions with the surrounding environment also significantly determine their stability. It is crucial to understand these factors and their effects on MXene stability to tailor their properties, enhance their performance, and ensure their long-term functionality in various applications. By gaining a comprehensive understanding of MXene stability, researchers can develop strategies to improve stability and design MXene-based materials with desired properties for specific applications [336].

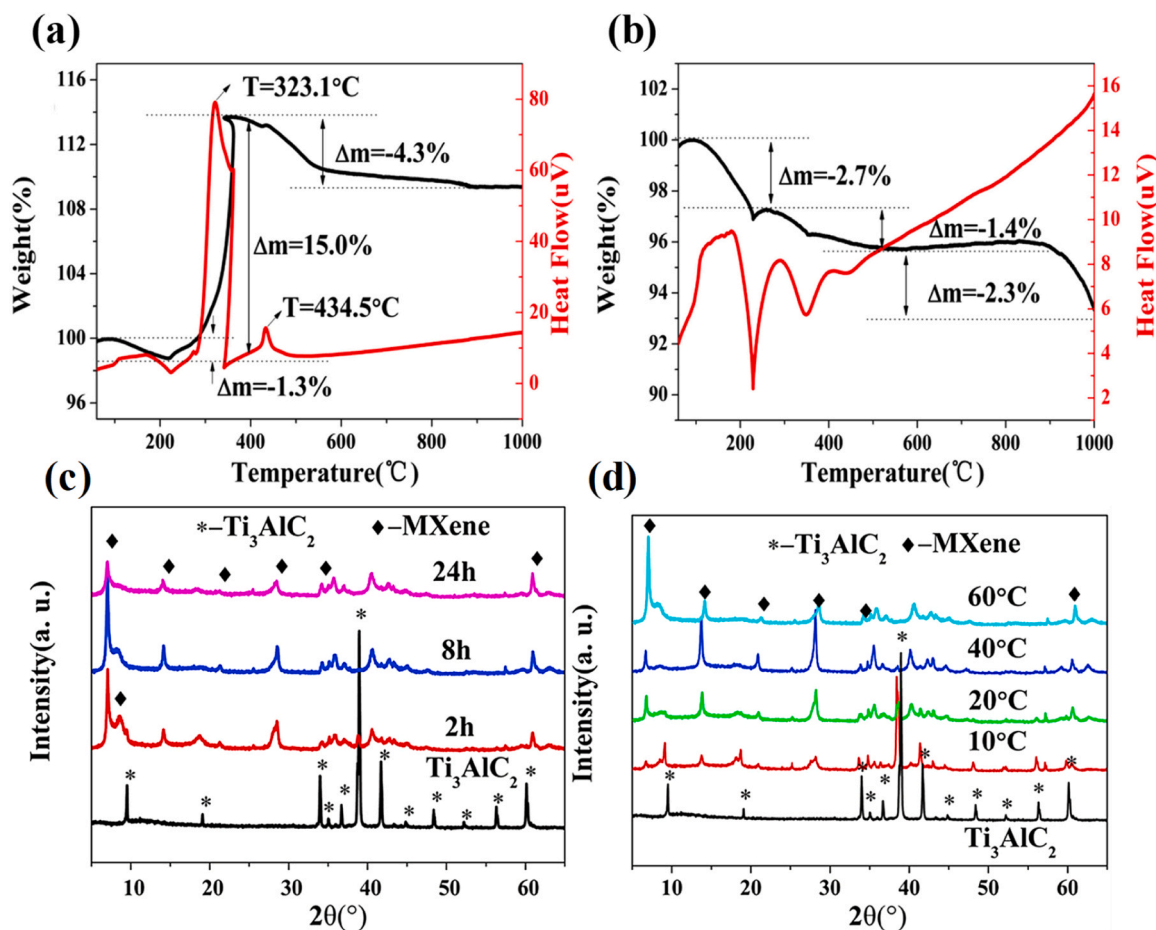The inadequate oxidation stability of MXenes in ambient conditions

Fig. 35. a-b) TG and DTA curves of Ti$_3$C$_2$ from room temperature to 1000 °C in oxygen atmosphere, and argon atmosphere. XRD patterns of Ti$_3$AlC$_2$ and samples exfoliated by NH$_4$HF$_2$: (c) at 60 °C for different time; (d) at different temperatures for 8 h [349].

is a significant issue that hinders their practical implementation. The gradual degradation of 2D MXenes into a composite of metal-oxide nanoparticles and amorphous carbon is caused by exposure to water, air, heat, and light, as reported in a recent publication [337]. According to a study, the process of oxidation in MXene nanosheets typically commences at surface defects or edges and subsequently spreads rapidly to other regions of the nanosheets [338]. It has been observed that MXene nanosheets having smaller flakes and/or high-defect density are more susceptible to rapid oxidation as compared to their larger and/or less defective structured counterparts [339]. The presence of defects in MXene nanosheets is inevitable due to two reasons. Firstly, defects in the parent MAX phase are directly inherited in the as-synthesized MXene. Secondly, the contact of the top and bottom atomic layers of the MXene with the acidic etchant solution after the successful elimination of "A" layers from the parent MAX phase precursor, which consists of stacked MXene nanosheets separated by the "A" element atomic layers, leads to the formation of cation vacancies and atoms on the surface [340–342]. The synthesis of MXene predominantly follows a top-down methodology, whereby the size and purity of the parent MAX phase considerably influence the dimensions and quality of the MXene flake. The size of the flakes and the defect structure of MXene nanosheets are also affected by the synthesis conditions, such as the type of etchant and the duration of etching [343–345]. The etchant solution primarily influences the composition of surface terminal groups. Specifically, direct-HF etching results in the prevalence of −F functional groups, whereas in situ HF etching promotes the formation of −O terminations [346]. Furthermore, the HF synthesis methodology necessitates the incorporation of an extra organic molecule intercalation step, followed by ultrasonication

synthesis conditions, to effectively delaminate the multilayered MXene into nanosheets that are only a few atoms thick. This process has the potential to decrease the size of the flakes and lead to the formation of defects [347]. Therefore, the utilization of this technique is expected to result in characteristics such as reduced defect structure and increased flake size, which contribute to the enhancement of oxidation stability in MXene nanosheets. The oxidation behavior of MXenes is contingent upon the number of atomic layers comprising the material. Specifically, an increase in the number of atomic layers results in heightened oxidation stability of the MXene. According to a study, the Ti$_3$C$_2$T$_x$ MXene exhibits a higher level of oxidation stability in comparison to the Ti$_2$CT$_x$, Mo$_2$C, and Nb$_2$C MXenes [348]. Moreover, Feng et al. employed a one-step technique to generate a greater interplanar spacing of 2D MXene Ti$_3$C$_2$ by means of NH$_4$HF$_2$ etching of Ti$_3$AlC$_2$ [349]. The thermogravimetry (TG) and differential thermal analyzer (DTA) were utilized to investigate the thermal stability of Ti$_3$C$_2$, as depicted in Fig. 35. The study revealed that the lattice parameter of the Ti$_3$C$_2$ obtained was measured to be as high as 24.9 Å. Additionally, it was observed that the larger interplanar spacing of Ti$_3$C$_2$ was comparatively more stable than the sample exfoliated by HF. The investigation of the transition temperature in air from NH$_4$HF$_2$-etched Ti$_3$C$_2$ to anatase TiO$_2$ has revealed that it exceeds 500 °C. Furthermore, the multilayered structure of Ti$_3$C$_2$, can be effectively preserved even after undergoing heat treatment at 900 °C. In contrast, the value of HF-etched Ti$_3$C$_2$ is lower, measuring less than 350 °C. This study holds significance in investigating a secure approach for synthesizing 2D MXene materials and comprehending their thermal stability.

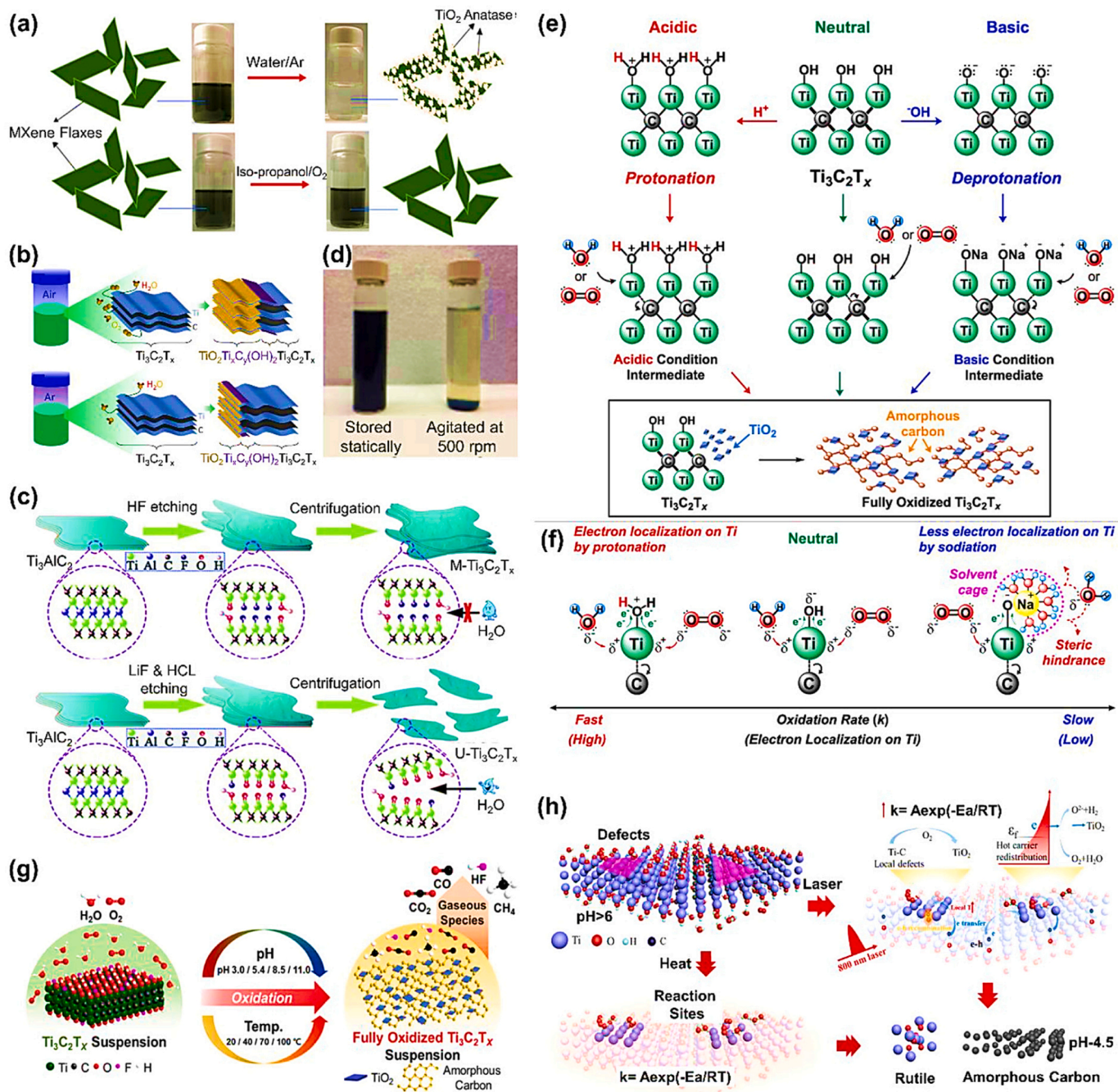However, the XRD styles of reaction samples at 60 °C for exclusive

Fig. 36. a) Oxidation of the MXene stored in water/Ar and isopropyl alcohol/O_2 medium. (b) Schematics showing the degradation of the $Ti_3C_2T_x$ MXene aqueous solution in air and Ar atmospheres at room temperature. (c) Multilayer (direct-HF etching method) and monolayer $Ti_3C_2T_x$ MXenes interaction with water in the aqueous dispersion. (d) Digital images showing the dispersion stability of the aqueous $Ti_3C_2T_x$ MXene nanosheet dispersion (concentration ~3.6 mg/mL) stored statically and agitated using magnetic stirring at 500 rpm [349]. (e–g) Oxidation of $Ti_3C_2T_x$ MXene suspension by varying pH (neutral, acidic, and base) and temperature conditions [352]. (h) Defect-induced degradation processes of $Ti_3C_2T_x$ MXene under the exposure to heat and laser light [353].

time are proven in Fig. 35c. The product specially includes Ti_3C_2 and the function top (39.2°) of Ti_3AlC_2 obviously disappears. It is really worth bringing up that the peaks at 7.1° and 8.6° appear simultaneously, which belong to the Ti_3C_2 with distinctive layer spacing. In order to illuminate the effect of temperature, they exfoliated exceptional samples via NH_4HF_2 at unique temperatures. As proven in Fig. 35d, the XRD patterns of different Ti_3C_2 nanocrystals are discriminating. However, the higher temperature above 60 °C is unlawful due to the viable oxidation of Ti_3C_2 [350]. Based on the results displayed above, the optimal reaction conditions between Ti_3AlC_2 and NH_4HF_2 are found, and they are as follows: the time is 8 h, and the temperature is 60 °C over which the

thermal stability of the MXene is extremely high.

In addition, the primary factors responsible for the oxidation of MXene are the presence of water and dissolved oxygen in the dispersing medium [329] depicted in Fig. 36a-b. The degradation of aqueous MXenes occurs within a short span of time, typically a few days, and is contingent upon the size of the flakes and the presence of structural defects. Multilayered MXenes, which are composed of densely packed monolayer nanosheets, demonstrate superior oxidation resistance in comparison to their single-layer counterparts due to their ability to impede the reaction of water and dissolved oxygen with the inner layers of the MXene nanosheets (Fig. 36c). By way of comparison, the presence
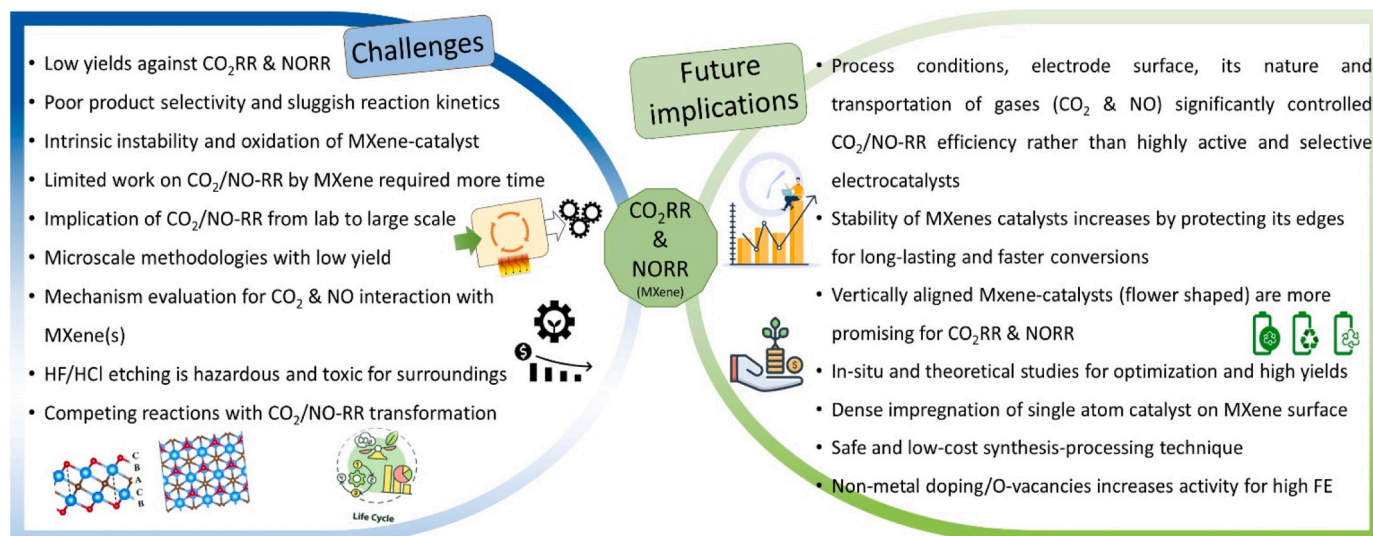
Fig. 37. Current challenges and future implications of CO_2RR and NORR with MXene-based catalysts.

of steric shielding between nanosheets in a solution with high concentration impedes the exposure of the surface/edges of the nanosheets to water or dissolved oxygen, thus extending the stability of oxidation in the MXenes. The longevity of MXene can be extended by preserving it in an undisturbed aqueous solution, as any agitation can interfere with the steric shielding of the nanosheets, as depicted in Fig. 36d [351]. According to a recent study [352], it has been observed that the oxidation of MXenes can be effectively slowed down under a basic pH condition as compared to an acidic pH condition presented in Fig. 36e-g. The basic condition leads to the emergence of OH- ions, which deprotonate the hydroxyl terminal groups of the MXene. This results in the formation of stabilized Ti-O-Na$^+$ intermediates that confer high oxidation stability to MXenes. In contrast, the acidic condition does not exhibit such properties. The Ti-O-Na$^+$ intermediates exhibit reduced electrophilicity and can generate a voluminous solvent cage surrounding the MXene nanosheets, thereby diminishing the interactions of H_2O and O_2 through steric hindrance [352].

Another parameter that effects the stableness of MXenes is temperature/ light supply. Hence, the know-how MXene sensitivity closer to those two parameters is critical, especially within the photocatalysis studies where it is of utmost significance because the catalytic reaction takes region in a water medium under light illumination. Moreover, the hybridization of MXene nanosheets with other photocatalysts to shape heterojunctions calls for harsh reaction situations such as a hydrothermal response below high temperature or thermal annealing outdoors. Low temperatures can slow down the oxidation kinetics of an aqueous MXene by way of minimizing the response of the MXene nanosheets with water and dissolved oxygen within the dispersion medium (Fig. 36g-h) [353]. In comparison, at better temperatures, the MXenes, without difficulty, decompose to their derivatives relying on the surrounding environment. Thermal annealing at 500 K in air transformed the Ti_2CT_x MXene into TiO_2 and graphitic carbon, whilst no noticeable degradation became determined when annealing was performed by way of changing the air surroundings with Ar, N_2, and the mixture of N_2 and H_2 [354]. However, the response of $Ti_3C_2T_x$ MXene with the surface terminal organizations (−O or −OH) at an annealing temperature of 500 °C brought about the formation of TiO_2 no matter the lifestyles of inert surroundings [355]. Further, Naguib et al. Reported that either the hydrothermal reaction or thermal annealing under a CO_2 ecosystem at temperatures ≥ 100 and 50 °C ought to degrade $Ti_3C_2T_x$ MXene into its derivatives, and those reaction situations beneath which other MXenes degrade into their derivatives were generalized by demonstrating that the hydrothermal reaction ended in 2D Nb_2C MXene degradation into

Nb_2O_5/C [356]. Further, Li et al. [357] proven that the plasmonic laser illumination can also boost the $Ti_3C_2T_x$ MXene oxidation. In specific, 808 nm laser illumination, that is toward the 770 nm absorption area of the $Ti_3C_2T_x$ MXene, results in extensive oxidation compared to the 532 and 980 nm laser illuminations, and this will be controlled by way of tuning the excitation strength of the laser. Further, the authors noticed an advanced oxidation of the aqueous $Ti_3C_2T_x$ MXene with the increasing temperature from 40 to 60 °C. However, the 808 nm laser illumination degraded the $Ti_3C_2T_x$ MXene more aggressively than uniform heating at 40 °C. Moreover, Feng et al. [348] discovered the most beneficial reaction conditions between Ti_3AlC_2 and NH_4HF_2, at special temperatures to test out the thermal stability of the as-synthesized MXene.

6. Challenges and future prospects

In the last decade, incredible improvements have been reported about CO_2RR and NORR through MXene-based catalysts. Besides, several challenges including performance, sustainability, design of electrolyzers and selectivity of CO_2, NO/NO_x are still need to be addressed. As the N_2 and CO_2 solubility at the surface of catalyst is major issue, which tried to improve through reactors and electrodes. After conversion these feed gases (CO_2, NO_x) the separation of generated products could be designed to have better separation of cathodic/anodic products as well as control the reaction kinetics at the three-phase boundary. For example, gas diffusion electrodes (GDE) have been widely studied as critical components in gas-phase electrolyzers for overcoming diffusion limitations of gas molecules from the bulk solution to the electrode surface [358]. This exploration is still limited within MXene catalyst community and could be an area of opportunity to increase the FE and yield rates. 2D MXenes offer great opportunities to repurpose emitted CO_2 into C-based fuels and provide lower energy routes to NH_3 production via (photo)electrochemical and photochemical routes and, therefore, should continue to be studied and investigated.

One critical question that arises for using MXenes as NORR catalyst is, 'can the energy produced from NH_3 compensate the energy input for preparing MXene catalysts and synthesis of NH_3 itself? Without inclusive environmental and energy evaluations, it is impossible to provide proper proof of a sustainable NH3 energy landscape for MXenes. In this context, life cycle assessment (LCA) is a primary tool and international standardized method to comprehensively evaluate the environmental impact of proposed methods (both qualitatively and quantitively),

Table 4

Various techniques for the conversion of CO_2/CO_x and NO_x pollutants into products/energy with all their pros and cons.

Air Pollutants	Technique	Product	Advantages	Disadvantages	Ref.
CO	Catalytic Oxidation	CO_2	• Low operating cost, low energy usage. • Ease of Operation. • Smaller footprint, easy installation. • Low maintenance (aside from catalyst poisoning and replacement).	• System is sensitive to changes in energy-content in the gas. • Risk of dioxin-forming in the presence of chlorinated compounds. • All catalysts are subject to catalyst poisons and polluting substances. • Produces CO_2, a greenhouse gas.	[360]
CO	Carbon Monoxide Fuel Cells	Electricity	• High Efficiency- when utilizing co-generation, fuel cells can attain over 80% energy efficiency. • Good reliability- the quality of power provided does not degrade over time. • Environmentally beneficial- significantly reduces CO_2 and harmful pollutant emissions.	• Expensive to manufacture due to the high cost of catalysts (platinum), • Lack of infrastructure to support the distribution of hydrogen. • Many currently available fuel cell technology is in the prototype stage and not yet validated.	[361]
NO_x	Selective Catalytic Reduction (SCR)	N_2, H_2	• Heavy-duty engines which use SCR receive a fuel economy improvement up to 5%. • SCR catalyst technology allows much greater NOx conversion efficiency so the engine can be fully optimized, contributing to this fuel economy improvement. • Less frequent Diesel Particulate Filter (DPF) cleaning is required, further reducing costs.	• SCR systems increase the complexity and cost of heavy-duty engines. • They require a constant supply of reducing agents like ammonia or urea.	[362]
CO_2	Electrochemical Reduction of CO_2	Methane, methanol or carbon monoxide (for Syngas)	• The process operates at mild conditions and can be tuned to selective products • It allows modular design, and provide opportunities to integrate renewable electricity with CO_2 reduction in carbon-intensive manufacturing industries such as iron and steel making.	• Concentration of products, especially liquid products, leaving the electrolyzer are low. • Low CO_2 solubility and competitive HER remain major challenges in inorganic salts-based aqueous electrolytes.	[363]
NO_x	Electrochemical Reduction of NO_x	N_2, NH_3	• Electrochemical processes eliminate the requirement for chemicals before and after the treatment • Disposing of sludge generation • Low investment costs	• The mechanisms for electrochemical conversion of nitrate to nitrogen gas are highly complex. • The products and stable intermediates are affected by electrode composition, crystal structure, pH and supporting electrolyte.	[364]
CO_x	Photocatalytic Conversion	CH_4, Syngas	• Photocatalysts can have relatively long lifespans and remain active for extended periods if properly maintained. • Photocatalysis can be applied to a variety of CO_x sources, including industrial emissions, vehicle exhaust, and even atmospheric CO_2, making it versatile.	• The photocatalyst's surface can become contaminated over time, reducing its effectiveness. Regular cleaning or replacement may be required. • Some unwanted byproducts may be produced, which could be harmful or require additional treatment.	[365]
NO_x	Photocatalytic Conversion	Nitrate (NO_3^-)	• Photocatalytic conversion does not rely on additional chemicals or reagents. • Once the photocatalyst is installed, it can operate with minimal ongoing costs. • The process primarily relies on sunlight or UV light for activation.	• The efficiency of photocatalytic conversion is influenced by environmental factors that can lead to variable performance in different locations and weather conditions. • Photocatalytic conversion can have slower reaction rates compared to other NOx reduction methods.	[366]

considering all inputs and emissions from the NH_3 production. Using the given methodology, the produced greenhouse gas emission (in the unit of CO_2–equivalent) as well as indirect and direct energy use throughout the life cycle from synthesis, extraction, manufacturing, production, and disposal (known as cumulative energy demand) can be compared with the existing HB process. Sustainable electrocatalytic and photocatalytic NH_3 production would only reduce environmental impacts (preferable LCA results) by coupling renewable electricity supplies with high-capacity factors. It is reasonable because intermittency, seasonal, and geographic constraints are associated with the nature of renewable energy, making NH_3 production pathways utilizing renewable energy less attractive. Therefore, significant research should be carried out to realize the system integration of NH_3 production with reliable and low-cost electricity sources to compete with the current-day HB process [359]. A summary of current challenges and future perspectives is displayed in Fig. 37, which could be helpful for the researchers [234,271, 281,343,358].

However, according to the whole discussion and in the light of critical analysis, there are several pros and cons of MXene materials towards the timing of GHG's and its conversion into green energy. In light of the existing literature and its overall evaluation, Table 4 elaborates on the various factors of MXene and its applications.

7. Conclusion remarks

The pressing need to address environmental issues stemming from greenhouse gas emissions and energy-intensive chemical manufacturing processes has spurred a significant movement towards sourcing fuels, fertilizers, and feedstock's from renewable materials and chemicals, while also prioritizing energy efficiency. An emerging approach that has been highlighted in this review involves the utilization of MXene catalysts for carbon dioxide reduction reaction (CO_2RR) and nitrogen oxide reduction reaction (NO_xRR). This strategy shows promise as a potentially environmentally sustainable and cost-effective option. In order to achieve commercially feasible 2D catalysts, novel approaches are being explored that leverage the adjustable structures, energetics, and mechanical characteristics of MXenes. These strategies aim to reduce activation energy barriers for chemisorption and hydrogenation processes involving CO_2 and NO_2, thereby enhancing reaction kinetics and selectivity.

This article provides a comprehensive summary of the latest developments in the utilization of (photo)electrochemical and photochemical processes to create MXene catalysts for CO_2RR and NORR. In this discourse, we examine the appropriate electronic and physical configurations, as well as the diverse methods of synthesis. Additionally, we explore potential reaction mechanisms, encompassing ultimate products. Furthermore, we delve into the existing advancements in theoretical and experimental investigations pertaining to both of these procedures. Despite recent efforts in the field of two-dimensional (2D) materials and their heterostructures aimed at enhancing the inherent catalytic activity, it is critical to recognize that the processes of CO_2RR and NORR continue to face challenges due to low reaction rates and insufficient product selectivity. In practice, there are still several uncultivated 'lands' for rational design of CO_2RR and NORR catalysts based on MXenes, which remain to be 'ploughed' for reaching the efficiency, stability, and cost needed for industrial applications.

First, most MXene synthesis involves etching the MAX A-layer with hazardous HF or HF substitutes. The wastewater generated during the etching process in very poisonous and caustic, posing a significant environmental risk. As a result, the development of a safe and ecologically acceptable MXene synthesis technique is critical.

Second, it is commonly observed that the active sites of the majority of intrinsic MXenes are typically confined to the edges. Exploring various approaches such as inducing strain, inducing phase change, introducing defects, and functionalizing the inert basal planes, as well as manipulating different morphologies such as vertically oriented 2D materials and flower-shaped structures, hold significant potential in enhancing the efficiency of CO_2RR and NORR. In addition, a great deal of work has been done on Ti-based MXenes, but less work has been done on non-Ti-based, Double-M, and Double-X MXenes for supercapacitor applications.

Third, the existing methodologies for synthesizing MXenes are intricate and predominantly conducted at the microscale. Hence, there is an urgent need for the industrial-scale production and manufacturing of these two-dimensional (2D) materials, ensuring low-cost, repeatability, and high stability, in order to facilitate the commercialization of these catalysts. Several scalable synthesis routes that could be considered include liquid exfoliation, chemical exfoliation, and hydrothermal growth.

Forth, it is crucial to optimize various factors such as catalysts (including composition, size, shape, oxidation state, and crystallographic structure), electrolytes (including cation, anion, concentration, and pH), temperature, pressure, and applied potentials in order to enhance the efficiency of the CO_2RR and NORR processes. In addition, selectivity and FE are still difficult because of the complex response mechanism concerning multiple H/e- steps and competitive aspect reactions. Therefore, beyond the electrochemical performance, the proper selection of electrode to reap energy efficiency want to be looked after. Overall, such MXene catalysts are not industrially viable yet for CO_2RR and NORR due to low yields and conversion efficiencies. Therefore, the immediate challenge of MXenes for CO_2RR and NORR is understanding how to enhance and control the catalytic activities and then scaling up the appropriate catalysts.

To solve such troubles, there may be a need for progressive heterojunctions with improved redox capability and superior interfacial alignments that may provide green and multi-dimensional electrocatalysts with advanced activity, selectivity, and sturdiness. In addition, Interfacial and geometry designs want to be carefully monitored to convey extra balance. Furthermore, the band shape of MXenes has to be measured experimentally as it's far essential to knowledge the MXene's fundamental features, which have no longer been reported. Besides the mechanistic understanding and catalyst development, future research efforts also need to go beyond the catalyst to focus on the surrounding microenvironment to understand how the catalytic site is affected by these other reaction conditions. For example, trace impurities in the electrolyte can deactivate catalytic sites and affect catalyst performance,

while nonaqueous and ionic-liquid electrolyte could increase the CO_2 and N_2 solubility and product selectivity. Therefore, in the future, more extensive research has to be done in the field of cost-effective designing and fabrication of novel MXenes-based catalysts for commercial energy and environmental applications via conversion of CO_2 and NO/NO_x.

CRediT authorship contribution statement

Li Changping: Funding acquisition, Project administration, Supervision. **Abbas Aumber:** Writing – review & editing. **Hussain Ijaz:** Software, Writing – review & editing. **Rashad Muhammad:** Resources, Writing – original draft, Writing – review & editing. **Aldosari Obaid Fahad:** Software, Writing – review & editing. **Sharif Hafiz Muhammad Adeel:** Conceptualization, Data curation, Software, Writing – original draft.

Declaration of Competing Interest

The authors declare that they have no known competing financial interests or personal relationships that could have appeared to influence the work reported in this paper.

Data Availability

Data will be made available on request.

Acknowledgements

Appendix A. Supporting information

Supplementary data associated with this article can be found in the online version at doi:10.1016/j.apcatb.2023.123585.

References

[1] E. Olale, T.O. Ochuodho, V. Lantz, J. El Armali, The environmental Kuznets curve model for greenhouse gas emissions in Canada, J. Clean. Prod. 184 (2018) 859–868, https://doi.org/10.1016/j.jclepro.2018.02.178.

[2] A. Abdullah, A. Ahmed, P. Akhter, A. Razzaq, M. Zafar, M. Hussain, N. Shahzad, K. Majeed, S. Khurrum, M.S.A. Bakar, Y.K. Park, Bioenergy potential and thermochemical characterization of lignocellulosic biomass residues available in Pakistan, Korean J. Chem. Eng. 37 (2020) 1899–1906, https://doi.org/10.1007/s11814-020-0624-0.

[3] H.W. Yen, S.H. Ho, C.Y. Chen, J.S. Chang, CO_2, NOx and SOx removal from flue gas via microalgae cultivation: a critical review, Biotechnol. J. 10 (6) (2015) 829–839, https://doi.org/10.1002/biot.201400707.

[4] F. Cereceda-Balic, M. Toledo, V. Vidal, F. Guerrero, L.A. Diaz-Robles, X. Petit-Breuilh, M. Lapuerta, Emission factors for PM2. 5, CO, CO_2, NOx, SO2 and particle size distributions from the combustion of wood species using a new controlled combustion chamber 3CE, Sci. Total Environ. 584 (2017) 901–910, https://doi.org/10.1016/j.scitotenv.2017.01.136.

[5] D.J. Hofmann, J.H. Butler, E.J. Dlugokencky, J.W. Elkins, K. Masarie, S. A. Montzka, P. Tans, The role of carbon dioxide in climate forcing from 1979 to 2004: introduction of the Annual Greenhouse Gas Index, Tellus B 58 (2006) 614–619, https://doi.org/10.1111/j.1600-0889.2006.00201.x.

[6] R. Cassia, M. Nocioni, N. Correa-Aragunde, L. Lamattina, Climate change and the impact of greenhouse gasses: CO_2 and NO, friends and foes of plant oxidative stress, Front. Plant Sci. 9 (2018), 273, https://doi.org/10.3389/fpls.2018.00273.

[7] H. Qiao, F. Zheng, H. Jiang, K. Dong, The greenhouse effect of the agriculture-economic growth-renewable energy nexus: evidence from G20 countries, Sci. Total Environ. 671 (2019) 722–731, https://doi.org/10.1016/j.scitotenv.2019.03.336.

[8] D.W. Kweku, O. Bismark, A. Maxwell, K.A. Desmond, K.B. Danso, E.A. Oti-Mensah, A.T. Quachie, B.B. Adormaa, Greenhouse effect: greenhouse gases and their impact on global warming, J. Sci. Res. Rep. 17 (6) (2018) 1–9, https://doi.org/10.9734/JSRR/2017/39630.

[9] G.A. Schmidt, R.A. Ruedy, R.L. Miller, A.A. Lacis, Attribution of the present-day total greenhouse effect, J. Geophys. Res.: Atmosph. 115 (D20) (2010), https://doi.org/10.1029/2010JD014287.

[10] F. Joos, G.K. Plattner, T.F. Stocker, O. Marchal, A. Schmittner, Global warming and marine carbon cycle feedbacks on future atmospheric CO2, Science 284 (5413) (1999) 464–467, https://doi.org/10.1126/science.284.5413.464.

[11] B. Ekwurzel, J. Boneham, M.W. Dalton, R. Heede, R.J. Mera, M.R. Allen, P. C. Frumhoff, The rise in global atmospheric CO2, surface temperature, and sea level from emissions traced to major carbon producers, Clim. Change 144 (4) (2017) 579–590, https://doi.org/10.1007/s10584-017-1978-0.

[12] F. Jamil, M. Aslam, A.A.H. Al-Muhtaseb, A. Bokhari, S. Rafiq, Z. Khan, A. Inayat, A. Ahmed, S. Hossain, M.S. Khurram, M.S. Abu Bakar, Greener and sustainable production of bioethylene from bioethanol: current status, opportunities and perspectives, Rev. Chem. Eng. 38 (2) (2022) 185–207, https://doi.org/10.1515/revce-2019-0026.

[13] R.R. Appannagari, Environmental pollution causes and consequences: a study, North Asian Int. Res. J. Soc. Sci. Humanit. 3 (8) (2017) 151–161, https://doi.org/10.3389/fpubh.2020.00014.

[14] G. McCarron, Air Pollution and human health hazards: a compilation of air toxins acknowledged by the gas industry in Queensland's Darling Downs, Int. J. Environ. Stud. 75 (1) (2018) 171–185, https://doi.org/10.1080/00207233.2017.1413221.

[15] K.H. Kim, P. Kumar, J.E. Szulejko, A.A. Adelodun, M.F. Junaid, M. Uchimiya, S. Chambers, Toward a better understanding of the impact of mass transit air pollutants on human health, Chemosphere 174 (2017) 268–279, https://doi.org/10.1016/j.chemosphere.2017.01.113.

[16] P. Aggarwal, S. Jain, Impact of air pollutants from surface transport sources on human health: a modeling and epidemiological approach, Environ. Int. 83 (2015) 146–157, https://doi.org/10.1016/j.envint.2015.06.010.

[17] M. Kargarfard, A. Shariat, B.S. Shaw, I. Shaw, E.T. Lam, A. Kheiri, A. Eatemadyboroujeni, S.B. Tamrin, Effects of polluted air on cardiovascular and hematological parameters after progressive maximal aerobic exercise, Lung 193 (2015) 275–281, https://doi.org/10.1007/s00408-014-9679-1.

[18] S.J. Hall, D. Huber, N.B. Grimm, Soil N2O and NO emissions from an arid, urban ecosystem, J. Geophys. Res.: Biogeosci. 113 (G1) (2008), https://doi.org/10.1029/2007JG000523.

[19] A. Ahmad, M. Ali, A.G. Al-Sehemi, A.A. Al-Ghamdi, J.W. Park, H. Algarni, H. Anwer, Carbon-integrated semiconductor photocatalysts for removal of volatile organic compounds in indoor environments, Chem. Eng. J. 452 (2023), 139436, https://doi.org/10.1016/j.cej.2022.139436.

[20] N.H. Solangi, S.A. Mazari, N.M. Mubarak, R.R. Karri, N. Rajamohan, D.V.N. Vo, Recent trends in MXene-based material for biomedical applications, Environ. Res. (2023), 115337, https://doi.org/10.1016/j.envres.2023.115337.

[21] http://www.osha.gov/dts/sltc/methods/ino rganic/id172/id172.html [accessed 23 December 2014].

[22] F. Normann, K. Andersson, B. Leckner, F. Johnsson, Emission control of nitrogen oxides in the oxy-fuel process, Prog. Energy Combust. Sci. 35 (5) (2009) 385–397, https://doi.org/10.1016/j.pecs.2009.04.002.

[23] A. Gaba, S.F. Iordache, Reduction of air pollution by combustion processes. The Impact of Air Pollution on Health, Economy, Environment and Agricultural Sources, InTech: London UK, 2011, pp. 119–142, https://doi.org/10.5772/16959.

[24] Q. Song, J. Li, L. Wang, Y. Qin, L. Pang, H. Liu, Stable single-atom cobalt as a strong coupling bridge to promote electron transfer and separation in photoelectrocatalysis, J. Catal. 370 (2019) 176–185, https://doi.org/10.1002/aenm.201903802.

[25] X. Li, 2016. Yu JG Wageh S. Al-Ghamdi AA Xie J. Small, 12, pp.6640–6696. https://doi.org/10.1002/smll.201600382.

[26] D.H. Ho, Y.Y. Choi, S.B. Jo, J.M. Myoung, J.H. Cho, Sensing with MXenes: progress and prospects, Adv. Mater. 33 (47) (2021) 2005846, https://doi.org/10.1002/adma.202005846.

[27] J. Jimmy, B. Kandasubramanian, Mxene functionalized polymer composites: synthesis and applications, Eur. Polym. J. 122 (2020) 109367, https://doi.org/10.1016/j.eurpolymj.2019.109367.

[28] J. Yang, W. Bao, P. Jaumaux, S. Zhang, C. Wang, G. Wang, MXene-based composites: synthesis and applications in rechargeable batteries and supercapacitors, Adv. Mater. Interfaces 6 (8) (2019), 1802004, https://doi.org/10.1002/admi.201802004.

[29] P. Kuang, J. Low, B. Cheng, J. Yu, J. Fan, MXene-based photocatalysts, J. Mater. Sci. Technol. 56 (2020) 18–44, https://doi.org/10.1016/j.jmst.2020.02.037.

[30] L. Cheng, X. Li, H. Zhang, Q. Xiang, Two-dimensional transition metal MXene-based photocatalysts for solar fuel generation, J. Phys. Chem. Lett. 10 (12) (2019) 3488–3494, https://doi.org/10.1021/acs.jpclett.9b00736.

[31] Y. Sun, C. Dall'Agnese, C. Zhang, L. Yang, X. Jin, Y. Dall'Agnese, X.F. Wang, Applications of MXenes and their composites in catalysis and photoelectrocatalysis. In *Mxenes and their Composites*, Elsevier, 2022, pp. 449–498, https://doi.org/10.1016/B978-0-12-823361-0.00007-1.

[32] F. Xu, D. Zhang, Y. Liao, G. Wang, X. Shi, H. Zhang, Q. Xiang, Synthesis and photocatalytic H2–production activity of plasma-treated Ti3C2Tx MXene modified graphitic carbon nitride, J. Am. Ceram. Soc. 103 (2) (2020) 849–858, https://doi.org/10.1111/jace.16798.

[33] I. Ihsanullah, Potential of MXenes in water desalination: current status and perspectives, Nano-Micro Lett. 12 (1) (2020) 20, https://doi.org/10.1007/s40820-020-0411-9.

[34] B. Anasori, Û.G. Gogotsi, 2D metal carbides and nitrides (MXenes), Vol. 416, Berlin: Springer, 2019, https://doi.org/10.1038/natrevmats.2016.98.

[35] Y.Y. Wu, T. Bo, J. Zhang, Z. Lu, Z. Wang, Y. Li, B.T. Wang, Novel two-dimensional tetragonal vanadium carbides and nitrides as promising materials for Li-ion batteries, Phys. Chem. Chem. Phys. 21 (35) (2019) 19513–19520, https://doi.org/10.1039/C9CP03954F.

[36] Y. Zhuang, Y. Liu, X. Meng, Fabrication of TiO2 nanofibers/MXene Ti3C2 nanocomposites for photocatalytic H2 evolution by electrostatic self-assembly, Appl. Surf. Sci. 496 (2019), 143647, https://doi.org/10.1016/j.apsusc.2019.143647.

[37] H. Wang, Y. Sun, Y. Wu, W. Tu, S. Wu, X. Yuan, G. Zeng, Z.J. Xu, S. Li, J.W. Chew, Electrical promotion of spatially photoinduced charge separation via interfacial-built-in quasi-alloying effect in hierarchical Zn2In2S5/Ti3C2 (O, OH) x hybrids toward efficient photocatalytic hydrogen evolution and environmental remediation, Appl. Catal. B: Environ. 245 (2019) 290–301, https://doi.org/10.1016/j.apcatb.2018.12.051.

[38] J. Low, L. Zhang, T. Tong, B. Shen, J. Yu, TiO2/MXene Ti3C2 composite with excellent photocatalytic CO2 reduction activity, J. Catal. 361 (2018) 255–266, https://doi.org/10.1002/adfm.201806500.

[39] X. Cheng, L. Zu, Y. Jiang, D. Shi, X. Cai, Y. Ni, S. Lin, Y. Qin, A titanium-based photo-Fenton bifunctional catalyst of mp-MXene/TiO 2– x nanodots for dramatic enhancement of catalytic efficiency in advanced oxidation processes, Chem. Commun. 54 (82) (2018) 11622–11625, https://doi.org/10.1039/C8CC05866K.

[40] H. Huang, Y. Song, N. Li, D. Chen, Q. Xu, H. Li, J. He, J. Lu, One-step in-situ preparation of N-doped TiO2@ C derived from Ti3C2 MXene for enhanced visible-light driven photodegradation, Appl. Catal. B: Environ. 251 (2019) 154–161, https://doi.org/10.1016/j.apcatb.2019.03.066.

[41] Q. Liu, L. Ai, J. Jiang, MXene-derived TiO 2@ C/gC 3 N 4 heterojunctions for highly efficient nitrogen photofixation, J. Mater. Chem. A 6 (9) (2018) 4102–4110, https://doi.org/10.1039/C7TA09350K.

[42] M. Alhabeb, K. Maleski, B. Anasori, P. Lelyukh, L. Clark, S. Sin, Y. Gogotsi, Guidelines for synthesis and processing of two-dimensional titanium carbide (Ti3C2T x MXene), Chem. Mater. 29 (18) (2017) 7633–7644, https://doi.org/10.1021/acs.chemmater.7b02847.

[43] R. Ghamsarizade, B. Ramezanzadeh, H.E. Mohammadloo, A review on recent advances in 2D-transition metal carbonitride-MXenes nano-sheets/polymer composites' electromagnetic shields, mechanical and thermal properties, J. Taiwan Inst. Chem. Eng. 144 (2023), 104740, https://doi.org/10.1016/j.jtice.2023.104740.

[44] J. Peng, X. Chen, W.J. Ong, X. Zhao, N. Li, Surface and heterointerface engineering of 2D MXenes and their nanocomposites: insights into electro-and photocatalysis, Chem 5 (1) (2019) 18–50, https://doi.org/10.1016/j.chempr.2018.08.003.

[45] Z. Liu, T. He, Q. Jiang, W. Wang, J. Tang, A review of heteroatomic doped two-dimensional materials as electrocatalysts for hydrogen evolution reaction, Int. J. Hydrog. Energy 47 (69) (2022) 29698–29729, https://doi.org/10.3390/mi13091499.

[46] Y.R. Kumar, K. Deshmukh, T. Kovářík, S.K. Pasha, A systematic review on 2D materials for volatile organic compound sensing, Coord. Chem. Rev. 461 (2022), 214502, https://doi.org/10.1016/j.ccr.2022.214502.

[47] X. Jiang, A.V. Kuklin, A. Baev, Y. Ge, H. Ågren, H. Zhang, P.N. Prasad, Two-dimensional MXenes: from morphological to optical, electric, and magnetic properties and applications, Phys. Rep. 848 (2020) 1–58, https://doi.org/10.1016/j.physrep.2019.12.006.

[48] A. Mahmood, A. Irfan, J.L. Wang, Machine learning and molecular dynamics simulation-assisted evolutionary design and discovery pipeline to screen efficient small molecule acceptors for PTB7-Th-based organic solar cells with over 15% efficiency, J. Mater. Chem. A 10 (8) (2022) 4170–4180, https://doi.org/10.1039/D1TA09762H.

[49] A. Mahmood, J.L. Wang, A time and resource efficient machine learning assisted design of non-fullerene small molecule acceptors for P3HT-based organic solar cells and green solvent selection, J. Mater. Chem. A 9 (28) (2021) 15684–15695, https://doi.org/10.1039/D1TA04742F.

[50] Y. Yue, N. Liu, Y. Ma, S. Wang, W. Liu, C. Luo, H. Zhang, F. Cheng, J. Rao, X. Hu, J. Su, Highly self-healable 3D microsupercapacitor with MXene–graphene composite aerogel, ACS Nano 12 (5) (2018) 4224–4232, https://doi.org/10.1021/acsnano.7b07528.

[51] M. Okubo, A. Sugahara, S. Kajiyama, A. Yamada, MXene as a charge storage host, Acc. Chem. Res. 51 (3) (2018) 591–599, https://doi.org/10.1021/acs.accounts.7b00481.

[52] H. Wang, Y. Wu, X. Yuan, G. Zeng, J. Zhou, X. Wang, J.W. Chew, Clay-inspired MXene-based electrochemical devices and photo-electrocatalyst: state-of-the-art progresses and challenges, Adv. Mater. 30 (12) (2018), 1704561, https://doi.org/10.1002/adma.201704561.

[53] X. Zhang, J. Lei, D. Wu, X. Zhao, Y. Jing, Z. Zhou, A Ti-anchored Ti 2 CO 2 monolayer (MXene) as a single-atom catalyst for CO oxidation, J. Mater. Chem. A 4 (13) (2016) 4871–4876, https://doi.org/10.1039/C6TA00554C.

[54] X. Zhang, Z. Zhang, J. Li, X. Zhao, D. Wu, Z. Zhou, Ti 2 CO 2 MXene: a highly active and selective photocatalyst for CO 2 reduction, J. Mater. Chem. A 5 (25) (2017) 12899–12903, https://doi.org/10.1039/C7TA03557H.

[55] C.E. Ren, K.B. Hatzell, M. Alhabeb, Z. Ling, K.A. Mahmoud, Y. Gogotsi, Charge-and size-selective ion sieving through Ti3C2T x MXene membranes, J. Phys. Chem. Lett. 6 (20) (2015) 4026–4031, https://doi.org/10.1021/acs.jpclett.5b01895.

[56] B. Xu, M. Zhu, W. Zhang, X. Zhen, Z. Pei, Q. Xue, C. Zhi, P. Shi, Ultrathin MXene-micropattern-based field-effect transistor for probing neural activity, Adv. Mater. 28 (17) (2016) 3333–3339, https://doi.org/10.1002/adma.201504657.

[57] U. Asghar, S. Rafiq, A. Anwar, T. Iqbal, A. Ahmed, F. Jamil, M.S. Khurram, M. M. Akbar, A. Farooq, N.S. Shah, Y.K. Park, Review on the progress in emission control technologies for the abatement of CO2, SOx and NOx from fuel

combustion, J. Environ. Chem. Eng. 9 (5) (2021), 106064, https://doi.org/10.1016/j.jece.2021.106064.

[58] R. Ben-Mansour, M.A. Habib, O.E. Bamidele, M. Basha, N. Qasem, A. A. Peedikakkal, A. Laoui, T, M. Ali, Carbon capture by physical adsorption: materials, experimental investigations and numerical modeling and simulations—a review, Appl. Energy 161 (2016) 225–255, https://doi.org/10.1016/j.apenergy.2015.10.011.

[59] M.R.M. Abu-Zahra, A. Sodiq, P.H.M. Feron, Commercial liquid absorbent-based PCC processes, Absorpt. -Based Post-Combust. Capture Carbon Dioxide (2016) 757–778, https://doi.org/10.1016/B978-0-08-100514-9.00029-9.

[60] C. Nwaoha, T. Supap, R. Idem, C. Saiwan, P. Tontiwachwuthikul, M.J. AL-Marri, A. Benamor, Advancement and new perspectives of using formulated reactive amine blends for post-combustion carbon dioxide (CO₂) capture technologies, Petroleum 3 (1) (2017) 10–36, https://doi.org/10.1016/j.petlm.2016.11.002.

[61] A. Mukherjee, J.A. Okolie, A. Abdelrasoul, C. Niu, A.K. Dalai, Review of post-combustion carbon dioxide capture technologies using activated carbon, J. Environ. Sci. 83 (2019) 46–63, https://doi.org/10.1016/j.jes.2019.03.014.

[62] A.E. Ogungbenro, D.V. Quang, K. Al-Ali, M.R. Abu-Zahra, Activated carbon from date seeds for CO₂ capture applications, Energy Procedia 114 (2017) 2313–2321, https://doi.org/10.1016/j.egypro.2017.03.1370.

[63] S. Salehi, M. Anbia, High CO₂ adsorption capacity and CO₂/CH4 selectivity by nanocomposites of MOF-199, Energy Fuels 31 (5) (2017) 5376–5384, https://doi.org/10.1021/acs.energyfuels.6b03347.

[64] M. Kacem, M. Pellerano, A. Delebarre, Pressure swing adsorption for CO₂/N2 and CO₂/CH4 separation: comparison between activated carbons and zeolites performances, Fuel Process. Technol. 138 (2015) 271–283, https://doi.org/10.1016/j.fuproc.2015.04.032.

[65] R. Ahmed, G. Liu, B. Yousaf, Q. Abbas, H. Ullah, M.U. Ali, Recent advances in carbon-based renewable adsorbent for selective carbon dioxide capture and separation-a review, J. Clean. Prod. 242 (2020) 118409, https://doi.org/10.1016/j.jclepro.2019.118409.

[66] S. Rafiq, L. Deng, M.B. Hägg, Role of facilitated transport membranes and composite membranes for efficient CO₂ capture–a review, ChemBioEng Rev. 3 (2) (2016) 68–85, https://doi.org/10.1002/cben.201500013.

[67] X. He, N. Robertson, A. Jazayeri, A.G. Gasperina, G. Schertler, X. Li, Large scale expression and purification of the rat 5-HT2c receptor, Protein Expr. Purif. 106 (2015) 1–9, https://doi.org/10.1016/j.pep.2014.10.010.

[68] C.H. Yu, C.H. Huang, C.S. Tan, A review of CO₂ capture by absorption and adsorption, Aerosol Air Qual. Res. 12 (5) (2012) 745–769, https://doi.org/10.4209/aaqr.2012.05.0132.

[69] https://books.google.com/books?hl=en&lr=&id=cd_M4kYmn0YC&oi=fnd&pg=PR9&dq=CONTROLTECHNIQUES+FOR+L+NITROGEN+OXIDES+EMISSIONS+FROM+STATIONARY+SOURCE+SECOND+EDITION&ots=B66aX0VFQb&sig=lcl_yOKBFhY7kUWZ28WFpGX00W4

[70] C.E. Baukal, R. Hayes, M. Grant, P. Singh, D. Foote, Nitrogen oxides emissions reduction technologies in the petrochemical and refining industries, Environ. Prog. 23 (1) (2004) 19–28, https://doi.org/10.1002/ep.10000.

[71] M. Kovács, M. Papp, T. Turányi, T. Nagy, A novel active parameter selection strategy for the efficient optimization of combustion mechanisms, Proc. Combust. Inst. (2022), https://doi.org/10.1016/j.pecs.2018.01.002.

[72] Y. Zhang, J. Zhu, Q. Lyu, J. Liu, F. Pan, J. Zhang, The ultra-low NOx emission characteristics of pulverized coal combustion after high temperature preheating, Fuel 277 (2020) 118050, https://doi.org/10.1016/j.fuel.2020.118050.

[73] M. Radojevic, Reduction of nitrogen oxides in flue gases, Environ. Pollut. 102 (1) (1998) 685–689, https://doi.org/10.1016/B978-0-08-043201-4.50097-6.

[74] ⟨https://www.powerblanket.com/wp-content/uploads/2020/01/Selective-Catalytic-Reduction-01-768x436.png⟩.

[75] H.M.A. Sharif, M.B. Asif, Y. Wang, K. Khan, Y. Cai, X. Xiao, C. Li, Construction and elucidation of zerovalent iron@ terephthalic acid/iron oxide catalyst to activate peroxymonosulfate for accelerating and long-lasting NOx removal, Chem. Eng. J. 465 (2023), 142782, https://doi.org/10.1016/j.cej.2023.142782.

[76] H.M.A. Sharif, M. Ali, A. Mahmood, M.B. Asif, M.A.U. Din, M. Sillanpää, A. Mahmood, B. Yang, Separation of Fe from wastewater and its use for NOx reduction; a sustainable approach for environmental remediation, Chemosphere 303 (2022), 135103, https://doi.org/10.1016/j.chemosphere.2022.135103.

[77] A. Yamasaki, An emphasizing doi. org/10.1252/jcej. 36.361. CO₂ sequestration overview of options, CO J. 2 (2003) 361–375, https://doi.org/10.1252/jcej.36.361.

[78] A. Theerthagiri, J. Park, H.T. Das, N. Rahamathulla, E.S. Cardoso, A.P. Murthy, G. Maia, D.V.N. Vo, M.Y. Choi, Electrocatalytic conversion of nitrate waste into ammonia: a review, Environ. Chem. Lett. 20 (5) (2022) 2929–2949, https://doi.org/10.1007/s10311-022-01469-y.

[79] T. Najam, S.S.A. Shah, L. Peng, M.S. Javed, M. Imran, M.Q. Zhao, P. Tsiakaras, Synthesis and nano-engineering of MXenes for energy conversion and storage applications: recent advances and perspectives, Coord. Chem. Rev. 454 (2022), 214339, https://doi.org/10.1016/j.ccr.2021.214339.

[80] J. Liu, L. Mckeon, J. Garcia, S. Pinilla, S. Barwich, M. Möbius, P. Stamenov, J. N. Coleman, V. Nicolosi, Additive manufacturing of Ti3C2–MXene-functionalized conductive polymer hydrogels for electromagnetic-interference shielding, Adv. Mater. 34 (5) (2022), 2106253, https://doi.org/10.1002/adma.202106253.

[81] K. Khan, A.K. Tareen, M. Iqbal, Z. Ye, Z. Xie, A. Mahmood, N. Mahmood, H. Zhang, Recent progress in emerging Novel MXenes based materials and their fascinating sensing applications, Small (2023), 2206147, https://doi.org/10.1002/smll.202206147.

[82] J.X. Yang, W.B. Yu, C.F. Li, W.D. Dong, L.Q. Jiang, N. Zhou, Z.P. Zhuang, J. Liu, Z. Y. Hu, H. Zhao, Y. Li, PtO nanodots promoting Ti3C2 MXene in-situ converted

Ti3C2/TiO2 composites for photocatalytic hydrogen production, Chem. Eng. J. 420 (2021), 129695, https://doi.org/10.1016/j.cej.2021.129695.

[83] M. Sokol, V. Natu, S. Kota, M.W. Barsoum, On the chemical diversity of the MAX phases, Trends Chem. 1 (2) (2019) 210–223, https://doi.org/10.1016/j.trechm.2019.02.016.

[84] A.K. Tareen, K. Khan, M. Iqbal, S. Golovynskyi, Y. Zhang, A. Mahmood, N. Mahmood, J. Long, A. Al-Ghamdi, C. Li, H. Zhang, Recent advances in MXenes: new horizons in biomedical technologies, Mater. Today Chem. 26 (2022), 101205, https://doi.org/10.1016/j.mtchem.2022.101205.

[85] J.N. Coleman, M. Lotya, A. O'Neill, S.D. Bergin, P.J. King, U. Khan, K. Young, A. Gaucher, S. De, R.J. Smith, I.V. Shvets, Two-dimensional nanosheets produced by liquid exfoliation of layered materials, Science 331 (6017) (2011) 568–571, https://doi.org/10.1002/adma.201102306.

[86] M. Naguib, V.N. Mochalin, M.W. Barsoum, Y. Gogotsi, 25th anniversary article: MXenes: a new family of two-dimensional materials, Adv. Mater. 26 (7) (2014) 992–1005, https://doi.org/10.1002/adma.201304138.

[87] W. Hong, B.C. Wyatt, S.K. Nemani, B. Anasori, Double transition-metal MXenes: atomistic design of two-dimensional carbides and nitrides, Mrs Bull. 45 (10) (2020) 850–861, https://doi.org/10.1557/mrs.2020.251.

[88] L. Chen, M. Wakeel, T.U. Haq, N.S. Alharbi, C. Chen, X. Ren, Recent progress in environmental remediation, colloidal behavior and biological effects of MXene: a review, Environ. Sci.: Nano (2022), https://doi.org/10.1039/D2EN00340F.

[89] S. Yu, H. Tang, D. Zhang, S. Wang, M. Qiu, G. Song, D. Fu, B. Hu, X. Wang, MXenes as emerging nanomaterials in water purification and environmental remediation, Sci. Total Environ. 811 (2022), 152280, https://doi.org/10.1016/j.scitotenv.2021.152280.

[90] A.K. Tareen, K. Khan, M. Iqbal, Y. Zhang, J. Long, A. Mahmood, N. Mahmood, Z. Xie, C. Li, H. Zhang, Recent advance in two-dimensional MXenes: new horizons in flexible batteries and supercapacitors technologies, Energy Storage Mater. (2022), https://doi.org/10.1016/j.ensm.2022.09.030.

[91] S.S.A. Shah, T. Najam, M.S. Javed, M.M. Rahman, P. Tsiakaras, Novel Mn-/Co-N x moieties captured in N-doped carbon nanotubes for enhanced oxygen reduction activity and stability in acidic and alkaline media, ACS Appl. Mater. Interfaces 13 (19) (2021) 23191–23200, https://doi.org/10.1021/acsami.1c03477.

[92] S.S. Rameshwar, B. Sivaprakash, N. Rajamohan, B.A. Mohamed, D.V.N. Vo, Remediation of tetracycline pollution using MXene and nano-zero-valent iron materials: a review, Environ. Chem. Lett. 21 (5) (2023) 2995–3022, https://doi.org/10.1007/s10311-023-01623-0.

[93] S.S.A. Shah, T. Najam, M.K. Aslam, M. Ashfaq, M.M. Rahman, K. Wang, P. Tsiakaras, S. Song, Y. Wang, Recent advances on oxygen reduction electrocatalysis: correlating the characteristic properties of metal organic frameworks and the derived nanomaterials, Appl. Catal. B: Environ. 268 (2020), 118570, https://doi.org/10.1016/j.apcatb.2019.118570.

[94] Y.T. Liu, P. Zhang, N. Sun, B. Anasori, Q.Z. Zhu, H. Liu, Y. Gogotsi, B. Xu, Self-assembly of transition metal oxide nanostructures on MXene nanosheets for fast and stable lithium storage, Adv. Mater. 30 (23) (2018), 1707334, https://doi.org/10.1002/adma.201707334.

[95] Z.M. Sun, Progress in research and development on MAX phases: a family of layered ternary compounds, Int. Mater. Rev. 56 (3) (2011) 143–166, https://doi.org/10.1179/1743280410Y.0000000001.

[96] J. Zhou, X. Zha, X. Zhou, F. Chen, G. Gao, S. Wang, C. Shen, T. Chen, C. Zhi, P. Eklund, S. Du, Synthesis and electrochemical properties of two-dimensional hafnium carbide, ACS Nano 11 (4) (2017) 3841–3850, https://doi.org/10.1021/acsnano.7b00030.

[97] M. Ghidiu, M.R. Lukatskaya, M.Q. Zhao, Y. Gogotsi, M.W. Barsoum, Conductive two-dimensional titanium carbide 'clay' with high volumetric capacitance, Nature 516 (7529) (2014) 78–81, https://doi.org/10.1038/nature13970.

[98] L. Verger, V. Natu, M. Carey, M.W. Barsoum, MXenes: an introduction of their synthesis, select properties, and applications, Trends Chem. 1 (7) (2019) 656–669, https://doi.org/10.1016/j.trechm.2019.04.006.

[99] M. Liu, G. Zeng, K. Wang, Q. Wan, L. Tao, X. Zhang, Y. Wei, Recent developments in polydopamine: an emerging soft matter for surface modification and biomedical applications, Nanoscale 8 (38) (2016) 16819–16840, https://doi.org/10.1039/C5NR09078D.

[100] S.M. Eichfeld, L. Hossain, Y.C. Lin, A.F. Piasecki, B. Kupp, A.G. Birdwell, R. A. Burke, N. Lu, X. Peng, J. Li, A. Azcatl, Highly scalable, atomically thin WSe2 grown via metal–organic chemical vapor deposition, ACS Nano 9 (2) (2015) 2080–2087, https://doi.org/10.1021/nn5073286.

[101] H. Deng, L. Deng, L. Yang, H. Wu, H. Zhang, C. Zhou, B. Liu, Z. Shi, Novel Prussian blue analogues@ MXene nanocomposite as heterogeneous activator of peroxymonosulfate for the degradation of coumarin: The nonnegligible role of Lewis-acid sites on MXene, Chem. Eng. J. 416 (2021), 128071, https://doi.org/10.1016/j.cej.2020.128071.

[102] Y. Li, C. Pan, C. Kamdem, X.J. Jin, Binder-free two-dimensional MXene/acid activated carbon for high-performance supercapacitors and methylene blue adsorption, Energy Fuels 34 (8) (2020) 10120–10130, https://doi.org/10.1021/acs.energyfuels.0c01352.

[103] C. Wang, R. Cheng, P.X. Hou, Y. Ma, A. Majeed, X. Wang, C. Liu, MXene-carbon nanotube hybrid membrane for robust recovery of Au from trace-level solution, ACS Appl. Mater. Interfaces 12 (38) (2020) 43032–43041, https://doi.org/10.1021/acsami.0c09310.

[104] Y. Ma, X. Lv, D. Xiong, X. Zhao, Z. Zhang, Catalytic degradation of ranitidine using novel magnetic Ti3C2-based MXene nanosheets modified with nanoscale zero-valent iron particles, Appl. Catal. B: Environ. 284 (2021) 119720, https://doi.org/10.1016/j.apcatb.2020.119720.

[105] S. Wang, L. Wang, Z. Li, P. Zhang, K. Du, L. Yuan, S. Ning, Y. Wei, W. Shi, Highly efficient adsorption and immobilization of U (VI) from aqueous solution by alkalized MXene-supported nanoscale zero-valent iron, J. Hazard. Mater. 408 (2021), 124949, https://doi.org/10.1016/j.jhazmat.2020.124949.

[106] X. Feng, Z. Yu, R. Long, X. Li, L. Shao, H. Zeng, G. Zeng, Y. Zuo, Self-assembling 2D/2D (MXene/LDH) materials achieve ultra-high adsorption of heavy metals Ni2+ through terminal group modification, Sep. Purif. Technol. 253 (2020), 117525, https://doi.org/10.1016/j.seppur.2020.117525.

[107] H. Li, Y. Wen, X. Zhu, J. Wang, L. Zhang, B. Sun, Novel heterostructure of a MXene@ NiFe-LDH nanohybrid with superior peroxidase-like activity for sensitive colorimetric detection of glutathione, ACS Sustain. Chem. Eng. 8 (1) (2019) 520–526, https://doi.org/10.1021/acssuschemeng.9b05987.

[108] Y. Li, P. Kamdem, X.J. Jin, A freeze-and-thaw-assisted approach to fabricate MXene/ZIF-8 composites for high-performance supercapacitors and methylene blue adsorption, J. Electrochem. Soc. 167 (11) (2020), 110562 https://iopscience.iop.org/article/10.1149/1945-7111/aba934/meta.

[109] Y. Wu, X. Li, Q. Yang, D. Wang, F. Yao, J. Cao, Z. Chen, X. Huang, Y. Yang, X. Li, Mxene-modulated dual-heterojunction generation on a metal-organic framework (MOF) via surface constitution reconstruction for enhanced photocatalytic activity, Chem. Eng. J. 390 (2020), 124519, https://doi.org/10.1016/j.cej.2020.124519.

[110] J. Chen, H. Zheng, Y. Zhao, M. Que, W. Wang, X. Lei, Morphology and photocatalytic activity of TiO2/MXene composites by in-situ solvothermal method, Ceram. Int. 46 (12) (2020) 20088–20096, https://doi.org/10.1016/j.ceramint.2020.05.083.

[111] Y. Zhou, M. Yu, H. Liang, J. Chen, L. Xu, J. Niu, Novel dual-effective Z-scheme heterojunction with g-C3N4, Ti3C2 MXene and black phosphorus for improving visible light-induced degradation of ciprofloxacin, Appl. Catal. B: Environ. 291 (2021), 120105, https://doi.org/10.1016/j.apcatb.2021.120105.

[112] Y. Cui, M. Liu, H. Huang, D. Zhang, J. Chen, L. Mao, N. Zhou, F. Deng, X. Zhang, Y. Wei, A novel one-step strategy for preparation of Fe3O4-loaded Ti3C2 MXenes with high efficiency for removal organic dyes, Ceram. Int. 46 (8) (2020) 11593–11601, https://doi.org/10.1016/j.ceramint.2020.01.188.

[113] C. Zhu, J.X. Liang, Y.G. Wang, J. Li, Non-noble metal single-atom catalyst with MXene support: Fe1/Ti2CO2 for CO oxidation, Chin. J. Catal. 43 (7) (2022) 1830–1841, https://doi.org/10.1016/S1872-2067(21)64027-5.

[114] Y. Zhang, Z. Cui, B. Sa, N. Miao, J. Zhou, Z. Sun, Computational design of double transition metal MXenes with intrinsic magnetic properties, Nanoscale Horiz. 7 (3) (2022) 276–287, https://doi.org/10.1039/D1NH00621E.

[115] H. Kim, H.N. Alshareef, MXetronics: MXene-enabled electronic and photonic devices, ACS Mater. Lett. 2 (1) (2019) 55–70, https://doi.org/10.1021/acsmaterialslett.9b00419.

[116] B. Anasori, J. Halim, J. Lu, C.A. Voigt, L. Hultman, M.W. Barsoum, Mo2TiAlC2: a new ordered layered ternary carbide, Scr. Mater. 101 (2015) 5–7, https://doi.org/10.1016/j.scriptamat.2014.12.024.

[117] I. Persson, A. El Ghazaly, Q. Tao, J. Halim, S. Kota, V. Darakchieva, J. Palisaitis, M.W. Barsoum, J. Rosen, P.O. Persson, Tailoring structure, composition, and energy storage properties of MXenes from selective etching of in-plane, chemically ordered MAX phases, Small 14 (17) (2018), 1703676, https://doi.org/10.1002/smll.201703676.

[118] B. Anasori, Y. Xie, M. Beidaghi, J. Lu, B.C. Hosler, L. Hultman, P.R. Kent, Y. Gogotsi, M.W. Barsoum, Two-dimensional, ordered, double transition metals carbides (MXenes), ACS Nano 9 (10) (2015) 9507–9516, https://doi.org/10.1021/acsnano.5b03591.

[119] J. Yang, M. Naguib, M. Ghidiu, L.M. Pan, J. Gu, J. Nanda, J. Halim, Y. Gogotsi, M. W. Barsoum, Two-dimensional Nb-based M4C3 solid solutions (MXenes), J. Am. Ceram. Soc. 99 (2) (2016) 660–666, https://doi.org/10.1111/jace.13922.

[120] H. Gao, R. Shi, Y. Liu, Y. Zhu, J. Zhang, L. Li, X. Hu, Facet-dependent catalytic activity of two-dimensional Ti3C2Tx MXene on hydrogen storage performance of MgH2, J. Magnes. Alloy. (2022), https://doi.org/10.1016/j.jma.2022.02.006.

[121] I. Persson, A. El Ghazaly, Q. Tao, J. Halim, S. Kota, V. Darakchieva, J. Palisaitis, M.W. Barsoum, J. Rosen, P.O. Persson, Tailoring structure, composition, and energy storage properties of MXenes from selective etching of in-plane, chemically ordered MAX phases, Small 14 (17) (2018), 1703676, https://doi.org/10.1002/smll.201703676.

[122] X. Liang, Y. Rangom, C.Y. Kwok, Q. Pang, L.F. Nazar, Interwoven MXene nanosheet/carbon-nanotube composites as Li–S cathode hosts, Adv. Mater. 29 (3) (2017), 1603040, https://doi.org/10.1002/adma.201603040.

[123] X. Tang, X. Guo, W. Wu, G. Wang, 2D metal carbides and nitrides (MXenes) as high-performance electrode materials for Lithium-based batteries, Adv. Energy Mater. 8 (33) (2018), 1801897, https://doi.org/10.1002/aenm.201801897.

[124] Q. Tao, J. Lu, M. Dahlqvist, A. Mockute, S. Calder, A. Petruhins, R. Meshkian, O. Rivin, D. Potashnikov, E.A.N. Caspi, H. Shaked, Atomically layered and ordered rare-earth i-MAX phases: a new class of magnetic quaternary compounds, Chem. Mater. 31 (7) (2019) 2476–2485, https://doi.org/10.1021/acs.chemmater.8b05298.

[125] Q. Zhao, C. Zhang, R. Hu, Z. Du, J. Gu, Y. Cui, X. Chen, W. Xu, Z. Cheng, S. Li, B. Li, Selective etching quaternary MAX phase toward single atom copper immobilized MXene (Ti3C2Cl x) for efficient CO2 electroreduction to methanol, ACS nano 15 (3) (2021) 4927–4936Z, https://doi.org/10.1021/acsnano.0c09755.

[126] M. Khazaei, M. Arai, T. Sasaki, A. Ranjbar, Y. Liang, S. Yunoki, OH-terminated two-dimensional transition metal carbides and nitrides as ultralow work function materials, Phys. Rev. B 92 (7) (2015), 075411, https://doi.org/10.1103/PhysRevB.92.075411.

[127] Liu, Y., Xiao, H. and Goddard I.I.I., W.A., 2016. Schottky-barrier-free contacts with two-dimensional semiconductors by surface-engineered MXenes. Journal of the American Chemical Society, 138(49), pp.15853–15856. https://doi.org/10.1021/jacs.6b10834.

[128] Y. Xie, P.R.C. Kent, Hybrid density functional study of structural and electronic properties of functionalized Ti n+ 1 X n (X= C, N) monolayers, Phys. Rev. B 87 (23) (2013), 235441 https://journals.aps.org/prb/abstract/10.1103/PhysRevB.87.235441.

[129] P. Li, J. Zhu, A.D. Handoko, R. Zhang, H. Wang, D. Legut, X. Wen, Z. Fu, Z.W. Seh, Q. Zhang, High-throughput theoretical optimization of the hydrogen evolution reaction on MXenes by transition metal modification, J. Mater. Chem. A 6 (10) (2018) 4271–4278, https://doi.org/10.1039/C8TA00173A.

[130] V.M.H. Ng, H. Huang, K. Zhou, P.S. Lee, W. Que, J.Z. Xu, L.B. Kong, Recent progress in layered transition metal carbides and/or nitrides (MXenes) and their composites: synthesis and applications, J. Mater. Chem. A 5 (7) (2017) 3039–3068, https://doi.org/10.1039/C6TA06772G.

[131] I.R. Shein, A.L. Ivanovskii, Graphene-like titanium carbides and nitrides Tin+ 1Cn, Tin+ 1Nn (n= 1, 2, and 3) from de-intercalated MAX phases: first-principles probing of their structural, electronic and relative stability, Comput. Mater. Sci. 65 (2012) 104–114, https://doi.org/10.1016/j.commatsci.2012.07.011.

[132] Q. Tang, Z. Zhou, P. Shen, Are MXenes promising anode materials for Li ion batteries? Computational studies on electronic properties and Li storage capability of Ti3C2 and Ti3C2X2 (X= F, OH) monolayer, J. Am. Chem. Soc. 134 (40) (2012) 16909–16916, https://doi.org/10.1021/ja308463r.

[133] A.N. Enyashin, A.L. Ivanovskii, Two-dimensional titanium carbonitrides and their hydroxylated derivatives: structural, electronic properties and stability of MXenes Ti3C2− xNx (OH) 2 from DFTB calculations, J. Solid State Chem. 207 (2013) 42–48, https://doi.org/10.1016/j.jssc.2013.09.010.

[134] S.N. Mishra, Electronic structure and magnetic properties of dilute Cr alloys with transition-metal impurities, Phys. Rev. B 77 (22) (2008), 224402 https://journals.aps.org/prb/abstract/10.1103/PhysRevB.77.224402.

[135] Lane, N.J., Barsoum, M.W. and Rondinelli, J.M., 2013. Correlation effects and spin-orbit interactions in two-dimensional hexagonal 5d transition metal carbides, Tan+ 1Cn (n= 1, 2, 3). Europhysics Letters, 101(5), p.57004. https://iopscience.iop.org/article/10.1209/0295-5075/101/57004/meta.

[136] K. Kannan, M.H. Sliem, A.M. Abdullah, K.K. Sadasivuni, B. Kumar, Fabrication of ZnO-Fe-MXene based nanocomposites for efficient CO2 reduction, Catalysts 10 (5) (2020) 549, https://doi.org/10.3390/catal10050549.

[137] M. Khazaei, M. Arai, T. Sasaki, C.Y. Chung, N.S. Venkataramanan, M. Estili, Y. Sakka, Y. Kawazoe, Novel electronic and magnetic properties of two-dimensional transition metal carbides and nitrides, Adv. Funct. Mater. 23 (17) (2013) 2185–2192, https://doi.org/10.1002/adfm.201202502.

[138] M. Kurtoglu, M. Naguib, Y. Gogotsi, M.W. Barsoum, First principles study of two-dimensional early transition metal carbides, Mrs Commun. 2 (2012) 133–137, https://doi.org/10.1557/mrc.2012.25.

[139] H. Lashgari, M.R. Abolhassani, A. Boochani, S.M. Elahi, J. Khodadadi, Electronic and optical properties of 2D graphene-like compounds titanium carbides and nitrides: DFT calculations, Solid State Commun. 195 (2014) 61–69, https://doi.org/10.1016/j.ssc.2014.06.008.

[140] A.N. Enyashin, A.L. Ivanovskii, Structural and electronic properties and stability of MX enes Ti2C and Ti3C2 functionalized by methoxy groups, J. Phys. Chem. C. 117 (26) (2013) 13637–13643, https://doi.org/10.1021/jp401820b.

[141] Y. Lee, S.B. Cho, Y.C. Chung, Tunable indirect to direct band gap transition of monolayer Sc2CO2 by the strain effect, ACS Appl. Mater. Interfaces 6 (16) (2014) 14724–14728, https://doi.org/10.1021/am504233d.

[142] Y. Lee, Y. Hwang, S.B. Cho, Y.C. Chung, Achieving a direct band gap in oxygen functionalized-monolayer scandium carbide by applying an electric field, Phys. Chem. Chem. Phys. 16 (47) (2014) 26273–26278, https://doi.org/10.1039/C4CP03811H.

[143] M. Han, K. Maleski, C.E. Shuck, Y. Yang, J.T. Glazar, A.C. Foucher, K. Hantanasirisakul, A. Sarycheva, N.C. Frey, S.J. May, V.B. Shenoy, Tailoring electronic and optical properties of MXenes through forming solid solutions, J. Am. Chem. Soc. 142 (45) (2020) 19110–19118, https://doi.org/10.1021/jacs.0c07395.

[144] Y. Gogotsi, B. Anasori, The rise of MXenes, ACS Nano 13 (8) (2019) 8491–8494, https://doi.org/10.1021/acsnano.9b06394.

[145] M. Dahlqvist, J. Rosen, Predictive theoretical screening of phase stability for chemical order and disorder in quaternary 312 and 413 MAX phases, Nanoscale 12 (2) (2020) 785–794, https://doi.org/10.1039/C9NR08675G.

[146] K. Eid, Q. Lu, S. Abdel-Azeim, A. Soliman, A.M. Abdullah, A.M. Abdelgwad, R. P. Forbes, K.I. Ozoemena, R.S. Varma, M.F. Shibl, Highly exfoliated Ti 3C 2 T x MXene nanosheets atomically doped with Cu for efficient electrochemical CO2 reduction: An experimental and theoretical study, J. Mater. Chem. A 10 (4) (2022) 1965–1975, https://doi.org/10.1039/D1TA09471H.

[147] N. Li, J. Peng, Z. Shi, P. Zhang, X. Li, Charge transfer and orbital reconstruction of non-noble transition metal single-atoms anchored on Ti2CTx-MXenes for highly selective CO2 electrochemical reduction, Chin. J. Catal. 43 (7) (2022) 1906–1917, https://doi.org/10.1016/S1872-2067(21)64018-4.

[148] Y.H. Chen, M.Y. Qi, Y.H. Li, Z.R. Tang, T. Wang, J. Gong, Y.J. Xu, Activating two-dimensional Ti3C2Tx-MXene with single-atom cobalt for efficient CO2 photoreduction, Cell Rep. Phys. Sci. 2 (3) (2021), https://doi.org/10.1016/j.xcrp.2021.100371.

[149] J. Su, Y. Liu, Y. Song, L. Huang, W. Guo, X. Cao, Y. Dou, L. Cheng, G. Li, Q. Hu, R. Ye, Recent development of nanomaterials for carbon dioxide electroreduction, SmartMat 3 (1) (2022) 35–53, https://doi.org/10.1002/smm2.1106.

[150] B. Wang, S. Chen, Z. Zhang, D. Wang, Low-dimensional material supported single-atom catalysts for electrochemical CO_2 reduction, SmartMat 3 (1) (2022) 84–110, https://doi.org/10.1002/smm2.1101.

[151] K.P. Kuhl, T. Hatsukade, E.R. Cave, D.N. Abram, J. Kibsgaard, T.F. Jaramillo, Electrocatalytic conversion of carbon dioxide to methane and methanol on transition metal surfaces, J. Am. Chem. Soc. 136 (40) (2014) 14107–14113, https://doi.org/10.1021/ja505791r.

[152] R. Kortlever, J. Shen, K.J.P. Schouten, F. Calle-Vallejo, M.T. Koper, Catalysts and reaction pathways for the electrochemical reduction of carbon dioxide, J. Phys. Chem. Lett. 6 (20) (2015) 4073–4082, https://doi.org/10.1021/acs.jpclett.5b01559.

[153] A. Nikokavoura, C. Trapalis, Alternative photocatalysts to TiO2 for the photocatalytic reduction of CO_2, Appl. Surf. Sci. 391 (2017) 149–174, https://doi.org/10.1016/j.apsusc.2016.06.172.

[154] S.S.A. Shah, T. Najam, M. Wen, S.Q. Zang, A. Waseem, H.L. Jiang, Metal–organic framework-based electrocatalysts for CO_2 reduction, Small Struct. 3 (5) (2022), 2100090, https://doi.org/10.1002/sstr.202100090.

[155] J. Li, M. Zhang, Q. Li, J. Yang, Enhanced visible light activity on direct contact Z-scheme g-C3N4-TiO2 photocatalyst, Appl. Surf. Sci. 391 (2017) 184–193, https://doi.org/10.1016/j.apsusc.2016.06.145.

[156] M. Tahir, B. Tahir, N.A.S. Amin, H. Alias, Selective photocatalytic reduction of CO_2 by H2O/H2 to CH4 and CH3OH over Cu-promoted In2O3/TiO2 nanocatalyst, Appl. Surf. Sci. 389 (2016) 46–55, https://doi.org/10.1016/j.apsusc.2016.06.155.

[157] Z. Xiong, Z. Lei, C.C. Kuang, X. Chen, B. Gong, Y. Zhao, J. Zhang, C. Zheng, J.C. Wu, Selective photocatalytic reduction of CO_2 into CH4 over Pt-Cu2O TiO2 nanocrystals: the interaction between Pt and Cu2O cocatalysts, Appl. Catal. B: Environ. 202 (2017) 695–703, https://doi.org/10.1016/j.apcatb.2016.10.001.

[158] S. Bera, J.E. Lee, S.B. Rawal, W.I. Lee, Size-dependent plasmonic effects of Au and Au@ SiO2 nanoparticles in photocatalytic CO_2 conversion reaction of Pt/TiO2, Appl. Catal. B: Environ. 199 (2016) 55–63, https://doi.org/10.1016/j.apcatb.2016.06.025.

[159] P.N. Paulino, V.M.M. Salim, N.S. Resende, Zn-Cu promoted TiO2 photocatalyst for CO_2 reduction with H2O under UV light, Appl. Catal. B: Environ. 185 (2016) 362–370, https://doi.org/10.1016/j.apcatb.2015.12.037.

[160] H. Assad, I. Fatma, A. Kumar, S. Kaya, D.V.N. Vo, A. Al-Gheethi, A. Sharma, An overview of MXene-Based nanomaterials and their potential applications towards hazardous pollutant adsorption, Chemosphere 298 (2022), 134221, https://doi.org/10.1016/j.chemosphere.2022.134221.

[161] J. Low, J. Yu, W. Ho, Graphene-based photocatalysts for CO_2 reduction to solar fuel, J. Phys. Chem. Lett. 6 (21) (2015) 4244–4251, https://doi.org/10.1021/acs.jpclett.5b01610.

[162] S. Kawamura, H. Zhang, M. Tamba, T. Kojima, M. Miyano, Y. Yoshida, M. Yoshiba, Y. Izumi, Efficient volcano-type dependence of photocatalytic CO_2 conversion into methane using hydrogen at reaction pressures up to 0.80 MPa, J. Catal. 345 (2017) 39–52, https://doi.org/10.1016/j.jcat.2016.10.024.

[163] J. Heo, N. Her, M. Jang, C.M. Park, A. Son, J. Han, Y. Yoon, Photocatalytic and electrocatalytic reduction of CO_2 by MXene-based nanomaterials: a review, Crit. Rev. Environ. Sci. Technol. 53 (9) (2023) 987–1008, https://doi.org/10.1080/10643389.2022.2101857.

[164] B.M. Jun, S. Kim, J. Heo, C.M. Park, N. Her, M. Jang, Y. Huang, J. Han, Y. Yoon, Review of MXenes as new nanomaterials for energy storage/delivery and selected environmental applications, Nano Res. 12 (2019) 471–487, https://doi.org/10.1007/s12274-018-2225-3.

[165] J. Hu, J. Ding, Q. Zhong, Ultrathin 2D Ti3C2 MXene Co-catalyst anchored on porous g-C3N4 for enhanced photocatalytic CO_2 reduction under visible-light irradiation, J. Colloid Interface Sci. 582 (2021) 647–657, https://doi.org/10.1016/j.jcis.2020.08.047.

[166] Z. Wu, C. Li, Z. Li, K. Feng, M. Cai, D. Zhang, S. Wang, M. Chu, C. Zhang, J. Shen, Z. Huang, Niobium and titanium carbides (MXenes) as superior photothermal supports for CO_2 photocatalysis, ACS nano 15 (3) (2021) 5696–5705, https://doi.org/10.1021/acsnano.1c00990.

[167] S.D. Chakraborty, P. Bhattacharya, T. Mishra, Recent advances in 2D MXene-based heterostructured photocatalytic materials, Sustain. Mater. Solut. Sol. Energy Technol. (2021) 329–362, https://doi.org/10.1016/B978-0-12-821592-0.00005-4.

[168] Z. Li, N.H. Attanayake, J.L. Blackburn, E.M. Miller, Carbon dioxide and nitrogen reduction reactions using 2D transition metal dichalcogenide (TMDC) and carbide/nitride (MXene) catalysts, Energy Environ. Sci. 14 (12) (2021) 6242–6286, https://doi.org/10.1039/D1EE03211A.

[169] A. Sreedhar, I.N. Reddy, J.S. Noh, Photocatalytic and electrocatalytic reduction of CO_2 and N2 by Ti3C2 MXene supported composites for a cleaner environment: a review, J. Clean. Prod. 328 (2021), 129647, https://doi.org/10.1016/j.jclepro.2021.129647.

[170] Q. Zhong, Y. Li, G. Zhang, Two-dimensional MXene-based and MXene-derived photocatalysts: recent developments and perspectives, Chem. Eng. J. 409 (2021), 128099, https://doi.org/10.1016/j.cej.2020.128099.

[171] W. Chen, B. Han, Y. Xie, S. Liang, H. Deng, Z. Lin, Ultrathin Co-Co LDHs nanosheets assembled vertically on MXene: 3D nanoarrays for boosted visible-light-driven CO_2 reduction, Chem. Eng. J. 391 (2020), 123519, https://doi.org/10.1016/j.cej.2019.123519.

[172] S.S.A. Shah, M.S. Javed, T. Najam, C. Molochas, N.A. Khan, M.A. Nazir, M. Xu, P. Tsiakaras, S.J. Bao, Metal oxides for the electrocatalytic reduction of carbon dioxide: mechanism of active sites, composites, interface and defect engineering strategies, Coord. Chem. Rev. 471 (2022), 214716, https://doi.org/10.1016/j.ccr.2022.214716.

[173] A. Ali Khan, M. Tahir, Construction of an S-scheme heterojunction with oxygen-vacancy-rich trimetallic CoAlLa-LDH anchored on titania-sandwiched Ti3C2 multilayers for boosting photocatalytic CO_2 reduction under visible light, Ind. Eng. Chem. Res. 60 (45) (2021) 16201–16223, https://doi.org/10.1021/acs.iecr.1c03242.

[174] J. Low, L. Zhang, T. Tong, B. Shen, J. Yu, TiO2/MXene Ti3C2 composite with excellent photocatalytic CO_2 reduction activity, J. Catal. 361 (2018) 255–266, https://doi.org/10.1016/j.jcat.2018.03.009.

[175] T.N. Huan, N. Ranjbar, G. Rousse, M. Sougrati, A. Zitolo, V. Mougel, F. Jaouen, M. Fontecave, Electrochemical reduction of CO_2 catalyzed by Fe-NC materials: a structure–selectivity study, ACS Catal. 7 (3) (2017) 1520–1525, https://doi.org/10.1021/acscatal.6b03353.

[176] T. Amrillah, A.R. Supandi, V. Puspasari, A. Hermawan, Z.W. Seh, MXene-based photocatalysts and electrocatalysts for CO_2 conversion to chemicals, Trans. Tianjin Univ. 28 (4) (2022) 307–322, https://doi.org/10.1007/s12209-022-00328-9.

[177] T.P. Nguyen, D.M.T. Nguyen, H.K. Le, D.V.N. Vo, S.S. Lam, R.S. Varma, M. Shokouhimehr, C.C. Nguyen, Q. Van Le, MXenes: Applications in electrocatalytic, photocatalytic hydrogen evolution reaction and CO_2 reduction, Mol. Catal. 486 (2020), 110850, https://doi.org/10.1016/j.mcat.2020.110850.

[178] J. Shen, Z. Wu, C. Li, C. Zhang, A. Genest, G. Rupprechter, L. He, Emerging applications of MXene materials in CO_2 photocatalysis, FlatChem 28 (2021), 100252, https://doi.org/10.1016/j.flatc.2021.100252.

[179] S. Cao, B. Shen, T. Tong, J. Fu, J. Yu, 2D/2D heterojunction of ultrathin MXene/Bi2WO6 nanosheets for improved photocatalytic CO_2 reduction, Adv. Funct. Mater. 28 (21) (2018), 1800136, https://doi.org/10.1002/adfm.201800136.

[180] Q. Zhu, Y. Cui, Y. Zhang, Z. Cao, Y. Shi, J. Gu, Z. Du, B. Li, S. Yang, Strategies for engineering the MXenes toward highly active catalysts, Mater. Today Nano 13 (2021), 100104, https://doi.org/10.1016/j.mtnano.2020.100104.

[181] X. Luo, Y. Guo, F. Ding, H. Zhao, G. Cui, H. Li, C. Wang, Significant improvements in CO_2 capture by pyridine-containing anion-functionalized ionic liquids through multiple-site cooperative interactions, Angew. Chem. 126 (27) (2014) 7173–7177, https://doi.org/10.1002/anie.201400957.

[182] B. Wang, A. Zhou, F. Liu, J. Cao, L. Wang, Q. Hu, Carbon dioxide adsorption of two-dimensional carbide MXenes, J. Adv. Ceram. 7 (2018) 237–245, https://doi.org/10.1007/s40145-018-0275-3.

[183] Z. Li, Y. Cui, Z. Wu, C. Milligan, L. Zhou, G. Mitchell, B. Xu, E. Shi, J.T. Miller, F.H. Ribeiro, Y. Wu, Reactive metal–support interactions at moderate temperature in two-dimensional niobium-carbide-supported platinum catalysts, Nat. Catal. 1 (5) (2018) 349–355, https://doi.org/10.1038/s41929-018-0067-8.

[184] Z. Li, L. Yu, C. Milligan, T. Ma, L. Zhou, Y. Cui, Z. Qi, N. Libretto, B. Xu, J. Luo, E. Shi, Two-dimensional transition metal carbides as supports for tuning the chemistry of catalytic nanoparticles, Nat. Commun. 9 (1) (2018), 5258, https://doi.org/10.1038/s41467-018-07502-5.

[185] B. Govindan, R. Madhu, M. Abu Haija, F.V. Kusmartsev, F. Banat, Pd-decorated 2D MXene (2D Ti3C2Tix) as a high-performance electrocatalyst for reduction of carbon dioxide into fuels toward climate change mitigation, Catalysts 12 (10) (2022) 1180, https://doi.org/10.3390/catal12101180.

[186] X. Jiang, J. Wang, T. Huang, G. Fu, Y. Tang, X. Qiu, J. Zhou, J.M. Lee, Sub-5 nm palladium nanoparticles in situ embedded in N-doped carbon nanoframes: facile synthesis, excellent sinter resistance and electrocatalytic properties, J. Mater. Chem. A 7 (46) (2019) 26243–26249, https://doi.org/10.1039/C9TA11097F.

[187] Y. Cao, Q. Deng, Z. Liu, D. Shen, T. Wang, Q. Huang, S. Du, N. Jiang, C.T. Lin, J. Yu, Enhanced thermal properties of poly (vinylidene fluoride) composites with ultrathin nanosheets of MXene, RSC Adv. 7 (33) (2017) 20494–20501, https://doi.org/10.1039/C7RA00184C.

[188] Q.X. Xia, J. Fu, J.M. Yun, R.S. Mane, K.H. Kim, High volumetric energy density annealed-MXene-nickel oxide/MXene asymmetric supercapacitor, RSC Adv. 7 (18) (2017) 11000–11011, https://doi.org/10.1039/C6RA27880A.

[189] M. Hu, T. Hu, Z. Li, Y. Yang, R. Cheng, J. Yang, C. Cui, X. Wang, Surface functional groups and interlayer water determine the electrochemical capacitance of Ti3C2 T x MXene, ACS Nano 12 (4) (2018) 3578–3586, https://doi.org/10.1021/acsnano.8b00676.

[190] G. Fan, X. Li, C. Xu, W. Jiang, Y. Zhang, D. Gao, J. Bi, Y. Wang, Palladium supported on titanium carbide: A highly efficient, durable, and recyclable bifunctional catalyst for the transformation of 4-chlorophenol and 4-nitrophenol, Nanomaterials 8 (3) (2018) 141, https://doi.org/10.3390/nano8030141.

[191] L. Zhang, P. Ma, L. Dai, Z. Bu, X. Li, W. Yu, Y. Cao, J. Guan, Removal of pollutants via synergy of adsorption and photocatalysis over MXene-based nanocomposites, Chem. Eng. J. Adv. 10 (2022), 100285, https://doi.org/10.1016/j.ceja.2022.100285.

[192] M. Halmann, Photoelectrochemical reduction of aqueous carbon dioxide on p-type gallium phosphide in liquid junction solar cells, Nature 275 (5676) (1978) 115–116, https://doi.org/10.1038/275115a0.

[193] F. Liang, K. Zhang, L. Zhang, Y. Zhang, Y. Lei, X. Sun, Recent development of electrocatalytic CO_2 reduction application to energy conversion, Small 17 (44) (2021), 2100323, https://doi.org/10.1002/smll.202100323.

[194] H. Jiang, Y. Zhao, L. Wang, Y. Kong, F. Li, P. Li, Electrochemical CO_2 reduction to formate on Tin cathode: influence of anode materials, J. CO_2 Util. 26 (2018) 408–414, https://doi.org/10.1016/j.jcou.2018.05.029.

[195] M. Aresta, A. Dibenedetto, A. Angelini, Catalysis for the valorization of exhaust carbon: from CO_2 to chemicals, materials, and fuels. Technological use of CO_2, Chem. Rev. 114 (3) (2014) 1709–1742, https://doi.org/10.1021/cr4002758.

[196] L. Wang, W. Chen, D. Zhang, Y. Du, R. Amal, S. Qiao, J. Wu, Z. Yin, Surface strategies for catalytic CO_2 reduction: from two-dimensional materials to

nanoclusters to single atoms, Chem. Soc. Rev. 48 (21) (2019) 5310–5349, https://doi.org/10.1039/C9CS00163H.

[197] N. Li, X. Chen, W.J. Ong, D.R. MacFarlane, X. Zhao, A.K. Cheetham, C. Sun, Understanding of electrochemical mechanisms for CO2 capture and conversion into hydrocarbon fuels in transition-metal carbides (MXenes), ACS Nano 11 (11) (2017) 10825–10833, https://doi.org/10.1021/acsnano.7b03738.

[198] L. Liu, A. Corma, Metal catalysts for heterogeneous catalysis: from single atoms to nanoclusters and nanoparticles, Chem. Rev. 118 (10) (2018) 4981–5079, https://doi.org/10.1021/acs.chemrev.7b00776.

[199] J. Li, Z. Wang, H. Chen, Q. Zhang, H. Hu, L. Liu, J. Ye, D. Wang, A surface-alkalinized Ti 3C 2 MXene as an efficient cocatalyst for enhanced photocatalytic CO 2 reduction over ZnO, Catal. Sci. Technol. 11 (14) (2021) 4953–4961, https://doi.org/10.1039/D1CY00716E.

[200] M. Tahir, A. Ali Khan, S. Tasleem, R. Mansoor, W.K. Fan, Titanium carbide (Ti3C2) MXene as a promising co-catalyst for photocatalytic CO2 conversion to energy-efficient fuels: a review, Energy Fuels 35 (13) (2021) 10374–10404, https://doi.org/10.1021/acs.energyfuels.1c00958.

[201] Z. Wang, W. Zhou, X. Wang, X. Zhang, H. Chen, H. Hu, L. Liu, J. Ye, D. Wang, Enhanced photocatalytic CO2 reduction over TiO2 using metalloporphyrin as the cocatalyst, Catalysts 10 (6) (2020) 654, https://doi.org/10.3390/catal10060654.

[202] L. Li, Y. Yang, L. Yang, X. Wang, Y. Zhou, Z. Zou, 3D hydrangea-like InVO4/Ti3C2Tx hierarchical heterosystem collaborating with 2D/2D interface interaction for enhanced photocatalytic CO2 reduction, ChemNanoMat 7 (7) (2021) 815–823, https://doi.org/10.1002/cnma.202100100.

[203] Q. Shi, X. Zhang, Y. Yang, J. Huang, X. Fu, T. Wang, X. Liu, A. Sun, J. Ge, J. Shen, Y. Zhou, 3D hierarchical architecture collaborating with 2D/2D interface interaction in NiAl-LDH/Ti3C2 nanocomposite for efficient and selective photoconversion of CO2, J. Energy Chem. 59 (2021) 9–18, https://doi.org/10.1016/j.jechem.2020.10.038.

[204] L. Li, Y. Yang, B. Zhou, Y. Zhou, Z. Zou, Dimensional matched ultrathin BiVO4/Ti3C2Tx heterosystem for efficient photocatalytic conversion of CO2 to methanol, Mater. Lett. 306 (2022), 130937, https://doi.org/10.1016/j.matlet.2021.130937.

[205] M. Tahir, B. Tahir, In-situ growth of TiO2 imbedded Ti3C2TA nanosheets to construct PCN/Ti3C2TA MXenes 2D/3D heterojunction for efficient solar driven photocatalytic CO2 reduction towards CO and CH4 production, J. Colloid Interface Sci. 591 (2021) 20–37, https://doi.org/10.1016/j.jcis.2021.01.099.

[206] N. Liu, N. Lu, H. Yu, S. Chen, X. Quan, Efficient day-night photocatalysis performance of 2D/2D Ti3C2/Porous g-C3N4 nanolayers composite and its application in the degradation of organic pollutants, Chemosphere 246 (2020), 125760, https://doi.org/10.1016/j.chemosphere.2019.125760.

[207] X. Xiong, Y. Zhao, R. Shi, W. Yin, Y. Zhao, G.I. Waterhouse, T. Zhang, Selective photocatalytic CO2 reduction over Zn-based layered double hydroxides containing tri or tetravalent metals, Sci. Bull. 65 (12) (2020) 987–994, https://doi.org/10.1016/j.scib.2020.03.032.

[208] T. Su, Z.D. Hood, M. Naguib, L. Bai, S. Luo, C.M. Rouleau, I.N. Ivanov, H. Ji, Z. Qin, Z. Wu, Monolayer Ti3C2 T x as an effective co-catalyst for enhanced photocatalytic hydrogen production over TiO2, ACS Appl. Energy Mater. 2 (7) (2019) 4640–4651, https://doi.org/10.1021/acsaem.8b02268.

[209] Z. Yao, H. Sun, H. Sui, X. Liu, 2D/2D heterojunction of R-scheme Ti 3C2 MXene/MoS2 nanosheets for enhanced photocatalytic performance, Nanoscale Res. Lett. 15 (1) (2020) 12, https://link.springer.com/article/10.1186/s11671-020-03314-z.

[210] X. Yi, J. Yuan, H. Tang, Y. Du, B. Hassan, K. Yin, Y. Chen, X. Liu, Embedding few-layer Ti3C2Tx into alkalized g-C3N4 nanosheets for efficient photocatalytic degradation, J. Colloid Interface Sci. 571 (2020) 297–306, https://doi.org/10.1016/j.jcis.2020.03.061.

[211] N.H. Attanayake, H.R. Banjade, A.C. Thenuwara, B. Anasori, Q. Yan, D. R. Strongin, Electrocatalytic CO 2 reduction on earth abundant 2D Mo 2C and Ti 3C 2 MXenes, Chem. Commun. 57 (13) (2021) 1675–1678, https://doi.org/10.1039/D0CC05822J.

[212] F. Li, H. Ai, C. Shi, K.H. Lo, H. Pan, Single transition metal atom catalysts on Ti2CN2 for efficient CO2 reduction reaction, Int. J. Hydrog. Energy 46 (24) (2021) 12886–12896, https://doi.org/10.1016/j.ijhydene.2021.01.096.

[213] H. Jin, C. Guo, X. Liu, J. Liu, A. Vasileff, Y. Jiao, Y. Zheng, S.Z. Qiao, Emerging two-dimensional nanomaterials for electrocatalysis, Chem. Rev. 118 (13) (2018) 6337–6408, https://doi.org/10.1021/acs.chemrev.7b00689.

[214] Y. Xiao, W. Zhang, High throughput screening of M 3C 2 MXenes for efficient CO 2 reduction conversion into hydrocarbon fuels, Nanoscale 12 (14) (2020) 7660–7673, https://doi.org/10.1039/C9NR10598K.

[215] A.D. Handoko, H. Chen, Y. Lum, Q. Zhang, B. Anasori, Z.W. Seh, Two-dimensional titanium and molybdenum carbide MXenes as electrocatalysts for CO 2 reduction, iScience 23 (2020), 101181, https://doi.org/10.1016/j.isci.2020.101181.

[216] A.D. Handoko, K.H. Khoo, T.L. Tan, H. Jin, Z.W. Seh, Establishing new scaling relations on two-dimensional MXenes for CO 2 electroreduction, J. Mater. Chem. A 6 (44) (2018) 21885–21890, https://doi.org/10.1039/C8TA06567E.

[217] A.A. Peterson, F. Abild-Pedersen, F. Studt, J. Rossmeisl, J.K. Nørskov, How copper catalyzes the electroreduction of carbon dioxide into hydrocarbon fuels, Energy Environ. Sci. 3 (9) (2010) 1311–1315, https://doi.org/10.1039/C0EE00071J.

[218] A.A. Peterson, J.K. Nørskov, Activity descriptors for CO2 electroreduction to methane on transition-metal catalysts, J. Phys. Chem. Lett. 3 (2) (2012) 251–258, https://doi.org/10.1021/jz201461p.

[219] H. Chen, A.D. Handoko, J. Xiao, X. Feng, Y. Fan, T. Wang, D. Legut, Z.W. Seh, Q. Zhang, Catalytic effect on CO2 electroreduction by hydroxyl-terminated two-dimensional MXenes, ACS Appl. Mater. Interfaces 11 (40) (2019) 36571–36579, https://doi.org/10.1021/acsami.9b09941.

[220] M. Ye, X. Wang, E. Liu, J. Ye, D. Wang, Boosting the photocatalytic activity of P25 for carbon dioxide reduction by using a surface-alkalinized titanium carbide MXene as cocatalyst, ChemSusChem 11 (10) (2018) 1606–1611, https://doi.org/10.1002/cssc.201800083.

[221] J. Low, L. Zhang, T. Tong, B. Shen, J. Yu, TiO2/MXene Ti3C2 composite with excellent photocatalytic activity, J. Catal. 361 (2018) 255–266, https://doi.org/10.1016/j.jcat.2018.03.009.

[222] Y. He, H. Rao, K. Song, J. Li, Y. Yu, Y. Lou, C. Li, Y. Han, Z. Shi, S. Feng, 3D hierarchical ZnIn2S4 nanosheets with rich Zn vacancies boosting photocatalytic CO2 reduction, Adv. Funct. Mater. 29 (45) (2019), 1905153, https://doi.org/10.1002/adfm.201905153.

[223] B. Wang, A. Zhou, F. Liu, J. Cao, L. Wang, Q. Hu, Carbon dioxide adsorption of two-dimensional carbide MXenes, J. Adv. Ceram. 7 (2018) 237–245, https://doi.org/10.1007/s40145-018-0275-3.

[224] Q. Tang, Z. Sun, S. Deng, H. Wang, Z. Wu, Decorating g-C3N4 with alkalinized Ti3C2 MXene for promoted photocatalytic CO2 reduction performance, J. Colloid Interface Sci. 564 (2020) 406–417, https://doi.org/10.1016/j.jcis.2019.12.091.

[225] A. Houmam, Electron transfer initiated reactions: Bond formation and bond dissociation, Chem. Rev. 108 (7) (2008) 2180–2237, https://doi.org/10.1021/cr068070x.

[226] Q. Zhao, J. Wang, Z. Li, Y. Guo, B. Tang, A. Abudula, G. Guan, Two-dimensional Ti3C2TX-nanosheets/Cu2O composite as a high-performance photocatalyst for decomposition of tetracycline, Carbon Resour. Convers. 4 (2021) 197–204, https://doi.org/10.1016/j.crcon.2021.05.002.

[227] K. Xiong, P. Wang, G. Yang, Z. Liu, H. Zhang, S. Jin, X. Xu, Functional group effects on the photoelectronic properties of MXene (Sc2CT2, T= O, F, OH) and their possible photocatalytic activities, Sci. Rep. 7 (1) (2017), 15095, https://doi.org/10.1038/s41598-017-15233-8.

[228] B. Tunca, T. Lapauw, O.M. Karakulina, M. Batuk, T. Cabioc'h, J. Hadermann, R. Delville, K. Lambrinou, J. Vleugels, Synthesis of MAX phases in the Zr-Ti-Al-C system, Inorg. Chem. 56 (6) (2017) 3489–3498, https://doi.org/10.1021/acs.inorgchem.6b03057.

[229] G. Li, V. Natu, T. Shi, M.W. Barsoum, L.V. Titova, Two-dimensional MXenes Mo2Ti2C3T z and Mo2TiC2T z: microscopic conductivity and dynamics of photoexcited carriers, ACS Appl. Energy Mater. 3 (2) (2020) 1530–1539, https://doi.org/10.1021/acsaem.9b01966.

[230] D. Geng, X. Zhao, Z. Chen, W. Sun, W. Fu, J. Chen, W. Liu, W. Zhou, K.P. Loh, Direct synthesis of large-area 2D Mo2C on in situ grown graphene, Adv. Mater. 29 (35) (2017), 1700072, https://doi.org/10.1002/adma.201700072.

[231] G.R. Berdiyorov, Effect of surface functionalization on the electronic transport properties of Ti3C2 MXene, Europhys. Lett. 111 (6) (2015) 67002, https://doi.org/10.1209/0295-5075/111/67002.

[232] J.L. Hart, K. Hantanasirisakul, A.C. Lang, B. Anasori, D. Pinto, Y. Pivak, J.T. van Omme, S.J. May, Y. Gogotsi, M.L. Taheri, Control of MXenes' electronic properties through termination and intercalation, Nat. Commun. 10 (1) (2019), 522, https://doi.org/10.1038/s41467-018-08169-8.

[233] M.G. Quesne, A. Roldan, N.H. de Leeuw, C.R.A. Catlow, Carbon dioxide and water co-adsorption on the low-index surfaces of TiC, VC, ZrC and NbC: a DFT study, Phys. Chem. Chem. Phys. 21 (20) (2019) 10750–10760, https://doi.org/10.1039/C9CP00924H.

[234] M. Hu, H. Zhang, T. Hu, B. Fan, X. Wang, Z. Li, Emerging 2D MXenes for supercapacitors: status, challenges and prospects, Chem. Soc. Rev. 49 (18) (2020) 6666–6693, https://doi.org/10.1039/D0CS00175A.

[235] P.K. Kalambate, N.S. Gadhari, X. Li, Z. Rao, S.T. Navale, Y. Shen, V.R. Patil, Y. Huang, Recent advances in MXene–based electrochemical sensors and biosensors, TrAC Trends Anal. Chem. 120 (2019), 115643, https://doi.org/10.1016/j.trac.2019.115643.

[236] J. Zhou, X. Zha, F.Y. Chen, Q. Ye, P. Eklund, S. Du, Q. Huang, A two-dimensional zirconium carbide by selective etching of Al3C3 from nanolaminated Zr3Al3C5, Angew. Chem. Int. Ed. 55 (16) (2016) 5008–5013, https://doi.org/10.1002/anie.201510432.

[237] C. Xu, L. Wang, Z. Liu, L. Chen, J. Guo, N. Kang, X.L. Ma, H.M. Cheng, W. Ren, Large-area high-quality 2D ultrathin Mo2C superconducting crystals, Nat. Mater. 14 (11) (2015) 1135–1141, https://doi.org/10.1038/nmat4374.

[238] A. Sherryna, M. Tahir, Role of surface morphology and terminating groups in titanium carbide MXenes (Ti3C2Tx) cocatalysts with engineering aspects for modulating solar hydrogen production: a critical review, Chem. Eng. J. 433 (2022), 134573, https://doi.org/10.1016/j.cej.2022.134573.

[239] Y. Tan, Z. Zhu, X. Zhang, J. Zhang, Y. Zhou, H. Li, H. Qin, Y. Bo, Z. Pan, Nb4C3Tx (MXene) as a new stable catalyst for the hydrogen evolution reaction, Int. J. Hydrog. Energy 46 (2) (2021) 1955–1966, https://doi.org/10.1016/j.ijhydene.2020.10.046.

[240] Z. Sun, D. Music, R. Ahuja, S. Li, J.M. Schneider, Bonding and classification of nanolayered ternary carbides, Phys. Rev. B 70 (9) (2004), 092102, https://doi.org/10.1103/PhysRevB.70.092102.

[241] X. Li, Y. Bai, X. Shi, J. Huang, K. Zhang, R. Wang, L. Ye, Mesoporous g-C3N4/MXene (Ti3C2Tx) heterojunction as a 2D electronic charge transfer for efficient photocatalytic CO2 reduction, Appl. Surf. Sci. 546 (2021), 149111, https://doi.org/10.1016/j.apsusc.2021.149111.

[242] K. Li, X. Lu, Y. Zhang, K. Liu, Y. Huang, H. Liu, Bi3TaO7/Ti3C2 heterojunctions for enhanced photocatalytic removal of water-borne contaminants, Environ. Res. 185 (2020), 109409, https://doi.org/10.1016/j.envres.2020.109409.

[243] K. Wang, Q. Wang, K. Zhang, G. Wang, H. Wang, Selective solar-driven CO2 reduction mediated by 2D/2D Bi2O2SiO3/MXene nanosheets heterojunction, J. Mater. Sci. Technol. 124 (2022) 202–208, https://doi.org/10.1016/j.jmst.2021.10.059.

[244] K. Wang, X. Li, N. Wang, Q. Shen, M. Liu, J. Zhou, N. Li, Z-scheme core–shell meso-TiO2@ ZnIn2S4/Ti3C2 MXene enhances visible light-driven CO2-to-CH4 selectivity, Ind. Eng. Chem. Res. 60 (24) (2021) 8720–8732, https://doi.org/10.1021/acs.iecr.1c00713.

[245] A. Pan, X. Ma, S. Huang, Y. Wu, M. Jia, Y. Shi, Y. Liu, P. Wangyang, L. He, Y. Liu, CsPbBr3 perovskite nanocrystal grown on MXene nanosheets for enhanced photoelectric detection and photocatalytic CO2 reduction, J. Phys. Chem. Lett. 10 (21) (2019) 6590–6597, https://doi.org/10.1021/acs.jpclett.9b02605.

[246] C. Yang, Q. Tan, Q. Li, J. Zhou, J. Fan, B. Li, J. Sun, K. Lv, 2D/2D Ti3C2 MXene/g-C3N4 nanosheets heterojunction for high efficient CO2 reduction photocatalyst: dual effects of urea, Appl. Catal. B: Environ. 268 (2020), 118738, https://doi.org/10.1016/j.apcatb.2020.118738.

[247] F. He, B. Zhu, B. Cheng, J. Yu, W. Ho, W. Macyk, 2D/2D/0D TiO2/C3N4/Ti3C2 MXene composite S-scheme photocatalyst with enhanced CO2 reduction activity, Appl. Catal. B: Environ. 272 (2020), 119006, https://doi.org/10.1016/j.apcatb.2020.119006.

[248] Z. Zhang, B. Wang, H.B. Zhao, J.F. Liao, Z.C. Zhou, T. Liu, B. He, Q. Wei, S. Chen, H.Y. Chen, D.B. Kuang, Self-assembled lead-free double perovskite-MXene heterostructure with efficient charge separation for photocatalytic CO2 reduction, Appl. Catal. B: Environ. 312 (2022), 121358, https://doi.org/10.1016/j.apcatb.2022.121358.

[249] H. Wang, Q. Tang, Z. Wu, Construction of few-layer Ti3C2 MXene and boron-doped g-C3N4 for enhanced photocatalytic CO2 reduction, ACS Sustain. Chem. Eng. 9 (25) (2021) 8425–8434, https://doi.org/10.1021/acssuschemeng.1c01155.

[250] J. Shen, J. Shen, W. Zhang, X. Yu, H. Tang, M. Zhang, Q. Liu, Built-in electric field induced CeO2/Ti3C2-MXene Schottky-junction for coupled photocatalytic tetracycline degradation and CO2 reduction, Ceram. Int. 45 (18) (2019) 24146–24153, https://doi.org/10.1016/j.ceramint.2019.08.123.

[251] J. Dignon, NOx and SOx emissions from fossil fuels: a global distribution, Atmos. Environ. Part A. Gen. Top. 26 (6) (1992) 1157–1163, https://doi.org/10.1016/0960-1686(92)90047-O.

[252] H.M.A. Sharif, M.B. Asif, Y. Wang, Y.N. Hou, B. Yang, X. Xiao, C. Li, Spontaneous intra-electron transfer within rGO@ Fe2O3-MnO catalyst promotes long-term NOx reduction at ambient conditions, J. Hazard. Mater. 441 (2023), 129951, https://doi.org/10.1016/j.jhazmat.2022.129951.

[253] M. Khazaei, A. Mishra, N.S. Venkataramanan, A.K. Singh, S. Yunoki, Recent advances in MXenes: From fundamentals to applications, Current Opinion in Solid State and Materials Science 23 (3) (2019) 164–178.

[254] S. Zhao, Y. Li, Z. Guo, C. Tang, B. Sa, N. Miao, J. Zhou, Z. Sun, Breaking scaling relations in nitric oxide reduction by surface functionalization of MXenes, J. Mater. Chem. A 10 (47) (2022) 25201–25211, https://doi.org/10.1039/D2TA06354A.

[255] J. Liang, Q. Liu, A.A. Alshehri, X. Sun, Recent advances in nanostructured heterogeneous catalysts for N-cycle electrocatalysis, Nano Res. Energy 1 (2) (2022), e9120010, https://doi.org/10.26599/NRE.2022.9120010.

[256] H. Shen, C. Choi, J. Masa, X. Li, J. Qiu, Y. Jung, Z. Sun, Electrochemical ammonia synthesis: mechanistic understanding and catalyst design, Chem 7 (7) (2021) 1708–1754, https://doi.org/10.1016/j.chempr.2021.01.009.

[257] Y. Gao, Y. Yang, L. Hao, S. Hong, X. Tan, T.S. Wu, Y.L. Soo, A.W. Robertson, Q. Yang, Z. Sun, Single Nb atom modified anatase TiO2 (110) for efficient electrocatalytic nitrogen reduction reaction, Chem. Catal. 2 (9) (2022) 2275–2288, https://doi.org/10.1016/j.checat.2022.06.010.

[258] Z. Du, J. Liang, S. Li, Z. Xu, T. Li, Q. Liu, Y. Luo, F. Zhang, Y. Liu, Q. Kong, X. Shi, Alkylthiol surface engineering: an effective strategy toward enhanced electrocatalytic N2-to-NH3 fixation by a CoP nanoarray, J. Mater. Chem. A 9 (24) (2021) 13861–13866, https://doi.org/10.1039/D1TA02424H.

[259] Y. Luo, P. Shen, X. Li, Y. Guo, K. Chu, Sulfur-deficient Bi2S3− x synergistically coupling Ti3C2T x-MXene for boosting electrocatalytic N2 reduction, Nano Res. 15 (5) (2022) 3991–3999, https://doi.org/10.1007/s12274-022-4097-9.

[260] G. Qing, R. Ghazfar, S.T. Jackowski, F. Habizadeh, M.M. Ashtiani, C.P. Chen, M. R. Smith, 3rd and TW Hamann, Chem. Rev. 120 (2020) 5437–5516, https://doi.org/10.1021/acs.chemrev.9b00659.

[261] Q. Wan, Q. Huang, M. Liu, D. Xu, H. Huang, X. Zhang, Y. Wei, Aggregation-induced emission active luminescent polymeric nanoparticles: non-covalent fabrication methodologies and biomedical applications, Appl. Mater. Today 9 (2017) 145–160, https://doi.org/10.1016/j.apmt.2017.06.004.

[262] J. Long, S. Chen, Y. Zhang, C. Guo, X. Fu, D. Deng, J. Xiao, Direct electrochemical ammonia synthesis from nitric oxide, Angew. Chem. Int. Ed. 59 (24) (2020) 9711–9718, https://doi.org/10.1002/anie.202002337.

[263] K. Chen, P. Shen, N. Zhang, D. Ma, K. Chu, Electrocatalytic NO reduction to NH3 on Mo2C nanosheets, Inorg. Chem. 62 (2) (2023) 653–658, https://doi.org/10.1021/acs.inorgchem.2c03714.

[264] W.P. Mounfield III, B. Huang, B. Cai, Y. Shao-Horn, Y. Román-Leshkov, Synthesis of unsupported two-dimensional molybdenum carbide nanosheets for hydrogen evolution, Mater. Lett. 261 (2020), 126987, https://doi.org/10.1016/j.matlet.2019.126987.

[265] P. Liu, J. Liang, J. Wang, L. Zhang, J. Li, L. Yue, Y. Ren, T. Li, Y. Luo, N. Li, B. Tang, High-performance NH3 production via NO electroreduction over a NiO nanosheet array, Chem. Commun. 57 (99) (2021) 13562–13565, https://doi.org/10.1039/D1CC06113E.

[266] S. Zhao, Y. Li, Z. Guo, C. Tang, B. Sa, N. Miao, J. Zhou, Z. Sun, Breaking scaling relations in nitric oxide reduction by surface functionalization of MXenes, J. Mater. Chem. A 10 (47) (2022) 25201–25211, https://doi.org/10.1039/D2TA06354A.

[267] A. Fujishima, K. Honda, Electrochemical photolysis of water at a semiconductor electrode, nature 238 (5358) (1972) 37–38, https://doi.org/10.1038/238037a0.

[268] M.L. Zhang, K.Q. Peng, X. Fan, J.S. Jie, R.Q. Zhang, S.T. Lee, N.B. Wong, Preparation of large-area uniform silicon nanowires arrays through metal-assisted chemical etching, J. Phys. Chem. C. 112 (12) (2008) 4444–4450, https://doi.org/10.1021/jp077471t.

[269] D.S. Bhachu, S.J. Moniz, S. Sathasivam, D.O. Scanlon, A. Walsh, S.M. Bawaked, M. Mokhtar, A.Y. Obaid, I.P. Parkin, J. Tang, C.J. Carmalt, Bismuth oxyhalides: synthesis, structure and photoelectrochemical activity, Chem. Sci. 7 (8) (2016) 4832–4841, https://doi.org/10.1039/C6SC00389C.

[270] A. Hermawan, T. Hasegawa, Y. Asakura, S. Yin, Enhanced visible-light-induced photocatalytic NOx degradation over (Ti, C)-BiOBr/Ti3C2Tx MXene nanocomposites: role of Ti and C doping, Sep. Purif. Technol. 270 (2021), 118815, https://doi.org/10.1016/j.seppur.2021.118815.

[271] A. Nikokavoura, C. Trapalis, Graphene and g-C3N4 based photocatalysts for NOx removal: a review, Appl. Surf. Sci. 430 (2018) 18–52, https://doi.org/10.1016/j.apsusc.2017.08.192.

[272] H. Wang, R. Zhao, H. Hu, X. Fan, D. Zhang, D. Wang, 0D/2D heterojunctions of Ti3C2 MXene QDs/SiC as an efficient and robust photocatalyst for boosting the visible photocatalytic NO pollutant removal ability, ACS Appl. Mater. Interfaces 12 (36) (2020) 40176–40185, https://doi.org/10.1021/acsami.0c01013.

[273] T. Xiong, H. Wang, Y. Zhou, Y. Sun, W. Cen, H. Huang, Y. Zhang, F. Dong, KCl-mediated dual electronic channels in layered gC 3 N 4 for enhanced visible light photocatalytic NO removal, Nanoscale 10 (17) (2018) 8066–8074, https://doi.org/10.1039/C8NR01433G.

[274] X. Hu, Y. Wang, Z. Ling, H. Song, Y. Cai, Z. Li, D. Zu, C. Li, Ternary g-C3N4/TiO2/Ti3C2 MXene S-scheme heterojunction photocatalysts for NOx removal under visible light, Appl. Surf. Sci. 556 (2021), 149817, https://doi.org/10.1016/j.apsusc.2021.149817.

[275] J. Li, Q. Zhang, Y. Zou, Y. Cao, W. Cui, F. Dong, Y. Zhou, Ti3C2 MXene modified g-C3N4 with enhanced visible-light photocatalytic performance for NO purification, J. Colloid Interface Sci. 575 (2020) 443–451, https://doi.org/10.1016/j.jcis.2020.04.119.

[276] X. Zhang, J. Nie, F. Rao, H. Liu, Y. Wang, D. Qu, W. Wu, P. Zhong, G. Zhu, Ti3C2@ TiO2/g-C3N4 heterojunction photocatalyst with improved charge transfer for enhancing visible-light NO selective removal, Ceram. Int. 47 (22) (2021) 31302–31310, https://doi.org/10.1016/j.ceramint.2021.08.003.

[277] Y. Wang, X. Hu, H. Song, Y. Cai, Z. Li, D. Zu, P. Zhang, D. Chong, N. Gao, Y. Shen, C. Li, Oxygen vacancies in actiniae-like Nb2O5/Nb2C MXene heterojunction boosting visible light photocatalytic NO removal, Appl. Catal. B: Environ. 299 (2021), 120677, https://doi.org/10.1016/j.apcatb.2021.120677.

[278] Y. Duan, M. Zhang, L. Wang, F. Wang, L. Yang, X. Li, C. Wang, Plasmonic Ag-TiO2− x nanocomposites for the photocatalytic removal of NO under visible light with high selectivity: the role of oxygen vacancies, Appl. Catal. B: Environ. 204 (2017) 67–77, https://doi.org/10.1016/j.apcatb.2016.11.023.

[279] G. Jiang, X. Li, M. Lan, T. Shen, X. Lv, F. Dong, S. Zhang, Monodisperse bismuth nanoparticles decorated graphitic carbon nitride: Enhanced visible-light-response photocatalytic NO removal and reaction pathway, Appl. Catal. B: Environ. 205 (2017) 532–540, https://doi.org/10.1016/j.apcatb.2017.01.009.

[280] J. Yi, J. Liao, K. Xia, Y. Song, J. Lian, X. She, Y. Liu, S. Yuan, F. Dong, H. Xu, H. Li, Integrating the merits of two-dimensional structure and heteroatom modification into semiconductor photocatalyst to boost NO removal, Chem. Eng. J. 370 (2019) 944–951, https://doi.org/10.1016/j.cej.2019.03.182.

[281] K. Huang, Z. Li, J. Lin, G. Han, P. Huang, Two-dimensional transition metal carbides and nitrides (MXenes) for biomedical applications, Chem. Soc. Rev. 47 (14) (2018) 5109–5124, https://doi.org/10.1039/C7CS00838D.

[282] H. Lin, X. Wang, L. Yu, Y. Chen, J. Shi, Two-dimensional ultrathin MXene ceramic nanosheets for photothermal conversion, Nano Lett. 17 (1) (2017) 384–391, https://doi.org/10.1021/acs.nanolett.6b04339.

[283] R. Jiang, M. Liu, H. Huang, L. Mao, Q. Huang, Y. Wen, Q.Y. Cao, J. Tian, X. Zhang, Y. Wei, Ultrafast construction and biological imaging applications of AIE-active sodium alginate-based fluorescent polymeric nanoparticles through a one-pot microwave-assisted Döbner reaction, Dyes Pigments 153 (2018) 99–105, https://doi.org/10.1016/j.dyepig.2018.02.008.

[284] J. Chen, Q. Huang, H. Huang, L. Mao, M. Liu, X. Zhang, Y. Wei, Recent progress and advances in the environmental applications of MXene related materials, Nanoscale 12 (6) (2020) 3574–3592, https://doi.org/10.1039/C9NR08542D.

[285] Y. Xin, Q. Zhu, T. Gao, X. Li, W. Zhang, H. Wang, D. Ji, Y. Huang, M. Padervand, F. Yu, C. Wang, Photocatalytic NO removal over defective Bi/BiOBr nanoflowers: The inhibition of toxic NO2 intermediate via high humidity, Appl. Catal. B: Environ. 324 (2023), 122238, https://doi.org/10.1016/j.apcatb.2022.122238.

[286] X. Zhang, Z. Ma, X. Zhao, Q. Tang, Z. Zhou, Computational studies on structural and electronic properties of functionalized MXene monolayers and nanotubes, J. Mater. Chem. A 3 (9) (2015) 4960–4966, https://doi.org/10.1039/C4TA06557C.

[287] C. Wang, S. Chen, L. Song, Tuning 2D MXenes by surface controlling and interlayer engineering: methods, properties, and synchrotron radiation characterizations, Adv. Funct. Mater. 30 (47) (2020), 2000869, https://doi.org/10.1002/adfm.202000869.

[288] M. Naguib, O. Mashtalir, J. Carle, V. Presser, J. Lu, L. Hultman, Y. Gogotsi, M. W. Barsoum, Two-dimensional transition metal carbides, ACS Nano 6 (2) (2012) 1322–1331, https://doi.org/10.1021/nn204153h.

[289] H. Javed, M.S. Mateen, A. Ali, S. Zhang, X. Hussain, M. Imran, M. Shah, S.S.A. Han W, The emergence of 2D MXenes based Zn-ion batteries: recent development and prospects, Small 18 (26) (2022), 2201989, https://doi.org/10.1002/smll.202201989.

[290] R. Jiang, X. Xiao, J. Zheng, M. Chen, L. Chen, Remarkable hydrogen absorption/ desorption behaviors and mechanism of sodium alanates in-situ doped with Ti-based 2D MXene, Mater. Chem. Phys. 242 (2020), 122529, https://doi.org/10.1016/j.matchemphys.2019.122529.

[291] Z. Li, Z. Zhuang, F. Lv, H. Zhu, L. Zhou, M. Luo, J. Zhu, Z. Lang, S. Feng, W. Chen, L. Mai, The marriage of the FeN4 moiety and MXene boosts oxygen reduction catalysis: Fe 3d electron delocalization matters, Adv. Mater. 30 (43) (2018), 1803220, https://doi.org/10.1002/adma.201803220.

[292] Y. Xia, T.S. Mathis, M.Q. Zhao, B. Anasori, A. Dang, Z. Zhou, H. Cho, Y. Gogotsi, S. Yang, Thickness-independent capacitance of vertically aligned liquid-crystalline MXenes, Nature 557 (7705) (2018) 409–412, https://doi.org/10.1038/s41586-018-0109-z.

[293] Z. Jin, Y. Fang, X. Wang, G. Xu, S. Wei, C. Zhou, Y. Zhang, Y. Xu, Ultra-efficient electromagnetic wave absorption with ethanol-thermally treated two-dimensional Nb2CTx nanosheets, J. Colloid Interface Sci. 537 (2019) 306–315, https://doi.org/10.1016/j.jcis.2018.11.034.

[294] F. Shahzad, M. Alhabeb, C.B. Hatter, B. Anasori, S. Man Hong, C.M. Koo, Y. Gogotsi, Electromagnetic interference shielding with 2D transition metal carbides (MXenes), Science 353 (6304) (2016) 1137–1140, https://www.science.org/doi/abs/10.1126/science.aag2421.

[295] M. Boota, B. Anasori, C. Voigt, M.Q. Zhao, M.W. Barsoum, Y. Gogotsi, Pseudocapacitive electrodes produced by oxidant-free polymerization of pyrrole between the layers of 2D titanium carbide (MXene), Adv. Mater. 28 (7) (2016) 1517–1522, https://doi.org/10.1002/adma.201504705.

[296] R. Sun, H.B. Zhang, J. Liu, X. Xie, R. Yang, Y. Li, S. Hong, Z.Z. Yu, Highly conductive transition metal carbide/carbonitride (MXene)@ polystyrene nanocomposites fabricated by electrostatic assembly for highly efficient electromagnetic interference shielding, Adv. Funct. Mater. 27 (45) (2017), 1702807, https://doi.org/10.1002/adfm.201702807.

[297] Z. Ling, C.E. Ren, M.Q. Zhao, J. Yang, J.M. Giammarco, J. Qiu, M.W. Barsoum, Y. Gogotsi, Flexible and conductive MXene films and nanocomposites with high capacitance, Proc. Natl. Acad. Sci. 111 (47) (2014) 16676–16681, https://doi.org/10.1073/pnas.1414215111.

[298] Z.W. Gao, W. Zheng, L.Y.S. Lee, Highly enhanced pseudocapacitive performance of vanadium-doped mxenes in neutral electrolytes, Small 15 (40) (2019), 1902649, https://doi.org/10.1002/smll.201902649.

[299] X. Liang, A. Garsuch, L.F. Nazar, Sulfur cathodes based on conductive MXene nanosheets for high-performance lithium–sulfur batteries, Angew. Chem. 127 (13) (2015) 3979–3983, https://doi.org/10.1002/ange.201410174.

[300] W. Bao, C.E. Shuck, W. Zhang, X. Guo, Y. Gogotsi, G. Wang, Boosting performance of Na–S batteries using sulfur-doped Ti3C2T x MXene nanosheets with a strong affinity to sodium polysulfides, ACS Nano 13 (10) (2019) 11500–11509, https://doi.org/10.1021/acsnano.9b04977.

[301] H. Li, X. Wang, H. Li, S. Lin, B. Zhao, J. Dai, W. Song, X. Zhu, Y. Sun, Capacitance improvements of V4C3Tx by NH3 annealing. J. Alloy. Compd. 784 (2019) 923–930, https://doi.org/10.1016/j.jallcom.2019.01.111.

[302] R. Liu, W. Cao, D. Han, Y. Mo, H. Zeng, H. Yang, W. Li, Nitrogen-doped Nb2CTx MXene as anode materials for lithium ion batteries, J. Alloy. Compd. 793 (2019) 505–511, https://doi.org/10.1016/j.jallcom.2019.03.209.

[303] Y. Yoon, A.P. Tiwari, M. Choi, T.G. Novak, W. Song, H. Chang, T. Zyung, S.S. Lee, S. Jeon, K.S. An, Precious-metal-free electrocatalysts for activation of hydrogen evolution with nonmetallic electron donor: chemical composition controllable phosphorous doped vanadium carbide MXene, Adv. Funct. Mater. 29 (30) (2019), 1903443, https://doi.org/10.1002/adfm.201903443.

[304] A.N. Kumar, K. Pal, Amine-functionalized stable Nb 2 CT x MXene toward room temperature ultrasensitive NO 2 gas sensor, Mater. Adv. 3 (12) (2022) 5151–5162, https://doi.org/10.1039/D2MA00301E.

[305] M. Liu, G. Zeng, K. Wang, Q. Wan, L. Tao, X. Zhang, Y. Wei, Recent developments in polydopamine: an emerging soft matter for surface modification and biomedical applications, Nanoscale 8 (38) (2016) 16819–16840, https://doi.org/10.1039/C5NR09078D.

[306] H. Riazi, M. Anayee, K. Hantanasirisakul, A.A. Shamsabadi, B. Anasori, Y. Gogotsi, M. Soroush, Surface modification of a MXene by an aminosilane coupling agent, Adv. Mater. Interfaces 7 (6) (2020), 1902008, https://doi.org/10.1002/admi.201902008.

[307] L. Liao, D. Jiang, K. Zheng, M. Zhang, J. Liu, Industry-scale and environmentally stable Ti3C2Tx MXene based film for flexible energy storage devices, Adv. Funct. Mater. 31 (35) (2021), 2103960, https://doi.org/10.1002/adfm.202103960.

[308] J. Hu, D. Chen, N. Li, Q. Xu, H. Li, J. He, J. Lu, 3D aerogel of graphitic carbon nitride modified with perylene imide and graphene oxide for highly efficient nitric oxide removal under visible light, Small 14 (19) (2018) 1800416, https://doi.org/10.1002/smll.201800416.

[309] Y. Huang, P. Wang, Z. Wang, Y. Rao, J.J. Cao, S. Pu, W. Ho, S.C. Lee, Protonated g-C3N4/Ti3+ self-doped TiO2 nanocomposite films: room-temperature preparation, hydrophilicity, and application for photocatalytic NOx removal, Appl. Catal. B: Environ. 240 (2019) 122–131, https://doi.org/10.1016/j.apcatb.2018.08.078.

[310] D. Liu, D. Chen, N. Li, Q. Xu, H. Li, J. He, J. Lu, ZIF-67–Derived 3D hollow mesoporous crystalline Co3O4 wrapped by 2D g-C3N4 nanosheets for photocatalytic removal of nitric oxide, Small 15 (31) (2019), 1902291, https://doi.org/10.1002/smll.201902291.

[311] M. Fatima, J. Fatheema, N.B. Monir, A.H. Siddique, B. Khan, A. Islam, D. Akinwande, S. Rizwan, Nb-doped MXene with enhanced energy storage capacity and stability, Front. Chem. 8 (2020), 168, https://doi.org/10.3389/fchem.2020.00168.

[312] J. Tian, R. Ning, Q. Liu, A.M. Asiri, A.O. Al-Youbi, X. Sun, Three-dimensional porous supramolecular architecture from ultrathin g-C3N4 nanosheets and reduced graphene oxide: solution self-assembly construction and application as a highly efficient metal-free electrocatalyst for oxygen reduction reaction, ACS Appl. Mater. Interfaces 6 (2) (2014) 1011–1017, https://doi.org/10.1021/am404536w.

[313] Y. Li, Z. Ruan, Y. He, J. Li, K. Li, Y. Jiang, X. Xu, Y. Yuan, K. Lin, In situfabrication of hierarchically porous g-C3N4 and understanding on its enhanced photocatalytic activity based on energy absorption, Appl. Catal. B: Environ. 236 (2018) 64–75, https://doi.org/10.1016/j.apcatb.2018.04.082.

[314] T. Ke, S. Shen, K. Rajavel, K. Yang, D. Lin, In situ growth of TiO2 nanoparticles on nitrogen-doped Ti3C2 with isopropyl amine toward enhanced photocatalytic activity, J. Hazard. Mater. 402 (2021), 124066, https://doi.org/10.1016/j.jhazmat.2020.124066.

[315] C. Peng, X. Xie, W. Xu, T. Zhou, P. Wei, J. Jia, K. Zhang, Y. Cao, H. Wang, F. Peng, R. Yang, Engineering highly active Ag/Nb2O5@ Nb2CTx (MXene) photocatalysts via steering charge kinetics strategy, Chem. Eng. J. 421 (2021), 128766, https://doi.org/10.1016/j.cej.2021.128766.

[316] Y.H. Li, F. Zhang, Y. Chen, J.Y. Li, Y.J. Xu, Photoredox-catalyzed biomass intermediate conversion integrated with H 2 production over Ti 3C 2 T x/CdS composites, Green. Chem. 22 (1) (2020) 163–169, https://doi.org/10.1039/C9GC03332G.

[317] Y. Yang, D. Zhang, Q. Xiang, Plasma-modified Ti 3C 2 T x/CdS hybrids with oxygen-containing groups for high-efficiency photocatalytic hydrogen production, Nanoscale 11 (40) (2019) 18797–18805, https://doi.org/10.1039/C9NR07242J.

[318] V. Kamysbayev, A.S. Filatov, H. Hu, X. Rui, F. Lagunas, D. Wang, R.F. Klie, D. V. Talapin, Covalent surface modifications and superconductivity of two-dimensional metal carbide MXenes, Science 369 (6506) (2020) 979–983, https://doi.org/10.1126/science.aba8311.

[319] I.C. Onyia, S.O. Ezeonu, D. Bessarabov, K.O. Obodo, Density functional theory studies of transition metal doped Ti3N2 MXene monolayer, Comput. Mater. Sci. 197 (2021), 110613, https://doi.org/10.1016/j.commatsci.2021.110613.

[320] T. Zhou, W. Zhao, K. Yang, Q. Yao, Y. Li, B. Wu, J. Liu, Atomic vacancy defect, frenkel defect and transition metals (Sc, V, Zr) doping in Ti4N3 MXene nanosheet: a first-principles investigation, Appl. Sci. 10 (7) (2020) 2450, https://doi.org/10.3390/app10072450.

[321] O. Mashtalir, K.M. Cook, V.N. Mochalin, M. Crowe, M.W. Barsoum, Y. Gogotsi, Dye adsorption and decomposition on two-dimensional titanium carbide in aqueous media, J. Mater. Chem. A 2 (35) (2014) 14334–14338, https://doi.org/10.1039/C4TA02638A.

[322] M. Cao, F. Wang, L. Wang, W. Wu, W. Lv, J. Zhu, Room temperature oxidation of Ti3C2 MXene for supercapacitor electrodes, J. Electrochem. Soc. 164 (14) (2017) A3933, https://doi.org/10.1149/2.1541714jes.

[323] J. Palisaitis, I. Persson, J. Halim, J. Rosen, P.O. Persson, On the structural stability of MXene and the role of transition metal adatoms, Nanoscale 10 (23) (2018) 10850–10855, https://doi.org/10.1039/C8NR01986J.

[324] T. Habib, X. Zhao, S.A. Shah, Y. Chen, W. Sun, H. An, J.L. Lutkenhaus, M. Radovic, M.J. Green, Oxidation stability of Ti3C2Tx MXene nanosheets in solvents and composite films, npj 2D Mater. Appl. 3 (1) (2019), 8, https://doi.org/10.1038/s41699-019-0089-3.

[325] J. Zhu, E. Ha, G. Zhao, Y. Zhou, D. Huang, G. Yue, L. Hu, N. Sun, Y. Wang, L.Y. S. Lee, C. Xu, Recent advance in MXenes: a promising 2D material for catalysis, sensor and chemical adsorption, Coord. Chem. Rev. 352 (2017) 306–327, https://doi.org/10.1016/j.ccr.2017.09.012.

[326] Y. Vasseghian, E.N. Dragoi, F. Almomani, A comprehensive review on MXenes as new nanomaterials for degradation of hazardous pollutants: deployment as heterogeneous sonocatalysis, Chemosphere 287 (2022), 132387, https://doi.org/10.1016/j.chemosphere.2021.132387.

[327] K. Nasrin, V. Sudharshan, K. Subramani, M. Sathish, Insights into 2D/2D MXene heterostructures for improved synergy in structure toward next-generation supercapacitors: a review, Adv. Funct. Mater. 32 (18) (2022), 2110267, https://doi.org/10.1002/adfm.202110267.

[328] S. Biswas, P.S. Alegaonkar, MXene: evolutions in chemical synthesis and recent advances in applications, Surfaces 5 (1) (2021) 1–34, https://www.mdpi.com/2571-9637/5/1/1.

[329] K. Mondal, P. Ghosh, Exfoliation of Ti2C and Ti3C2 Mxenes from bulk trigonal phases of titanium carbide: a theoretical prediction, Solid State Commun. 299 (2019), 113657, https://doi.org/10.1016/j.ssc.2019.113657.

[330] J. Jiang, S. Bai, J. Zou, S. Liu, J.P. Hsu, N. Li, G. Zhu, Z. Zhuang, Q. Kang, Y. Zhang, Improving stability of MXenes, Nano Res. 15 (7) (2022) 6551–6567, https://doi.org/10.1007/s12274-022-4312-8.

[331] X. Xie, N. Zhang, Z.R. Tang, M. Anpo, Y.J. Xu, Ti3C2Tx MXene as a Janus cocatalyst for concurrent promoted photoactivity and inhibited photocorrosion, Appl. Catal. B: Environ. 237 (2018) 43–49, https://doi.org/10.1016/j.apcatb.2018.05.070.

[332] X. Yu, A. Manthiram, Electrochemical energy storage with a reversible nonaqueous room-temperature aluminum–sulfur chemistry, Adv. Energy Mater. 7 (18) (2017), 1700561, https://doi.org/10.1002/aenm.201700561.

[333] J. Guo, Q. Peng, H. Fu, G. Zou, Q. Zhang, Heavy-metal adsorption behavior of two-dimensional alkalization-intercalated MXene by first-principles calculations, J. Phys. Chem. C 119 (36) (2015) 20923–20930, https://doi.org/10.1021/acs.jpcc.5b05426.

[334] R. Fernandez-Prini, Le Chatelier's principle and the prediction of the effect of temperature on solubilities, J. Chem. Educ. 59 (7) (1982) 550, https://doi.org/10.1021/ed059p550.

[335] L. Zhang, W. Song, H. Liu, H. Ding, Y. Yan, R. Chen, Influencing factors on synthesis and properties of MXene: a review, Processes 10 (9) (2022) 1744, https://doi.org/10.3390/pr10091744.

[336] A. Iqbal, J. Hong, T.Y. Ko, C.M. Koo, Improving oxidation stability of 2D MXenes: synthesis, storage media, and conditions, Nano Converg. 8 (1) (2021) 1–22, https://doi.org/10.1186/s40580-021-00259-6.

[337] F. Xia, J. Lao, R. Yu, X. Sang, J. Luo, Y. Li, J. Wu, Ambient oxidation of Ti3C2 MXene initialized by atomic defects, Nanoscale 11 (48) (2019) 23330–23337, https://doi.org/10.1039/C9NR07236E.

[338] C.J. Zhang, S. Pinilla, N. McEvoy, C.P. Cullen, B. Anasori, E. Long, S.H. Park, Chem. Mater. 29 (11) (2017) 4848–4856, https://doi.org/10.1021/acs.chemmater.7b00745. A. s. Seral-Ascaso, A. Shmeliov and D. Krishnan.

[339] W. Cui, Z.Y. Hu, R.R. Unocic, G. Van Tendeloo, X. Sang, Atomic defects, functional groups and properties in MXenes, Chin. Chem. Lett. 32 (1) (2021) 339–344, https://doi.org/10.1016/j.cclet.2020.04.024.

[340] A. Bandyopadhyay, D. Ghosh, S.K. Pati, Effects of point defects on the magnetoelectronic structures of MXenes from first principles, Phys. Chem. Chem. Phys. 20 (6) (2018) 4012–4019, https://doi.org/10.1039/C7CP07165E.

[341] L.H. Karlsson, J. Birch, J. Halim, M.W. Barsoum, P.O. Persson, Atomically resolved structural and chemical investigation of single MXene sheets, Nano Lett. 15 (8) (2015) 4955–4960, https://doi.org/10.1021/acs.nanolett.5b00737.

[342] K. Rajavel, T. Ke, K. Yang, D. Lin, Condition optimization for exfoliation of two dimensional titanium carbide (Ti3C2Tx), Nanotechnology 29 (9) (2018), 095605 https://iopscience.iop.org/article/10.1088/1361-6528/aaa687/meta.

[343] G. Murali, J. Rawal, J.K.R. Modigunta, Y.H. Park, J.H. Lee, S.Y. Lee, S.J. Park, I. In, A review on MXenes: new-generation 2D materials for supercapacitors, Sustain. Energy Fuels 5 (22) (2021) 5672–5693, https://doi.org/10.1039/D1SE00918D.

[344] A. Lipatov, M. Alhabeb, M.R. Lukatskaya, A. Boson, Y. Gogotsi, A. Sinitskii, Effect of synthesis on quality, electronic properties and environmental stability of individual monolayer Ti3C2 MXene flakes, Adv. Electron. Mater. 2 (12) (2016), 1600255, https://doi.org/10.1002/aelm.201600255.

[345] M.A. Hope, A.C. Forse, K.J. Griffith, M.R. Lukatskaya, M. Ghidiu, Y. Gogotsi, C. P. Grey, NMR reveals the surface functionalisation of Ti 3C 2 MXene, Phys. Chem. Chem. Phys. 18 (7) (2016) 5099–5102, https://pubs.rsc.org/en/content/articlehtml/2016/cp/c6cp00330c.

[346] M. Alhabeb, K. Maleski, B. Anasori, P. Lelyukh, L. Clark, S. Sin, Y. Gogotsi, Guidelines for synthesis and processing of two-dimensional titanium carbide (Ti3C2T x MXene), Chem. Mater. 29 (18) (2017) 7633–7644, https://doi.org/10.1021/acs.chemmater.7b02847.

[347] M. Seredych, C.E. Shuck, D. Pinto, M. Alhabeb, E. Precetti, G. Deysher, B. Anasori, N. Kurra, Y. Gogotsi, High-temperature behavior and surface chemistry of carbide MXenes studied by thermal analysis, Chem. Mater. 31 (9) (2019) 3324–3332, https://doi.org/10.1021/acs.chemmater.9b00397.

[348] A. Feng, Y. Yu, F. Jiang, Y. Wang, L. Mi, Y. Yu, L. Song, Fabrication and thermal stability of NH4HF2-etched Ti3C2 MXene, Ceram. Int. 43 (8) (2017) 6322–6328, https://doi.org/10.1016/j.ceramint.2017.02.039.

[349] X. Zhao, A. Vashisth, J.W. Blivin, Z. Tan, D.E. Holta, V. Kotasthane, S.A. Shah, T. Habib, S. Liu, J.L. Lutkenhaus, M. Radovic, pH, nanosheet concentration, and antioxidant affect the oxidation of Ti3C2Tx and Ti2CTx MXene dispersions, Adv. Mater. Interfaces 7 (20) (2020), 2000845, https://doi.org/10.1002/admi.202000845.

[350] H. Zhang, L. Wang, Q. Chen, P. Li, A. Zhou, X. Cao, Q. Hu, Preparation, mechanical and anti-friction performance of MXene/polymer composites, Mater. Des. 92 (2016) 682–689, https://doi.org/10.1016/j.matdes.2015.12.084.

[351] S. Doo, A. Chae, D. Kim, T. Oh, T.Y. Ko, S.J. Kim, D.Y. Koh, C.M. Koo, Mechanism and kinetics of oxidation reaction of aqueous Ti3C2T x suspensions at different pHs and temperatures, ACS Appl. Mater. Interfaces 13 (19) (2021) 22855–22865, https://doi.org/10.1021/acsami.1c04663 s.

[352] T. Habib, X. Zhao, S.A. Shah, Y. Chen, W. Sun, H. An, J.L. Lutkenhaus, M. Radovic, M.J. Green, Oxidation stability of Ti3C2Tx MXene nanosheets in solvents and composite films, npj 2D Mater. Appl. 3 (1) (2019), 8, https://doi.org/10.1038/s41699-019-0089-3.

[353] R.B. Rakhi, B. Ahmed, M.N. Hedhili, D.H. Anjum, H.N. Alshareef, Effect of postetch annealing gas composition on the structural and electrochemical properties of Ti2CT x MXene electrodes for supercapacitor applications, Chem. Mater. 27 (15) (2015) 5314–5323, https://doi.org/10.1021/acs.chemmater.5b01623.

[354] K. Wang, Y. Zhou, W. Xu, D. Huang, Z. Wang, M. Hong, Fabrication and thermal stability of two-dimensional carbide Ti3C2 nanosheets, Ceram. Int. 42 (7) (2016) 8419–8424, https://doi.org/10.1016/j.ceramint.2016.02.059.

[355] M. Naguib, O. Mashtalir, M.R. Lukatskaya, B. Dyatkin, C. Zhang, V. Presser, Y. Gogotsi, M.W. Barsoum, One-step synthesis of nanocrystalline transition metal oxides on thin sheets of disordered graphitic carbon by oxidation of MXenes, Chem. Commun. 50 (56) (2014) 7420–7423, https://pubs.rsc.org/en/content/articlehtml/2014/cc/c4cc01646g.

[356] J. Li, R. Qin, L. Yan, Z. Chi, Z. Yu, N. Li, M. Hu, H. Chen, G. Shan, Plasmonic light illumination creates a channel to achieve fast degradation of Ti3C2T x nanosheets, Inorg. Chem. 58 (11) (2019) 7285–7294, https://doi.org/10.1021/acs.inorgchem.9b00329.

[357] X. Zhan, C. Si, J. Zhou, Z. Sun, MXene and MXene-based composites: synthesis, properties and environment-related applications, Nanoscale Horiz. 5 (2) (2020) 235–258, https://doi.org/10.1039/C9NH00571D.

[358] T.N. Nguyen, C.T. Dinh, Gas diffusion electrode design for electrochemical carbon dioxide reduction, Chem. Soc. Rev. 49 (21) (2020) 7488–7504, https://doi.org/10.1039/D0CS00230E.

[359] T. Amrillah, A. Hermawan, V.N. Alviani, Z.W. Seh, S. Yin, MXenes and their derivatives as nitrogen reduction reaction catalysts: recent progress and perspectives, Mater. Today Energy 22 (2021) 100864, https://doi.org/10.1016/j.mtener.2021.100864.

[360] S. Abdolhosseinzadeh, X. Jiang, H. Zhang, J. Qiu, C.J. Zhang, Perspectives on solution processing of two-dimensional MXenes, Mater. Today 48 (2021) 214–240, https://doi.org/10.1016/j.mattod.2021.02.010.

[361] H. Zou, B. He, P. Kuang, J. Yu, K. Fan, Metal–organic framework-derived nickel–cobalt sulfide on ultrathin mxene nanosheets for electrocatalytic oxygen evolution, ACS Appl. Mater. Interfaces 10 (26) (2018) 22311–22319, https://doi.org/10.1021/acsami.8b06272.

[362] M. Khazaei, A. Ranjbar, K. Esfarjani, D. Bogdanovski, R. Dronskowski, S. Yunoki, Insights into exfoliation possibility of MAX phases to MXenes, Phys. Chem. Chem. Phys. 20 (13) (2018) 8579–8592, https://doi.org/10.1039/C7CP08645H.

[363] Y. Wei, L. Xiang, H. Ou, F. Li, Y. Zhang, Y. Qian, L. Hao, J. Diao, M. Zhang, P. Zhu, Y. Liu, MXene-based conductive organohydrogels with long-term environmental stability and multifunctionality, Adv. Funct. Mater. 30 (48) (2020), 2005135, https://doi.org/10.1002/adfm.202005135.

[364] M.Q. Zhao, M. Torelli, C.E. Ren, M. Ghidiu, Z. Ling, B. Anasori, M.W. Barsoum, Y. Gogotsi, 2D titanium carbide and transition metal oxides hybrid electrodes for Li-ion storage, Nano Energy 30 (2016) 603–613, https://doi.org/10.1016/j.nanoen.2016.10.062.

[365] H. Tang, Q. Hu, M. Zheng, Y. Chi, X. Qin, H. Pang, Q. Xu, MXene–2D layered electrode materials for energy storage, Prog. Nat. Sci.: Mater. Int. 28 (2) (2018) 133–147, https://doi.org/10.1016/j.pnsc.2018.03.003.

[366] A. Nikkhah, H. Nikkhah, A. Nouri, A.W. Mohammad, A.W. Lun, N. law Yong, R. Rohani, E. Mahmoudi, MXene: from synthesis to environment remediation, Chin. J. Chem. Eng. (2023), https://doi.org/10.1016/j.cjche.2023.02.028.